

<sup>1</sup> Observation of the Higgs boson in the  $WW^*$   
<sup>2</sup> channel and search for Higgs boson pair  
<sup>3</sup> production in the  $b\bar{b}b\bar{b}$  channel with the  
<sup>4</sup> ATLAS detector

<sup>5</sup> A DISSERTATION PRESENTED  
<sup>6</sup> BY  
<sup>7</sup> TOMO LAZOVICH  
<sup>8</sup> TO  
<sup>9</sup> THE DEPARTMENT OF PHYSICS

<sup>10</sup> IN PARTIAL FULFILLMENT OF THE REQUIREMENTS  
<sup>11</sup> FOR THE DEGREE OF  
<sup>12</sup> DOCTOR OF PHILOSOPHY  
<sup>13</sup> IN THE SUBJECT OF  
<sup>14</sup> PHYSICS

<sup>15</sup> HARVARD UNIVERSITY  
<sup>16</sup> CAMBRIDGE, MASSACHUSETTS  
<sup>17</sup> MAY 2016

<sup>18</sup> ©2016 – TOMO LAZOVICH

<sup>19</sup> ALL RIGHTS RESERVED.

20    **Observation of the Higgs boson in the  $WW^*$  channel and search  
21    for Higgs boson pair production in the  $b\bar{b}b\bar{b}$  channel with the  
22    ATLAS detector**

23    **ABSTRACT**

24    This dissertation presents two studies: the observation and measurement of the Higgs boson in the  
25     $H \rightarrow WW^* \rightarrow \ell\nu\ell\nu$  channel at  $\sqrt{s} = 7$  TeV and  $\sqrt{s} = 8$  TeV and a search for Higgs pair pro-  
26    duction in the  $HH \rightarrow b\bar{b}b\bar{b}$  channel at  $\sqrt{s} = 13$  TeV with the ATLAS detector in  $pp$  collisions at the  
27    Large Hadron Collider.

28    First, the discovery of a particle consistent with the Higgs in  $4.8 \text{ fb}^{-1}$  at  $\sqrt{s} = 7$  TeV and  $5.8 \text{ fb}^{-1}$  at  
29     $\sqrt{s} = 8$  TeV is discussed. Then, the measurement of the Higgs boson signal strength and cross section  
30    in both the gluon fusion and vector boson fusion (VBF) production modes using  $20.3 \text{ fb}^{-1}$  of  $\sqrt{s} =$   
31     $8$  TeV data combined with  $4.8 \text{ fb}^{-1}$  of  $7$  TeV data is shown. The combined signal strength is measured  
32    to be  $\mu = 1.09^{+0.23}_{-0.21}$ . The total observed significance of the  $H \rightarrow WW^*$  process is observed to be  
33     $6.1\sigma$  (with  $5.8\sigma$  expected). Advanced methods for background reduction and estimation, particularly in  
34    same-flavor lepton final states, are shown. The VBF signal strength is measured to be  $\mu_{\text{VBF}} = 1.27^{+0.53}_{-0.45}$   
35    with an observed significance of  $3.2\sigma$  (with  $2.7\sigma$  expected). In the VBF channel, a selection requirement  
36    based method, the precursor to the final multivariate technique used for the result, is detailed.

37    Finally, a search for Higgs pair production in the  $b\bar{b}b\bar{b}$  final state with  $3.2 \text{ fb}^{-1}$  at  $\sqrt{s} = 13$  TeV  
38    is presented. A particular focus is placed on a tailored signal region for resonant production of Higgs  
39    pairs at high masses, utilizing novel techniques in object reconstruction to increase signal acceptance in  
40    boosted final state topologies. No significant excesses are observed, and upper limits on cross sections are  
41    placed for spin-2 Randall Sundrum gravitons (RSG) and narrow spin-0 resonances. The cross section of  
42     $\sigma(pp \rightarrow G_{\text{KK}}^* \rightarrow hh \rightarrow b\bar{b}b\bar{b})$  with  $k/\bar{M}_{\text{Pl}} = 1$  is constrained to be less than  $70 \text{ fb}$  for masses in the  
43    range  $600 < m_{G_{\text{KK}}^*} < 3000 \text{ GeV}$ . For the RSG model with  $k/\bar{M}_{\text{Pl}} = 2$ , cross sections limits between

Dissertation advisors: Professors João Guimarães da Costa  
and Melissa Franklin

Tomo Lazovich

- <sup>44</sup> 40 fb and 200 fb are set for the mass range of  $500 < m_{G_{\text{KK}}^*} < 3000$  GeV. The cross section upper  
<sup>45</sup> limits for  $\sigma(pp \rightarrow H \rightarrow hh \rightarrow b\bar{b}b\bar{b})$  ranges from 30 to 300 fb in the mass range of  $500 < m_H <$   
<sup>46</sup> 3000 GeV.

# Contents

47

48	o INTRODUCTION	I
49	I Theoretical and Experimental Background	5
50	I.1 THE PHYSICS OF THE HIGGS BOSON	6
51	1.1 The Standard Model of Particle Physics . . . . .	6
52	1.2 Electroweak Symmetry Breaking and the Higgs . . . . .	8
53	1.3 Higgs Boson Production and Decay . . . . .	II
54	1.4 Higgs Pair Production in the Standard Model . . . . .	15
55	1.5 Higgs Pair Production in Theories Beyond the Standard Model . . . . .	16
56	1.6 Conclusion . . . . .	21
57	2 THE ATLAS DETECTOR AND THE LARGE HADRON COLLIDER	22
58	2.1 The Large Hadron Collider . . . . .	23
59	2.2 The ATLAS Detector . . . . .	25
60	2.3 The ATLAS Muon New Small Wheel Upgrade . . . . .	36
61	2.4 Object Reconstruction in ATLAS . . . . .	40
62	II Observation and measurement of Higgs boson decays to $WW^*$ in LHC	
63	Run 1 at $\sqrt{s} = 7$ and 8 TeV	49
64	3 $H \rightarrow WW^* \rightarrow \ell\nu\ell\nu$ ANALYSIS STRATEGY	50
65	3.1 Introduction . . . . .	50
66	3.2 The $H \rightarrow WW^* \rightarrow \ell\nu\ell\nu$ signal in ATLAS . . . . .	51
67	3.3 Background processes . . . . .	52
68	3.4 Shared signal region selection requirements . . . . .	55
69	3.5 Background reduction in same-flavor final states . . . . .	58
70	3.6 Parameters of interest and statistical treatment . . . . .	63
71	4 THE DISCOVERY OF THE HIGGS BOSON AND THE ROLE OF THE $H \rightarrow WW^* \rightarrow \ell\nu\ell\nu$ CHANNEL	
72	4.1 Introduction . . . . .	69

74	4.2	Data and simulation samples . . . . .	70
75	4.3	$H \rightarrow WW \rightarrow e\nu\mu\nu$ search . . . . .	70
76	4.4	$H \rightarrow \gamma\gamma$ search . . . . .	75
77	4.5	$H \rightarrow ZZ \rightarrow 4\ell$ search . . . . .	76
78	4.6	Combined results . . . . .	77
79	4.7	Conclusion . . . . .	79
80	5	OBSERVATION OF VECTOR BOSON FUSION PRODUCTION OF $H \rightarrow WW^* \rightarrow \ell\nu\ell\nu$	82
81	5.1	Introduction . . . . .	82
82	5.2	Data and simulation samples . . . . .	83
83	5.3	Object selection . . . . .	87
84	5.4	Analysis selection . . . . .	90
85	5.5	Background estimation . . . . .	98
86	5.6	Systematic uncertainties . . . . .	109
87	5.7	Results . . . . .	113
88	6	COMBINED RUN I $H \rightarrow WW^* \rightarrow \ell\nu\ell\nu$ RESULTS	118
89	6.1	Introduction . . . . .	118
90	6.2	Results of gluon fusion $H \rightarrow WW^* \rightarrow \ell\nu\ell\nu$ search . . . . .	119
91	6.3	Signal strength measurements in ggF and VBF production . . . . .	121
92	6.4	Measurement of Higgs couplings to vector bosons and fermions . . . . .	124
93	6.5	Higgs production cross section measurement . . . . .	125
94	6.6	Conclusion . . . . .	126
95	III	Search for Higgs pair production in the $HH \rightarrow b\bar{b}b\bar{b}$ channel in LHC	
96		Run 2 at $\sqrt{s} = 13$ TeV	128
97	7	SEARCH FOR HIGGS PAIR PRODUCTION IN BOOSTED $b\bar{b}b\bar{b}$ FINAL STATES	129
98	7.1	Introduction . . . . .	129
99	7.2	Motivation . . . . .	130
100	7.3	Data and simulation samples . . . . .	132
101	7.4	Event reconstruction and object selection . . . . .	134
102	7.5	Event selection . . . . .	137
103	7.6	Data-driven background estimation . . . . .	140
104	7.7	Systematic uncertainties . . . . .	146
105	7.8	Results . . . . .	149

106	8 COMBINED LIMITS FROM BOOSTED AND RESOLVED SEARCHES	151
107	8.1 Introduction . . . . .	151
108	8.2 Resolved results . . . . .	152
109	8.3 Search technique and results . . . . .	152
110	8.4 Limit setting . . . . .	153
111	IV Looking ahead	157
112	9 CONCLUSION	158
113	APPENDIX A OPTIMIZATION OF $b$ -TAGGING WORKING POINT IN $X \rightarrow HH \rightarrow b\bar{b}b\bar{b}$	
114	SEARCH	160
115	APPENDIX B $b$ -TAGGING PERFORMANCE AT HIGH $p_T$	162
116	B.1 MV2 algorithm overview . . . . .	162
117	B.2 Changes in MV2 score at high $p_T$ . . . . .	163
118	B.3 Tagging efficiency by individual jet . . . . .	166
119	B.4 Effect of multiple $b$ -quarks inside one jet . . . . .	167
120	B.5 Changes in track quality at high $p_T$ . . . . .	168
121	REFERENCES	170

# Listing of figures

123	1.1	The particles of the Standard Model and their properties [6]. . . . .	7
124	1.2	The four most common Higgs boson production modes at the LHC: (a) gluon-gluon fu-	
125		sion, (b) vector boson fusion, (c) $W/Z + H$ production, (d) $t\bar{t}H$ production . . . . .	11
126	1.3	Higgs production cross sections as a function of center of mass energy ( $\sqrt{s}$ ) at a $pp$ collider [18]. .	12
127	1.4	Higgs boson branching ratios as a function of $m_H$ [18]. . . . .	14
128	1.5	The two leading diagrams for Standard Model di-Higgs production at the LHC: (a) box di-	
129		agram, (b) Higgs self coupling . . . . .	16
130	1.6	Diagrams with new vertices for non-resonant Higgs pair production arising in composite	
131		Higgs models . . . . .	17
132	1.7	Generic Feynman diagram for resonant Higgs pair production in BSM theories . . . . .	18
133	1.8	Branching ratios for a spin-2 Randall-Sundrum graviton as a function of mass computed in	
134		MadGraph with the CP3-Origins implementation [24, 30] . . . . .	18
135	1.9	$\sigma \times BR(HH)$ for RSG as a function of mass computed in MadGraph with the CP3-Origins	
136		implementation [24, 30] . . . . .	19
137	1.10	RSG width as a function of mass computed in MadGraph with the CP3-Origins implemen-	
138		tation [24, 30] . . . . .	20
139	1.11	Branching ratios for heavy Higgs $H$ in Type I (left) and Type II (right) 2HDM models with	
140		$\tan \beta = 1.5$ and $\cos(\beta - \alpha) = 0.1(0.01)$ for Type I (Type II). [28] . . . . .	21
141	2.1	A schematic view of the LHC ring [36] . . . . .	23
142	2.2	A full diagram of the ATLAS detector [32] . . . . .	26
143	2.3	The ATLAS coordinate system . . . . .	27
144	2.4	Layout of the ATLAS Inner Detector system [40] . . . . .	28
145	2.5	Layout of the ATLAS calorimeter system [32] . . . . .	30
146	2.6	Layout of the ATLAS muon system [32] . . . . .	32
147	2.7	Predicted field integral as a function of $ \eta $ for the ATLAS magnet system [32] . . . . .	34
148	2.8	ATLAS trigger rates for Level-1 triggers as a function of instantaneous luminosity in 2012	
149		and 2015 operation. These are single object triggers for electromagnetic clusters (EM), muons	
150		(MU), jets (J), missing energy (XE), and $\tau$ leptons (TAU). The threshold of the trigger is given	
151		in the name in GeV. [42] . . . . .	35
152	2.9	Instantaneous luminosity as a function of time for data recorded by ATLAS at different cen-	
153		ter of mass energies [43, 44] . . . . .	36

154	2.10	MDT tube hit (solid) and segment (dashed) efficiency as a function of hit rate per tube [45]	37
155	2.11	Trigger rate as a function of $p_T$ threshold with and without the NSW upgrade [45]	38
156	2.12	Illustrations of the geometry (left) and operating principle (right) of the micromegas detector [45]	39
158	2.13	Geometry of the sTGC detector [45]	40
159	2.14	Illustration of particle interactions in ATLAS [48]	41
160	2.15	Electron performance: (a) reconstruction efficiency as a function of electron $E_T$ [50] (b) energy resolution in simulation as a function of $ \eta $ for different energy electrons [51]	42
162	2.16	Muon performance: (a) reconstruction efficiency as a function of muon $p_T$ (b) dimuon mass resolution as a function of average $p_T$ [52]	44
164	2.17	Jet energy response after calibration as a function of true $p_T$ in simulation [56]	45
165	2.18	Light jet rejection (1/efficiency) vs. $b$ -jet efficiency for MV1 and its input algorithms (a) [57] and MV2 (b) [58] in simulated $t\bar{t}$ events. The numbers in the algorithm names in (b) refer to the fraction of charm events used in the MV2 training.	46
168	2.19	Resolution of $E_T^{\text{miss}}$ components as a function of $\sum E_T$ before pileup suppression with different pileup techniques [60]	48
170	3.1	Branching ratios for a $WW$ system. $q$ refers to quarks. $\ell$ can be either an electron or muon, and the leptonic branching ratios of the $\tau$ are included. For example, the $\ell\nu qq$ final state includes one $W$ decaying to $e\nu$ , $\mu\nu$ , or $\tau\nu$ . $\tau_h$ refer to hadronic decays of the $\tau$ .	52
172	3.2	Feynman diagram for Standard Model $WW$ production	53
174	3.3	Feynman diagrams for top pair production (left) and $Wt$ production (right)	53
175	3.4	An example Feynman diagram of $W$ +jets production	54
176	3.5	An example Feynman diagram of $Z$ +jets production	55
177	3.6	An illustration of the unique analysis signal regions [61]. The most sensitive regions for both gluon fusion and vector boson fusion production are underlined.	56
179	3.7	A graphical illustration of the $E_{T,\text{rel}}^{\text{miss}}$ calculation	57
180	3.8	Predicted backgrounds (compared with data) as a function of $n_j$ (a and b) and $n_b$ (c) after pre-selection requirements	59
182	3.9	An event display of a $Z/\gamma^*$ + jets event illustrating the effect of pileup interactions	60
183	3.10	The RMS of different missing transverse momentum definitions as a function of the average number of interactions per bunch crossing	60
184	3.11	The difference between the true and reconstructed values of the missing transverse momentum (a) and $m_T$ (b) in a gluon fusion signal sample	62
186	3.12	Comparison of $f_{\text{recoil}}$ distributions for $Z/\gamma^*$ +jets, $H \rightarrow WW^*$ , and other backgrounds with real neutrinos.	63
188	3.13	Signal significance as a function of required value for $f_{\text{recoil}}$ and $p_{T,\text{rel}}^{\text{miss}(\text{trk})}$ in the ggF $H \rightarrow WW^*$ with $n_j = 0$	64

191	4.1	Jet multiplicity distribution in data and MC after applying lepton, jet, and $E_{\text{T},\text{rel}}^{\text{miss}}$ selections. The $WW$ and top backgrounds have been normalized using control samples, and the hashed band indicates the total uncertainty on the prediction. [1] . . . . .	71
192			
193	4.2	Comparison of $m_{\text{T}}$ between data and simulation in the $n_j = 0$ $WW$ (a) and $n_j = 1$ top (b) control samples [1] . . . . .	73
194			
195	4.3	$m_{\text{T}}$ distribution in the $H \rightarrow WW \rightarrow e\nu\mu\nu$ $n_j \leq 1$ channels for 8 TeV data [1]. . . . .	75
196			
197	4.4	Diphoton mass spectrum in 7 and 8 TeV data. Panel a) shows the unweighted data distri- bution superimposed on the background fit, while panel c) shows the data where each event category is weighted by its signal to background ratio. Panels b) and d) show the respective distributions with background subtracted [1]. . . . .	76
198			
199	4.5	Four lepton invariant mass spectrum ( $m_{4\ell}$ ) in 7 and 8 TeV data compared to background estimate. A 125 GeV SM Higgs signal is shown in blue [1]. . . . .	77
200			
201	4.6	Local $p_0$ distribution as a function of hypothesized Higgs mass for the $H \rightarrow ZZ^* \rightarrow 4\ell$ (a), $H \rightarrow \gamma\gamma$ (b), and $H \rightarrow WW^* \rightarrow \ell\nu\ell\nu$ (c) channels. Dashed curves show expected results, while solid curves show observed. Red curves are from 7 TeV data, blue curves from 8 TeV, and black curved combined [1]. . . . .	79
202			
203	4.7	Combined 95% CL limits (a), local $p_0$ values (b), and signal strength measurement (c) as a function of Higgs mass [1]. . . . .	80
204			
205	4.8	Comparison of measured signal strength $\mu$ for a 126 GeV Higgs in the 7 and 8 TeV datasets [1]. . . . .	81
206			
207	4.9	Two dimensional likelihood as a function of signal strength $\mu$ and Higgs mass $m_H$ [1]. . . . .	81
208			
209	5.1	A comparison of the subleading lepton $p_{\text{T}}$ spectrum between VBF $H \rightarrow WW^*$ production and $t\bar{t}$ background . . . . .	84
210			
211	5.2	Leading jet $\eta$ in VBF $H \rightarrow WW^*$ (red) and $t\bar{t}$ (black) . . . . .	92
212			
213	5.3	Distributions of (a) $m_{jj}$ , (b) $\Delta y_{jj}$ , (c) $C_{\ell 1}$ , and (d) $\sum m_{\ell j}$ , for the VBF analysis. The top panels compare simulation and data, while the bottom panels show normalized distributions for all background processes and signal [61]. . . . .	94
214			
215	5.4	A cartoon of the $WW$ final state. Momenta are represented with thin arrows, spins with thick arrows. [61] . . . . .	95
216			
217	5.5	Event display of a VBF candidate event [61]. . . . .	96
218			
219	5.6	Distributions of $m_{\ell\ell}$ (top left), $\Delta\phi_{\ell\ell}$ (top right), and $m_{\text{T}}$ (bottom), Higgs topology vari- ables used in the selection requirements of the cut-based signal region and as inputs to the BDT result. These are plotted after all of the BDT pre-training selection cuts [61]. . . . .	99
220			
221	5.7	Distributions of $m_{jj}$ (top left), $\Delta y_{jj}$ (top right), $\sum C_{\ell}$ (bottom), VBF topology variables used in the selection requirements of the cut-based signal region and as inputs to the BDT result. These are plotted after all of the BDT pre-training selection cuts [61]. . . . .	100
222			
223	5.8	Distributions of $m_{jj}$ (a) and $O_{\text{BDT}}$ (b) in the VBF $n_b = 1$ top CR [61]. . . . .	102
224			

227	5.9	Comparison of $m_{jj}$ shape in a same flavor $Z \rightarrow \ell\ell$ control region and the VBF cut-based signal region. . . . .	104
228	5.10	General illustration of the ABCD region definitions for $Z/\gamma^* \rightarrow \ell\ell$ background estimation. . . . .	105
231	5.11	Distribution of $m_{T2}$ in the $WW$ validation region of the VBF analysis [61]. . . . .	106
232	5.12	Extrapolation factors for the $W + \text{jets}$ estimate derived for muons (a) and electrons (b) as a function of lepton $p_T$ [61]. . . . .	108
234	5.13	Background composition in final VBF signal region [61]. . . . .	109
235	5.14	Variations in the top background extrapolation factor in the cut-based analysis due to PDF uncertainties, binned in $m_T$ . . . . .	III
237	5.15	Variations in the top background extrapolation factor in the cut-based analysis due to QCD scale uncertainties, binned in $m_T$ . . . . .	II2
239	5.16	Post-fit distributions in the cut-based VBF analysis. Panel (a) shows the one-dimensional $m_T$ distribution, while (b) shows the data candidates split into the bins of $m_T$ and $m_{jj}$ used in the final fit [61]. . . . .	II5
242	5.17	Postfit distributions in the BDT VBF analysis [61]. . . . .	II6
243	5.18	Overlap between cut-based and BDT VBF signal region candidates in the $m_{jj}$ - $m_T$ plane. .	II6
244	6.1	Post-fit $m_T$ distribution in the $n_j \leq 1$ regions [61]. . . . .	120
245	6.2	Best fit signal strength $\hat{\mu}$ as a function of hypothesized $m_H$ [61]. . . . .	122
246	6.3	Local $p_0$ as a function of $m_H$ [61]. . . . .	122
247	6.4	Likelihood as a function of $\mu_{\text{VBF}}/\mu_{\text{ggF}}$ [61]. . . . .	123
248	6.5	Likelihood scan as a function of $\mu_{\text{VBF}}$ and $\mu_{\text{ggF}}$ [61]. . . . .	124
249	6.6	Likelihood scan as a function of $\kappa_F$ and $\kappa_V$ [61]. . . . .	125
250	6.7	Comparison of signal strength measurements in different Higgs decay channels on ATLAS [90].	127
251	7.1	Parton luminosity ratios as a function of resonance mass $M_X$ for 13/8 TeV and 7/8 TeV [91].	130
252	7.2	Summary of $HH$ branching ratios [92]. . . . .	131
253	7.3	Minimum $\Delta R$ between $B$ decay vertices for different RSG masses in a $G_{\text{KK}}^* \rightarrow HH \rightarrow 4b$ sample with $c = 1$ . . . . .	132
255	7.4	Trigger efficiency for events passing all signal region selections as a function of mass in $G_{\text{KK}}^* \rightarrow HH \rightarrow 4b$ samples with $c = 1$ [101]. In the trigger names, “j” refers to a jet or jets. “ht” refers to $H_T$ , the scalar sum of transverse momenta in the event. “bloose” refers to a loose b-tagging requirement applied to the jet. “aor” refers to anti- $k_T$ jets with $R = 1.0$ . The numbers at the end are the thresholds on the given quantity in GeV. . . . .	134
258	7.5	Comparison of untrimmed and trimmed jet masses for large radius jets in a RSG sample with $m_{G_{\text{KK}}^*} = 1$ TeV. JES (JMS) refers to the standard jet energy (mass) scale calibration for ATLAS [56].	135

262	7.6 Efficiency of finding two $b$ -jets from each Higgs in an RSG event using calorimeter jets with $R = 0.3$ or different track jet radii [105] . . . . .	136
263		
264	7.7 Illustration of the boosted selection requirements on Higgs candidates. Each large-radius calorime- ter jet (Higgs candidate) must contain two track jets . . . . .	138
265		
266	7.8 Acceptance $\times$ efficiency as a function of mass for (a) RSG and (b) narrow heavy scalar sig- nal models [107]. . . . .	139
267		
268	7.9 Efficiency of requiring 3 or 4 $b$ -tagged track jets vs. RSG mass. The efficiency quoted is rel- ative to the previous selection requirements (rather than an absolute efficiency). . . . .	140
269		
270	7.10 $M_J^{\text{sublead}}$ vs. $M_J^{\text{lead}}$ in a 2 $b$ -tag data sample. The signal region is defined by the inner black contour ( $X_{hh} < 1.6$ ) and the sideband region is defined by the outer contour ( $R_{hh} >$ 35.8 GeV). The region between the black contours is the control region. The mass region which is enriched in $t\bar{t}$ background is also shown for illustration. [107] . . . . .	142
271		
272		
273		
274	7.II An illustration of the data-driven background estimation technique for the boosted anal- ysis . . . . .	143
275		
276	7.12 Leading large-R jet mass in the 3 $b$ (a) and 4 $b$ (b) sideband regions. The multijet and $t\bar{t}$ back- grounds are estimated using the data-driven methods described above. Because their normal- izations are derived in the sideband region, the total background normalization is constrained by default to match the normalization of the data [107]. . . . .	144
277		
278		
279		
280	7.13 Di-jet invariant mass ( $M_{2,J}$ ) in the 3 $b$ (a) and 4 $b$ (b) control regions. The multijet and $t\bar{t}$ back- grounds are estimated using the data-driven methods described above [107]. . . . .	145
281		
282	7.14 Di-jet invariant mass ( $M_{2,J}$ ) in the 3 $b$ (a) and 4 $b$ (b) signal regions. The multijet and $t\bar{t}$ back- grounds are estimated using the data-driven methods described above. In the 3 $b$ region, a graviton signal with $m_{G_{KK}^*} = 1.8$ TeV and $c = 1$ is overlaid, with the cross section mul- tiplied by a factor of 50 so that the signal is visible. In the 4 $b$ region, signals with $m_{G_{KK}^*} =$ 1.0 TeV and $m_{G_{KK}^*} = 1.5$ TeV are overlaid, both with $c = 1$ and the yields multiplied by factors of 2 and 5 respectively [107]. . . . .	146
283		
284		
285		
286		
287		
288	8.1 Di-jet invariant mass ( $M_{2,J}$ ) in the resolved signal region. A graviton signal with $m_{G_{KK}^*} =$ 800 GeV and $c = 1$ is overlaid. [107]. . . . .	153
289		
290	8.2 Expected and observed upper limit as a function of mass for $G_{KK}^*$ in the RSG model with (a) $c = 1$ and (b) $c = 2$ , as well as (c) $H$ with fixed $\Gamma_H = 1$ GeV, at the 95% confidence	
291		
292	level in the $CL_s$ method. [107] . . . . .	156
293		
294	A.I Estimated significance as a function of signal mass for RSG $c = 1$ models in the 3 $b$ (a) and 4 $b$ (b) regions for different $b$ -tagging efficiency working points . . . . .	161
295		
296	B.I Summary of the inputs to the MV2 $b$ -tagging algorithm . . . . .	163
297	B.2 $p_T$ of the leading track jet in the leading calorimeter jet for different signal masses in RSG $c =$ 1 models . . . . .	164

298	B.3	MV <sub>2c2o</sub> score for the leading track jet (a) and subleading track jet (b) of the leading calorime-	
299		ter jet for different signal masses in RSG $c = 1$ models . . . . .	164
300	B.4	IP <sub>3D</sub> log-likelihood ratio ( $\log(p_b/p_u)$ ) of the leading track jet in the leading calorimeter jet	
301		for different signal masses in RSG $c = 1$ models . . . . .	165
302	B.5	Mass (a) and number of tracks (b) for the secondary vertices computed with the SV <sub>1</sub> algo-	
303		rithm. When no secondary vertex is found, the quantities are assigned to default negative val-	
304		ues. . . . .	165
305	B.6	Mass (a) and number of tracks (b) for vertices computed with the JetFitter algorithm. When	
306		no vertices are found, the quantities are assigned to default negative values. . . . .	166
307	B.7	MV <sub>2c2o</sub> $b$ -tagging efficiency for each of the four track jets in the boosted $4b$ selection as a func-	
308		tion of RSG mass for $c = 1$ models. . . . .	167
309	B.8	MV <sub>2c2o</sub> score (a) and SV <sub>1</sub> mass (b) for leading track jets with two truth $b$ quarks ( $n_{tb,lead} =$	
310		2) compared to those with only one truth $b$ ( $n_{tb,lead} = 1$ ). . . . .	168
311	B.9	Track fit $\chi^2/n_{DOF}$ (a) and number of pixel detector hits (b) for the leading track of the lead-	
312		ing track jet in different mass RSG $c = 1$ samples . . . . .	169
313	B.10	MV <sub>2c2o</sub> score (a) and SV <sub>1</sub> mass (b) for leading track jets whose leading track jet has at least	
314		four pixel hits ( $N_{pix} \geq 4$ ) compared to those which do not ( $N_{pix} < 4$ ). . . . .	169

# Listing of tables

315

316	1.1	Production cross sections for a 125 GeV Higgs boson at $\sqrt{s} = 8$ TeV with scale and PDF uncertainties [18]. . . . .	13
317			
318	1.2	Branching ratios for a 125 GeV Higgs boson [18]. . . . .	15
319	1.3	Possible channels for Higgs searches. Checkmarks denote the most sensitive production modes [5]. . . . .	15
320			
321	1.4	Production cross sections for pair production of a 125 GeV Higgs boson at $\sqrt{s} = 14$ TeV with total uncertainty [19]. The uncertainties include QCD scale and PDF variations as well as uncertainties on $\alpha_S$ . . . . .	16
322			
323			
324	2.1	Evolution of LHC machine conditions [38, 39] . . . . .	25
325	2.2	Performance requirements for the ATLAS detector [32]. . . . .	37
326	2.3	Signal efficiencies for $WH$ production with $H \rightarrow b\bar{b}$ and $H \rightarrow WW^* \rightarrow \mu\nu qq$ under different trigger configurations [45]. . . . .	40
327			
328	3.1	A summary of backgrounds to the $H \rightarrow WW^* \rightarrow \ell\nu\ell\nu$ signal . . . . .	55
329			
330	4.1	Monte carlo generators used to model signal and background for the Higgs search [1]. . . . .	70
331	4.2	Normalization factors (ratio of data and MC yields in a control sample) for the Standard Model $WW$ and top backgrounds in the $H \rightarrow WW^* \rightarrow \ell\nu\ell\nu$ analysis [1]. Only statistical uncertainties are shown. . . . .	73
332			
333	4.3	Data and expected yields for signal and background in the final $H \rightarrow WW^* \rightarrow \ell\nu\ell\nu$ signal region. Uncertainties shown are both statistical and systematic. [1] . . . . .	74
334			
335	4.4	Summary of the expected and observed significance and measured signal strengths in the combined 7 and 8 TeV datasets for the Higgs discovery analysis [1]. . . . .	78
336			
337	5.1	Single lepton triggers used for electrons and muons. A logical “or” of the triggers listed for each lepton type is taken. Units are in GeV, and the $i$ denotes an isolation requirement in the trigger. . . . .	84
338			
339			
340	5.2	Di-lepton triggers used for different flavor combinations. The two thresholds listed refer to leading and sub-leading leptons, respectively. The di-muon trigger only requires a single lepton at level-1. . . . .	84
341			
342			

343	5.3 Trigger efficiency for signal events and relative gain of adding a dilepton trigger on top of the single lepton trigger selection. The first lepton is the leading, while the second is the sub-leading. Efficiencies shown here are for the ggF signal in the $n_j = 0$ category but are comparable for the VBF signal. . . . .	85
344		
345		
346		
347	5.4 Monte Carlo samples used to model the signal and background processes [61]. . . . .	86
348		
349		
350	5.5 $p_T$ dependent isolation requirements for muons. Muons are required to have the amount of calorimeter or track based cone sums be less than this fraction of their $p_T$ . . . . .	88
351		
352	5.6 $p_T$ dependent requirements for electrons. Electrons are required to have the amount of calorimeter or track based cone sums be less than this fraction of their $E_T$ . . . . .	89
353		
354	5.7 Event selection for the $n_j \geq 2$ VBF analysis in the 8 TeV cut-based analysis [61]. . . . .	97
355		
356	5.8 Top normalization factors computed at each stage of the cut-based selection. Uncertainties are statistical only. . . . .	101
357		
358	5.9 Top normalization factors computed for each bin of $O_{\text{BDT}}$ . Uncertainties are statistical only. . . . .	101
359		
360	5.10 $Z/\gamma^* \rightarrow \tau\tau$ correction factors for the VBF cut-based analysis. Uncertainties are statisti-	
361	cal only. . . . .	104
362		
363	5.11 $Z/\gamma^* \rightarrow \ell\ell$ normalization factors for cut-based and BDT analyses. Uncertainties are sta-	
364	tistical only. . . . .	106
365		
366	5.12 Systematic uncertainties for various processes in the cut-based VBF analysis, given in units of % change in yield. Values are given for the low $m_{jj}$ signal region. . . . .	110
367		
368	5.13 Composition of the post-fit uncertainties (in %) on the total signal ( $N_{\text{sig}}$ ), total background ( $N_{\text{bkg}}$ ), and individual background yields in the VBF analysis [61]. . . . .	113
369		
370	5.14 Event selection for the VBF BDT analysis. The event yields in (a) are shown after the pre-	
371	selection and the additional requirements applied before the BDT classification (see text).	
372		
373	The event yields in (b) are given in bins in $O_{\text{BDT}}$ after the classification [61]. . . . .	114
374		
375		
376		
377		
378	6.1 All signal regions definitions input into final statistical fit [61]. . . . .	119
379		
380	6.2 Post-fit yields in the different ggF and VBF dedicated signal regions [61]. . . . .	120
381		
382		
383	7.1 Summary of requirements on objects used in the $X \rightarrow HH \rightarrow b\bar{b}b\bar{b}$ search . . . . .	137
384		
385	7.2 Effect of boosted selection on data, RSG signal models, $t\bar{t}$ , and $Z + \text{jets}$ . The numbers from simula-	
386	tion are normalized with the MC generator cross section and do not take into account the data driven estimates described in section 7.6 [108]. . . . .	141
387		
388	7.3 Mass region definitions used for background estimation . . . . .	142
389		
390	7.4 Parameters derived for exponential fit to background $M_{2J}$ shape in the 3 $b$ and 4 $b$ signal re-	
391	gions [108] . . . . .	145
392		
393	7.5 The number of events in data and predicted background events in the boosted 3-tag and 4-	
394	tag sideband and control regions. The uncertainties shown are statistical only. [107] . . . . .	146
395		
396		
397		
398		
399		
400		
401		
402		
403		
404		
405		
406		
407		
408		
409		
410		
411		
412		
413		
414		
415		
416		
417		
418		
419		
420		
421		
422		
423		
424		
425		
426		
427		
428		
429		
430		
431		
432		
433		
434		
435		
436		
437		
438		
439		
440		
441		
442		
443		
444		
445		
446		
447		
448		
449		
450		
451		
452		
453		
454		
455		
456		
457		
458		
459		
460		
461		
462		
463		
464		
465		
466		
467		
468		
469		
470		
471		
472		
473		
474		
475		
476		
477		
478		
479		
480		
481		
482		
483		
484		
485		
486		
487		
488		
489		
490		
491		
492		
493		
494		
495		
496		
497		
498		
499		
500		
501		
502		
503		
504		
505		
506		
507		
508		
509		
510		
511		
512		
513		
514		
515		
516		
517		
518		
519		
520		
521		
522		
523		
524		
525		
526		
527		
528		
529		
530		
531		
532		
533		
534		
535		
536		
537		
538		
539		
540		
541		
542		
543		
544		
545		
546		
547		
548		
549		
550		
551		
552		
553		
554		
555		
556		
557		
558		
559		
560		
561		
562		
563		
564		
565		
566		
567		
568		
569		
570		
571		
572		
573		
574		
575		
576		
577		
578		
579		
580		
581		
582		
583		
584		
585		
586		
587		
588		
589		
590		
591		
592		
593		
594		
595		
596		
597		
598		
599		
600		
601		
602		
603		
604		
605		
606		
607		
608		
609		
610		
611		
612		
613		
614		
615		
616		
617		
618		
619		
620		
621		
622		
623		
624		
625		
626		
627		
628		
629		
630		
631		
632		
633		
634		
635		
636		
637		
638		
639		
640		
641		
642		
643		
644		
645		
646		
647		
648		
649		
650		
651		
652		
653		
654		
655		
656		
657		
658		
659		
660		
661		
662		
663		
664		
665		
666		
667		
668		
669		
670		
671		
672		
673		
674		
675		
676		
677		
678		
679		
680		
681		
682		
683		
684		
685		
686		
687		
688		
689		
690		
691		
692		
693		
694		
695		
696		
697		
698		
699		
700		
701		
702		
703		
704		
705		
706		
707		
708		
709		
710		
711		
712		
713		
714		
715		
716		
717		
718		
719		
720		
721		
722		
723		
724		
725		
726		
727		
728		
729		
730		
731		
732		
733		
734		
735		
736		
737		
738		
739		
740		
741		
742		
743		
744		
745		
746		
747		
748		
749		
750		
751		
752		
753		
754		
755		
756		
757		
758		
759		
760		
761		
762		
763		
764		
765		
766		
767		
768		
769		
770		
771		
772		
773		
774		
775		
776		
777		
778		
779		
780		
781		
782		
783		
784		
785		
786		
787		
788		
789		
790		
791		
792		
793		
794		
795		
796		
797		
798		
799		
800		
801		
802		
803		
804		
805		
806		
807		
808		
809		
810		
811		
812		
813		
814		
815		
816		
817		
818		
819		
820		
821		
822		
823		
824		
825		
826		
827		
828		
829		
830		
831		
832		
833		
834		
835		
836		
837		
838		

378	7.6 Summary of systematic uncertainties in the total background and signal event yields (expressed in %) in the boosted 3-tag and 4-tag signal regions. Systematic uncertainties on the signal normalization are shown for models with $m_{G_{KK}^*} = 1.5$ TeV and both $c = 1$ and $c = 2$ as well as a narrow width heavy scalar. . . . .	148
382	7.7 Alternate fit functions used to model the $M_{JJ}$ distribution in the QCD multijet background. In the equations, $x = M_{JJ}/\sqrt{s}$ . . . . .	149
384	7.8 Observed yields in the 3-tag and 4-tag signal regions for the boosted analysis compared to the predicted number of background events Errors correspond to the total uncertainties in the predicted event yields. The yields for a graviton with $m_{G_{KK}^*} = 1$ TeV and $c = 1$ are also shown. [107] . . . . .	150
388	8.1 Observed yields in the resolve selection 4-tag signal region compared to the predicted num- ber of background events Errors correspond to the total uncertainties in the predicted event yields. The yields for a graviton with $m_{G_{KK}^*} = 800$ GeV and $c = 1$ are also shown. [107] .	152
389		
390		



# Acknowledgments

393 I have been a member of the Harvard ATLAS group for many years now, first as an undergraduate and  
394 then as a graduate student. As a result, I have had the privilege of interacting with many amazing people  
395 there over the years and have accumulated a large list of folks to thank.

396 First and foremost, I must thank the two people who have effectively been my academic parents since  
397 I started in the Harvard group: João Guimarães da Costa and Melissa Franklin. Melissa Franklin and  
398 João Guimarães da Costa. They have both been so important to both my academic and personal devel-  
399 opment that I can't even put one before the other. João has been an excellent PhD advisor, showing me  
400 how to look at the big picture and helping me navigate the sometimes complicated politics of ATLAS.  
401 He got me started on my first projects with ATLAS as a young college sophomore before there was even  
402 beam in the LHC (go cosmic ray muons!). He has also been a constant source of advice and support,  
403 even when we have been on different continents. Melissa gave me my start in HEP as a summer student  
404 on CDF and has been an unbelievable mentor throughout my time at Harvard. I still remember our  
405 weekly chalkboard particle physics lessons after that first summer. She also graciously took me on as a  
406 co-advisee after João moved on to his new position at IHEP. I am incredibly lucky to have had both of  
407 them as advisors.

408 Another mentor who was essential to my development as a graduate student is Paolo Giromini. His  
409 uncanny knowledge and intuition about detectors is unmatched and I am very grateful to have had the  
410 chance to work with him on the micromegas for the ATLAS New Small Wheel upgrade project. I owe  
411 essentially all my practical knowledge about detectors (and building things in general) to him. I also  
412 appreciated his unique sense of humor which made sometimes difficult tasks much easier to get through.

413 I am grateful to John Huth and Masahiro Morii for their helpful advice as the other professors in the  
414 Harvard ATLAS group as well. I especially thank John for helping me get started on the micromegas  
415 trigger project and being a great professor to TF particle physics for. Additionally I thank Howard

416 Georgi for serving as my third committee member and offering me feedback throughout my graduate  
417 career.

418 I also owe enormous thanks to Hugh Skottowe, the postdoc that I worked most closely with in my  
419 early years as a graduate student. He was always able to help me through complicated tasks in everything  
420 from writing code to understanding difficult physics concepts. I particularly enjoyed walking down to  
421 his office in Palfrey at random times and talking through whatever problem I was tackling on that day.

422 Alex Tuna, the second postdoc that I worked closely with at Harvard, deserves great thanks as well.  
423 He helped me push through to the end of my graduate career and offered great advice along the way.

424 Being at Harvard, I have seen an incredible array of graduate students graduate before me: Ben Smith,  
425 Verena Martinez Outschoorn, Srivas Prasad, Michael Kagan, Giovanni Zevi Della Porta, Laura Jeanty,  
426 Kevin Mercurio, William Spearman, and Andy Yen. I want to thank them all for showing me what a  
427 good physicist looks like and for patiently answering my questions and offering insightful advice about  
428 physics and life.

429 Getting through graduate school would not have been possible without the support and friendship  
430 of the other students in our group. Thanks to Emma Tolley for geeking out with me about cool com-  
431 puting stuff, going to taste delicious beers with me, and helping start the Palfrey tradition of Taco Tues-  
432 days. Thanks to Brian Clark for being a great friend and housing companion both in Kirkland House  
433 and in our tiny summer apartment in Geneva (and thanks to his partner Allison Goff for the same rea-  
434 sons!). Thanks to Siyuan Sun for giving me my first aikido lesson and always being there for great con-  
435 versations, big and small. Tony (Baojia) Tong deserves special recognition for working with me on the  
436 4b analysis and putting up with my sometimes strange requests (and giving me rides to the Val Thoiry  
437 Migros so I wouldn't have to pay exorbitant Geneva grocery prices!). Stephen Chan is probably the only  
438 student in the group who both understands my references to the Sopranos and makes some of his own.  
439 To the younger graduate students - Karri Di Petrillo, Jennifer Roloff, Julia Gonski, and Ann Wang - I  
440 want to say thank you for making the group a fun and lively place to be and giving all of us energy that  
441 the older graduate students like myself can sometimes lack.

442 I'd like to thank Annie Wei and Gray Putnam, the two undergraduates I have worked with as a gradu-

443 ate student. Their unbelievable intuition and quickness in picking up difficult particle physics concepts  
444 is inspiring.

445 I would also like to thank all of the postdocs that I have interacted with in my time in the Harvard  
446 group: Kevin Black, Alberto Belloni (who would always ask me “Do you have it?”...I can now say that  
447 I do!), Shulamit Moed, Corrinne Mills, Geraldine Conti, David Lopez Mateos, Chris Rogan, Valerio  
448 Ippolito, and Stefano Zambito.

449 There are many people on ATLAS who have helped me get to this point as well. In the *WW* group,  
450 I have to thank Jonathan Long, Joana Machado Miguens, Ben Cerio, Philip Chang, Bonnie Chow,  
451 Richard Polifka, Heberth Torres, Tae Min Hong, and Jennifer Hsu for being wonderful colleagues and  
452 making the entire analysis run smoothly. In the *4b* group, I have to thank Qi Zeng, Tony Tong, Alex  
453 Tuna, Michael Kagan, Max Bellomo, John Alison, and Patrick Bryant.

454 Kirkland House was my home for the last three years of graduate school and was an wonderful envi-  
455 ronment and support system. I want to thank my fellow tutors, especially Brian Clark and Allison Goff  
456 (again), Zach Abel, Kelly Bodwin, Alex Lupsasca, John and Pam Park, Luke and Erin Walczewski, and  
457 Philip Gant for their friendship and support. I also want to thank Kate Drizos Cavell, Bob Butler, and  
458 the Faculty Deans Tom and Verena Conley.

459 There are still a few friends that haven’t been covered yet and deserve great thanks. Jake Connors and  
460 Meredith MacGregor have been absolutely wonderful friends and I thank them in particular for the  
461 many home-cooked meals and great conversations we’ve had in their apartment. Nihar Shah has been  
462 my friend and confidant since we were both wee freshmen in Harvard Yard. Gareth Kafka, though he  
463 sits on the “neutrino” side of Palfrey House, has made days there more fun and has also been an enthusi-  
464 astic participant in the Palfrey Taco Tuesdays.

465 Being at Harvard necessarily means having to navigate through bureaucracy at some point or another.  
466 I thank Lisa Cacciabuado, Carol Davis, and Jacob Barandes for always having open doors and being the  
467 most kind, helpful people in the Physics department.

468 I thank Venky Narayananamurti for putting on a great SPU course that I was proud to be a part of and  
469 TF for. I’d also like to thank Jim Waldo for offering me much advice about working in Computer Science

<sup>470</sup> and giving me a fun data project to be a part of in my free time.

<sup>471</sup> I grew up in a very tight knit Serbian community on the south side of Chicago which helped make  
<sup>472</sup> me the person I am today. I would like to thank all of the people at St. Simeon Mirotochivi Serbian  
<sup>473</sup> Orthodox Church who have always been sources of enthusiasm and support in my life.

<sup>474</sup> I would not be here without the unconditional love and constant support and encouragement of my  
<sup>475</sup> family. To my pokojni Dedas Branko and Miloje, my pokojni Baba Milka, and my Baba Desa, I want to  
<sup>476</sup> say thank you for instilling in me at an early age the love of curiosity and storytelling that I have carried  
<sup>477</sup> throughout my life. To my sister Angelina, I want to say thank you for always loving me and being my  
<sup>478</sup> partner in crime throughout our childhoods. To my parents, Miroljub and Nada, Tata and Mama, I  
<sup>479</sup> really cannot express how grateful I am to you and how much I owe you. As I look back now I see how  
<sup>480</sup> I am a combination of both of your best qualities and every day I am in situations where I understand  
<sup>481</sup> more and more the lessons you made sure to teach me and the sacrifices you made to make sure I got the  
<sup>482</sup> best possible education. I love you all.

<sup>483</sup> Finally, I have to thank my soul mate, the one person in my life who understands me more than any-  
<sup>484</sup> one else, my fiancée Kelly Brock. You are my sounding board, my support system, my cheerleader (fig-  
<sup>485</sup> uratively and literally!), my best friend, my role model, and my everything. I would not have gotten  
<sup>486</sup> through graduate school without you and my life would not be the same without you. I cannot wait to  
<sup>487</sup> start our new lives together as the married doctors, tackling whatever comes our way with the same zeal  
<sup>488</sup> with which we tackled graduate school. I love you with all my heart and soul.

# 0

489

490

## Introduction

491 The Higgs boson is often described as one of the cornerstones of the Standard Model. Since the con-  
492 ception of the Higgs mechanism as the source of electroweak symmetry breaking in the early 1960s,  
493 countless collider experiments have searched for this elusive particle. This dissertation presents multi-  
494 ple studies of the Higgs boson with the ATLAS detector at the Large Hadron Collider (LHC).

495 One of the first priorities of the early LHC was the search for the Higgs boson. This search was first  
496 tackled in three main channels:  $H \rightarrow \gamma\gamma$ ,  $H \rightarrow ZZ^*$ , and  $H \rightarrow WW^*$ . Each channel has its own  
497 merits, but the  $WW^*$  is particularly suited to searching over a wide range of masses. The  $H \rightarrow WW$   
498 branching ratio is large and it is the primary decay channel above the  $2m_W$  mass threshold.

499 While the rate of events produced in  $H \rightarrow WW^*$  is large, the channel poses some challenges. First,  
500 the most common mode of study for this channel is  $H \rightarrow WW^* \rightarrow \ell\nu\ell\nu$ . With neutrinos in the  
501 final state, it is not possible to fully reconstruct the invariant mass of the parent Higgs like the  $\gamma\gamma$  and  
502  $ZZ \rightarrow 4\ell$  channels. Second, the final state topology is mimicked by a wide variety of backgrounds that

503 need to be properly estimated. This means tailored selection requirements for background reduction  
504 and robust background estimation techniques must both be developed.

505 In 2012, the ATLAS and CMS experiments announced the discovery of a new particle consistent with  
506 the Higgs boson [1, 2]. In ATLAS, this discovery was made with  $4.8 \text{ fb}^{-1}$  collected at  $\sqrt{s} = 7 \text{ TeV}$  and  
507  $5.8 \text{ fb}^{-1}$  at  $\sqrt{s} = 8 \text{ TeV}$ . The  $H \rightarrow WW^* \rightarrow \ell\nu\ell\nu$  analysis played an important role in this discovery.  
508 After the discovery, measurement of the properties of the newly discovered particle and confirmation  
509 of its consistency with the Standard Model Higgs were the main priorities. The  $WW^*$  channel is also  
510 uniquely suited to these types of measurements. Because of its good rate, it offers some of the best cross  
511 section measurements available among the various Higgs decay modes. It is also suited for measurement  
512 of multiple Higgs production modes, like the vector boson fusion (VBF) mode, where incoming quarks  
513 radiate  $W/Z$  bosons which fuse to make a Higgs. In VBF production with the  $WW^*$  decay channel,  
514 the coupling of the Higgs to the  $W$  boson is present in both the production and decay which allows for  
515 more precise measurements of this coupling than other channels which rely on gluon fusion production  
516 (where gluons couple to the Higgs through a top loop in the production). The measurement of VBF  
517 carries the additional challenge that its cross section is an order of magnitude smaller than that of gluon  
518 fusion, meaning that the large branching ratio to  $WW^*$  offers an additional advantage in isolating this  
519 production mode. In the final ATLAS Run 1 results, combining  $20.3 \text{ fb}^{-1}$  taken at  $\sqrt{s} = 8 \text{ TeV}$  with  
520 the  $4.8 \text{ fb}^{-1}$  collected at  $\sqrt{s} = 7 \text{ TeV}$ , the  $WW^*$  channel achieved its first observation of VBF produc-  
521 tion of the Higgs.

522 After Run 1 of the LHC, with the existence of the Higgs now firmly established, the focus shifted to  
523 searches for physics beyond the Standard Model. In particular, searches for high mass resonances benefit  
524 from the LHC's increase to  $\sqrt{s} = 13 \text{ TeV}$  in Run 2. The newly discovered Higgs can be used as a tool  
525 in these searches. Higgs pair production in the Standard Model has a low cross section that requires large  
526 datasets (on the order of the LHC's lifetime) for full measurement. However, new physics can modify  
527 this cross section, especially new resonances which decay to two Higgs bosons. A search for Higgs pair  
528 production in the  $HH \rightarrow b\bar{b}b\bar{b}$  final state was performed with  $3.2 \text{ fb}^{-1}$  collected with ATLAS at  $\sqrt{s} =$   
529  $13 \text{ TeV}$  in 2015.

530 This dissertation begins by discussing the discovery of the Higgs and the role of the  $H \rightarrow WW^* \rightarrow$   
531  $\ell\nu\ell\nu$  channel. It then discusses the first observation of the VBF production mode in  $H \rightarrow WW^* \rightarrow$   
532  $\ell\nu\ell\nu$  with the full ATLAS Run 1 dataset, as well as the final combined Run 1 measurements from this  
533 channel. Finally, it presents a search for Higgs pair production in the  $HH \rightarrow b\bar{b}b\bar{b}$  channel. It is orga-  
534 nized into four parts.

535 Part 1 presents the theoretical and experimental background required for the subsequent parts. Chap-  
536 ter 1 gives an overview of Higgs physics, particularly single and double Higgs production in the Standard  
537 Model and beyond. Chapter 2 presents details regarding the Large Hadron Collider and the ATLAS  
538 experiment. The evolution of machine conditions, descriptions of the ATLAS sub-detectors, and an  
539 overview of object reconstruction in ATLAS are all shown. A brief interlude on the ATLAS Muon New  
540 Small Wheel upgrade is also given, as this upgrade has been a focus of my graduate work and will have  
541 important impact on ATLAS' ability to study the Higgs at the High Luminosity LHC.

542 Part 2 discusses the observation and measurement of the Higgs in the  $H \rightarrow WW^* \rightarrow \ell\nu\ell\nu$   
543 channel in the ATLAS Run 1 dataset at  $\sqrt{s} = 7$  and 8 TeV. Because I worked in this channel from  
544 before the discovery through to the final analysis of the Run 1 dataset, Part 2 is organized in such a way  
545 to allow easy presentation of multiple analyses on different subsets of the full Run 1 dataset. Chapter 3  
546 presents a general overview of the  $H \rightarrow WW^*$  analysis strategy and defines many of the variables and  
547 common elements used in the rest of Part 2. Chapter 4 presents the discovery of the Higgs boson, fo-  
548 cusing on the role of the  $WW^*$  channel in this discovery. Chapter 5 presents the first observation of the  
549 VBF production mode of the Higgs in the  $WW^*$  channel, a study which was done on the full Run 1  
550 ATLAS dataset. In this chapter, the focus is mainly on the selection cut-based VBF analysis. The cut-  
551 based analysis was an important first step to the final VBF result which used a Boosted Decision Tree  
552 (BDT). Where appropriate, connections between the cut-based and BDT analyses are shown and their  
553 compatibility is discussed. Finally, the VBF analysis was an important input into the combined Run 1  
554  $H \rightarrow WW^* \rightarrow \ell\nu\ell\nu$  result, which used both the gluon fusion and VBF channels in a combined  
555 fit to infer properties of the Higgs, including its couplings to the gauge bosons and its production cross  
556 section. This is the topic of Chapter 6.

557 Part 3 presents a search for Higgs pair production in the  $HH \rightarrow b\bar{b}b\bar{b}$  channel. Chapter 7 presents  
558 an overview of this search in the boosted regime, where the Higgs pairs are the result of the decay of a  
559 heavy resonance. Chapter 8 shows the combined results between the boosted regime and the resolved  
560 regime, which is sensitive to lower mass resonances and non-resonant Higgs pair production. Finally,  
561 Part 4 presents a conclusion and brief outlook of future Higgs physics with ATLAS.

562

## Part I

563

### Theoretical and Experimental Background

*In modern physics, there is no such thing as “nothing.”*

Richard Morris

# 1

564

565

## The Physics of the Higgs Boson

566 This chapter presents an overview of the Standard Model of Particle Physics and in particular the physics  
567 of the Higgs boson. First, a brief overview of the Standard Model and its history are presented. Then, a  
568 description of the Higgs mechanism of electroweak symmetry breaking is given. Next, the physics of sin-  
569 gle Higgs boson production and decay is described. The Standard Model also allows for production of  
570 two Higgs bosons and this is detailed as well. Finally, di-Higgs production in two beyond the Standard  
571 Model (BSM) theories - Randall-Sundrum gravitons (RSG) and Two Higgs Doublet Models (2HDM) -  
572 is shown.

### 573 I.I THE STANDARD MODEL OF PARTICLE PHYSICS

574 The Standard Model (SM) of Particle Physics is a quantum field theory describing the fundamental  
575 particles of nature and the forces that govern their interactions. Several comprehensive treatments of  
576 the SM already exist in the literature [3–8] and this section will not rehash those. Rather, this section

577 presents a brief overview of the SM particles and forces in order to define them for subsequent discus-  
 578 sions.

579 The Standard Model consists of two primary categories of fundamental particles: fermions (spin 1/2  
 580 particles) and bosons (integer spin particles). The SM also describes three forces: electromagnetism, the  
 581 weak nuclear force, and the strong nuclear force. Gravity is not included in the theory and is largely irrele-  
 582 vant at the scales currently probed by collider experiments. Within the fermions, there are both quarks  
 583 (which interact via all three forces) and the leptons. The charged leptons interact via electromagnetic and  
 584 weak interactions, while neutrinos (neutral leptons) interact only via the weak force. Within the bosons,  
 585 there are the  $W^\pm$  and  $Z$  bosons (the mediators of the weak force), the gluon ( $g$ , the mediator of the  
 586 strong force), and the photon ( $\gamma$ ), the mediator of the electromagnetic force. Finally, there is the Higgs  
 587 boson, a fundamental spin-0 particle resulting from the Higgs mechanism of electroweak symmetry  
 588 breaking. Figure 1.1 summarizes the fermions and bosons of the SM.

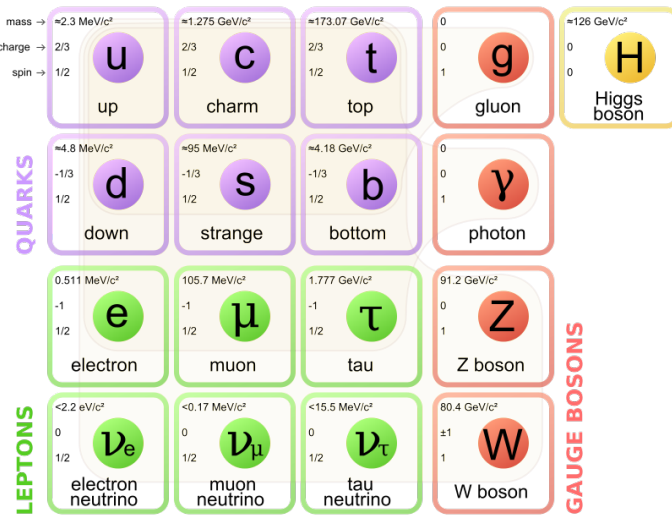


Figure 1.1: The particles of the Standard Model and their properties [6].

589 The Standard Model coalesced into a unified theoretical framework in the 1960s through the work  
 590 of Glashow, Weinberg, Salam, and others on the theory of electroweak interactions [9–12]. This theory  
 591 characterized both the electromagnetic and weak interactions as unified under a single gauge symmetry  
 592 group, namely  $SU(2) \times U(1)$ . At low enough energy scales (on the order of the  $W$  and  $Z$  masses,  
 593 the electroweak symmetry is broken, as evidenced by the fact that the weak bosons have mass while the

594 photon does not. The discovery of the Higgs boson in 2012 confirmed the Higgs mechanism as the most  
 595 likely candidate for this electroweak symmetry breaking [1, 2]. The electroweak theory is then combined  
 596 with the theory of quantum chromodynamics (which models the strong sector as a non-Abelian  $SU(3)$   
 597 gauge group) to form the complete SM [13].

## 598 1.2 ELECTROWEAK SYMMETRY BREAKING AND THE HIGGS

599 In the Standard Model Lagrangian, it is difficult to include mass terms for the  $W$  and  $Z$  bosons without  
 600 breaking the fundamental gauge symmetry of the Lagrangian. A traditional mass term does not preserve  
 601 the  $SU(2) \times U(1)$  symmetry. Additionally, scattering of massive  $W$  and  $Z$  bosons violate unitarity  
 602 and these diagrams diverge at high energy scales. In the 1960s, Higgs, Brout, Englert, Guralnik, Kibble,  
 603 and Hagen developed a mechanism for spontaneous symmetry breaking via the addition of a complex  
 604 scalar doublet to the SM. Three of the four real degrees of freedom of this complex field would go to the  
 605 longitudinal modes of the  $W^\pm$  and  $Z$ , thus allowing them to have mass [14–17]. The remaining degree  
 606 of freedom would manifest as an additional scalar, known now as the Higgs boson.

607 The mechanism works by introducing a Lagrangian for the newly introduced field that still respects  
 608 the symmetry of the Standard Model inherently, but with a minimum at a non-zero vacuum expectation  
 609 value for the field. In this minimum of the potential, the electroweak symmetry is broken. Specifically,  
 610 consider a complex scalar doublet  $\Phi$  with four degrees of freedom, as shown in equation 1.1.

$$\Phi = \begin{pmatrix} \phi^+ \\ \phi^0 \end{pmatrix} = \frac{1}{\sqrt{2}} \begin{pmatrix} \phi_1^+ + i\phi_2^+ \\ \phi_1^0 + i\phi_2^0 \end{pmatrix} \quad (1.1)$$

611 The minimal potential of a self-interacting Higgs that still respects the SM symmetry is given in equa-  
 612 tion 1.2.

$$V(\Phi) = \mu^2 \Phi^\dagger \Phi + \lambda (\Phi^\dagger \Phi)^2 \quad (1.2)$$

613 If the  $\mu^2$  term of this potential is positive, then the potential has a minimum at  $\Phi = 0$  and the SM

<sup>614</sup> symmetry is preserved. However, if instead  $\mu^2 < 0$ , then the minimum is at a finite value of  $\Phi$ , namely

$$\Phi_{\min} = \frac{1}{\sqrt{2}} \begin{pmatrix} 0 \\ v \end{pmatrix} \quad (1.3)$$

<sup>615</sup> where  $v = \sqrt{\mu^2/\lambda}$ . Because this is the location of the minimum, it corresponds to the vacuum expecta-  
<sup>616</sup> tion value for the field ( $\langle \Phi \rangle = \Phi_{\min}$ ). The excitations of the Higgs can then be parameterized as

$$\Phi = \frac{1}{\sqrt{2}} \begin{pmatrix} 0 \\ v + H \end{pmatrix} \quad (1.4)$$

<sup>617</sup> The full scalar Lagrangian, including the kinetic term, is then given as

$$\mathcal{L}_s = (D^\mu \Phi)^\dagger (D_\mu \Phi) - V(\Phi) \quad (1.5)$$

<sup>618</sup> where the covariant derivative is defined as

$$D_\mu = \partial_\mu + \frac{ig}{2} \tau^a W_\mu^a + ig' Y B_\mu \quad (1.6)$$

<sup>619</sup> and  $W^1, W^2, W^3$  and  $B$  are the  $SU(2)$  and  $U(1)$  gauge fields of the electroweak theory, respectively.  $g$   
<sup>620</sup> and  $g'$  are the corresponding coupling constants. With the scalar Lagrangian in place, the physical gauge  
<sup>621</sup> fields can then be written as

$$W_\mu^\pm = \frac{1}{\sqrt{2}} (W_\mu^1 \mp i W_\mu^2) \quad (1.7)$$

<sup>622</sup>

$$Z_\mu = \frac{-g' B_\mu + g W_\mu^3}{\sqrt{g^2 + g'^2}} \quad (1.8)$$

<sup>623</sup>

$$A_\mu = \frac{g B_\mu + g' W_\mu^3}{\sqrt{g^2 + g'^2}} \quad (1.9)$$

<sup>624</sup> Equation 1.7 corresponds to the charged  $W^+$  and  $W^-$  bosons, equation 1.8 corresponds to the neutral

625  $Z$  boson, and equation 1.9 corresponds to the neutral photon. The masses of the particles also arise from  
 626 the Lagrangian. The photon has zero mass, while the masses of the  $W$  and  $Z$  bosons are given in equa-  
 627 tion 1.10.

$$\begin{aligned} M_W^2 &= \frac{1}{4}g^2v^2 \\ M_Z^2 &= \frac{1}{4}(g^2 + g'^2)v^2 \end{aligned} \tag{1.10}$$

628 The fermion masses also arise through a coupling with the Higgs via the Yukawa interaction (for a de-  
 629 tailed description, see [8]). In this case the coupling between the Higgs and the fermions goes as

$$g_{Hf\bar{f}} = \frac{m_f}{v} \tag{1.11}$$

630 The full Lagrangian of Higgs interactions can be written as

$$\mathcal{L}_{\text{Higgs}} = -g_{Hf\bar{f}}\bar{f}fH + \frac{g_{HHH}}{6}H^3 + \frac{g_{HHHH}}{24}H^4 + \delta_V V_\mu V^\mu \left( g_{HV}VH + \frac{g_{HVV}}{2}H^2 \right) \tag{1.12}$$

631 with

$$\begin{aligned} g_{HV} &= \frac{2m_V^2}{v} & g_{HVV} &= \frac{2m_V^2}{v^2} \\ g_{HHH} &= \frac{3m_H^2}{v} & g_{HHHH} &= \frac{3m_H^2}{v^2} \end{aligned} \tag{1.13}$$

632 Here,  $V$  refers to the  $W^\pm$  and  $Z$ , and  $\delta_W = 1$  while  $\delta_Z = 1/2$ . Phenomenologically, there are a few  
 633 features of this Lagrangian that are useful to note. First, note that the Higgs mass is a free parameter  
 634 of the theory that must be determined experimentally. Second, note that the coupling of the Higgs to  
 635 the vector bosons and fermions scales with the masses of these particles, a fact that is important when  
 636 considering both the production and decays of the particle. Also note that the branching ratio of the  
 637 Higgs to  $W$  bosons will be twice that of the branching ratio to  $Z$  if the Higgs mass is large enough to  
 638 produce the particles on shell because of the extra symmetry factor associated with the  $W$  coupling.  
 639 Finally, note the presence of the cubic and quartic Higgs self interaction terms, which can lead to final  
 640 states with multiple Higgs bosons produced.

641 1.3 HIGGS BOSON PRODUCTION AND DECAY

642 This section discusses the properties of Higgs production and decay mechanisms. The details presented  
643 here will focus on the properties of a 125 GeV Higgs boson, as this is the mass closest to that of the  
644 newly discovered Higgs.

645 1.3.1 HIGGS PRODUCTION

646 The Higgs is produced by four main production modes at the Large Hadron Collider - gluon-gluon  
647 fusion (ggF), vector boson fusion (VBF), associated production with a  $W$  or  $Z$  boson, or associated  
648 production with top quarks ( $t\bar{t}H$ ). Figure 1.2 shows the Feynman diagrams for these four modes.

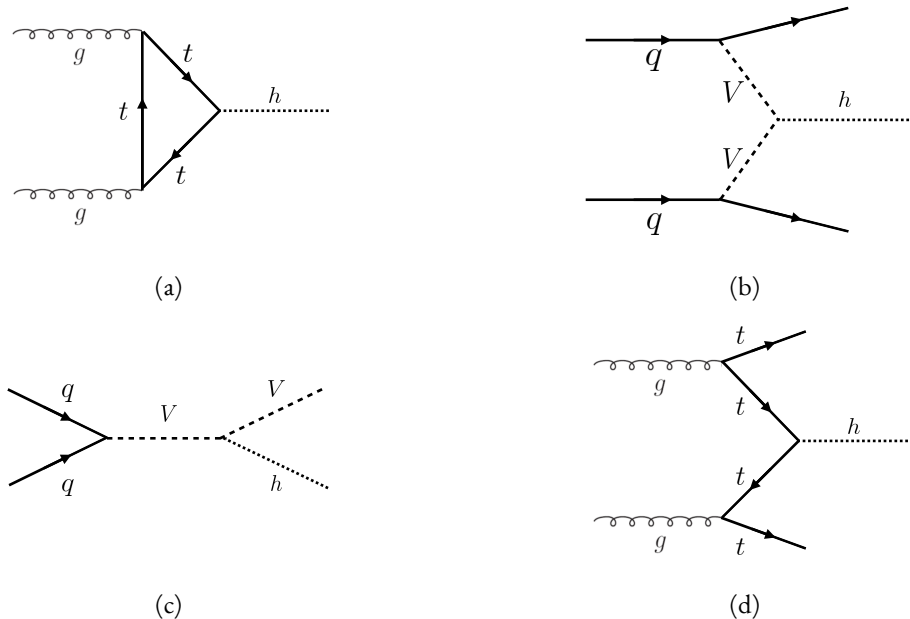


Figure 1.2: The four most common Higgs boson production modes at the LHC: (a) gluon-gluon fusion, (b) vector boson fusion, (c)  $W/Z + H$  production, (d)  $t\bar{t}H$  production

649 In gluon-gluon fusion, gluons from the incoming protons fuse via a top-quark loop to produce a  
650 Higgs. The top quark is the dominant contribution in the loop due to its heavy mass and the fact that  
651 the Higgs-fermion coupling constant scales with fermion mass. In vector boson fusion, the incoming  
652 quarks each radiate a  $W$  or  $Z$  boson which fuse to produce the Higgs. This production mode results in  
653 a final state with a Higgs boson and two additional jets which tend to be forward because they carry the

654 longitudinal momentum of the incoming partons. The Higgs can also be produced in association with a  
 655  $W$  or  $Z$  boson. The  $W/Z$  is produced normally and then radiates a Higgs (this mode is also sometimes  
 656 known as “Higgs-strahlung”). Finally, the Higgs can be produced in association with two top quarks.  
 657 Each incoming gluon splits into a  $t\bar{t}$  pair, and one of the top pairs combines to create a Higgs. Figure 1.3  
 658 shows the production cross section for a 125 GeV Higgs boson in each of these modes at a  $pp$  collider as  
 659 a function of center of mass energy.

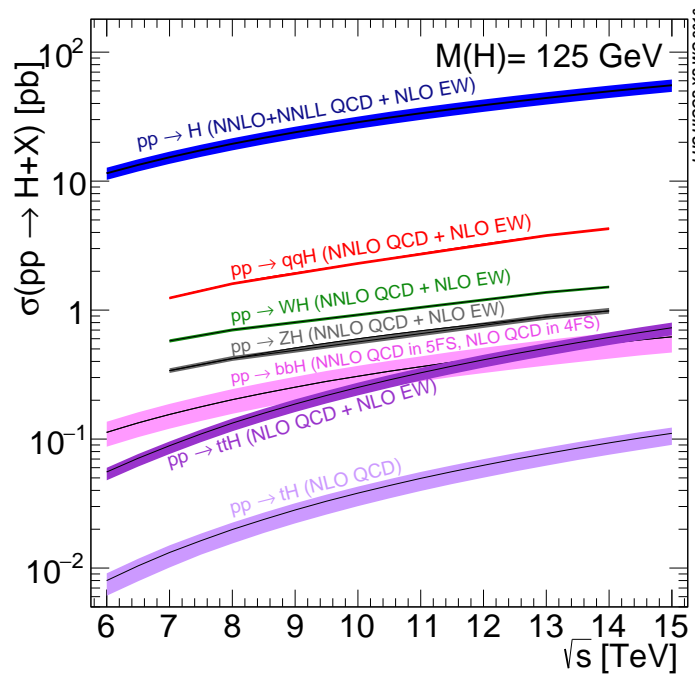


Figure 1.3: Higgs production cross sections as a function of center of mass energy ( $\sqrt{s}$ ) at a  $pp$  collider [18].

660 In figure 1.3, note that gluon fusion has the largest cross section, while VBF is the second largest at  
 661 approximately a factor of 10 smaller. The figure also includes the less commonly studied  $b\bar{b}H$  and  $tH$   
 662 modes. The  $b\bar{b}H$  and  $tH$  modes are not studied as commonly as  $t\bar{t}H$  due to the larger background con-  
 663 tributions and lower cross sections, respectively. At  $\sqrt{s} = 8$  TeV, ggF production of a 125 GeV Higgs  
 664 has a cross section of 19.47 pb, while VBF has a cross section of 1.601 pb [18]. The cross sections of all  
 665 of the main Higgs production modes at this center of mass energy, as well as their uncertainties from  
 666 varying the renormalization and factorization scales and PDFs, are summarized in table 1.1 for a 125 GeV  
 667 Higgs.

Production mode	$\sigma$ ( pb)	QCD scale uncert. (%)	PDF + $\alpha_s$ uncert. (%)
Gluon fusion	19.47	+7.3/ - 8.0	3.1
Vector boson fusion	1.601	+0.3/ - 0.2	2.2
$WH$	0.7026	+0.6/ - 0.9	2.0
$ZH$	0.4208	+2.9/ - 2.4	1.7
$t\bar{t}H$	0.1330	+4.1/ - 9.2	4.3
$bbH$	0.2021	+20.7/ - 22.3	
$tH$ ( $t$ -channel)	0.01869	+7.3/ - 16.5	4.6
$tH$ ( $s$ -channel)	$1.214 \times 10^{-3}$	+2.8/ - 2.4	2.8

Table 1.1: Production cross sections for a 125 GeV Higgs boson at  $\sqrt{s} = 8$  TeV with scale and PDF uncertainties [18].

### 668 1.3.2 HIGGS BRANCHING RATIOS

669 The fact that the Higgs couples more strongly to more massive particles is crucial for understanding its  
 670 branching ratios. The width for Higgs decays to fermions is given in equation 1.14 [5].

$$\Gamma(H \rightarrow f\bar{f}) = \frac{N_c \sqrt{2} G_F m_f^2 m_H}{8\pi} \quad (1.14)$$

671 In this case,  $N_c$  is the number of colors,  $G_F$  is the Fermi constant,  $m_f$  is the mass of the fermion, and  
 672  $m_H$  is the mass of the Higgs. Note that the width scales with the square of the fermion mass. (This also  
 673 assumes that the Higgs mass is large enough to decay with both the fermions on shell.)

674 The decay width to  $WW$  is given in equation 1.15 [5].

$$\Gamma(H \rightarrow W^+W^-) = \frac{\sqrt{2} G_F M_W^2 m_H}{16\pi} \frac{\sqrt{1-x_W}}{x_W} (3x_W^2 - 4x_W + 4) \quad (1.15)$$

675 where  $m_W$  is the mass of the  $W$  and  $x_W = 4M_W^2/m_H^2$ . To get the branching ratio to  $ZZ$ , the equa-  
 676 tion is divided by 2 to account for identical particles in the final state, and  $x_W$  is replaced with  $x_Z =$   
 677  $4M_Z^2/m_H^2$ . This is shown in equation 1.16 [5].

$$\Gamma(H \rightarrow ZZ) = \frac{\sqrt{2} G_F M_Z^2 m_H}{32\pi} \frac{\sqrt{1-x_Z}}{x_Z} (3x_Z^2 - 4x_Z + 4) \quad (1.16)$$

678 These formulas can also be visualized as a function of Higgs mass. Figure 1.4 shows the branching ratios  
as a function of the Higgs mass. There are a few interesting features to note in this figure. First, note that

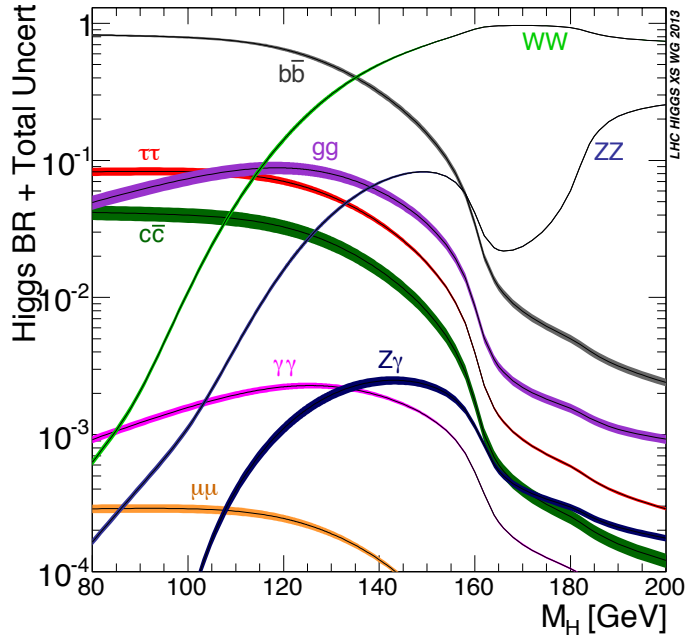


Figure 1.4: Higgs boson branching ratios as a function of  $m_H$  [18].

679  
680 at high Higgs masses, once on-shell production of both  $W$  and  $Z$  bosons is possible, these two decays  
681 are the dominant ones due to the large masses of the  $W/Z$ . Also note that the branching ratio to  $W$ s  
682 is twice that of  $Z$ s at these large masses due to the  $\delta_V$  symmetry factor noted previously. At 125 GeV,  
683 the Higgs is accessible through many different decay modes. The largest branching ratio is the decay  
684  $H \rightarrow b\bar{b}$  at 58.24% [18]. This branching is larger than the  $WW/ZZ$  decays because one of the two  
685 bosons must be produced off-shell for  $m_H = 125$  GeV. The second largest branching ratio is to  $WW^*$   
686 at 21.37 % (before taking into account the branching ratios of the  $W$ ). Table 1.2 summarizes the branch-  
687 ing ratios for a 125 GeV Higgs. Note that there is in fact a Higgs branching ratio to  $\gamma\gamma$  even though  
688 photons are massless. This decay happens through a loop (the largest contributions to the loop are top  
689 and  $W$ ) which suppresses the branching ratio.

690 Note that the branching ratios alone do not tell the full story of which Higgs channels are the most  
691 sensitive. For example, a  $H \rightarrow b\bar{b}$  search in gluon fusion production is incredibly difficult due to the

Decay	Branching ratio (%)
$b\bar{b}$	58.24
$WW^*$	21.37
$gg$	8.187
$\tau\tau$	6.272
$c\bar{c}$	2.891
$ZZ^*$	2.619
$\gamma\gamma$	0.2270
$Z\gamma$	0.1533
$\mu\mu$	0.02176

Table 1.2: Branching ratios for a 125 GeV Higgs boson [18].

large QCD dijet background at the LHC. However, in associated production of the Higgs, where a  $W$  or  $Z$  gives additional final state particles that can be used to reduce background, a search for  $H \rightarrow b\bar{b}$  can be sensitive. The combinations of production and decay modes that are most commonly studied are summarized in table 1.3 [5].

Decay	Inclusive (incl. ggF)	VBF	$WH/ZH$	$t\bar{t}H$
$H \rightarrow \gamma\gamma$	✓	✓	✓	✓
$H \rightarrow b\bar{b}$			✓	✓
$H \rightarrow \tau^+\tau^-$		✓		
$H \rightarrow WW^* \rightarrow \ell\nu\ell\nu$	✓	✓	✓	
$H \rightarrow ZZ \rightarrow 4\ell$	✓			
$H \rightarrow Z\gamma \rightarrow \ell\ell\gamma$	very low			

Table 1.3: Possible channels for Higgs searches. Checkmarks denote the most sensitive production modes [5].

#### 1.4 HIGGS PAIR PRODUCTION IN THE STANDARD MODEL

The Standard Model also allows for processes that produce two Higgs bosons in the final state, known as Higgs pair production or di-Higgs production. The two main production mechanisms are shown in figure 1.5. The two diagrams in figure 1.5 interfere destructively with one another, resulting in a low overall cross section for di-Higgs production at the LHC. Nevertheless, Higgs pair production is quite interesting to study because it gives direct access to the  $\lambda$  parameter of the Higgs potential, also known as the Higgs self coupling. The diagram in figure 1.5(b) is sensitive to this coupling through the triple Higgs

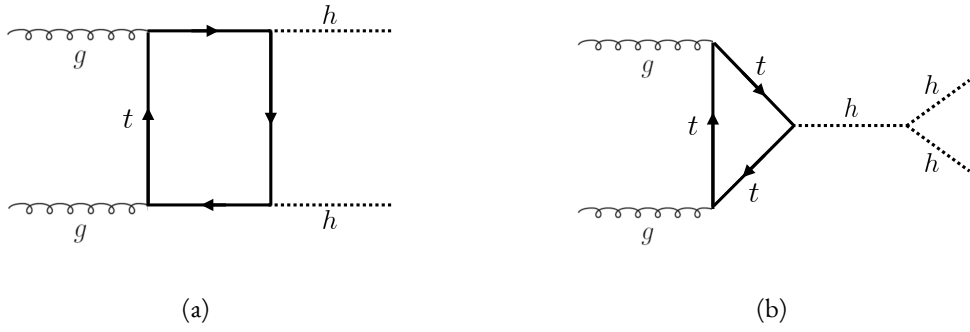


Figure 1.5: The two leading diagrams for Standard Model di-Higgs production at the LHC: (a) box diagram, (b) Higgs self coupling

703 vertex.

704 One can substitute the gluon fusion production of diagram 1.5(b) with any of the other production  
 705 modes previously discussed. These other modes do not suffer from interference with the box diagram  
 706 in figure 1.5(a) due to the presence of additional particles in the final state. They still have a lower cross  
 707 section than the gluon fusion mode, however. The cross sections for di-Higgs production in the differ-  
 708 ent modes, as well as their uncertainties, are shown in table 1.4 [19]. These are shown for  $\sqrt{s} = 14$  TeV  
 709 as the higher center of mass energy is more sensitive to this process. Note that the scale of cross section  
 quoted is now in fb rather than pb.

Production mode	$\sigma$ (fb)	Total uncert. (%)
Gluon fusion	33.89	+37.2 / - 27.8
Vector boson fusion	2.01	+7.6 / - 5.1
$W H H$	0.57	+3.7 / - 3.3
$Z H H$	0.42	+7.0 / - 5.5
$t \bar{t} H$	1.02	-

Table 1.4: Production cross sections for pair production of a 125 GeV Higgs boson at  $\sqrt{s} = 14$  TeV with total uncertainty [19]. The uncertainties include QCD scale and PDF variations as well as uncertainties on  $\alpha_S$ .

710

## 711 1.5 HIGGS PAIR PRODUCTION IN THEORIES BEYOND THE STANDARD MODEL

712 The Standard Model Higgs pair production cross section is rather small, and datasets on the scale of the  
 713 full lifetime of the LHC will be required to obtain sensitive measurements of the Higgs self-coupling.

714 However, the discovery of the Higgs also gives particle physicists a new tool that can be exploited in the  
 715 search for new physics beyond the Standard Model. In particular, Higgs pair production is a promising  
 716 channel in the search for new physics. The cross section for di-Higgs production can be altered through  
 717 both resonant and non-resonant production of Higgs pairs. In non-resonant production, di-Higgs pro-  
 718 duction vertices can arise from the presence of a new strong sector and additional colored particles [20–  
 719 22]. Figure 1.6 shows examples of the types of vertices that can arise. In the resonant case, new heavy par-  
 720 ticle can decay to Higgs pairs. Such new particles can include heavy Higgs bosons arising in two Higgs  
 721 doublet models (2HDM) or Higgs portal models as well as heavy gravitons in Randall-Sundrum theo-  
 722 ries [20, 23–29]. Figure 1.7 shows a generic diagram for a heavy resonance decaying to two Higgs bosons.  
 723 In the 2HDM,  $X$  corresponds to the heavy CP-even scalar  $H$ . In the Randall-Sundrum model,  $X$  cor-  
 724 responds to a heavy spin-2 graviton  $G$ . The next sections provide more detail on the phenomenology of

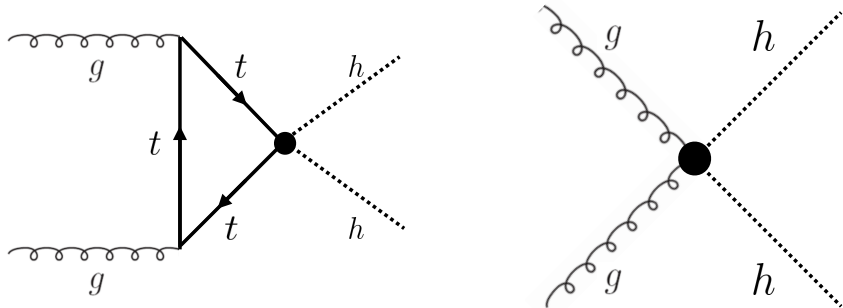


Figure 1.6: Diagrams with new vertices for non-resonant Higgs pair production arising in composite Higgs models

724  
 725 resonant Higgs production in Randall-Sundrum and 2HDM models, as these models will later be tested  
 726 in a dedicated search for resonant production of boosted Higgs pairs.

### 727 1.5.1 RANDALL-SUNDRUM GRAVITONS

728 The Randall-Sundrum model is a proposed solution to the hierarchy problem that posits a five-dimensional  
 729 warped spacetime that contains two branes: one where the force of gravity is very strong and a second  
 730 brane at the TeV scale corresponding to the known Standard Model sector [23]. In the theory, the  
 731 branes are weakly coupled and the graviton probability function drops exponentially going from the  
 732 gravity brane to the SM brane, rendering gravity weak on the SM brane. The experimental consequence

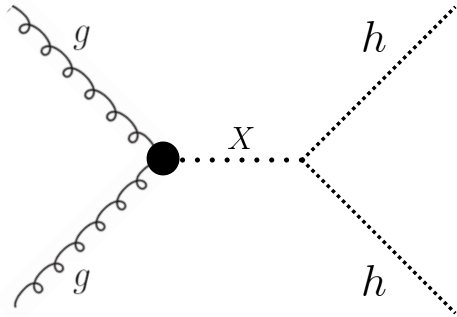


Figure 1.7: Generic Feynman diagram for resonant Higgs pair production in BSM theories

of this theory is a tower of widely spaced (in mass) Kaluza-Klein graviton resonances. In theories where the fermions are localized to the SM brane, production of gravitons from fermion pairs is suppressed and the primary mode of production is gluon fusion [24]. These gravitons have a substantial branching fraction to Higgs pairs, ranging from 6.43% for gravitons with a mass of 500 GeV to 7.66% at 3 TeV. Figure 1.8 shows the branching ratios of the spin-2 Randall Sundrum graviton (RSG) as a function of its mass. The predominant decays are to  $t\bar{t}$  above the mass threshold for that channel.

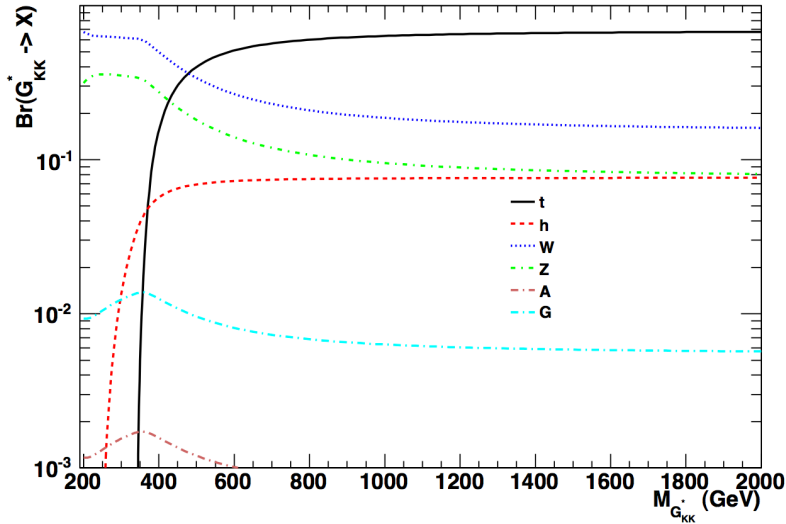


Figure 1.8: Branching ratios for a spin-2 Randall-Sundrum graviton as a function of mass computed in MadGraph with the CP3-Origins implementation [24, 30]

These models have two free parameters - the mass of the graviton and a curvature parameter  $k$ . Typically, rather than  $k$ , the theory is parameterized using  $c \equiv k/\bar{M}_{\text{pl}}$ , where  $\bar{M}_{\text{pl}}$  is the reduced Planck

mass. The cross section for production of the RSG decreases as a function of mass and is strongly dependent on the gluon PDF. The increase in center of mass energy from 8 to 13 TeV in LHC Run 2 greatly increases the cross section at higher mass. Figure 1.9 shows the cross section as a function of graviton mass at  $\sqrt{s} = 13$  TeV for RSG models with  $c = 1.0$  and  $c = 2.0$ .

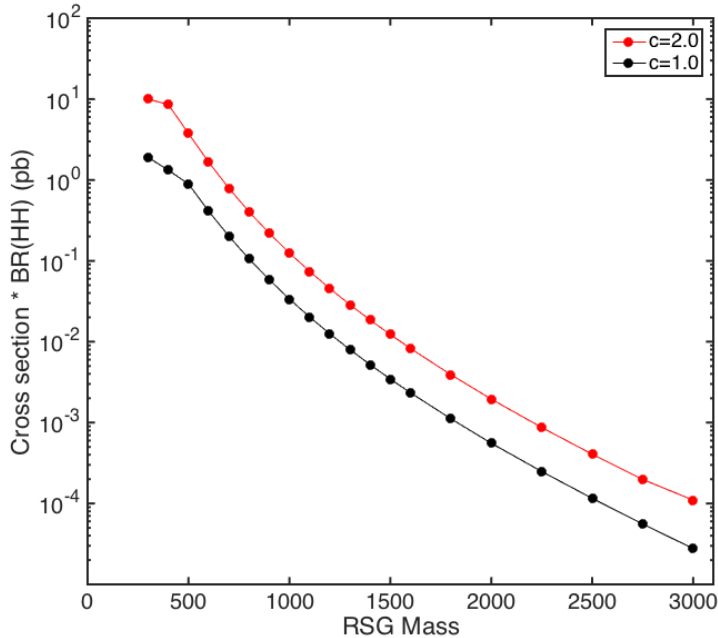


Figure 1.9:  $\sigma \times \text{BR}(HH)$  for RSG as a function of mass computed in MadGraph with the CP3-Origins implementation [24, 30]

Another interesting feature of the theory is that the width of the graviton increases with both  $c$  and  $m_G$ . Figure 1.10 shows the graviton width for both  $c = 1.0$  and  $c = 2.0$  as a function of mass. In  $c = 1.0$ , the width starts at 8.365 GeV for a mass of 300 GeV and increases to 187.2 GeV at a mass of 3 TeV. Similarly, with  $c = 2.0$ , the width starts at 33.46 GeV for  $m_G = 300$  GeV and increases to 748.8 GeV at a mass of 3 TeV.

### 1.5.2 TWO HIGGS DOUBLET MODELS

In Two Higgs Doublet Models (2HDM), a second complex scalar doublet is added to SM [26–28]. In this case, all four degrees of freedom in the second doublet correspond to new particles, meaning that

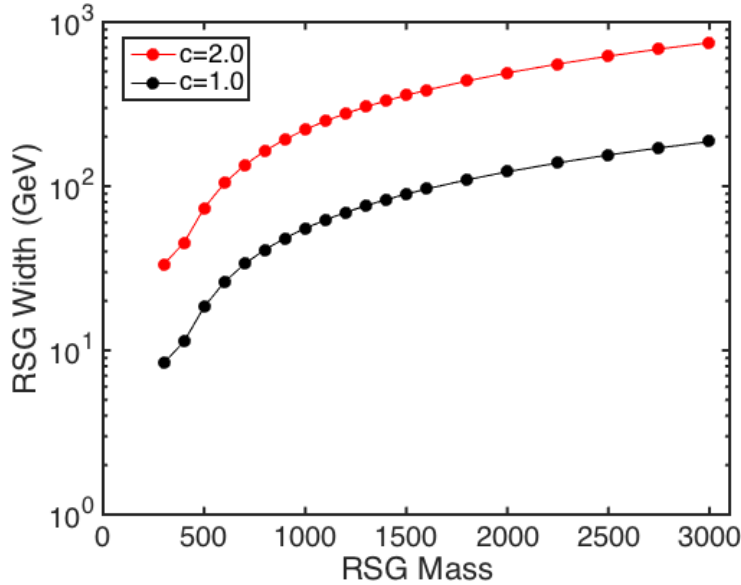


Figure 1.10: RSG width as a function of mass computed in MadGraph with the CP3-Origins implementation [24, 30]

753 there are five total scalars from the two Higgs doublets -  $h$  (light CP-even Higgs),  $H$  (heavy CP-even  
 754 Higgs),  $A$  (heavy CP-odd Higgs), and  $H^\pm$  (charged Higgs). The model is parameterized by two main  
 755 parameters. The first,  $\tan \beta \equiv \frac{v_2}{v_1}$ , is the ratio of the vacuum expectation values of the two Higgs dou-  
 756 blets (where  $v_1$  corresponds to the  $v$  in the SM Higgs model described above). The second parameter  
 757 is  $\alpha$ , a mixing angle between the heavy and light Higgs fields. Models are also often parameterized with  
 758  $\cos(\beta - \alpha)$  rather than  $\alpha$  directly. The limit where  $\cos(\beta - \alpha) = 0$  is called the alignment limit, and it  
 759 is in this limit that the light Higgs  $h$  has the same couplings as a Standard Model Higgs.

760 2HDM models are usually separated into two main types - Type I and Type II. In Type I models, the  
 761 charged fermions only couple to the second Higgs doublet, leading to a fermiophobic light Higgs. In  
 762 Type II models, up-type quarks couple to the first doublet while down-type quarks couple to the second  
 763 doublet. One specific realization of a Type II 2HDM is the Minimal Supersymmetric Standard Model  
 764 (MSSM).

765 Resonant di-Higgs production in this model can proceed through decays of the heavy CP-even Higgs  
 766  $H \rightarrow hh$ . The branching ratio for  $H \rightarrow hh$  depends on the model type as well as the values of  $\tan \beta$   
 767 and  $\cos \beta - \alpha$ . Figure 1.11 shows the branching ratios as a function of the mass of the heavy scalar  $H$  for

<sup>768</sup> both Type I and Type II models. Depending on the type of model  $hh$  can be a substantial fraction of the  
<sup>769</sup> decays of  $H$ .

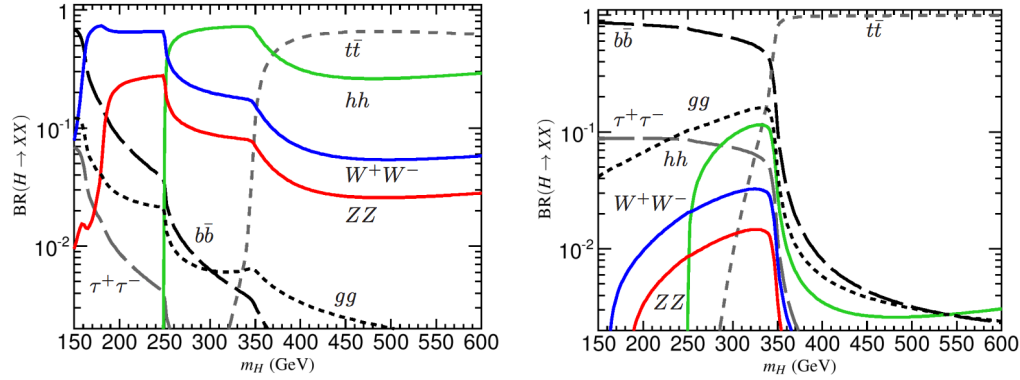


Figure 1.II: Branching ratios for heavy Higgs  $H$  in Type I (left) and Type II (right) 2HDM models with  $\tan \beta = 1.5$  and  $\cos(\beta - \alpha) = 0.1(0.01)$  for Type I (Type II). [28]

## <sup>770</sup> 1.6 CONCLUSION

<sup>771</sup> Studying the Higgs sector is essential for understanding the details of how mass arises in the Standard  
<sup>772</sup> Model and how the electroweak symmetry is broken. The discovery of the Higgs boson also opens the  
<sup>773</sup> door for its use as a tool to search for new physics, and Higgs pair production is an ideal candidate for  
<sup>774</sup> this study. Even if no BSM physics is found in Higgs pair production, searches for Higgs pairs will put  
<sup>775</sup> constraints on the Higgs self coupling and thus further knowledge of the Standard Model and the details  
<sup>776</sup> of the Higgs potential.

*The enthusiasm and motivation to explore particle  
physics at the high-energy frontier knows no borders  
between the nations and regions of the planet.*

Peter Jenni

# 2

777

778

779

## The ATLAS detector and the Large Hadron Collider

780 This chapter presents an overview of the experimental systems used to conduct the measurements pre-  
781 sented in this thesis. First, a brief overview of the accelerator, the Large Hadron Collider, will be given.  
782 In this section, the accelerator conditions relevant to data-taking are presented as well. Next, an overview  
783 of the ATLAS experiment is given. The basics of each sub-detector's role are summarized, as well as the  
784 details of the datasets accumulated. Then, a brief interlude on the ATLAS Muon New Small Wheel up-  
785 grade is presented. While this new detector does not have a direct impact on any of the datasets taken  
786 so far, it will have an impact on future analyses and the work done on it is briefly summarized here. Fi-  
787 nally, an overview of object reconstruction in ATLAS is given. While the details of all of the algorithms  
788 will not be presented in detail, aspects of the reconstruction performance such as object resolutions are  
789 shown as these are relevant to the two studies presented later in this thesis.

790 2.1 THE LARGE HADRON COLLIDER

791 The Large Hadron Collider (LHC) is a proton-proton collider at the CERN laboratory in Geneva,  
792 Switzerland [31]. It is designed for a maximum collision center of mass energy of  $\sqrt{s} = 14 \text{ TeV}$  and  
793 has a circumference of 26.7 kilometers. Four main experiments are located at the interaction points (IP)  
794 of the accelerator: ATLAS (A Toroidal LHC ApparatuS), CMS (the Compact Muon Solenoid), AL-  
795 ICE (A Large Ion Collider Experiment), and LHCb [32–35]. The studies performed in this thesis were  
796 all completed with the ATLAS detector. Figure 2.1 shows a schematic of the LHC ring and the various  
797 experiments.

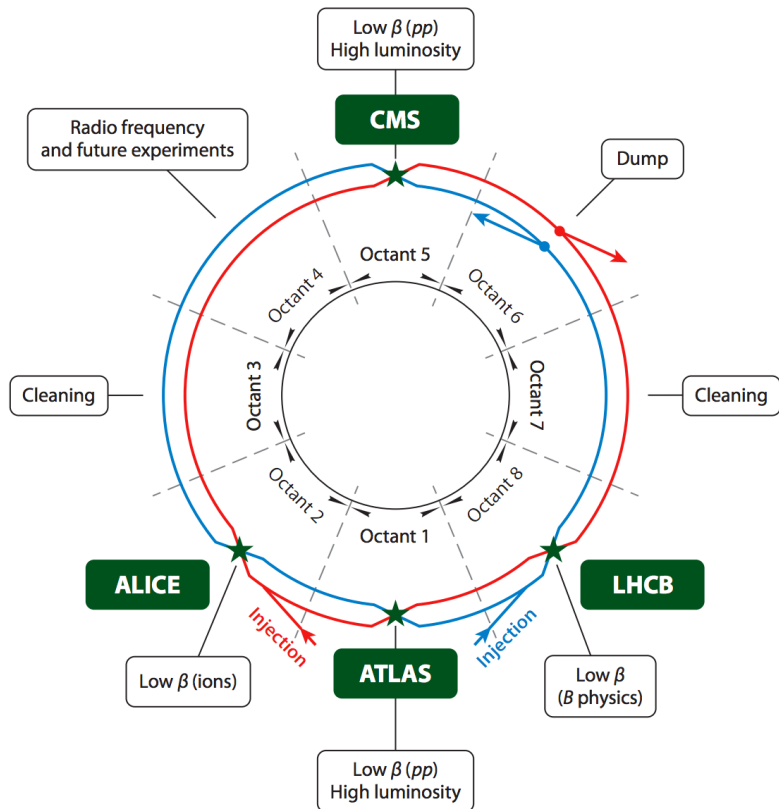


Figure 2.1: A schematic view of the LHC ring [36]

798 One of the most interesting features of the LHC is in its magnet design. Because the tunnel does not  
799 have room for separate superconducting magnets for each of the beam pipes, the LHC employs a twin-  
800 bore magnet design. Each magnet must hold an 8.3 Tesla magnetic field in order to bend the proton

801 beams at  $\sqrt{s} = 14$  TeV. The superconducting magnets are cooled to a temperature of 1.9 Kelvin with  
 802 superfluid helium.

803 2.1.1 INSTANTANEOUS LUMINOSITY

804 The rate of physics events expected from the accelerator is dependent on the instantaneous luminosity  
 805 of the machine and the cross section of the physics process,  $R_{\text{events}} = L\sigma$ . Here,  $R_{\text{events}}$  is the number  
 806 of events per second,  $L$  is the instantaneous luminosity of the machine, and  $\sigma$  is the cross section for the  
 807 physics process being measured. The instantaneous luminosity of the LHC is determined by numerous  
 808 factors related to machine conditions. Equation 2.1 gives the equation for instantaneous luminosity of  
 809 Gaussian beam profile [36].

$$L = \frac{N_b^2 n_b f_{\text{rev}} \gamma_r}{4\pi \epsilon_n \beta^*} F \quad (2.1)$$

810 The LHC collides protons in bunches, and in the above equation  $N_b$  is the number of protons per  
 811 bunch while  $n_b$  is the number of bunches per beam. Nominally, the LHC can hold up to 2808 pro-  
 812 ton bunches.  $f_{\text{rev}}$  is the revolution frequency.  $\epsilon_n$  is the normalized transverse beam emittance, a mea-  
 813 surement of the average spread of the particles position-momentum space which has the dimension of  
 814 length.  $\beta^*$  is the value of the *beta* function for the beam at the interaction point. It relates the emittance  
 815 to the Gaussian width of the beam with  $\sigma_{\text{beam}} = \sqrt{\epsilon \cdot \beta}$ .  $F$  is a reduction factor that corrects for the  
 816 fact that the beams are colliding at an angle at the IP.

817 Another way of writing the instantaneous luminosity is shown in equation 2.2. In this case, the in-  
 818 stantaneous luminosity is written as the ratio of the rate of inelastic collisions with the inelastic cross  
 819 section [37].

$$L = \frac{R_{\text{inel}}}{\sigma_{\text{inel}}} = \frac{\mu n_b f_{\text{rev}}}{\sigma_{\text{inel}}} \quad (2.2)$$

820 In this case,  $\mu$  is the average number of interactions per bunch crossing in the accelerator.  $\mu$  is a useful  
 821 parameter for characterizing the amount of activity recorded in an experiment. As the instantaneous  
 822 luminosity and thus  $\mu$  increase, there are more interactions per bunch crossing and more activity in the  
 823 detector. This is often characterized with  $\langle \mu \rangle$ , the measured per bunch crossing  $\mu$  value averaged over

824 all bunch crossings. The interactions inside each bunch crossing that are not the main physics process of  
 825 interest are often referred to as “pileup” interactions, and  $\langle \mu \rangle$  is a measurement of the level of pileup in  
 826 the detector.

827 **2.1.2 EVOLUTION OF MACHINE CONDITIONS**

828 This thesis uses datasets taken at three different center of mass energies:  $\sqrt{s} = 7\text{ TeV}$  data taken in  
 829 the year 2011,  $\sqrt{s} = 8\text{ TeV}$  data taken in the year 2012, and  $\sqrt{s} = 13\text{ TeV}$  data taken in the year  
 830 2015. In addition to increasing center of mass energy, the instantaneous luminosity and parameters that  
 831 determine it were evolving. Table 2.1 summarizes that machine conditions in each of these datasets.

	2011	2012	2015	Design
$\sqrt{s} [\text{TeV}]$	7	8	13	14
Number of bunches	1380	1380	1825	2808
Max. protons per bunch	$1.45 \times 10^{11}$	$1.7 \times 10^{11}$		$1.15 \times 10^{11}$
Bunch spacing [ns]	50	50	25	25
Max. instantaneous luminosity [ $\text{cm}^{-2}\text{s}^{-1}$ ]	$3.7 \times 10^{33}$	$7.7 \times 10^{33}$	$5 \times 10^{33}$	$10^{34}$
$\beta^* [\text{m}]$	1.0	0.6	0.8	0.55
$\langle \mu \rangle$	11.6	20.7	13.7	-

Table 2.1: Evolution of LHC machine conditions [38, 39]

832 **2.2 THE ATLAS DETECTOR**

833 The ATLAS detector is a multi-purpose particle detector experiment at the LHC’s Point 1 [32]. It has  
 834 nearly  $4\pi$  coverage in solid angle around the interaction point. It consists of an inner detector for mea-  
 835 suring charged particles, electromagnetic and hadronic calorimeters, and a muon spectrometer. Fig-  
 836 ure 2.2 gives an overview of the detector.

837 **2.2.1 COORDINATE SYSTEM**

838 Before defining the properties of the individual detectors, it is important to establish the coordinate  
 839 system used. Figure 2.3 shows a schematic of the coordinate system. The azimuthal plane (perpendicular



Figure 2.2: A full diagram of the ATLAS detector [32]

840 to the beam line) is defined as the  $x$ - $y$  plane. The angle in this plane is referred to as  $\phi$ . The angle relative  
 841 to the beam axis is referred to as  $\theta$ . Rather than using  $\theta$  directly as a coordinate, the experiment often  
 842 uses the pseudorapidity  $\eta$ .  $\eta$  is defined in equation 2.3.

$$\eta = \ln \left( \tan \left( \frac{\theta}{2} \right) \right) \quad (2.3)$$

843 Pseudorapidity is the massless approximation of rapidity, the angle used to parameterize boosts in  
 844 special relativity. This is important for two reasons. First, it means that differences in  $\eta$  are Lorentz in-  
 845 variant. Second, particle production is roughly constant in pseudorapidity. Particles with  $\eta$  close to zero  
 846 are referred to as “central”, while those at high  $|\eta|$  are called “forward”. In general, two main detector  
 847 topologies can be seen in figure 2.2. There are “barrel” elements, which surround the beam line cylin-  
 848 drically and are in the central region of the detector. In the forward region, there are “endcap” regions  
 849 which are arranged as disks perpendicular to the beam line.

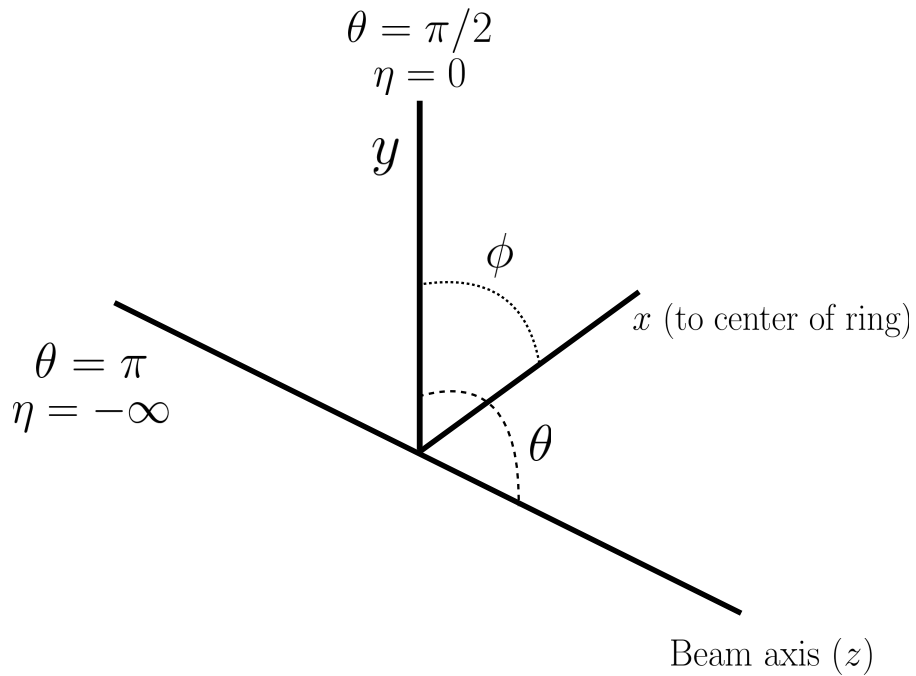


Figure 2.3: The ATLAS coordinate system

850 2.2.2 INNER DETECTOR

851 The ATLAS Inner Detector (ID) system is built for precision tracking of charged particles. It covers the  
 852 range  $|\eta| < 2.5$ . In this range, approximately 1000 particles are generated every bunch crossing in the  
 853 detector. This requires having fine granularity to achieve the resolutions required for good momentum  
 854 measurement and vertex reconstruction.

855 The ID consists of three sub-components: the pixel detector, semiconductor tracker (SCT), and trans-  
 856 sition radiation tracker (TRT). It is surrounded by a solenoid providing a 2 T axial magnetic field which  
 857 bends particles in the transverse plane to allow for momentum measurement. Figure 2.4 shows the layout  
 858 of each of these components.

859 PIXEL DETECTOR

860 The pixel detector is the first detector particles traverse after being generated in proton collisions and is  
 861 the most granular detector. Its operation is crucial for precision tracking and vertex reconstruction as



Figure 2.4: Layout of the ATLAS Inner Detector system [40]

well as higher level object reconstruction like tagging of jets from  $b$ -quarks. The basic sensing element in this subdetector is a silicon pixel detector. The operating principle for the silicon pixels is that of a  $p-n$  junction. When a charged particle passes through, it creates electron-hole pairs that are then separated by the electric field. The sensors are  $250 \mu\text{m}$  thick and use oxygenated  $n$ -type wafers with readout pixels on the  $n^+$  side of the detector [32]. Overall, the pixel detector has 1744 sensors and 80.4 million readout channels.

In the barrel region, the pixel detector has three concentric layers of sensors surrounding the beam-line. In the endcap region, it consists of disks perpendicular to the beam axis. The detector is segmented in the  $R-\phi$  plane and in  $z$ . Usually, three pixel layers are crossed by a charged particle track. The intrinsic accuracies of the sensors are  $10 \mu\text{m}$  in  $R-\phi$  and  $115 \mu\text{m}$  in  $z$  (or  $R$  for the endcap).

#### INSERTABLE B-LAYER

In Run 2, a new innermost pixel layer, known as the insertable B-layer (IBL), was added to the Inner Detector [41]. This layer was added to cope with the higher luminosities planned in LHC Run 2 and

875 at the high luminosity HL-LHC. Additionally it improves tracking position resolution which in turn  
876 improves the vertexing and  $b$ -tagging capabilities in ATLAS. The detector sits directly on a new beam  
877 pipe, only 33.25 mm away from the collision points in the azimuthal plane.

878 **SEMICONDUCTOR TRACKER (SCT)**

879 The semiconductor tracker (SCT) consists of silicon microstrips and comprises the next four layers of  
880 the ID. This sub-detector has 6.4cm long sensors that are daisy-chained into strips with a strip pitch  
881 of  $80\ \mu\text{m}$  [32]. Some of the strips have a small stereo angle to allow for measurement of both angular  
882 coordinates. In total there are 6.3 million readout channels. The intrinsic accuracies are  $17\ \mu\text{m}$  in  $R\phi$   
883 and  $580\ \mu\text{m}$  in  $z$  (or  $R$  in the endcap).

884 **TRANSITION RADIATION TRACKER (TRT)**

885 The transition radiation tracker (TRT) serves two purposes. First, it consists of 4mm diameter straw  
886 tubes filled with a 70/27/3% gas mixture of xenon, carbon dioxide, and oxygen to provide tracking of  
887 charged particles. Particles typically have 36 TRT straw tube hits per track. The material in between  
888 the straws is designed to induce transition radiation which can be useful for particle identification. As  
889 particles pass between media with different dielectric constants, they emit transition radiation that can  
890 cause additional showers in the TRT. In particular it is useful for discrimination between electrons and  
891 pions or other charged hadrons, as the amount of transition radiation is proportional to the Lorentz  
892 factor of the particle.

893 **2.2.3 CALORIMETERS**

894 The calorimeter system consists of two main sub-components: a fine granularity electromagnetic calorime-  
895 ter tailored for the measurement of photons and electrons and multiple coarser hadronic calorimeters  
896 dedicated to the measurement of hadronic showers [32]. The calorimeter system has broader cover-  
897 age than the inner detector, covering the region out to  $|\eta| < 4.9$ . It is also designed to deliver good  
898 containment of showers so as to limit leakage into the muon system. Figure 2.5 shows the layout of the  
899 calorimeter system.

900 Both the electromagnetic and hadronic calorimeters are sampling calorimeters. They alternate active  
901 material for energy measurement with passive material for energy absorption. The materials used for  
902 each purpose vary based on the type of calorimeter and its location in the detector.

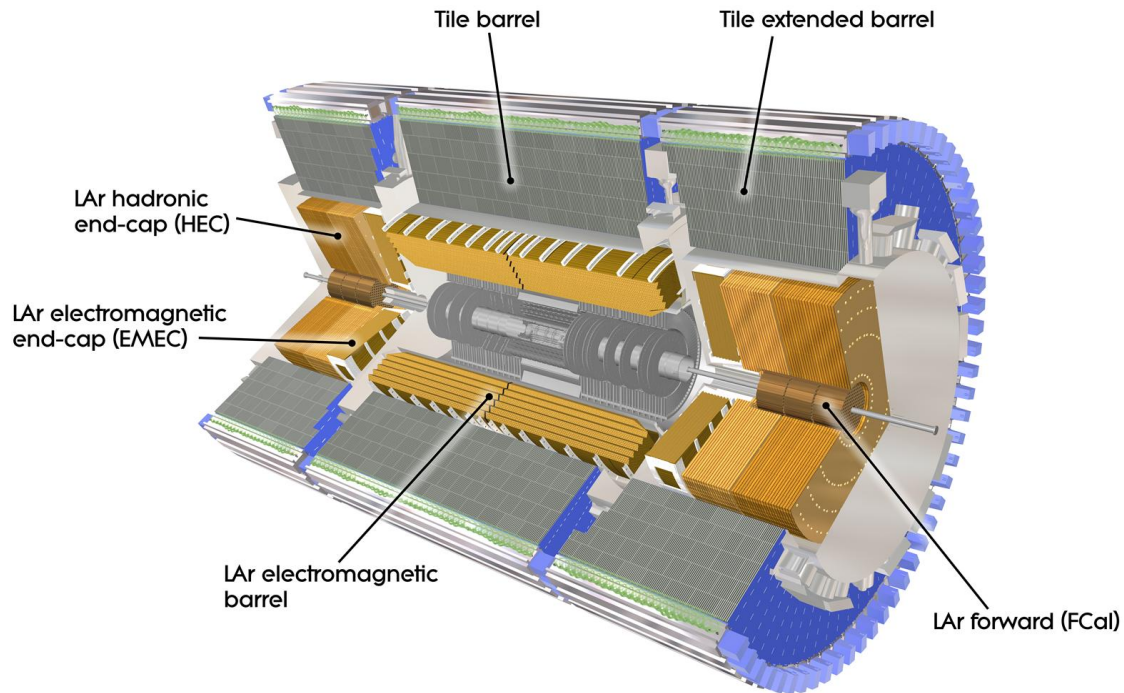


Figure 2.5: Layout of the ATLAS calorimeter system [32]

### 903 ELECTROMAGNETIC CALORIMETER

904 The electromagnetic calorimeter (EM calorimeter) use liquid Argon (LAr) as its active material and lead  
905 as its passive material. It is arrange in an accordion geometry to increase the absorption area while still  
906 allowing it to have no azimuthal cracks (complete symmetry in  $\phi$ ). The EM calorimeter is divided into a  
907 barrel portion that extends to  $|\eta| < 1.475$  and an endcap portion going from  $1.375 < |\eta| < 3.2$ . The  
908 region where these two units overlap is called the “transition region”.

909 In order to provide good containment the calorimeter depth must be optimized. Typically, for elec-  
910 tromagnetic calorimeters the depth is measured in radiation lengths. In general, the intensity of a par-  
911 ticle beam attenuates exponentially in distance with a constant equal to the radiation length. That is,

912  $I(x) = I_0 e^{-x/X_0}$ , where  $I$  is the intensity,  $x$  is the distance traveled, and  $X_0$  is the radiation length.

913 The ATLAS EM calorimeter is designed to have  $> 22$  radiation lengths in the barrel and  $> 24$  in the  
914 endcap [32].

915 **HADRONIC CALORIMETERS**

916 There are three types of hadronic calorimeters present in ATLAS: the tile calorimeter (TileCal), hadronic  
917 endcap (HEC), and forward calorimeter (FCal). Each one is optimized for stopping of hadronic showers  
918 and the materials chosen are specific to their placement in the detector.

919 The TileCal is a scintillating tile calorimeter placed directly outside the EM calorimeter. It uses steel as  
920 the absorber and plastic scintillator tiles as the active material. It has coverage in the barrel at  $|\eta| < 1.0$   
921 and in the “extended barrel” region of  $0.8 < |\eta| < 1.7$ .

922 The HEC had two wheels perpendicular to the beam line per endcap and is located directly behind  
923 the EM calorimeter endcap modules. The HEC covers the region from  $1.5 < |\eta| < 3.2$ , overlapping  
924 slightly with both the tile calorimeter and the forward calorimeter. Like the EM calorimeter, it uses liq-  
925 uid Argon as the active material, but it uses copper as the absorber.

926 The FCal covers the most forward regions of the calorimeter system, extending to the region of  $3.1 <$   
927  $|\eta| < 4.9$ . It again uses liquid argon as its active material. For absorber, it consists of an innermost  
928 module made of copper followed by a module made of tungsten.

929 The hadronic equivalent of radiation length is called the interaction length and is denoted as  $\lambda$ . In the  
930 barrel, the hadronic calorimeter depth is approximately  $9.7\lambda$ , while in the endcap is is  $10\lambda$ . The outer  
931 supports contribute an additional  $1.3\lambda$ . This is been shown to be sufficient to limit punch-through of  
932 showers to the muon system [32].

933 **2.2.4 MUON SPECTROMETER**

934 The muon spectrometer is dedicated to measuring the momentum and position of muons. It consists  
935 of tracking and trigger chambers which are unique in the barrel and endcap regions. The magnetic field  
936 for bending of muons is provided by a system of three large air-core toroid magnets (from which ATLAS

937 derives its name.) These magnets provide 1.5 to 5.5 Tm of bending power at  $0 < |\eta| < 1.4$  and approx-  
 938 imately 1 to 7.5 Tm in the endcap region of  $1.6 < |\eta| < 2.7$ . The entire muon system covers the range  
 939  $0 < |\eta| < 2.7$ . Monitored drift tubes (MDTs) are used for tracking in the barrel and the two outer  
 940 layers of the endcap, while cathode strip chambers (CSCs) are used to provide tracking in the innermost  
 941 endcap wheel. In the barrel, resistive plate chambers (RPCs) are used as trigger chambers while thin gap  
 942 chambers (TGCs) are used in the endcap. Figure 2.6 shows the layout of the ATLAS muon system. The  
 943 entire muon system is designed with the specification of providing a 10% momentum resolution for a  
 944 1 TeV muon.

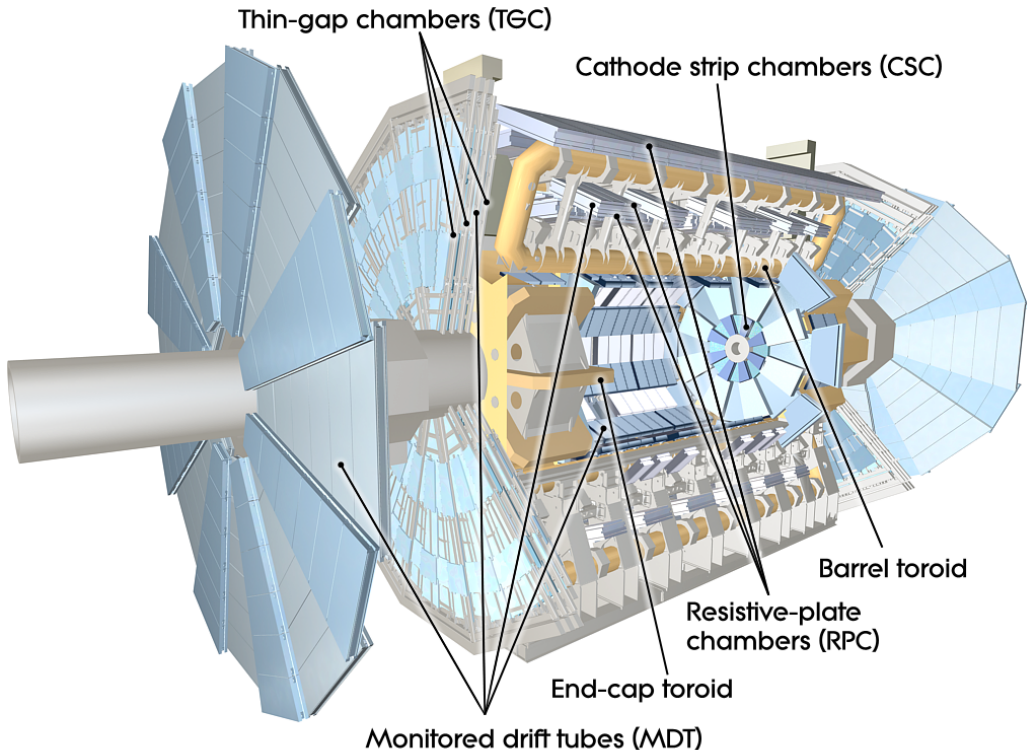


Figure 2.6: Layout of the ATLAS muon system [32]

#### 945 MONITORED DRIFT TUBES (MDTs)

946 The monitored drift tubes (MDTs) are aluminum 3cm diameter tubes filled with a 93/7 % mixture of  
 947 Argon and CO<sub>2</sub>, with trace amounts of water. As a charged particle traverses the tube, it ionizes the gas

948 and the ions drift to a wire at the center of the tube. The radial distance of traversal of the particle in the  
949 tube is determined by the drift time of the electrons, allowing for fine position resolution. The tubes  
950 have an average resolution of  $80 \mu\text{m}$  per tube and a maximum drift time of approximately 700ns. The  
951 tubes are oriented so that they give precision measurement in  $\eta$  and run along  $\phi$ . They cover  $|\eta| < 2.7$ ,  
952 except in the innermost layer of the endcap where they only go to  $|\eta| < 2.0$  [32].

### 953 CATHODE STRIP CHAMBERS (CSCs)

954 The cathode strip chambers cover a narrow window of the innermost endcap region at  $2.0 < |\eta| <$   
955 2.7. In this region the background rates in the cavern are particularly high and the CSCs are designed  
956 to handle these higher rates. The CSCs are multiwire proportional chambers with wires pointing in  
957 the radial direction (away from the beam pipe). The wire serves as an anode and there are two types of  
958 segmented cathode strip, one perpendicular to the wires which gives the precision measurement and one  
959 parallel which provides the transverse coordinate. It has an 80/20 gas mixture of Argon and CO<sub>2</sub> [32].

### 960 RESISTIVE PLATE CHAMBERS (RPCs)

961 The resistive plate chambers (RPCs) are gaseous electrode-plate detectors covering the region  $|\eta| <$   
962 1.05. They consist of two resistive plates separated by a distance of 2 mm. The gas mixture used is a  
963 94.7/5/0.3% mixture of C<sub>2</sub>H<sub>2</sub>F<sub>4</sub>, Iso-C<sub>4</sub>H<sub>10</sub>, and SF<sub>6</sub>. It has readout strips with a pitch of 23-35 mm  
964 for both  $\eta$  and  $\phi$  measurement and thus provides measurement of the azimuthal coordinate in the barrel  
965 that the MDTs do not. The thin gas gap allows for a quick response time which makes it ideal for use in  
966 the trigger. There are three layers of RPCs which are referred to as the three trigger stations. They allow  
967 for both a low  $p_T$  and high  $p_T$  trigger. The coincidence of hits in the innermost chambers allows for  
968 triggering of muons between 6 and 9 GeV, while the outermost layer allows the trigger to select high  
969 momentum tracks in the range of 9 to 35 GeV [32].

### 970 THIN GAP CHAMBERS (TGCs)

971 The thin gap chambers (TGCs) are multiwire proportional chambers where the wire to cathode distance  
972 (1.4mm) is smaller than the wire-to-wire distance (1.8 mm). They contain a gas mixture of CO<sub>2</sub> and

973 *n*-pentane and use a high electric field to gain good time resolution. They serve two functions in the  
 974 end-cap system. First, they serve as the trigger chambers. Second, they also provide azimuthal coordi-  
 975 nate measurement which the MDTs do not. They sit on the inner and middle layers of the endcap. The  
 976 outermost layer's azimuthal coordinate is determined by extrapolation [32].

### 977 2.2.5 MAGNET SYSTEM

978 As mentioned previously, there are two independent magnet systems in ATLAS. The first is a 2 T solenoid  
 979 field in the inner detector which provides bending in the azimuthal plane. The second is an approxi-  
 980 mately 0.5 T toroidal field in the muon system which provides bending in  $\eta$ . Figure 2.7 shows the pre-  
 981 dicted field integral as a function of  $|\eta|$  [32].

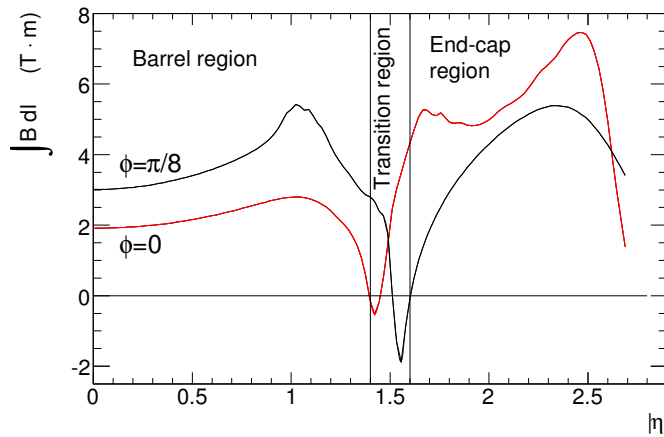


Figure 2.7: Predicted field integral as a function of  $|\eta|$  for the ATLAS magnet system [32]

### 982 2.2.6 TRIGGER SYSTEM

983 The ATLAS trigger system searches for signatures of muons, electrons, photons, hadronically decay-  
 984 ing  $\tau$  leptons, and jets in order to save these events for further analysis. The trigger system in ATLAS  
 985 is designed to reduce the maximum LHC event rate of 40 MHz to a more reasonable rate that can be  
 986 recorded. The trigger first consists of a fast, hardware based system called the Level-1 (L1) trigger. The  
 987 L1 trigger consists of independent dedicated detector sub-components that can seed regions of inter-  
 988 est (RoIs) for further analysis downstream. For muons, the RPCs and TGCs are used, while in the

989 calorimeter coarsely grained sections of calorimeter cells called towers are used. Once regions of interest  
 990 are seeded, a software based system called the High Level Trigger (HLT) is used to reconstruct objects  
 991 and integrate information from different parts of the detector. In Run 1 of ATLAS, the HLT consisted  
 992 of two separate stages: the level 2 (L2) trigger and the event filter (EF).

993 The maximum trigger rate that the L1 trigger can handle is 75 kHz. In the HLT, the rate of events  
 994 written to disk is approximately 200 Hz. Figure 2.8 shows the trigger rates for different L1 triggers in  
 995 2012 and 2015 for ATLAS [42].

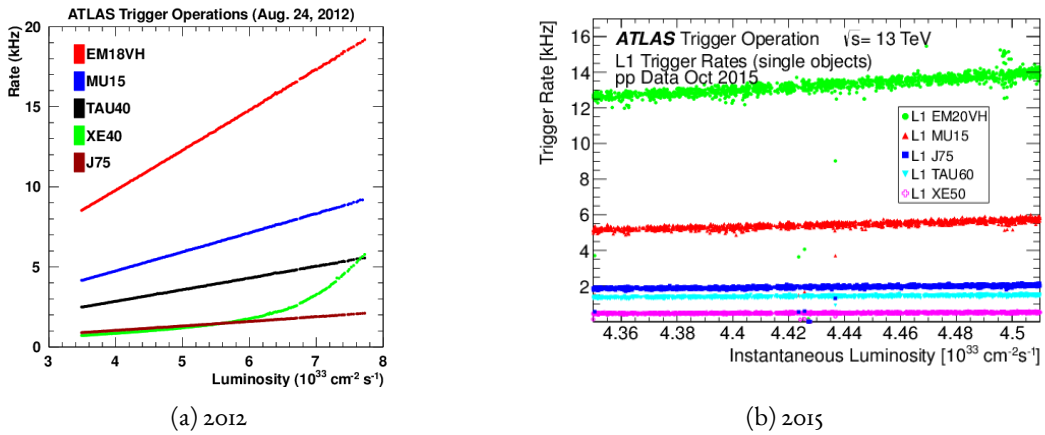


Figure 2.8: ATLAS trigger rates for Level-1 triggers as a function of instantaneous luminosity in 2012 and 2015 operation. These are single object triggers for electromagnetic clusters (EM), muons (MU), jets (J), missing energy (XE), and  $\tau$  leptons (TAU). The threshold of the trigger is given in the name in GeV. [42]

### 996 2.2.7 ATLAS DATASETS

997 ATLAS has collected data at center of mass energies of 7, 8, and 13 TeV. Figure 2.9 shows the integrated  
 998 luminosity as a function of time for each of the three collected datasets. At  $\sqrt{s} = 7$  TeV, ATLAS  
 999 recorded  $5.08 \text{ fb}^{-1}$ . Increased instantaneous luminosity in 2012 led to a larger dataset of  $21.3 \text{ fb}^{-1}$   
 1000 recorded at  $\sqrt{s} = 8$  TeV. After Long Shutdown 1 (LS1) of the LHC and a restart in 2015, ATLAS  
 1001 recorded  $3.9 \text{ fb}^{-1}$  of data at  $\sqrt{s} = 13$  TeV. [43, 44]

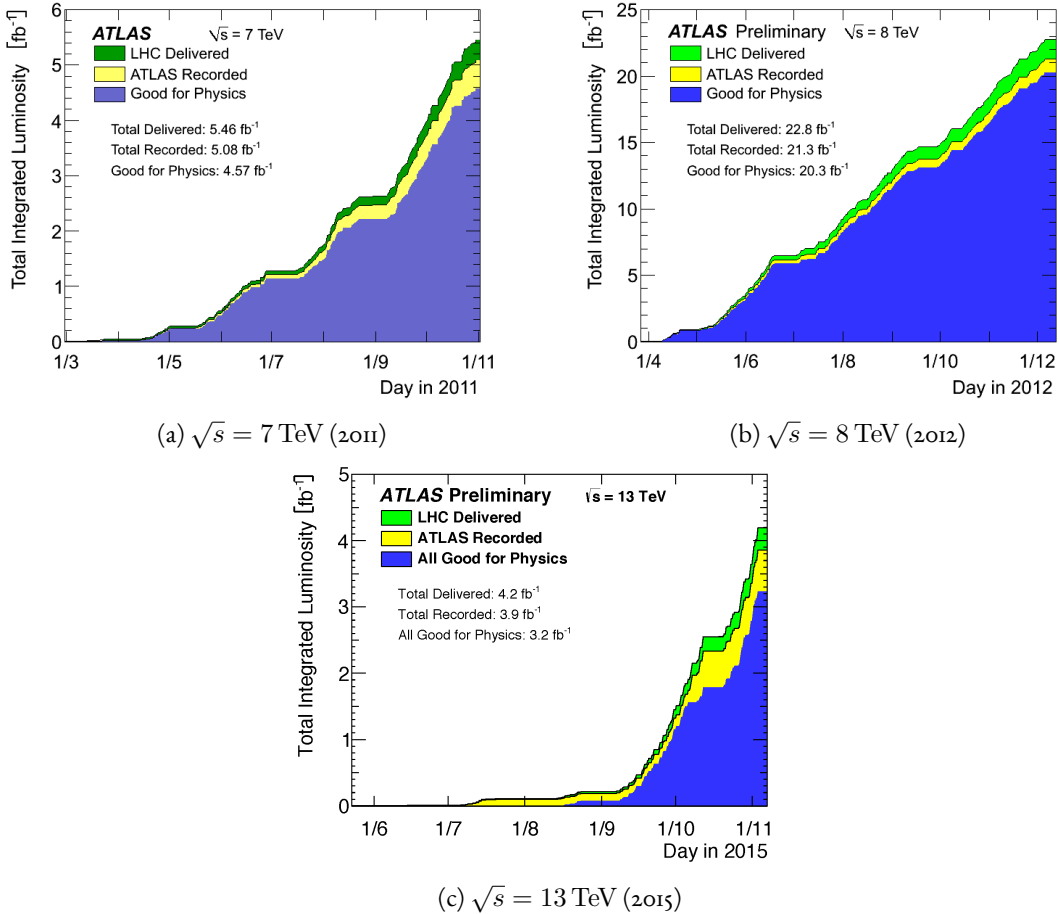


Figure 2.9: Instantaneous luminosity as a function of time for data recorded by ATLAS at different center of mass energies [43, 44]

### 2.2.8 DETECTOR PERFORMANCE

Table 2.2 summarizes the design requirements for each of the different sub-detectors. This table shows the energy and momentum resolution of each tracking, calorimetry, and muon measurements.

### 2.3 THE ATLAS MUON NEW SMALL WHEEL UPGRADE

As the LHC continues operation, it is scheduled to be upgraded in several phases to allow it to reach higher instantaneous luminosities and thus collect larger datasets. These conditions will open new doors for study of rare physics processes but will also present interesting challenges that must be faced. ATLAS will require new detector technologies to cope with the increased background rates in the cavern in these

	Required resolution
Tracking	$\sigma_{p_T}/p_T = 0.05\% p_T \oplus 1\%$
EM calorimetry	$\sigma_E/E = 10\%/\sqrt{E} \oplus 0.7\%$
Hadronic calorimetry	
Barrel and end-cap	$\sigma_E/E = 50\%/\sqrt{E} \oplus 3\%$
Forward	$\sigma_E/E = 100\%/\sqrt{E} \oplus 10\%$
Muon spectrometer	$\sigma_{p_T}/p_T$ at $p_T = 1$ TeV

Table 2.2: Performance requirements for the ATLAS detector [32].

high luminosity conditions. One such upgrade, scheduled to be installed during Long Shutdown 2 (LS2) of the LHC in 2018, is the ATLAS Muon New Small Wheel (NSW) upgrade [45]. The NSW will replace the innermost end-cap wheel of the muon system with new technologies, as this is the part of the muon detector closest to the beam and thus suffers from the highest rates.

### 2.3.1 MOTIVATION

The motivation of the NSW is two-fold. First, the objective is to alleviate the decreased tracking efficiency that comes in a high rate environment. As figure 2.10, at the LHC design luminosity both the efficiency of recording hits and reconstructing track segments in the MDTs decreases at the LHC design luminosity.

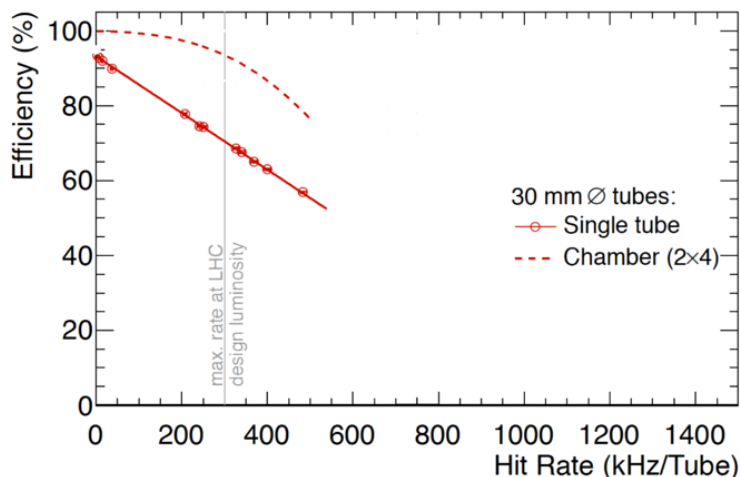


Figure 2.10: MDT tube hit (solid) and segment (dashed) efficiency as a function of hit rate per tube [45]

1019 Second, the NSW will work to alleviate the rate of fake triggers arising in the endcap. Figure 2.II  
 1020 shows the extrapolated trigger rates as a function of the  $p_T$  threshold with and without the NSW up-  
 1021 grade. As the figure shows, the NSW upgrade will reduce the trigger rate by an order of magnitude com-  
 1022 pared to the current endcap trigger system.

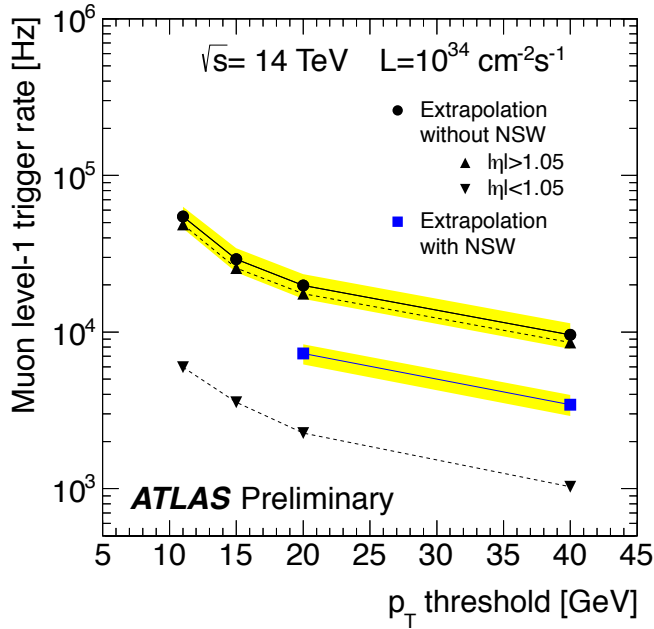


Figure 2.II: Trigger rate as a function of  $p_T$  threshold with and without the NSW upgrade [45]

### 1023 2.3.2 NSW DETECTOR TECHNOLOGIES

1024 The NSW will use two new detector technologies - micromesh gaseous structure detectors (micromegas)  
 1025 and small-strip thin gap chambers (sTGCs) [45, 46]. Unlike the previous detectors, both of these detec-  
 1026 tor technologies can be used for tracking or trigger. However, the micromegas is more suited to tracking  
 1027 because of its good spatial resolution, while the sTGCs have better time resolution and are more suited  
 1028 for the trigger. To maintain a fully redundant system, both technologies are used for both purposes.

1029 **MICROMEGAS**

1030 Micromegas detectors operate using a thin metallic mesh that sits approximately  $100\ \mu\text{m}$  away from  
1031 the readout electrodes to create the amplification region. Above this mesh, there is a drift region on the  
1032 order of a few mm in length capped by a drift electrode. As a charged particle traverses the detector, it  
1033 ionizes gas and the electrons drift down towards readout strips. The timing of the drift can be used to  
1034 reconstruct the angle of traversal of the particle. This is illustrated in figure 2.12. The micromegas used in  
1035 ATLAS will be resistive micromegas, where the readout electrodes are topped with resistive strips [47].  
1036 This alleviates the risk of sparking in the large area detectors that ATLAS will use.

1037 In ATLAS, the micromegas drift gap will be 5 mm and the amplification gap will be  $128\ \mu\text{m}$ . They  
1038 are filled with the same gas mixture as the MDTs. They will be stacked in an octuplet in an XXUV-  
1039 UVXX geometry, where X refers to straight strips and U and V refer to stereo strips at an angle of  $\pm 1.5^\circ$ .  
1040 This arrangement allows for measurement of the azimuthal coordinate and gives a large lever arm be-  
1041 tween the straight strips for triggering purposes. Figure 2.12 shows the geometry of a single micromegas  
1042 detector as well as its operating principle [45].

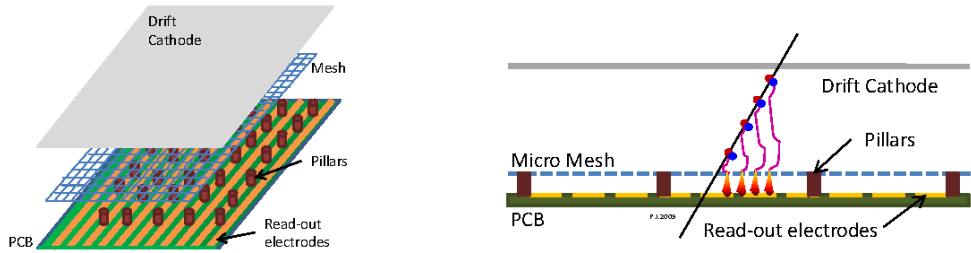


Figure 2.12: Illustrations of the geometry (left) and operating principle (right) of the micromegas detector [45]

1043 **sTGCs**

1044 The sTGCs are similar to the TGCs already described. They consist of gold-plated tungsten wires with  
1045 a 1.8 mm pitch between two cathode planes 1.4 mm away from the wire plane. One cathode plane  
1046 consists of strips with a 3.2 mm pitch (much smaller pitch than the TGCs), while the other consists  
1047 of coarser pads that are used for defining regions of interest in the sTGC trigger algorithm. Figure 2.13  
1048 shows the basic detector geometry.

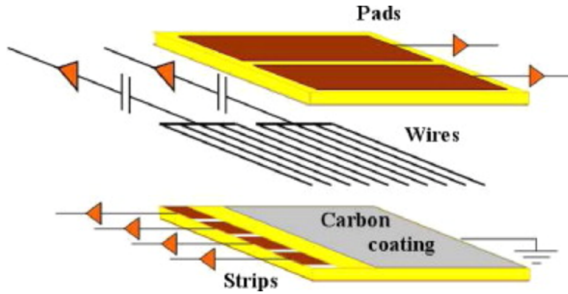


Figure 2.13: Geometry of the sTGC detector [45]

### 1049 2.3.3 PHYSICS IMPACT

1050 Maintaining low  $p_T$  thresholds for muons while still staying within the trigger rate budget at Level 1  
 1051 (20 kHz) for the muon system is crucial for physics analyses to be successful in high luminosity condi-  
 1052 tions. One realm where the lepton trigger threshold is especially important is in Higgs physics. In the  
 1053  $H \rightarrow WW^*$  analysis, one of the  $W$  bosons is off shell and tends to decay to soft leptons. In associated  
 1054 production of a Higgs with a  $W$ , the lepton is also important because the lepton provides the main han-  
 1055 dle which allows the event to be triggered. Table 2.3 shows the impact of increasing the trigger thresholds  
 1056 on these analyses. It shows that either raising the threshold or using only the barrel both have signifi-  
 1057 cant impacts on the signal efficiency. With the NSW, the signal efficiency is largely maintained and the  
 1058 triggers can be unprescaled.

Threshold	$H \rightarrow bb$ (%)	$H \rightarrow WW^*$ (%)
$p_T > 20$ GeV	93	94
$p_T > 40$ GeV	61	75
$p_T > 20$ GeV (barrel only)	43	72
$p_T > 20$ GeV (with NSW)	90	92

Table 2.3: Signal efficiencies for  $WH$  production with  $H \rightarrow b\bar{b}$  and  $H \rightarrow WW^* \rightarrow \mu\nu qq$  under different trigger configurations [45].

### 1059 2.4 OBJECT RECONSTRUCTION IN ATLAS

1060 ATLAS analyses first start by requiring the presence of certain reconstructed physics objects in the event.  
 1061 This section will present a brief overview of the algorithms used to reconstruct electrons, muons, jets

1062 (including  $b$ -jets), and missing energy\*. The performance of object reconstruction and measurement will  
 1063 also be discussed as these are relevant to the analyses presented later. Figure 2.14 gives an overview of the  
 1064 different sub-detectors that each type of particle will interact with in ATLAS.

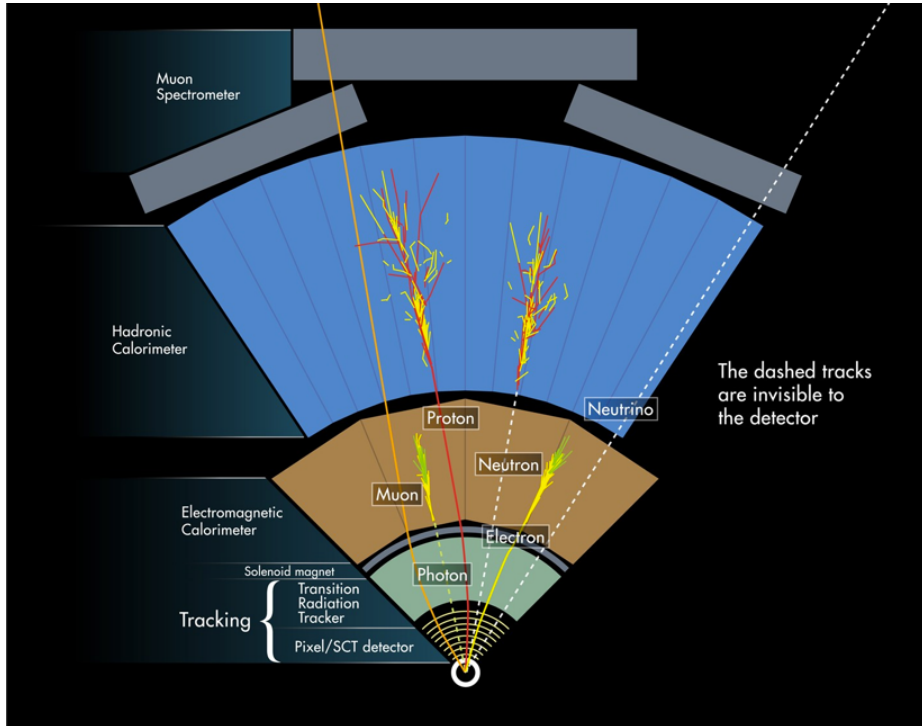


Figure 2.14: Illustration of particle interactions in ATLAS [48]

#### 1065 2.4.I ELECTRONS

1066 Electrons in ATLAS will leave tracks in the inner detector and energy deposits in the electromagnetic  
 1067 calorimeter. The algorithm for recognizing the signature of electrons proceeds in two steps: reconstruc-  
 1068 tion and identification.

1069 In reconstruction, an electron candidate is formed by matching EM calorimeter deposits with ID  
 1070 tracks. The algorithm first chooses seed clusters in the EM calorimeter by using a sliding window algo-  
 1071 rithm that searches for towers with transverse energy larger than 2.5 GeV. In addition to seed clusters,  
 1072 track candidates must be identified in the ID. The algorithm selects seed tracks with  $p_T > 1$  GeV that

---

\*Reconstruction algorithms for other objects, such as photons and  $\tau$  leptons, are not detailed here as these objects are not used in the presented studies.

1073 do not fit well with a pion hypothesis. Once candidate tracks are selected, they are re-fit with a Gaussian  
 1074 Sum Filter (GSF) algorithm to estimate electron parameters [49]. Finally, an electron candidate is  
 1075 formed if at least one track matches to a seed cluster in the calorimeter. The full details of the reconstruc-  
 1076 tion algorithm can be found in reference [50].

1077 Once an electron candidate is present, identification criteria must be applied in order to reject fake  
 1078 electrons from background. Many different variables are used for this identification, most of them re-  
 1079 lated to the shower shape in the EM calorimeter and the amount of leakage into the hadronic calorime-  
 1080 ter, as well as information from the ID and in particular the TRT. There are both cut-based and likelihood-  
 1081 based criteria that range from “loose” to “very tight”. For details, see reference [50].

1082 Figure 2.15 shows the algorithm’s reconstruction efficiency of true electrons for different identification  
 1083 criteria as well as the electron energy resolution in simulation [50, 51]. The reconstruction efficiency is  
 1084 measured using both  $Z$  and  $J/\psi$  tag and probe techniques.

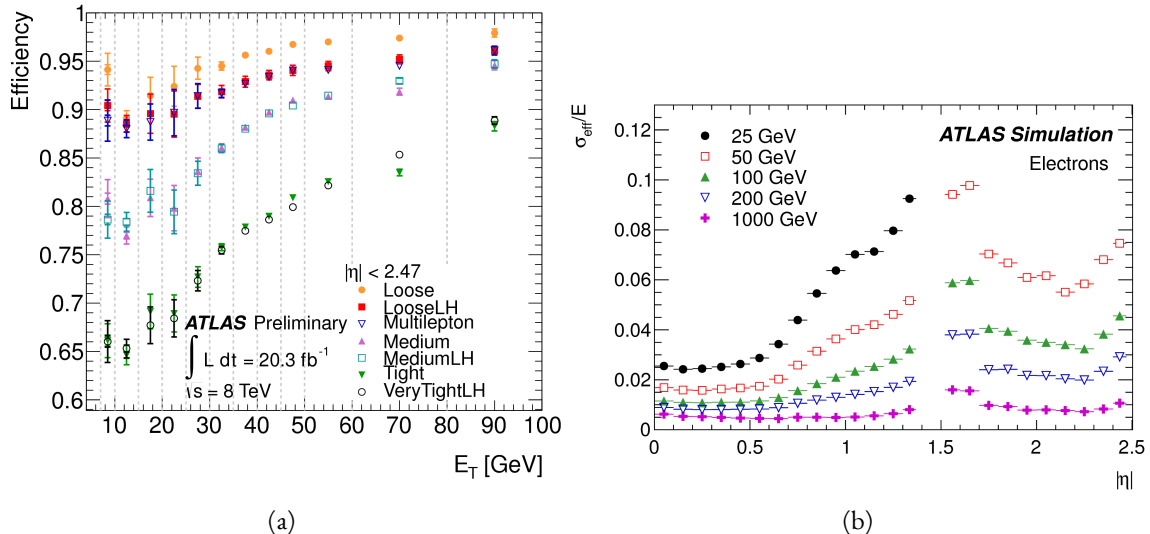


Figure 2.15: Electron performance: (a) reconstruction efficiency as a function of electron  $E_T$  [50] (b) energy resolution in simulation as a function of  $|\eta|$  for different energy electrons [51]

#### 1085 2.4.2 MUONS

1086 The ATLAS detector is designed to stop most particles before they reach the muon spectrometer. Muons,  
 1087 however, are minimum ionizing particles, meaning that they will not lose a significant amount of energy

1088 through interactions with the detector and will thus pass through. Therefore, the muon reconstruction  
1089 works to match tracks in the muon spectrometer with tracks in the inner detector.

1090 The first step of reconstruction is to reconstruct local straight line tracks, called segments, in each  
1091 muon chamber. Segments are then fit to larger tracks that traverse the entire muon spectrometer. Such  
1092 muon tracks are referred to as “standalone” tracks (SA) as they only use information from the muon  
1093 spectrometer. The standalone tracks are then matched to tracks in the inner detector to form “com-  
1094 bined” (CB) muons, where the combined ID and MS fit are used to determine the momentum and di-  
1095 rection of the muon. To improve acceptance, segment-tagged and calorimeter-tagged muons are also  
1096 reconstructed. In these cases, ID tracks are matched to segments in the MS and calorimeter deposits con-  
1097 sistent with a minimum ionizing particle, respectively. The details of the reconstruction can be found in  
1098 reference [52].

1099 As with electrons, once muon candidates are reconstructed they have identification criteria applied to  
1100 reduce background. These criteria include the  $\chi^2$  match between the ID and MS tracks, the number of  
1101 hits in the ID, overall ID and MS track fit quality, and additional variables [52]. The criteria range from  
1102 “loose” to “tight” as with electrons.

1103 Figure 2.16 shows the muon reconstruction efficiency (measured with  $Z$  and  $J/\psi$  tag and probe) and  
1104 invariant mass resolution [52].

#### 1105 2.4.3 JETS

1106 When a quark or gluon is produced in collisions, it is not measured directly in ATLAS. Rather, due to  
1107 QCD effects, it produces a collimated spray of hadrons in the direction of the original parton, which is  
1108 known as a jet. Jets are reconstructed in ATLAS using energy deposits in the hadronic calorimeter. The  
1109 first step is build “topological clusters” out of energy deposits in calorimeter cells [53, 54]. This is done  
1110 using strategy where seed cells are chosen by picking cells whose energy measurements are four times the  
1111 amount of noise expected for that cell. Adjacent cells with at least  $2\sigma$  energy measurements are added  
1112 to the cluster, then a final layer of clusters with energy above  $0\sigma$  are added. Once calorimeter clusters  
1113 are formed, they are clustered further into jet candidates using the anti- $k_T$  jet clustering algorithm [55].

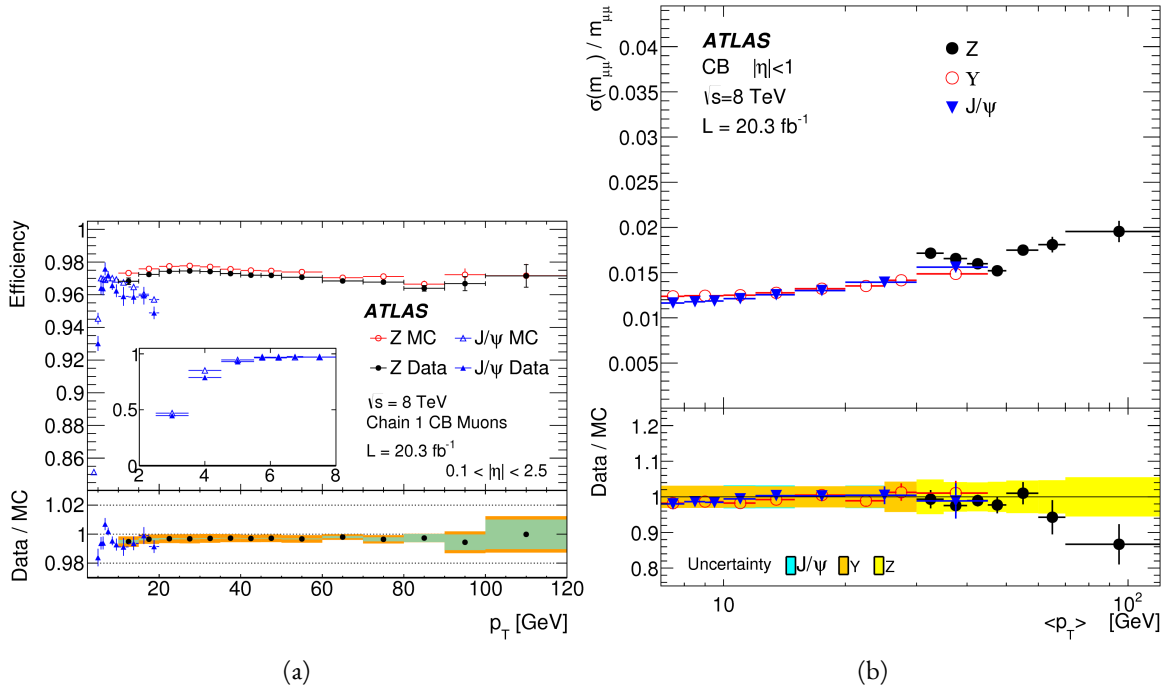


Figure 2.16: Muon performance: (a) reconstruction efficiency as a function of muon  $p_T$  (b) dimuon mass resolution as a function of average  $p_T$  [52]

1114 This algorithm uses a parameter  $R$  that appears in the denominator of the clustering distance metric and  
 1115 defines the radial size of the jet in  $\eta$ - $\phi$  space.

1116 The energy response of the calorimeter must be properly characterized in order to reconstruct jet en-  
 1117 ergy. Calorimeter clusters can be calibrated either with the EM calibration, where each cluster is assumed  
 1118 to have come from the energy deposit of an electron or photon, or the LCW calibration, where local  
 1119 cluster weights are computed to allow for local calibration of clusters as hadronic or electromagnetic.

1120 The details of the jet energy calibration are not detailed here and are discussed in reference [56].

1121 Figure 2.17 shows the jet energy response after calibration in Monte Carlo as a function of the true  $p_T$   
 1122 of the jet [56].

#### 1123 2.4.4 $b$ -TAGGING

1124 One important aspect of jet physics is the task of identifying the flavor of parton that produced the mea-  
 1125 sured jet. While in general this is very difficult, jets from  $b$ -quarks offer an interesting case where such  
 1126 identification is possible.  $B$  mesons have a lifetime on the order of  $10^{-12}$  seconds, which makes a  $c\tau$

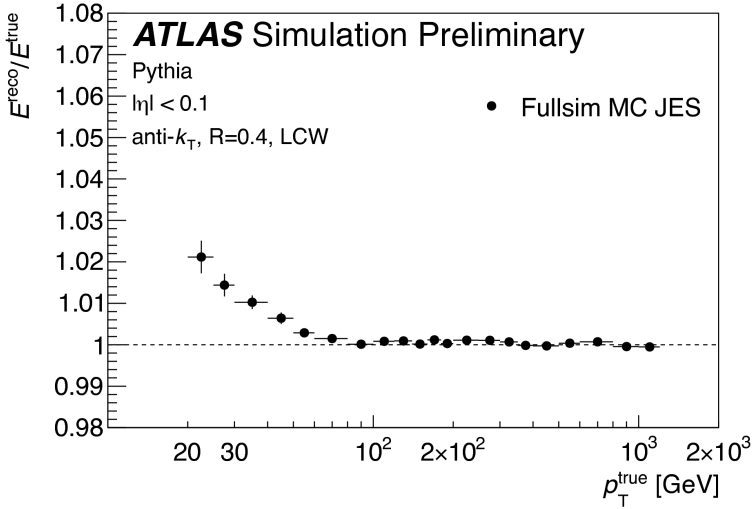


Figure 2.17: Jet energy response after calibration as a function of true  $p_T$  in simulation [56]

on the order of millimeters [6]. This type of displaced decay vertex can be identified in detectors like ATLAS and allows  $b$ -jets to be distinguished from other flavors of jets<sup>†</sup>.

ATLAS uses a multivariate machine learning algorithm to identify jets from  $b$ -quarks. The inputs to this algorithm are determined from lower level reconstruction algorithms. There are three distinct algorithms that reconstruct variables which are used as input to the multivariate technique.

The first family is referred to as IPxD (where the x can either be 2 or 3). These algorithms use the transverse and longitudinal impact parameters  $d_0$  and  $z_0$  of the tracks inside a jet to determine their consistency with the primary vertex. They two or three dimensional (hence the x) templates for light flavor, charm, and bottom jets and then evaluate the likelihood of the jet coming from each of these types. The likelihood ratios are used as inputs to the multivariate algorithm.

The next two algorithms used as input are referred to as the secondary vertex (SV) and JetFitter (JF) algorithms. The SV algorithm uses tracks inside the jet to fit for vertices that are displaced from the primary vertex. The JF algorithm attempts to reconstruct the full flight path of the  $b$  by looking for multiple displaced vertices along the same line (as  $B$  decays often result in subsequent  $c$  decays).

In Run 1, the multivariate  $b$ -tagging algorithm used a neural network and was referred to as MV1.

---

<sup>†</sup>Jets from charm quarks can also be detected in this way but they do not live quite as long so the displacement of the vertex is harder to distinguish

1142 The details of this algorithm and its inputs are given in reference [57]. In Run 2, the number of inputs  
 1143 was simplified and a boosted decision tree with 24 input variables was used, referred to as MV2. The  
 1144 details of this algorithm are in reference [58]. Figure 2.18 shows the performance of each of these algo-  
 1145 rithms.

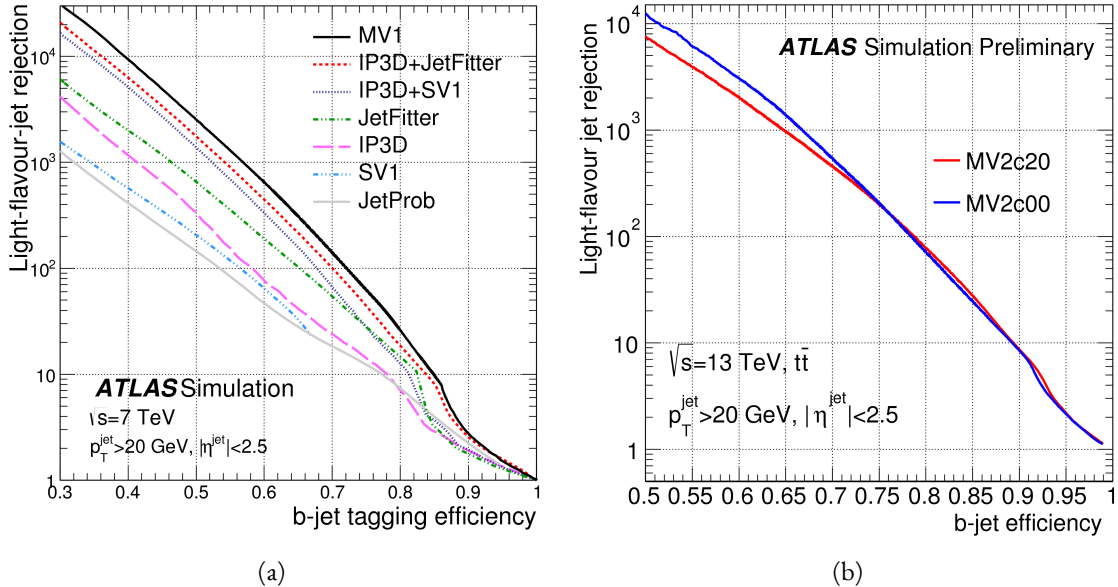


Figure 2.18: Light jet rejection (1/efficiency) vs.  $b$ -jet efficiency for MV1 and its input algorithms (a) [57] and MV2 (b) [58] in simulated  $t\bar{t}$  events. The numbers in the algorithm names in (b) refer to the fraction of charm events used in the MV2 training.

#### 1146 2.4.5 MISSING TRANSVERSE ENERGY

1147 As noted in figure 2.14, neutrinos produced in ATLAS will pass through the detector without inter-  
 1148 acting. The only way of detecting the presence of particles like neutrinos (or BSM particles that are  
 1149 long-lived) is to use missing transverse momentum. The basic principle of missing transverse energy is  
 1150 to use the momentum balance of the incoming protons to infer the presence of missing particles. The  
 1151 net longitudinal momentum of the incoming partons that collide is not known (since each carries an un-  
 1152 known fraction of the proton's momentum). However, the protons (and thus incoming partons) have  
 1153 no net momentum in the plane transverse to the beam line (the  $x$ - $y$  plane). Therefore, if there are no  
 1154 un-measured particles in the final state, the transverse momenta of all of the final state particles should

balance. The magnitude of this imbalance is known as missing transverse momentum ( $E_T^{\text{miss}}$ ).

The basic calculation of missing transverse momentum from calorimeter cells is given in equation 2.4 [59].

1157

$$\begin{aligned} E_x^{\text{miss}} &= -\sum_{i=1}^{N_{\text{cell}}} E_i \sin \theta_i \cos \phi_i \\ E_y^{\text{miss}} &= -\sum_{i=1}^{N_{\text{cell}}} E_i \sin \theta_i \sin \phi_i \end{aligned} \quad (2.4)$$

1158 The  $E_T^{\text{miss}}$  calculation is separated into different terms based on the objects that the calorimeter clusters  
1159 are associated with. This way, each cell's contribution is calibrated appropriately according to the object.

1160 This separation of terms is shown in equation 2.5 [59].

$$\begin{aligned} E_{x(y)}^{\text{miss,calo}} &= E_{x(y)}^{\text{miss},e} + E_{x(y)}^{\text{miss},\gamma} + E_{x(y)}^{\text{miss},\tau} + E_{x(y)}^{\text{miss,jets}} \\ &\quad + E_{x(y)}^{\text{miss,softjets}} + E_{x(y)}^{\text{miss},\mu} + E_{x(y)}^{\text{miss,CellOut}} \end{aligned} \quad (2.5)$$

1161 The CellOut term of the above equation corresponds to calorimeter cells with energy deposits that are  
1162 not associated with other objects. The soft jets term comes from cells associated to jets with  $p_T$  between  
1163 7 and 20 GeV, while the jets term comes from jets with  $p_T > 20$  GeV. Because muons do not deposit  
1164 significant energy in the calorimeter, the muon momentum is used for the muon term [59]. The final  
1165  $E_T^{\text{miss}}$  is calculated using equation 2.6.

$$E_T^{\text{miss}} = \sqrt{(E_x^{\text{miss}})^2 + (E_y^{\text{miss}})^2} \quad (2.6)$$

1166 Figure 2.19 shows the resolution of the components of the  $E_T^{\text{miss}}$  under different pileup suppression  
1167 techniques [60].

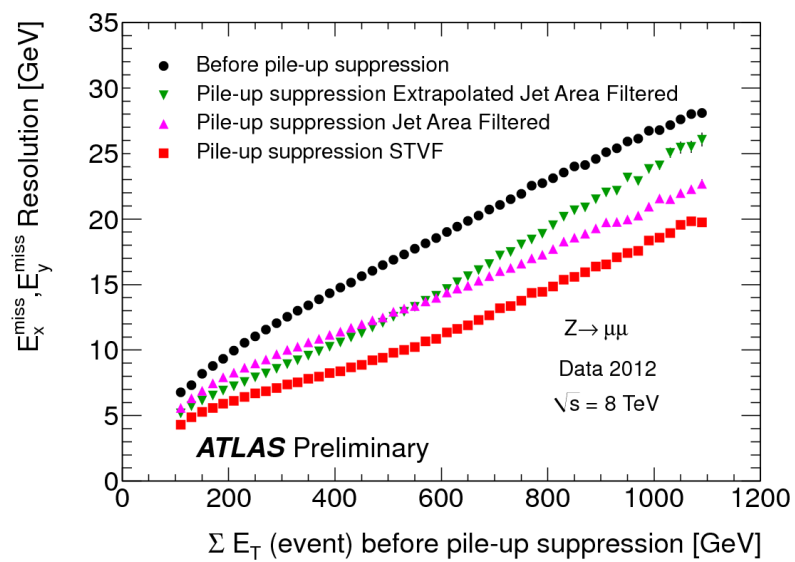


Figure 2.19: Resolution of  $E_T^{\text{miss}}$  components as a function of  $\sum E_T$  before pileup suppression with different pileup techniques [60]

## Part II

1168

Observation and measurement of Higgs

1169

boson decays to  $WW^*$  in LHC Run I at

1170

$\sqrt{s} = 7$  and 8 TeV

1171

*Basic research is what I am doing when I don't know  
what I am doing.*

Wernher von Braun

# 3

1172

1173

## $H \rightarrow WW^* \rightarrow \ell\nu\ell\nu$ Analysis Strategy

### 1174 3.1 INTRODUCTION

1175 This chapter presents an overview of the strategy for searching for a Higgs boson in the  $H \rightarrow WW^* \rightarrow$   
1176  $\ell\nu\ell\nu$  decay topology. Its purpose is to define in broad terms how the search and measurement are un-  
1177 dertaken, before going into details on the specific sub-categories within the larger analysis. First, the  
1178 properties of the Higgs signal are discussed and the associated backgrounds are presented. Next, the ob-  
1179 servables used to enhance the signal to background ratio are defined. Finally, the parameters of interest  
1180 in the search and measurement will be shown, along with a brief overview of the statistical treatment of  
1181 the final Higgs candidates.

1182 Following this chapter, the results of three different studies within the  $H \rightarrow WW^* \rightarrow \ell\nu\ell\nu$  channel  
1183 are shown. Chapter 4 presents a search for Higgs boson production in gluon fusion mode and the role  
1184 of the  $H \rightarrow WW^*$  channel in its discovery. Chapter 5 shows the search and first observation in ATLAS  
1185 of the Vector Boson Fusion (VBF) production mode of the Higgs in the  $H \rightarrow WW^*$  decay channel.

1186 Finally, chapter 6 shows the combined Run 1  $H \rightarrow WW^*$  results for the measurement of the Higgs  
1187 cross section and relative coupling strengths to other SM particles.

1188 3.2 THE  $H \rightarrow WW^* \rightarrow \ell\nu\ell\nu$  SIGNAL IN ATLAS

1189 The signal studied in this and subsequent chapters is the Higgs boson in the  $WW^*$  final state, where  
1190 each  $W$  boson subsequently decays into a charged lepton and a neutrino. In the simplest decay path,  
1191 the final state consists of two neutrinos and two charged leptons, each of which can be either an electron  
1192 or a muon. If a  $W$  decays to a  $\tau$  lepton, only leptonic decays of the  $\tau$  are considered. The  $\tau$  lepton pro-  
1193 duce additional neutrinos in the final state but still yield two charged leptons (where each lepton is an  
1194 electron or muon). Neutrinos are not detected in ATLAS, so the final state ultimately consists of two  
1195 reconstructed leptons and missing transverse momentum (denoted as  $E_T^{\text{miss}}$ ). Final states where both of  
1196 the charged leptons are electrons or muons are referred to as the “same flavor” ( $ee/\mu\mu$ ) final states, while  
1197 those with one electron and one muon are referred to as “different flavor” ( $e\mu$  or  $\mu e$ ).

1198 There can be additional jets produced in association with the Higgs boson. As described in detail  
1199 in Chapter 1, if the Higgs is produced via vector boson fusion production, there will be two additional  
1200 forward jets in the event. In gluon fusion, one or more jets can be produced through initial state radi-  
1201 ation from the incoming gluons. Because of the varying background composition as a function of jet  
1202 multiplicity, each bin in this variable has its own dedicated requirements applied in the search and mea-  
1203 surement. The  $n_j = 0$  and  $n_j = 1$  bins are dedicated to gluon fusion production, while the  $n_j \geq 2$  bin  
1204 has separate dedicated searches for ggF and VBF production.

1205 Figure 3.1 shows the relative branching fractions for the  $H \rightarrow WW^*$  process, calculated from the Par-  
1206 ticle Data Group values for the  $W$  and  $\tau$  branching ratios [6]. The largest branching ratio corresponds  
1207 to both  $W$  bosons decaying to quark pairs at 45.44%. The second largest ratio is for one  $W$  decaying lep-  
1208 tonically and the other decaying to quarks, a branching ratio of 34.18%. In all cases,  $\ell$  denotes either an  
1209 electron or muon, and the leptonic branching ratios of the  $\tau$  are included. For example, the  $\ell\nu qq$  final  
1210 state includes one  $W$  decaying to  $e\nu$ ,  $\mu\nu$ , or  $\tau\nu$ . In the case of the  $W \rightarrow \tau\nu$  decay, the  $\tau$  lepton then  
1211 decays to an electron or muon via  $\tau \rightarrow \nu_\tau \ell \nu_\ell$ . Final states with a  $\tau_h$  refer to hadronic decays of the  $\tau$ .

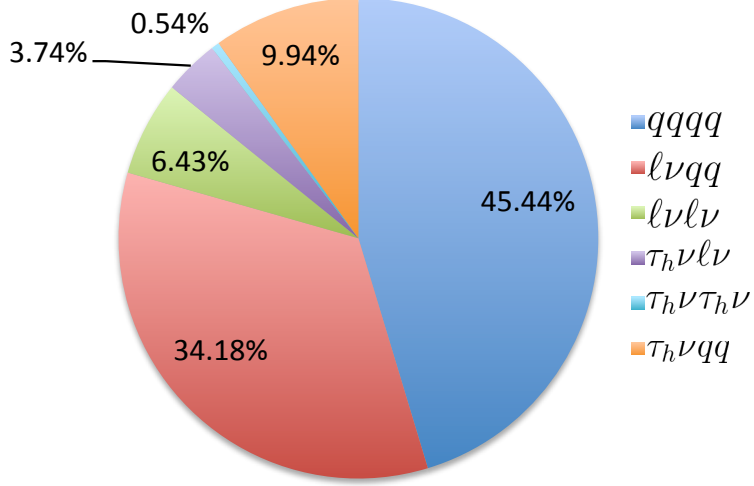


Figure 3.1: Branching ratios for a  $WW$  system.  $q$  refers to quarks.  $\ell$  can be either an electron or muon, and the leptonic branching ratios of the  $\tau$  are included. For example, the  $\ell\nu qq$  final state includes one  $W$  decaying to  $e\nu$ ,  $\mu\nu$ , or  $\tau\nu$ .  $\tau_h$  refer to hadronic decays of the  $\tau$ .

<sub>1212</sub> The branching ratio of the  $\ell\nu\ell\nu$  final state is 6.43%.

<sub>1213</sub> While the  $\ell\nu\ell\nu$  final state is not a large fraction of the branching ratio, there are significant advantages  
<sub>1214</sub> to using this channel in an analysis. First, both the  $qqqq$  and  $\ell\nu qq$  channels suffer from a large QCD  
<sub>1215</sub> multijet background, which is often difficult to model. Second, events in the the  $\ell\nu\ell\nu$  channel in data  
<sub>1216</sub> can be triggered more efficiently due to the presence of two leptons.

### <sub>1217</sub> 3.3 BACKGROUND PROCESSES

<sub>1218</sub> Many processes from the Standard Model can also produce a final state with two leptons and missing  
<sub>1219</sub> transverse momentum. This section describes the dominant backgrounds to Higgs production and fur-  
<sub>1220</sub> ther explains how they can be reduced. Table 3.1 summarizes the different background processes.

#### <sub>1221</sub> 3.3.1 STANDARD MODEL WW PRODUCTION

<sub>1222</sub> Non-resonant Standard Model diboson production, as shown in figure 3.2, is an irreducible background  
<sub>1223</sub> to Higgs boson production in the  $WW$  final state. It produces the same exact final state objects, namely

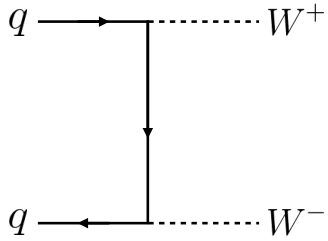


Figure 3.2: Feynman diagram for Standard Model WW production

1224 leptonically decaying W bosons. There are no additional objects in the final state that allow for back-  
1225 ground reduction. Therefore the analysis solely relies on the correlations between the leptons to reduce  
1226 this background.

### 1227 3.3.2 TOP QUARK PRODUCTION

1228 Top quark production can mimic the Higgs in the  $WW^*$  final state as well. Top quarks can be produced  
1229 either in pairs ( $t\bar{t}$  production) or singly ( $s$ -channel,  $t$ -channel, or associated production  $Wt$ ). The domi-  
1230 nant top background are  $t\bar{t}$  and  $Wt$  production.

1231 Because top quarks decay via  $t \rightarrow Wb$ , top pair production can produce a final state with two W  
1232 bosons that then decay leptonically. In  $Wt$  production, there are two real W bosons produced, as with  
1233  $t\bar{t}$ . In both cases, there is at least one  $b$ -jet in the final state. By vetoing on the presence of  $b$ -jets, these top  
1234 quark backgrounds can be reduced. Figure 3.3 shows the Feynman diagrams for  $t\bar{t}$  and  $Wt$  production.

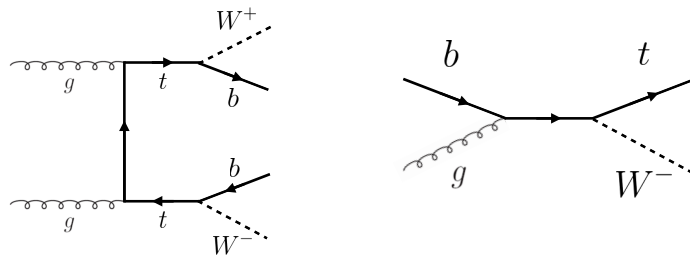


Figure 3.3: Feynman diagrams for top pair production (left) and  $Wt$  production (right)

1235    3.3.3     $W + \text{JETS BACKGROUND}$

1236    Single  $W$  boson production in association with jets is a unique background to Higgs production. The  
1237    other backgrounds considered thus far have all included two prompt leptons, each decaying from a  $W$   
1238    boson, in the final state. In  $W + \text{jets}$  production, however, only one reconstructed lepton originates from  
1239    a  $W$ . The second reconstructed lepton is either an algorithmic “fake” or the result of non-prompt de-  
1240    cays. In the first case, the lepton is a jet misidentified as a lepton by either the electron or muon recon-  
1241    struction algorithms. In the second case, the lepton may be a real lepton but coming from semi-leptonic  
1242    decays of particles inside the shower of the jet. This background can be reduced by requiring that the  
1243    reconstructed lepton have little activity in the surrounding region of the calorimeter (also known as an  
1244    “isolation”). Figure 3.4 shows the Feynman diagram for  $W + \text{jets}$  production.

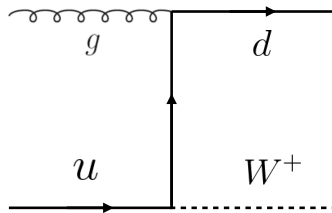


Figure 3.4: An example Feynman diagram of  $W + \text{jets}$  production

1245    3.3.4     $Z/\gamma^* + \text{JETS BACKGROUND}$

1246    Production of a  $Z$  boson or virtual photon (also known as Drell-Yan and denoted with  $Z/\gamma^*$ ) in associa-  
1247    tion with jets is also a background to Higgs production. The  $Z$  boson decays to two leptons of the same  
1248    flavor. When the  $Z/\gamma^*$  decays directly to electrons or muons, the background enters the same flavor fi-  
1249    nal state. When the  $Z$  decays to two  $\tau$  leptons the background can enter the different flavor final state as  
1250    well. Figure 3.5 shows the production of a  $Z$  in association with one jet. Because there are no neutrinos  
1251    in this final state, variables like  $E_T^{\text{miss}}$  can be used to reduce the background\*.

---

\*The  $E_T^{\text{miss}}$  cut is much more effective for the reduction of  $Z/\gamma^*$  production in the same flavor final state. If the background enters the different flavor final state through  $\tau$  decays, there will be neutrinos present. Other requirements on the lepton invariant mass are made to reduce the  $Z/\gamma^* \rightarrow \tau\tau$  background.



Figure 3.5: An example Feynman diagram of  $Z$ +jets production

### 1252 3.3.5 SUBDOMINANT BACKGROUNDS

1253 There are additional processes which contribute to the background composition. These backgrounds are  
 1254 subdominant and contribute less to the total background estimate than those discussed previously. The  
 1255 first process is referred to as  $VV$  or “Other diboson” processes and includes multiple Standard Model  
 1256 diboson processes, including  $WZ$ ,  $ZZ$ ,  $W\gamma$ ,  $W\gamma^*$ , and  $Z\gamma$  production. Additionally, there is a back-  
 1257 ground contribution from QCD multijet production. While the cross section for this process is large, its  
 1258 contribution to the  $WW^*$  final state is small because two jets must be misidentified as leptons.

Category	Process	Description
SM $WW$	$WW \rightarrow \ell\nu\ell\nu$	Real leptons and neutrinos
Top quark production	$t\bar{t} \rightarrow WbWb \rightarrow \ell\nu b\bar{\nu}b$	Real leptons, untagged $b$ s
	$tW \rightarrow WbW \rightarrow \ell\nu\ell\nu b$	Real leptons, untagged $b$
	$t\bar{b}, t\bar{q}\bar{b}$	Untagged $b$ , jet misidentified as lepton
Drell-Yan	$Z/\gamma^* \rightarrow ee, \mu\mu$	“Fake” $E_T^{\text{miss}}$
	$Z/\gamma^* \rightarrow \tau\tau \rightarrow \ell\nu\ell\nu\nu$	Real leptons and neutrinos
Other dibosons	$ZZ \rightarrow \ell\ell\nu\nu$	Real leptons and neutrinos
	$W\gamma^*, WZ \rightarrow \ell\nu\ell\ell, ZZ \rightarrow \ell\ell\ell\ell$	Unreconstructed leptons
	$W\gamma, Z\gamma$	$\gamma$ reconstructed as $e$ , unreconstructed lepton
$W$ +jets	$Wj \rightarrow \ell\nu j$	Jet reconstructed as lepton
QCD multijet	$jj$	Jets reconstructed as leptons

Table 3.1: A summary of backgrounds to the  $H \rightarrow WW^* \rightarrow \ell\nu\ell\nu$  signal

### 1259 3.4 SHARED SIGNAL REGION SELECTION REQUIREMENTS

1260 As presented in section 3.2, there are many different combinations of physics objects that can define a  
 1261  $H \rightarrow WW^* \rightarrow \ell\nu\ell\nu$  final state. The multiplicity of jets and the flavor combinations of the leptons

1262 both lead to many potential signal regions. Additionally, signal regions can be optimized separately to  
 1263 be sensitive to the distinct production modes of the Higgs. Gluon fusion, vector boson fusion, and asso-  
 1264 ciated production of a Higgs all lead to unique final state topologies. Figure 3.6 delineates the different  
 1265 signal regions used in the gluon fusion and vector boson fusion  $H \rightarrow WW^*$  analyses. While there are  
 1266 different optimizations possible in each signal region, there are also some commonly shared selections  
 1267 that will be described here.

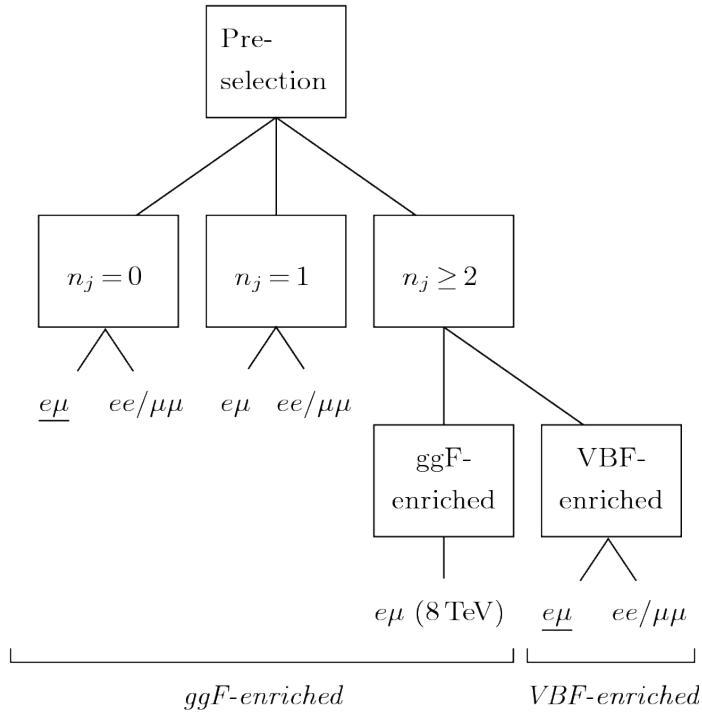


Figure 3.6: An illustration of the unique analysis signal regions [61]. The most sensitive regions for both gluon fusion and vector boson fusion production are underlined.

### 1268 3.4.I EVENT PRE-SELECTION

1269 Before being sorted into the distinct signal regions, basic requirements are applied to the reconstructed  
 1270 objects in the event to select Higgs-like event candidates. First, two oppositely charged leptons are re-  
 1271 quired. Once the leptons are selected, the last requirement for event pre-selection is the presence of  
 1272 neutrinos. As neutrinos cannot be detected directly in ATLAS,  $E_T^{\text{miss}}$  can be used as a proxy for the  
 1273 combined neutrino momentum in the transverse plane.

1274 In general, it is expected that the signal should have a harder  $E_T^{\text{miss}}$  spectrum than backgrounds, espe-  
 1275 cially if these backgrounds do not contain neutrinos in the final state. When using  $E_T^{\text{miss}}$ , it is possible  
 1276 mis-measurements of objects in the detector can lead to imbalances in the transverse plane. When such  
 1277 a mis-measurement occurs, the  $E_T^{\text{miss}}$  vector in the transverse plane will often point in the same direc-  
 1278 tion as the mis-measured object. Therefore, a new variable,  $E_{T,\text{rel}}^{\text{miss}}$ , is used in the pre-selection.  $E_{T,\text{rel}}^{\text{miss}}$  is  
 1279 defined in equation 3.1.

$$E_{T,\text{rel}}^{\text{miss}} = \begin{cases} E_T^{\text{miss}} \sin \Delta\phi_{\text{near}} & \text{if } \Delta\phi_{\text{near}} < \pi/2 \\ E_T^{\text{miss}} & \text{otherwise,} \end{cases} \quad (3.1)$$

1280 If the closest object to the  $E_T^{\text{miss}}$  vector is within  $\pi/2$  radians in the transverse plane, the  $E_T^{\text{miss}}$  is pro-  
 1281 jected away from this object. Otherwise, the normal  $E_T^{\text{miss}}$  vector is used. Figure 3.7 shows a graphical  
 1282 illustration of this concept.

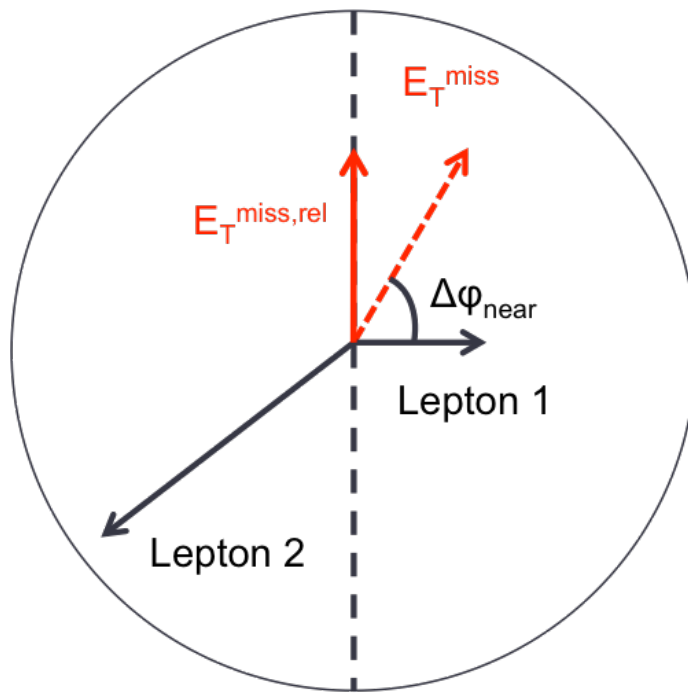


Figure 3.7: A graphical illustration of the  $E_{T,\text{rel}}^{\text{miss}}$  calculation

1283 Once the lepton and  $E_T^{\text{miss}}$  pre-selections are made, the analysis is divided into different regions ac-  
 1284 cording to jet multiplicity.

1285    3.4.2 JET MULTIPLICITY

1286    Jet multiplicity, denoted as  $n_j$ , is used to sub-divide the analysis into distinct signal regions. By creating  
1287    separate signal regions, each bin in jet multiplicity becomes sensitive to different modes of Higgs produc-  
1288    tion and different backgrounds.

1289    For example, the  $n_j \geq 2$  region is more sensitive to VBF production because of the two high momen-  
1290    tum jets produced at matrix element level. For gluon fusion production to enter this bin, two initial state  
1291    radiation jets must be emitted.

1292    Figure 3.8 shows the jet multiplicity in both the different flavor and same flavor regions after the pre-  
1293    selection. It also shows the background composition in the bins of  $n_b$ . A few trends from this distribu-  
1294    tion are worth noting. The first is that the Drell-Yan background dominates in the same flavor chan-  
1295    nels for  $n_j \leq 1$ . Second, the top background becomes a clear contributor to the total background for  
1296     $n_j \geq 1$ . Lastly, the SM WW production dominates in the  $n_j = 0$  bin, as it is an irreducible back-  
1297    ground to  $H \rightarrow WW^*$  production. Because of these distinct features, each jet multiplicity bin is treated  
1298    separately.

1299    3.5 BACKGROUND REDUCTION IN SAME-FLAVOR FINAL STATES

1300    As described in section 3.4.2, the background composition of the same flavor final states is different from  
1301    that of the different flavor states. In particular, Drell Yan processes play a much larger role because the  
1302     $Z/\gamma^*$  decays to same flavor leptons. Because real neutrinos are absent in the  $Z/\gamma^*$  decays to  $ee$  and  $\mu\mu$ ,  
1303    a requirement on  $E_T^{\text{miss}}$  should largely reduce the background. However, as this section will demon-  
1304    strate, with increasing pileup conditions the resolution of the calorimeter-based  $E_T^{\text{miss}}$  degrades greatly.  
1305    Therefore, two new variables for  $Z/\gamma^*$  background reduction are constructed and described in this sec-  
1306    tion.

1307    3.5.1 PILEUP AND  $E_T^{\text{miss}}$  RESOLUTION

1308    Secondary interactions of protons in the colliding bunches of the LHC (known as pileup interactions,  
1309    described in detail in Chapter 2) deposit energy into the ATLAS calorimeter in addition to the energy

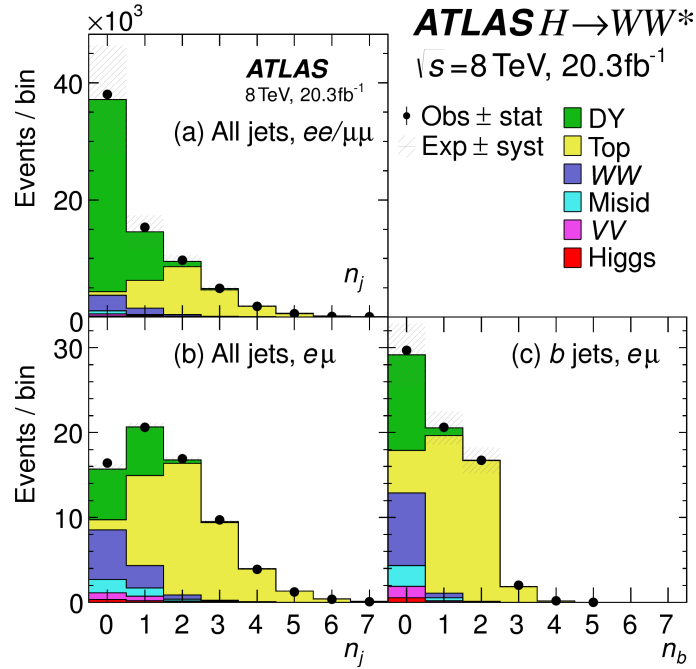


Figure 3.8: Predicted backgrounds (compared with data) as a function of  $n_j$  (a and b) and  $n_b$  (c) after pre-selection requirements

that comes from the hard scatter process of interest. The calculation of  $E_T^{\text{miss}}$  is fundamentally Poissonian. Summing up all of the energy deposits in individual calorimeter cells or clusters is similar to a counting experiment. The error on a mean of  $N$  in a Poisson distribution is  $\sqrt{N}$ , so the energy resolution scales as  $\sqrt{E}$ . As more energy is deposited in the calorimeter, the  $E_T^{\text{miss}}$  resolution degrades, meaning that the  $E_T^{\text{miss}}$  resolution is particularly sensitive to LHC instantaneous luminosity conditions.

Figure 3.9 shows an event display of a  $Z/\gamma^* + \text{jets}$  event candidate with the twenty-five reconstructed primary vertices. This display illustrates that while the interaction of interest only has tracks coming from the hardest primary vertex, all of the secondary interactions deposit energy in the calorimeter as well.

Figure 3.10 shows the RMS of the  $E_T^{\text{miss}}$  distribution in  $Z \rightarrow \mu\mu$  events (where there are no real neutrinos) as a function of the number of the average number of interactions. Under 2011 LHC conditions, this RMS was approximately 9 GeV, while under 2012 running conditions the resolution worsened to 12 GeV. The increase in pileup dilutes the  $E_T^{\text{miss}}$  variable's ability to reduce the  $Z/\gamma^*$  background.

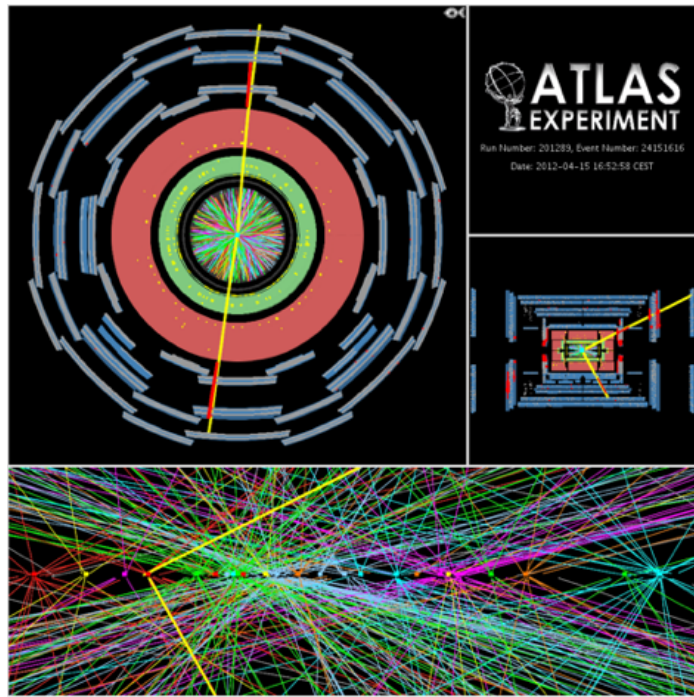


Figure 3.9: An event display of a  $Z/\gamma^* + \text{jets}$  event illustrating the effect of pileup interactions

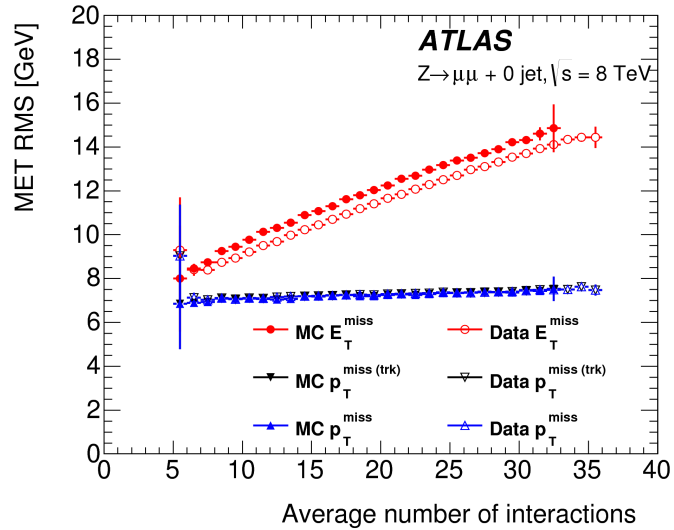


Figure 3.10: The RMS of different missing transverse momentum definitions as a function of the average number of interactions per bunch crossing

### 1323 3.5.2 TRACK-BASED DEFINITIONS OF MISSING TRANSVERSE MOMENTUM

1324 Because the increasing number of secondary proton-proton interactions degrades calorimeter-based  
 1325  $E_T^{\text{miss}}$  resolution, a new variable using only contributions from the primary interaction vertex is nec-

1326    essary to further reduce the  $Z/\gamma^*$  background. While it is not possible to associate calorimeter energy  
 1327    deposits with a particular vertex, individual charged particle tracks in the Inner Detector are associated to  
 1328    unique vertices. Thus, two track-based definitions of missing transverse momentum , using only tracks  
 1329    coming from the primary vertex in the event, are used in the analysis. The simplest variable,  $p_T^{\text{miss}(\text{trk})}$ ,  
 1330    is the vectorial sum of the  $p_T$  of all of the tracks from the primary vertex and the selected leptons (ex-  
 1331    cluding the tracks associated with the selected leptons to avoid double counting). Equation 3.2 defines  
 1332     $p_T^{\text{miss}(\text{trk})}$ .

$$p_T^{\text{miss}(\text{trk})} = - \left( \sum_{\text{selected leptons}} p_T + \sum_{\text{other tracks}} p_T \right), \quad (3.2)$$

1333    To further improve the resolution on the missing transverse momentum, the variable  $p_T^{\text{miss}}$  is used as  
 1334    defined in equation 3.3. For selected leptons and jets, the nominal  $p_T$  measurements are used. Tracks  
 1335    are used to estimate the soft component of the missing transverse momentum instead of calorimeter  
 1336    measurements.

$$p_T^{\text{miss}} = - \left( \sum_{\text{selected leptons}} p_T + \sum_{\text{selected jets}} p_T + \sum_{\text{other tracks}} p_T \right), \quad (3.3)$$

1337    Figure 3.10 illustrates that these two new variables accomplish their intended purpose. The resolution as  
 1338    a function of mean number of interactions for both  $p_T^{\text{miss}(\text{trk})}$  and  $p_T^{\text{miss}}$  is much flatter than the depen-  
 1339    dence for  $E_T^{\text{miss}}$ . Figure 3.11a shows the difference between the true and reconstructed values of missing  
 1340    transverse momentum using both the track-based  $p_T^{\text{miss}}$  and calorimeter based  $E_T^{\text{miss}}$ . The RMS of the  
 1341    distribution improves by 3.5 GeV when using  $p_T^{\text{miss}}$ .

### 1342    3.5.3 Distinguishing $Z/\gamma^*$ +JETS AND $H \rightarrow WW^*$ TOPOLOGIES

1343    In addition to measuring missing transverse momentum, another variable can be constructed to exploit  
 1344    kinematic and topological differences between the  $Z/\gamma^*$  background and  $H \rightarrow WW^*$  signal. Because  
 1345    there are no real neutrinos in the final state (in the case of  $Z/\gamma^* \rightarrow ee, \mu\mu$  decays), the dilepton system  
 1346    will be balanced with the jets produced in the hard scatter. A new variable,  $f_{\text{recoil}}$ , is constructed to es-  
 1347    timate the balance between the dilepton system and recoiling jets and is defined in equation 3.4. The  
 1348    transverse plane is divided into four sections, or quadrants, with one quadrant centered on the dilepton

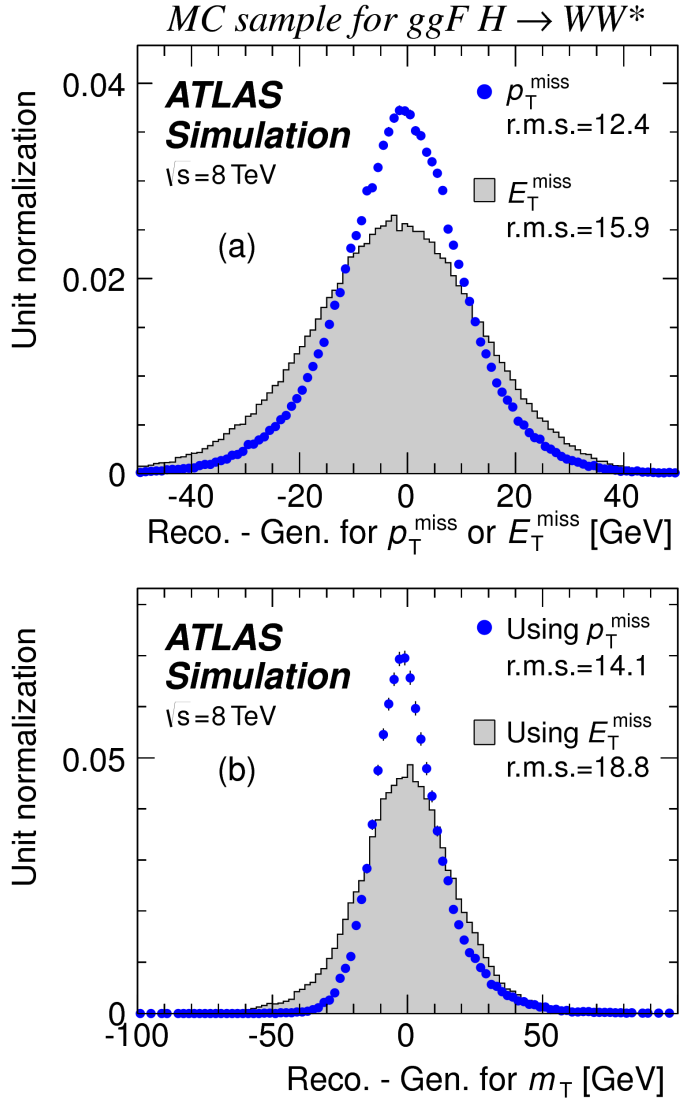


Figure 3.11: The difference between the true and reconstructed values of the missing transverse momentum (a) and  $m_T$  (b) in a gluon fusion signal sample

vector. The numerator of  $f_{\text{recoil}}$  is the magnitude of the vectorial sum of the  $p_T$  of jets in the quadrant opposite the dilepton system, weighted by each jet's Jet Vertex Fraction (JVF, described in chapter 2).  
 The denominator is the magnitude of the dilepton  $p_T$ .

$$f_{\text{recoil}} = \left| \sum_{\text{jets } j \text{ in } \wedge} \text{JVF}_j \cdot \mathbf{p}_T^j \right| / p_T^{\ell\ell}. \quad (3.4)$$

1352 Figure 3.12 shows a shape comparison of the  $f_{\text{recoil}}$  distribution in a simulated  $Z/\gamma^* + \text{jets}$  sample, a  
 1353  $H \rightarrow WW^*$  signal sample, and other backgrounds that contain real neutrinos. The  $Z/\gamma^* + \text{jets}$  events  
 1354 tend to be more balanced between the dilepton system and recoiling jets, while the processes containing  
 1355 real neutrinos are less balanced in the transverse plane. Thus, a requirement on  $f_{\text{recoil}}$  will reduce the  
 1356  $Z/\gamma^* + \text{jets}$  background while maintaining a good signal efficiency.

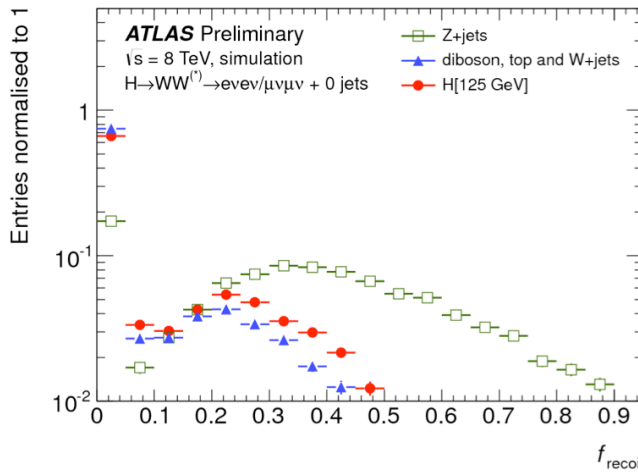


Figure 3.12: Comparison of  $f_{\text{recoil}}$  distributions for  $Z/\gamma^* + \text{jets}$ ,  $H \rightarrow WW^*$ , and other backgrounds with real neutrinos.

### 1357 3.5.4 OPTIMIZING BACKGROUND REDUCTION SELECTION REQUIREMENTS

1358 The requirements on  $p_T^{\text{miss}(\text{trk})}$  and  $f_{\text{recoil}}$  used to reduce the  $Z + \text{jets}$  background must be optimized to  
 1359 maximize expected signal significance in the same flavor channels. Figure 3.13 shows an optimization of  
 1360 the combination of the two requirements in the gluon fusion zero jet bin. Each bin shows the expected  
 1361 signal significance if the  $p_{T,\text{rel}}^{\text{miss}(\text{trk})}$  is required to be greater than the left edge of the bin and the  $f_{\text{recoil}}$  is  
 1362 required to be less than the top edge of the bin. The figure shows that the best signal significance comes  
 1363 from requiring low values of  $f_{\text{recoil}}$  ( $< 0.05$ ) and  $p_{T,\text{rel}}^{\text{miss}(\text{trk})}$  values greater than 45 GeV.

### 1364 3.6 PARAMETERS OF INTEREST AND STATISTICAL TREATMENT

1365 As with any search or measurement, there are particular parameters of the Higgs that the  $H \rightarrow WW^*$   
 1366 analysis is interested in measuring. In this case, the parameters of interest are the mass of the Higgs bo-

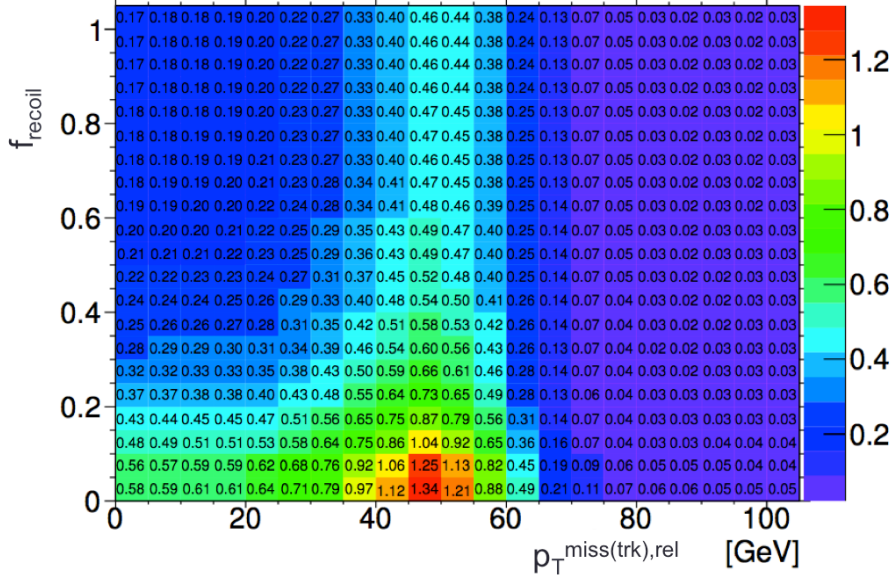


Figure 3.13: Signal significance as a function of required value for  $f_{\text{recoil}}$  and  $p_{T,\text{rel}}^{\text{miss}(\text{trk})}$  in the ggF  $H \rightarrow WW^*$  with  $n_j = 0$

son and its production cross section. Because the  $H \rightarrow WW^* \rightarrow \ell\nu\ell\nu$  process does not have a closed final state, it is not possible to measure the full invariant mass of the particle that may have produced the final state. However, a proxy for the invariant mass is defined using transverse plane information and detailed in section 3.6.1. The second parameter of interest is the ratio of the measured cross section to that expected from the Standard Model Higgs, which is denoted a  $\mu$ . This is defined in equation 3.5.

$$\mu = \frac{\sigma}{\sigma_{\text{SM}}} \quad (3.5)$$

All of the likelihoods used in the statistical analysis of the final signal region events are parameterized as a function of  $\mu$ .  $\mu$  is a natural variable for hypothesis testing, as  $\mu = 0$  corresponds to a background only hypothesis and  $\mu = 1$  corresponds exactly to a Standard Model Higgs.

### 3.6.1 TRANSVERSE MASS

The  $H \rightarrow WW^* \rightarrow \ell\nu\ell\nu$  analysis cannot reconstruct the full invariant mass of the Higgs because of the neutrinos in the final state. The transverse mass serves as a proxy for the full invariant mass by

1378 exploiting information from the transverse plane. The transverse mass is defined in equation 3.6.

$$m_T = \sqrt{(E_T^{\ell\ell} + p_T^{\text{miss}})^2 - |\vec{p}_T^{\ell\ell} + \vec{p}_T^{\text{miss}}|^2}, \quad (3.6)$$

1379 Here the  $E_T^{\ell\ell}$  and  $p_T^{\ell\ell}$  are the transverse energy and momentum of the dilepton system, while  $p_T^{\text{miss}}$  is a  
1380 proxy for the transverse momentum of the di-neutrino system. The track-based  $p_T^{\text{miss}}$  is used in the  $m_T$   
1381 rather than the calorimeter based  $E_T^{\text{miss}}$  because it has a better resolution on the true transverse mass.  
1382 Figure 3.11b shows the improvement in the RMS of the difference between the true and reconstructed  
1383 transverse mass in a ggF signal sample. The RMS improves by 4.7 GeV using  $p_T^{\text{miss}}$  in the  $m_T$  calcula-  
1384 tion.

### 1385 3.6.2 STATISTICAL TREATMENT<sup>†</sup>

#### 1386 LIKELIHOOD FUNCTION

1387 The statistical analysis of final event candidates is framed as a hypothesis test, where the null hypothe-  
1388 sis is background-only (no Standard Model Higgs). The first step in the analysis is to form a likelihood  
1389 function for the data. In its simplest form, this likelihood is the probability of observing the number  
1390 of events seen in the final signal region given knowledge of the signal strength. Because observation of  
1391 events is fundamentally a Poisson counting experiment, this simple likelihood can be expressed as a Pois-  
1392 son probability of observing  $N$  events given a total number of predicted signal and background events.  
1393 This basic likelihood is shown in equation 3.7.

$$\mathcal{L}(\mu) = P(N|\mu S + B) \quad (3.7)$$

1394 Here,  $P$  is the Poisson probability density function,  $N$  is the total number of observed events,  $\mu$  is the  
1395 signal strength,  $S$  is the predicted number of signal events, and  $B$  is the predicted number of back-  
1396 ground events.

1397 In particle physics, certain background estimates are commonly normalized in so-called “control” re-

---

<sup>†</sup>Many thanks to Aaron Armbruster, whose thesis [62] inspired parts of this section.

1398 gions and those predictions are scaled by the same normalization factor in the signal region. This leads  
 1399 to a slightly more complicated likelihood, which is a function of both the signal strength and the back-  
 1400 ground normalization. This is shown in equation 3.8.

$$\mathcal{L}(\mu, \theta) = P(N|\mu S + \theta B) P(N_{\text{CR}}|\theta B_{\text{CR}}) \quad (3.8)$$

1401 Here,  $\theta$  serves as a “nuisance parameter”, or a parameter that is not of primary interest but still enters the  
 1402 likelihood. The second Poisson term enforces that the background normalization be consistent with the  
 1403 number of observed events in data in the control region,  $N_{\text{CR}}$ .

1404 So far, these two formulations of likelihoods have assumed a single signal region and do not take into  
 1405 account any shape information of potential discriminating variables. The  $H \rightarrow WW^*$  analysis is di-  
 1406 vided into many different categories, the counting experiment described above can be performed in each  
 1407 individual category. As mentioned in section 3.6.1, the transverse mass is used as the primary discriminat-  
 1408 ing variable in many of the  $H \rightarrow WW^*$  sub-analyses. The same counting experiment can be performed  
 1409 in each bin of the  $m_T$  distribution to incorporate some shape information. Thus, the total likelihood  
 1410 becomes a product over signal regions and bins of the  $m_T$  distribution. Finally, there are usually many  
 1411 backgrounds that are normalized in control regions. The new formulation of the likelihood takes this  
 1412 into account by including a product over control regions in the second Poisson term. All of these modi-  
 1413 fications are shown in equation 3.9.

$$\mathcal{L}(\mu, \theta) = \prod_{\substack{\text{SRs } i \\ \text{bins } b}} P\left(N_{ib} \middle| \mu S_{ib} + \sum_{\text{bkg k}} \theta_k B_{kib}\right) \prod_{\text{CRs } l} P\left(N_l \middle| \sum_{\text{bkg k}} \theta_k B_{kl}\right) \quad (3.9)$$

1414 The final step to obtain the full likelihood used in the analysis is to add nuisance parameters for the  
 1415 systematic uncertainties. In cases where the uncertainty does not affect the shape of  $m_T$  bin-by-bin, each  
 1416 systematic uncertainty  $\epsilon$  is allowed to affect the expected event yields through a linear response function  
 1417 of the nuisance parameter, namely  $\nu(\theta) = (1 + \epsilon)\theta$ . If instead the uncertainty does affect the shape,  
 1418 the effect is instead parameterized by  $\nu_b(\theta) = 1 + \epsilon_b\theta$ . The value of the nuisance parameters for the  
 1419 systematic uncertainty are constrained with a Gaussian term that is added to the likelihood as well. This

<sup>1420</sup> is of the form  $g(\delta|\theta) = e^{-(\delta-\theta)^2/2}/\sqrt{2\pi}$ , where  $\delta$  is the central value and  $\theta$  is a nuisance parameter.

<sup>1421</sup> Finally, a last term is added to account for the statistical uncertainty in the Monte Carlo samples used,  
<sup>1422</sup> which adds an additional poisson term. The full likelihood used in the final statistical analysis is defined  
<sup>1423</sup> in equation 3.10.

$$\begin{aligned} \mathcal{L}(\mu, \boldsymbol{\theta}) = & \prod_{\substack{\text{SRs i} \\ \text{bins b}}} P \left( N_{ib} \middle| \mu S_{ib} \cdot \prod_{\substack{\text{sig.} \\ r}} \nu_{br}(\theta_r) + \sum_{\text{bkg k}} \theta_k B_{kib} \cdot \prod_{\substack{\text{bkg.} \\ s \\ \text{syst.}}} \nu_{bs}(\theta_s) \right) \\ & \cdot \prod_{\text{CRs l}} P \left( N_l \middle| \sum_{\text{bkg k}} \theta_k B_{kl} \right) \\ & \cdot \prod_{\substack{\text{syst.} \\ t}} g(\delta_t|\theta_t) \cdot \prod_{\text{bkg k}} P(\xi_k|\zeta_k \theta_k) \end{aligned} \quad (3.10)$$

<sup>1424</sup> The fourth term of the equation quantifies the uncertainty due to finite Monte Carlo sample size.

<sup>1425</sup> Here,  $\xi$  represents the central value of the background prediction,  $\theta$  is the associated nuisance parameter,  
<sup>1426</sup>  $\zeta = (B/\delta B)^2$ , where  $\delta B$  is the statistical uncertainty of  $B$ .

<sup>1427</sup> The best fit value of the signal strength  $\mu$  is determined by finding the values of  $\mu$  and  $\boldsymbol{\theta}$  that maximize  
<sup>1428</sup> the likelihood, while setting  $\delta = 0$  and  $\xi = \zeta$ . Once the likelihood is defined, a test statistic must  
<sup>1429</sup> be built for use in hypothesis testing.

## <sup>1430</sup> TEST STATISTIC

<sup>1431</sup> To distinguish whether the data match a background only or background and signal hypothesis, a test  
<sup>1432</sup> statistic must be used. The  $H \rightarrow WW^*$  analysis uses the profile likelihood technique [63]. The first step  
<sup>1433</sup> in formulating this test statistic is to define the profile likelihood ratio, shown in equation 3.11.

$$\lambda(\mu) = \frac{\mathcal{L}(\mu, \hat{\theta}_\mu)}{\mathcal{L}(\hat{\mu}, \hat{\theta})} \quad (3.11)$$

1434 Here  $\hat{\theta}_\mu$  is the value of  $\theta$  that maximizes the likelihood for the choice of  $\mu$  being tested. Additionally,  $\hat{\theta}$   
1435 and  $\hat{\mu}$  represent the values of  $\theta$  and  $\mu$  that gives the overall maximum value of the likelihood.

1436 Once this is defined, a test statistic  $q_\mu$  is constructed. This is shown in equation 3.12.

$$q_\mu = -2 \ln \lambda(\mu) \quad (3.12)$$

1437 A higher value of  $q_\mu$  indicates that the data are more incompatible with the hypothesized value of  $\mu$ , and  
1438  $q_0$  then corresponds to the value of the test statistic for the background only hypothesis. A  $p_0$  value is  
1439 then defined to quantify the compatibility between the data and the null hypothesis. The  $p_0$  value is the  
1440 probability of obtaining a value of  $q_0$  larger than the observed value, and this is shown in equation 3.13.

$$p_0 = \int_{q_0^{\text{obs}}}^{\infty} f(q_\mu | \mu = 0) dq_\mu \quad (3.13)$$

1441 Here  $f(q_\mu)$  is the probability distribution function of the test statistic. Finally, the  $p_0$  value can be con-  
1442 verted into a signal significance, using the formula in equation 3.14, or the one-sided tail of the Gaussian  
1443 distribution.

$$Z_0 = \sqrt{2} \operatorname{erf}^{-1}(1 - 2p_0) \quad (3.14)$$

1444 The threshold for discovery used in particle physics is  $Z_0 \geq 5$ , more commonly known as a value of  $5\sigma$ .

*The real voyage of discovery consists not in seeking new landscapes, but in having new eyes.*

Marcel Proust

# 4

1445

1446

1447

## The discovery of the Higgs boson and the role of the $H \rightarrow WW^* \rightarrow \ell\nu\ell\nu$ channel

1448 4.1 INTRODUCTION

1449 This chapter presents the results of the search for the Higgs boson in  $4.8 \text{ fb}^{-1}$  collected at  $\sqrt{s} = 7 \text{ TeV}$   
1450 and  $5.8 \text{ fb}^{-1}$  at  $\sqrt{s} = 8 \text{ TeV}$ . The results of three searches at  $\sqrt{s} = 8 \text{ TeV}$  in the  $H \rightarrow WW^* \rightarrow \ell\nu\ell\nu$ ,  
1451  $H \rightarrow \gamma\gamma$ , and  $H \rightarrow ZZ \rightarrow 4\ell$  channels are combined with results of searches at  $\sqrt{s} = 7 \text{ TeV}$   
1452 in the same search channels (as well as the  $H \rightarrow \tau\tau$  production and associated production searches for  
1453  $H \rightarrow b\bar{b}$ ). The results of this combination are a  $5.9\sigma$  detection of a new particle consistent with a Higgs  
1454 boson. Rather than going into detail for all of the different Higgs decay searches, this chapter will discuss  
1455 the three most sensitive channels and in particular focus on  $H \rightarrow WW^* \rightarrow \ell\nu\ell\nu$ . While the focus is  
1456 on  $WW^*$ , some of the  $ZZ^*$  and  $\gamma\gamma$  results are shown for completeness. The results not discussed here

1457 can be found in the ATLAS Higgs discovery publication [1].

1458 **4.2 DATA AND SIMULATION SAMPLES**

1459 The data sample used for the following results was taken in 2011 and 2012 at center of mass energies of 7  
1460 and 8 TeV, respectively, with  $4.8 \text{ fb}^{-1}$  collected at 7 TeV and  $5.8 \text{ fb}^{-1}$  collected at 8 TeV. Higgs pro-  
1461 duction in the gluon fusion and vector boson fusion modes is modeled with **POWHEG** for the hard scat-  
1462 tering event and **PYTHIA** for the showing and hadronization. Associated production of a Higgs with a  
1463 vector boson or top quarks is modeled via **PYTHIA**. Table 4.1 shows the Monte Carlo generators used for  
1464 modeling the signal and background processes relevant for the three analyses to be discussed.

Process	Generator
ggF, VBF $H$	<b>POWHEG + PYTHIA</b>
$WH, ZH, t\bar{t}H$	<b>PYTHIA</b>
$W + \text{jets}, Z/\gamma^* + \text{jets}$	<b>ALPGEN + HERWIG</b>
$t\bar{t}, tW, tb$	<b>MC@NLO + HERWIG</b>
$tqb$	<b>ACERMC + PYTHIA</b>
$q\bar{q} \rightarrow WW$	<b>MC@NLO + HERWIG</b>
$gg \rightarrow WW$	<b>GG2WW+ HERWIG</b>
$q\bar{q} \rightarrow ZZ$	<b>POWHEG + PYTHIA</b>
$gg \rightarrow ZZ$	<b>GG2ZZ+ HERWIG</b>
$WZ$	<b>MADGRAPH+ PYTHIA , HERWIG</b>
$W\gamma + \text{jets}$	<b>ALPGEN + HERWIG</b>
$W\gamma^*$	<b>MADGRAPH+ PYTHIA</b>
$q\bar{q}/gg \rightarrow \gamma\gamma$	<b>SHERPA</b>

Table 4.1: Monte carlo generators used to model signal and background for the Higgs search [1].

1465 **4.3  $H \rightarrow WW \rightarrow e\nu\mu\nu$  SEARCH**

1466 The  $H \rightarrow WW \rightarrow e\nu\mu\nu$  search is unique compared to the  $ZZ$  and  $\gamma\gamma$  channels. The Higgs mass can-  
1467 not be fully reconstructed due to the presence of neutrinos in the final state, so the transverse mass  $m_T$   
1468 is used as the final discriminating variable. Compared to the other channels, there are more backgrounds  
1469 here as well, as discussed in chapter 3. The same flavor final states are excluded from this search due to  
1470 high pileup in the 8 TeV dataset.

1471    4.3.I    EVENT SELECTION

1472    The analysis requires two opposite charge isolated leptons, with the leading (sub-leading) lepton required  
 1473    to have  $p_T > 25(15)$  GeV. The events are separated into different signal regions depending on which  
 1474    flavor of lepton is leading ( $e\mu$  for leading electron,  $\mu e$  for leading muon). Strict lepton quality cuts are  
 1475    applied to the sample to reduce backgrounds from fake leptons.

1476    Jets are reconstructed with the anti- $k_T$  algorithm with a radius parameter  $R = 0.4$ . The jets are  
 1477    required to have  $p_T > 25$  GeV and  $|eta| < 4.5$ , with jets in the tracking volume required to have a  
 1478    jet vertex fraction of 0.5 and jets in the forward region required to have  $p_T > 30$  GeV. The analysis is  
 1479    separated into three different signal regions based on jet multiplicity:  $n_j = 0, 1, \geq 2$ .

1480    To indicate the presence of neutrinos in the event, a requirement of  $E_{T,\text{rel}}^{\text{miss}} > 25$  GeV is made\*. This  
 1481    requirement significantly reduces the QCD multijet and  $Z/\gamma^*$  + jets backgrounds. Figure 4.1 shows the  
 1482    distribution of  $n_j$  in data and simulation after applying these “pre-selection” requirements.

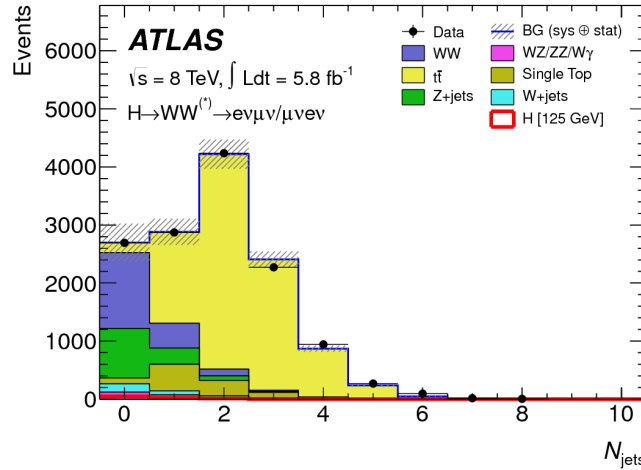


Figure 4.1: Jet multiplicity distribution in data and MC after applying lepton, jet, and  $E_{T,\text{rel}}^{\text{miss}}$  selections. The  $WW$  and top backgrounds have been normalized using control samples, and the hashed band indicates the total uncertainty on the prediction. [1]

1483    Additional selections are applied to require the dilepton topology to correspond to that of a SM  
 1484    Higgs. The requirements are presented here - more detailed discussion on the motivation for each re-  
 1485    quirement is saved for Chapter 5. In all of the jet multiplicity channels, the dilepton system is required to

\*For the definition of  $E_{T,\text{rel}}^{\text{miss}}$ , see chapter 3

1486 have a small gap in azimuthal angle,  $\Delta\phi_{\ell\ell} < 1.8$ . Similarly, the  $m_{\ell\ell}$  is required to be less than 50 GeV  
1487 in the lower jet multiplicity channels and less than 80 GeV in the  $n_j \geq 2$  channel. In the  $n_j = 0$  chan-  
1488 nel, the magnitude of the dilepton  $p_T$ ,  $p_T^{\ell\ell}$ , is required to be greater than 30 GeV.

1489 In the higher jet multiplicity channels ( $n_j \geq 1$ ), the top background is a more important component  
1490 and must be reduced. The total transverse momentum  $p_T^{\text{sum}}$  is thus required to be less than 30 GeV.  
1491 Additionally, the di- $\tau$  invariant mass  $m_{\tau\tau}$  (dilepton mass computed under the assumption that the neu-  
1492 trinos from the  $\tau$  decay are emitted collinear to the charged leptons) is used to reject  $Z \rightarrow \tau\tau$  events by  
1493 requiring  $|m_{\tau\tau} - m_Z| > 25$  GeV. These variables are also discussed in more detail in Chapter 5.

1494 In the  $n_j \geq 2$  channel, requirements are made to isolate the VBF contribution to Higgs production.  
1495 The kinematics of the two leading jets are used to make these requirements. In particular, the event must  
1496 have  $\Delta y_{jj} > 3.8$  and  $m_{jj} > 500$  GeV, along with a veto on having any additional jets with rapidity  
1497 between the two leading jets.

#### 1498 4.3.2 BACKGROUND ESTIMATION

1499 The details of the background estimation techniques used in the  $H \rightarrow WW^* \rightarrow \ell\nu\ell\nu$  analysis are dis-  
1500 cussed in section 5.5. As that section refers to a later iteration of the analysis, a general discussion is given  
1501 here for completeness. The dominant backgrounds are SM  $WW$  production and top (both pair and  
1502 single) production, and these backgrounds have their normalizations estimated from dedicated control  
1503 regions while their shapes are taken from simulation.

1504 The control sample for the Standard Model  $WW$  background is defined by making the same require-  
1505 ments as the signal region with the  $m_{\ell\ell}$  requirement inverted (now requiring  $m_{\ell\ell} > 80$  GeV) and  
1506 removing the  $\Delta\phi_{\ell\ell}$  requirement. This creates a control sample that is 70% (40%) pure in the 0(1)-jet  
1507 region. The correction to the pure MC-based background estimate is quantified by defining a normal-  
1508 ization factor  $\beta$  which is the ratio of the data yield to the MC yield ( $N_{\text{data}}/N_{\text{MC}}$ ) in this control sample.  
1509 Table 4.2 shows the  $WW$  normalization factors in the  $n_j = 0$  and  $n_j = 1$  bins (the  $n_j \geq 2$  estimate is  
1510 taken directly from MC).

1511 The top background estimate is also computed separately in each jet multiplicity bin. In the  $n_j = 0$

$n_j$	$\beta_{WW}$	$\beta_t$
= 0	$1.06 \pm 0.06$	$1.11 \pm 0.06$
= 1	$0.99 \pm 0.15$	$1.11 \pm 0.05$
$\geq 2$	-	$1.01 \pm 0.26$

Table 4.2: Normalization factors (ratio of data and MC yields in a control sample) for the Standard Model  $WW$  and top backgrounds in the  $H \rightarrow WW^* \rightarrow \ell\nu\ell\nu$  analysis [1]. Only statistical uncertainties are shown.

channel, the background is first normalized using data after pre-selection requirements with no selection on  $n_j$ . Then, a dedicated  $b$ -tagged control sample is used to evaluate the ratio of one-jet to two-jet events in data. The details of this technique are shown in reference [64]. In the  $n_j = 1$  and the  $n_j \geq 2$  regions, the top background is normalized in a control sample where the signal region selections are applied, but the  $b$ -jet veto is reversed and the Higgs topology requirements on  $m_{\ell\ell}$  and  $\Delta\phi_{\ell\ell}$  are removed. The resulting normalization factors for these techniques are shown in table 4.2.

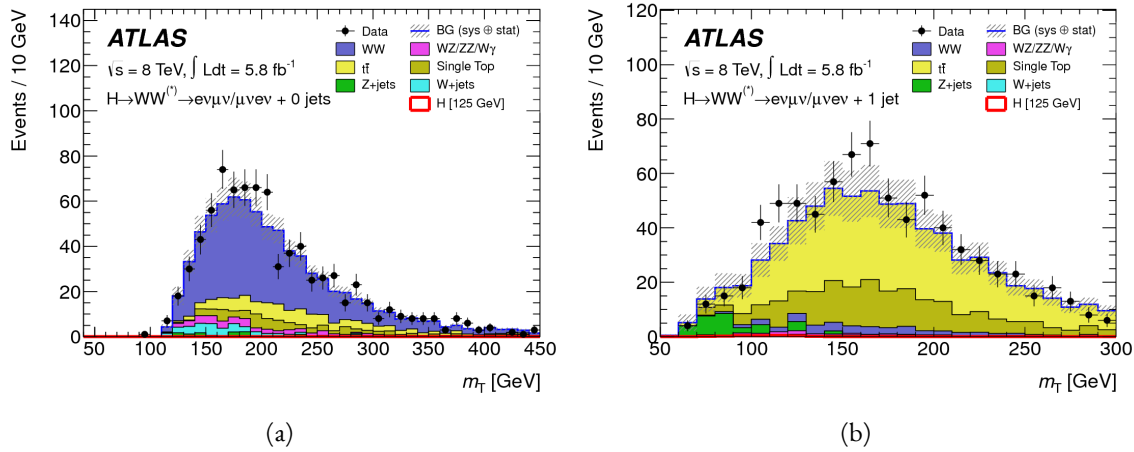


Figure 4.2: Comparison of  $m_T$  between data and simulation in the  $n_j = 0$   $WW$  (a) and  $n_j = 1$  top (b) control samples [1]

The control samples which are used for background normalization can also be used to validate the modeling of the  $m_T$  distribution for each background. Figure 4.2 shows the comparison between data and MC for the  $m_T$  distribution after correcting the normalization of the backgrounds in the  $WW$  and top control regions. Good agreement between data and simulation is seen in both cases.

The  $W+jets$  background estimate is taken entirely from data using a control sample with one well reconstructed lepton and one anti-identified lepton. All other backgrounds are taken purely from simu-

1524 lation.

1525 **4.3.3 SYSTEMATIC UNCERTAINTIES**

1526 The systematic uncertainties that have the largest impact on the analysis are the theoretical uncertainties  
1527 associated with the signal cross section, and these are shared with the  $ZZ^*$  and  $\gamma\gamma$  channels. The un-  
1528 certainties resulting from variations of the QCD scale are  $+7\% / -8\%$  on the final singal yield. Those  
1529 coming from variations of the parton distribution function (PDF) used in the simulation add a  $\pm 8\%$   
1530 uncertainty on the yield. The uncertainties on the branching ratios of the Higgs are  $\pm 5\%$ .

1531 The main experimental uncertainties come from variations of the jet energy scale (JES), jet energy  
1532 resolution, pile-up,  $E_T^{\text{miss}}$ ,  $b$ -tagging efficiency,  $W + \text{jets}$  background estimate, and integrated luminosity.  
1533 For more details, see reference [1].

1534 **4.3.4 RESULTS**

1535 Table 4.3 shows the signal and background yields in the final signal region after normalizing the back-  
1536 grounds according to the methods described above.

	$n_j = 0$	$n_j = 1$	$n_j \geq 2$
Signal	$20 \pm 4$	$5 \pm 2$	$0.34 \pm 0.07$
$WW$	$101 \pm 13$	$12 \pm 5$	$0.10 \pm 0.14$
Other dibosons	$12 \pm 3$	$1.9 \pm 1.1$	$0.10 \pm 0.10$
$t\bar{t}$	$8 \pm 2$	$6 \pm 2$	$0.15 \pm 0.10$
Single top	$3.4 \pm 1.5$	$3.7 \pm 1.6$	-
$Z/\gamma^* + \text{jets}$	$1.9 \pm 1.3$	$0.10 \pm 0.10$	-
$W + \text{jets}$	$15 \pm 7$	$2 \pm 1$	-
Total background	$142 \pm 16$	$26 \pm 6$	$0.35 \pm 0.18$
Observed in data	185	38	0

Table 4.3: Data and expected yields for signal and background in the final  $H \rightarrow WW^* \rightarrow \ell\nu\ell\nu$  signal region.  
Uncertainties shown are both statistical and systematic. [1]

1537 Figure 4.3 shows the  $m_T$  distribution in the  $n_j \leq 1$  channels for 8 TeV data. (No events are observed  
1538 in data in the  $n_j \geq 2$  channels in this dataset). The excess shown here relatively flat as a function of  
1539 hypothesized Higgs mass. The combined 7 and 8 TeV data gives an excess with local significance of  $2.8\sigma$   
1540 with an expected significance of  $2.3\sigma$ , corresponding to a  $\mu$  measurement of  $1.3 \pm 0.5$ .

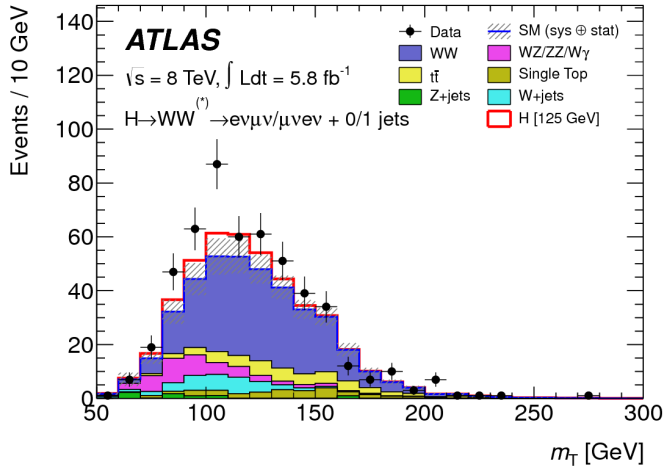


Figure 4.3:  $m_T$  distribution in the  $H \rightarrow WW \rightarrow e\nu\mu\nu n_j \leq 1$  channels for 8 TeV data [1].

#### 1541 4.4 $H \rightarrow \gamma\gamma$ SEARCH

1542 The  $H \rightarrow \gamma\gamma$  search is in essence a search for a peaked excess above the falling SM diphoton mass spec-  
 1543 trum, with  $m_{\gamma\gamma}$  as the ultimate discriminating variable. Events are selected by requiring two isolated  
 1544 photons, with the leading (sub-leading) photon required to have  $E_T > 40(30)$  GeV. In the 8 TeV  
 1545 data, the photons are required to pass cut-based identification criteria consistent with a photon in the  
 1546 electromagnetic calorimeter and little leakage in the hadronic calorimeter.

1547 The main challenges for this analysis are accurate mass reconstruction and background estimation.  
 1548 In order to accurately reconstruct the invariant mass of the di-photon system, both the energy and di-  
 1549 rection of the photons must be measured well. Therefore, the identification of the primary vertex of the  
 1550 hard interaction is particularly important, and is done using a multivariate likelihood which combines  
 1551 information about the photon direction and vertex position. The background is modeled with a falling  
 1552 spectrum in  $m_{\gamma\gamma}$  that is parameterized by different functions depending on the category of the event.

##### 1553 4.4.1 RESULTS

1554 The resulting diphoton mass spectrum is shown in figure 4.4. The best fit mass value in the  $\gamma\gamma$  channel  
 1555 alone in the combined 7 and 8 TeV data is 126.5 GeV. The local significance at this point is  $4.5\sigma$ , with  
 1556 an expected significance of  $2.5\sigma$ . Therefore, the measured signal strength  $\mu$  is  $1.8 \pm 0.5$  in this channel.

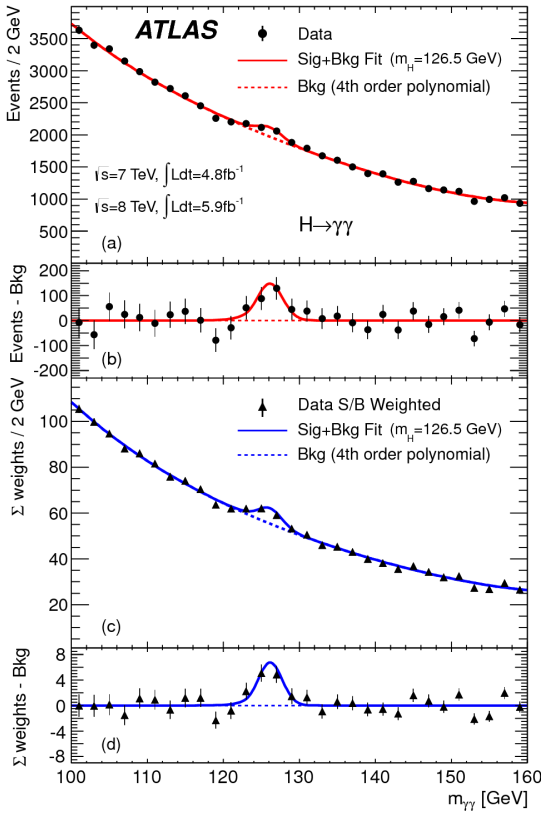


Figure 4.4: Diphoton mass spectrum in 7 and 8 TeV data. Panel a) shows the unweighted data distribution superimposed on the background fit, while panel c) shows the data where each event category is weighted by its signal to background ratio. Panels b) and d) show the respective distributions with background subtracted [1].

#### 1557 4.5 $H \rightarrow ZZ \rightarrow 4\ell$ SEARCH

1558 The  $H \rightarrow ZZ \rightarrow 4\ell$  analysis searches for a Standard Model Higgs boson decaying to two  $Z$  bosons,  
 1559 each of which decays to a pair of same flavor, opposite charge isolated leptons. The ultimate discriminat-  
 1560 ing variable is  $m_{4\ell}$ , or the invariant mass of the four selected leptons. The  $\ell$  denotes an  $e$  or  $\mu$  as with the  
 1561  $H \rightarrow WW^* \rightarrow \ell\nu\ell\nu$  analysis.

1562 Four distinct signal regions are constructed depending on the flavors of the final state, additionally  
 1563 separated by the flavor of the leading lepton pair. These are referred to as  $4e$ ,  $2e2\mu$ ,  $2\mu2e$ ,  $4\mu$ .

1564 The main backgrounds in the  $H \rightarrow ZZ \rightarrow 4\ell$  search are continuum  $ZZ^*$  production,  $Z +$  jets pro-  
 1565 duction, and  $t\bar{t}$ . The  $m_{4\ell}$  distribution for background is estimated from simulation. The normalization  
 1566 of the SM  $ZZ^*$  background is also taken from MC simulation, while the  $Z +$  jets and  $t\bar{t}$  normalizations

1567 are taken from data-driven methods.

1568 **4.5.1 RESULTS**

1569 Figure 4.5 shows the  $m_{4\ell}$  spectrum measured in the 7 and 8 TeV datasets. The total number of events  
1570 observed in the window between 120 and 130 GeV is 13, with 6 events in the  $4\mu$  channel, 2 events in  
1571 the  $4e$  channel, and 5 events in the  $2e2\mu/2\mu2e$ . The best fit  $\mu$  value in the combined 7 and 8 TeV data  
1572 occurs at 125 GeV and is measured to be  $1.2 \pm 0.6$ . The observed significance at this mass is  $3.6\sigma$ , with  
1573 an expected significance of  $2.7\sigma$ .

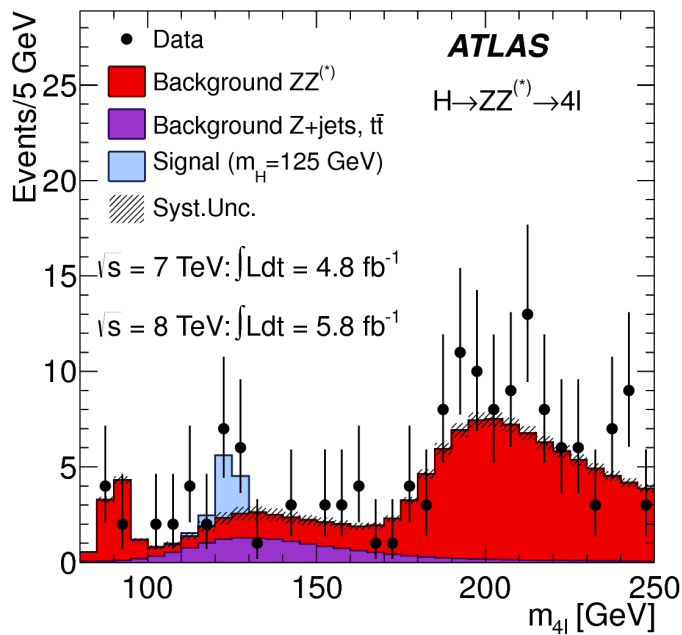


Figure 4.5: Four lepton invariant mass spectrum ( $m_{4\ell}$ ) in 7 and 8 TeV data compared to background estimate. A 125 GeV SM Higgs signal is shown in blue [1].

1574 **4.6 COMBINED RESULTS**

1575 The statistical interpretation of the combined results is undertaken as described in section 3.6.2, with a  
1576 hypothesis test based on a likelihood ratio parameterized by the Higgs signal strength  $\mu$ . The null hy-  
1577 pothesis corresponds to  $\mu = 0$ , while the SM Higgs corresponds to  $\mu = 1$ .

1578      Table 4.4 summarizes the properties of the individual channels as well as the significances of the ex-  
 1579      cesses seen. The most significant observed local excess comes from the  $\gamma\gamma$  channel. Figure 4.6 shows a  
 1580      comparison of the observed local  $p_0$  values as a function of hypothesized mass for the three different  
 1581      search channels. Both the  $ZZ^*$  and  $\gamma\gamma$  channels have very peaked excesses, while the  $WW^*$  excess can  
 1582      be seen as very broad because the  $m_T$  distribution does not provide detailed information about the true  
 1583      Higgs mass.

Channel	Fit var.	Observed $Z_l$	Expected $Z_l$	$\hat{\mu}$
$H \rightarrow ZZ^* \rightarrow 4\ell$	$m_{4\ell}$	3.6	2.7	$1.2 \pm 0.6$
$H \rightarrow \gamma\gamma$	$m_{\gamma\gamma}$	4.5	2.5	$1.8 \pm 0.5$
$H \rightarrow WW^* \rightarrow e\nu\mu\nu$	$m_T$	2.8	2.3	$1.3 \pm 0.5$
Combined	-	6.0	4.9	$1.4 \pm 0.3$

Table 4.4: Summary of the expected and observed significance and measured signal strengths in the combined 7 and 8 TeV datasets for the Higgs discovery analysis [1].

1584      Figure 4.7 shows the combined exclusion limit,  $p_0$ , and signal strength. The highest local excess comes  
 1585      at a value of 126.5 GeV and corresponds to a  $6.0\sigma$  observed excess.

1586      Figure 4.8 shows a comparison of the measured signal strengths between the different Higgs search  
 1587      channels. All measured  $\mu$  are consistent with unity within their uncertainty, and the combined  $\mu$  mea-  
 1588      surement is  $1.4 \pm 0.3$ .

1589      The likelihood can also be computed in a two-dimensional plane of  $m_H$  and  $\mu$ , and this is shown in  
 1590      figure 4.9. The figure shows that while the  $\gamma\gamma$  and  $ZZ^*$  channels have very good mass resolution, the  
 1591      excess in  $WW^*$  covers a broad mass range. The banana shape of the  $WW^*$  result is due to the fact that  
 1592      the excess in this channel can either be explained by increasing the signal strength or by changing the  
 1593      mass (and thus the cross section). The two parameters are correlated due to the lack of mass sensitivity in  
 1594      this channel.

1595      Because multiple Higgs mass points are searched for, the local significance must be corrected for a  
 1596      look-elsewhere effect to compute a true global significance. The global significance for finding a Higgs  
 1597      anywhere in the mass range of 110 GeV to 600 GeV is  $5.1\sigma$ . This increases slightly to  $5.3\sigma$  if only mass  
 1598      range from 110 to 150 GeV.

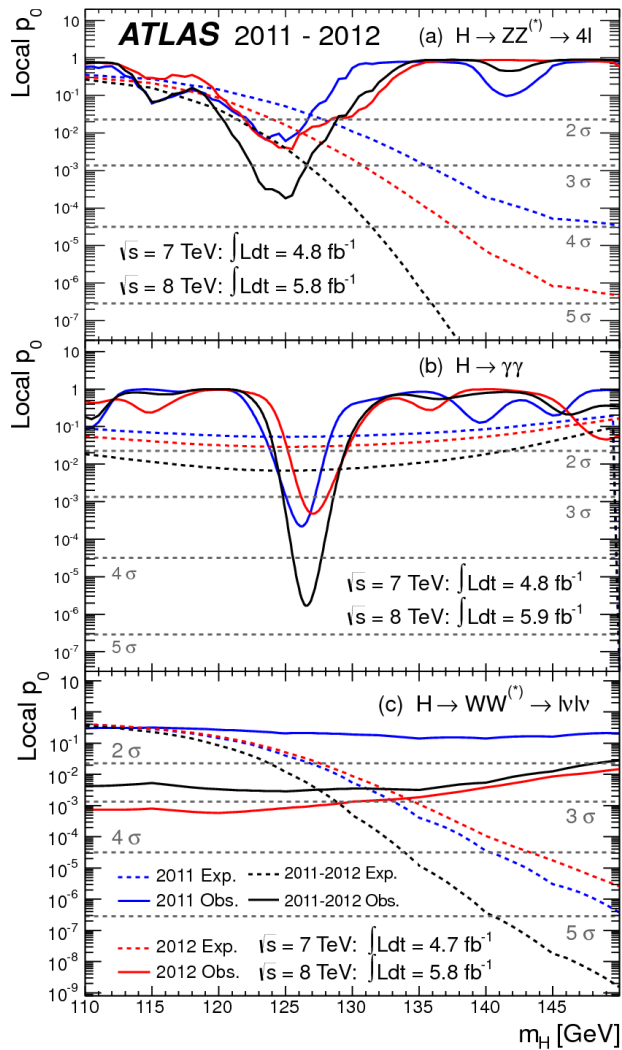


Figure 4.6: Local  $p_0$  distribution as a function of hypothesized Higgs mass for the  $H \rightarrow ZZ^* \rightarrow 4\ell$  (a),  $H \rightarrow \gamma\gamma$  (b), and  $H \rightarrow WW^* \rightarrow \ell\nu\ell\nu$  (c) channels. Dashed curves show expected results, while solid curves show observed. Red curves are from 7 TeV data, blue curves from 8 TeV, and black curved combined [1].

1599    4.7 CONCLUSION

1600    A search for the production of a Standard Model Higgs boson was conducted in  $4.8 \text{ fb}^{-1}$  collected at  
 1601     $\sqrt{s} = 7 \text{ TeV}$  and  $5.8 \text{ fb}^{-1}$  at  $\sqrt{s} = 8 \text{ TeV}$ . A new particle consistent with the Higgs boson was  
 1602    observed, with a mass of  $126.5 \text{ GeV}$  and a global (local) significance of  $5.1(6.0)\sigma$ . This is the first dis-  
 1603    covery level observation of a particle consistent with the Higgs.

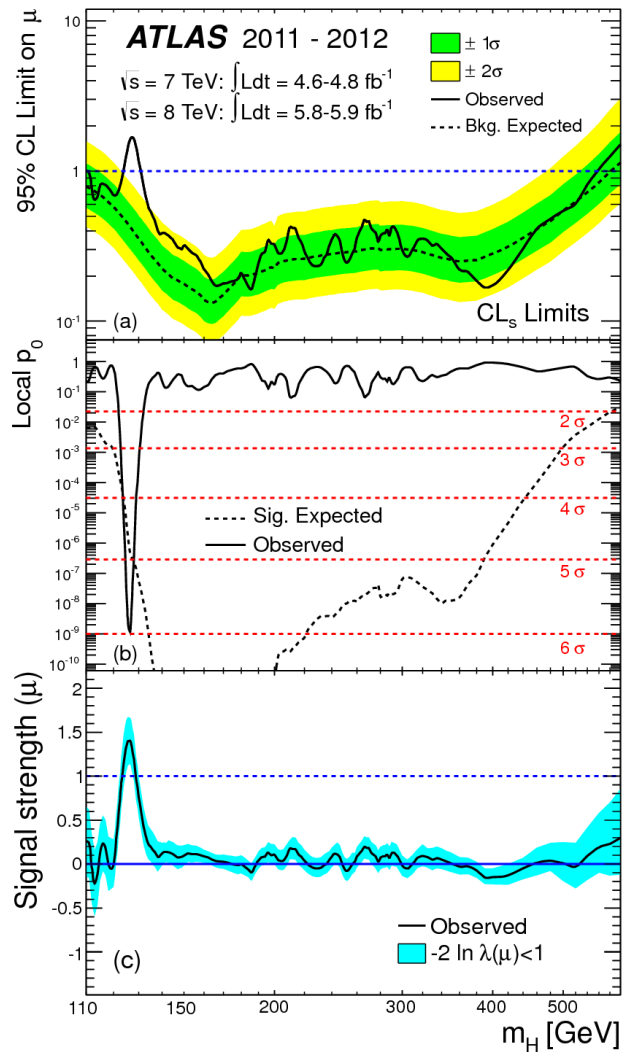


Figure 4.7: Combined 95% CL limits (a), local  $p_0$  values (b), and signal strength measurement (c) as a function of Higgs mass [1].

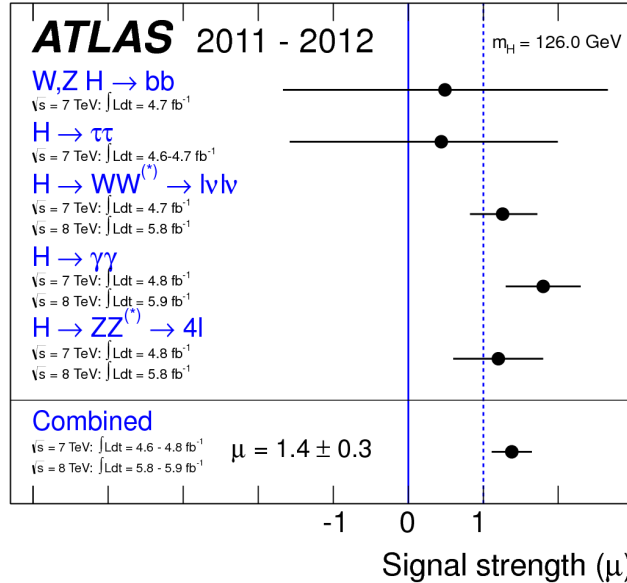


Figure 4.8: Comparison of measured signal strength  $\mu$  for a 126 GeV Higgs in the 7 and 8 TeV datasets [1].

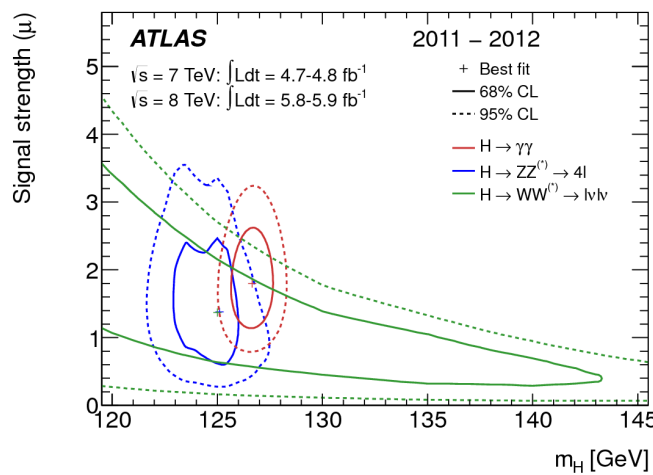


Figure 4.9: Two dimensional likelihood as a function of signal strength  $\mu$  and Higgs mass  $m_H$  [1].

*The imagination of nature is far, far greater than the  
imagination of man.*

Richard Feynman

# 5

1604

1605

## Observation of Vector Boson Fusion

1606

production of  $H \rightarrow WW^* \rightarrow \ell\nu\ell\nu$

1607

### 5.1 INTRODUCTION

1608 After the discovery of a particle consistent with the Higgs boson, the  $H \rightarrow WW^*$  analysis had two main  
1609 goals. The first goal was to increase the sensitivity of the analysis to fully confirm that the  $H \rightarrow WW^*$   
1610 process did indeed exist. The second goal was to characterize the particle as much as possible, including  
1611 searching for the lower cross-section production modes, in order to confirm that it was indeed a Higgs  
1612 boson. This chapter presents a dedicated search for Vector Boson Fusion (VBF) production of a Higgs  
1613 boson decaying via the  $H \rightarrow WW^* \rightarrow \ell\nu\ell\nu$  mode. First, basics of the topology of VBF production  
1614 are presented. Then, the details of the analysis are shown, including signal region definition, background  
1615 estimation techniques, and systematic uncertainties. Finally, the results of the analysis are presented. As

1616 will be shown, this analysis is the first and most sensitive observation of the VBF production mode of the  
1617 Higgs on ATLAS.

1618 In the VBF channel, there are both a selection requirement based signal region analysis (known as the  
1619 “cut-based”) and a multivariate analysis which uses a boosted decision tree (known as the BDT analysis).  
1620 The focus of this chapter will be on the cut-based signal region, as this is an important component of the  
1621 VBF analysis and in particular acts as strong validation for the final BDT result. Connections between  
1622 the cut-based and BDT analyses will be discussed where appropriate.

## 1623 5.2 DATA AND SIMULATION SAMPLES

1624 The results presented here are with  $20.3 \text{ fb}^{-1}$  taken at  $\sqrt{s} = 8 \text{ TeV}$  and  $4.5 \text{ fb}^{-1}$  taken at  $\sqrt{s} = 7 \text{ TeV}$ .  
1625 The details of the LHC and detector conditions during this period are given in Chapter 2. The trigger  
1626 selection defining the dataset is discussed in section 5.2.1. The simulation samples used for signal and  
1627 background modeling are given in section 5.2.2.

### 1628 5.2.1 TRIGGERS

1629 The analysis uses a combination of single lepton and dilepton triggers to allow lowering of the  $p_T$  thresh-  
1630 olds and increased signal acceptance. The  $p_T$  threshold on the leptons is a particularly important consid-  
1631 eration for this signal. Because the second  $W$  produced in the decay can be off-shell, it tends to pro-  
1632 duce lower momentum leptons. Thus, being able to lower the  $p_T$  threshold while still maintaining  
1633 a low background rate is critical. Figure 5.1 shows an example of the subleading lepton  $p_T$  for a VBF  
1634  $H \rightarrow WW^*$  signal compared to the corresponding  $t\bar{t}$  background. Note that the lepton  $p_T$  spectrum is  
1635 considerably softer in the signal sample.

1636 As discussed in Chapter 2, there are multiple levels in the ATLAS trigger system, and there are differ-  
1637 ent  $p_T$  thresholds imposed for the leptons at each level. Additionally, some triggers have a loose selection  
1638 on the isolation of the lepton (looser than that applied offline in the analysis object selection). Table 5.1  
1639 shows the thresholds used for single lepton triggers, while table 5.2 shows the thresholds coming from  
1640 di-lepton triggers. The single lepton trigger efficiency for muons that pass the analysis object selection is



Figure 5.1: A comparison of the subleading lepton  $p_T$  spectrum between VBF  $H \rightarrow WW^*$  production and  $t\bar{t}$  background

1641 70% for muons in the barrel region ( $|\eta| < 1.05$ ) and 90% in the endcap region. The electron trigger ef-  
1642 ficiency increases with electron  $p_T$  but the average is approximately 90%. These efficiencies are measured  
1643 by combined performance and trigger signature groups [65, 66].

	Level-1 threshold	High-level threshold
Electron	18	$24i$
	30	60
Muon	15	$24i$
		36

Table 5.1: Single lepton triggers used for electrons and muons. A logical “or” of the triggers listed for each lepton type is taken. Units are in GeV, and the  $i$  denotes an isolation requirement in the trigger.

	Level-1 threshold	High-level threshold
$ee$	10 and 10	12 and 12
$\mu\mu$	15	18 and 8
$e\mu$	10 and 6	12 and 8

Table 5.2: Di-lepton triggers used for different flavor combinations. The two thresholds listed refer to leading and sub-leading leptons, respectively. The di-muon trigger only requires a single lepton at level-1.

1644 The combination of all triggers shown gives good efficiency for signal events. This efficiency is sum-  
1645 marized in table 5.3. The relative improvement in efficiency by adding the dilepton triggers is also shown

1646 in the same table. The largest gain comes in the  $\mu\mu$  channel. Overall the trigger selection shows a good  
1647 efficiency for  $H \rightarrow WW^*$  signal events.

Channel	Trigger efficiency	Gain from $2\ell$ trigger
$ee$	97%	9.1%
$\mu\mu$	89%	18.5%
$e\mu$	95%	8.3%
$\mu e$	81%	8.2%

Table 5.3: Trigger efficiency for signal events and relative gain of adding a dilepton trigger on top of the single lepton trigger selection. The first lepton is the leading, while the second is the sub-leading. Efficiencies shown here are for the ggF signal in the  $n_j = 0$  category but are comparable for the VBF signal.

1648 **5.2.2 MONTE CARLO SAMPLES**

1649 Modeling of signal and background processes in the signal region, in particular for the  $m_T$  distribution,  
1650 is an important consideration for the final interpretation of the analysis. Therefore, careful consideration  
1651 must be paid to which Monte Carlo (MC) generators are used for specific processes. With the exception  
1652 of the  $W + \text{jet}$  and multijet backgrounds, the  $m_T$  shape used as the final discriminant is taken from simu-  
1653 lation. (Many backgrounds are normalized from data, as described in section 5.5).

1654 Table 5.4 shows the MC generators used for the signal and background processes, as well as their cross  
1655 sections. In order to include corrections up to next-to-leading order (NLO) in the QCD coupling con-  
1656 stant  $\alpha_s$ , the POWHEG [67] generator is often used. In some cases, only leading order generators like  
1657 ACERMC [68] and GG2VV [69] are available for the process in question. If the process requires good  
1658 modeling for very high parton multiplicities, the SHERPA [70] and ALPGEN [71] generators are used  
1659 to provide merged calculations for five or fewer additional partons. These matrix element level calcula-  
1660 tions must then be additionally matched to models of the underlying event, hadronization, and parton  
1661 shower. There are four possible generators for this: SHERPA, PYTHIA 6 [72], PYTHIA 8 [73], or HERWIG  
1662 [74] + JIMMY [75]. The simulation additionally requires an input parton distribution function (PDF).  
1663 The CT10 [76] PDFs are used for SHERPA and POWHEG simulated samples, while CTEQ6L1 [77] is used  
1664 for ALPGEN + HERWIG and ACERMC simulations. The Drell-Yan samples are reweighted to the MRST  
1665 [78] PDFs, as these are found to give the best agreement between data and simulation.

Process	MC generator	$\sigma \cdot \mathcal{B}$ (pb)
Signal		
ggF $H \rightarrow WW^*$	POWHEG +PYTHIA 8	0.435
VBF $H \rightarrow WW^*$	POWHEG +PYTHIA 8	0.0356
VH $H \rightarrow WW^*$	PYTHIA 8	0.0253
$WW$		
$q\bar{q} \rightarrow WW$ and $qg \rightarrow WW$	POWHEG +PYTHIA 6	5.68
$gg \rightarrow WW$	GG2VV +HERWIG	0.196
$(q\bar{q} \rightarrow W) + (q\bar{q} \rightarrow W)$	PYTHIA 8	0.480
$q\bar{q} \rightarrow WW$	SHERPA	5.68
VBS $WW + 2$ jets	SHERPA	0.0397
Top quarks		
$t\bar{t}$	POWHEG +PYTHIA 6	26.6
$Wt$	POWHEG +PYTHIA 6	2.35
$t\bar{q}\bar{b}$	ACERMC +PYTHIA 6	28.4
$t\bar{b}$	POWHEG +PYTHIA 6	1.82
Other dibosons ( $VV$ )		
$W\gamma$ ( $p_T^\gamma > 8$ GeV)	ALPGEN +HERWIG	369
$W\gamma^*$ ( $m_{\ell\ell} \leq 7$ GeV)	SHERPA	12.2
$WZ$ ( $m_{\ell\ell} > 7$ GeV)	POWHEG +PYTHIA 8	12.7
VBS $WZ + 2$ jets	SHERPA	0.0126
( $m_{\ell\ell} > 7$ GeV)		
$Z\gamma$ ( $p_T^\gamma > 8$ GeV)	SHERPA	163
$Z\gamma^*$ (min. $m_{\ell\ell} \leq 4$ GeV)	SHERPA	7.31
$ZZ$ ( $m_{\ell\ell} > 4$ GeV)	POWHEG +PYTHIA 8	0.733
$ZZ \rightarrow \ell\ell\nu\nu$ ( $m_{\ell\ell} > 4$ GeV)	POWHEG +PYTHIA 8	0.504
Drell-Yan		
$Z$ ( $m_{\ell\ell} > 10$ GeV)	ALPGEN +HERWIG	16500
VBF $Z + 2$ jets	SHERPA	5.36
( $m_{\ell\ell} > 7$ GeV)		

Table 5.4: Monte Carlo samples used to model the signal and background processes [61].

Once the basic hard scattering process is simulated, it must be passed through a detector simulation and additional pile-up events must be overlaid. The pile-up events are modeled with PYTHIA 8, and the ATLAS detector is simulated with GEANT4 [79]. Because of the unique phase space of the  $H \rightarrow WW^*$

1669 analysis, events are sometimes filtered at generator level to allow for more efficient generation of relevant  
1670 events. The efficiency of the trigger in MC simulation does not always match the measured efficiency in  
1671 data, so trigger scale factors are applied to correct the MC efficiency to the data. These are derived by the  
1672 combined performance groups [65, 66].

### 1673 5.3 OBJECT SELECTION

1674 In order to define the signal region, the analysis must first select the objects to be considered. The de-  
1675 tails of the object reconstruction algorithms are discussed in Chapter 2, while this section gives specific  
1676 selection cuts used in the  $H \rightarrow WW^*$  analysis.

1677 The first step in this process is to select a primary vertex candidates. The event's primary vertex is the  
1678 vertex with the largest sum of  $p_T^2$  for associated tracks and is required to have at least three tracks with  
1679  $p_T > 450$  MeV. Many of the object selection cuts are then made relative to this chosen primary vertex.

#### 1680 5.3.1 MUONS

1681 The analysis uses combined muon candidates, where a track in the Inner Detector has been matched  
1682 to a standalone track in the Muon Spectrometer. The track parameters are combined statistically in the  
1683 muon reconstruction algorithm [52]. The muons are required to be within  $|\eta| < 2.5$  and have a  $p_T >$   
1684 10 GeV. To reduce backgrounds coming from mis-reconstructed leptons, there are requirements on  
1685 the impact parameter of the muon relative to the primary vertex. The transverse impact parameter  $d_0$   
1686 is required to be small relative to its estimated uncertainty, the exact cut value being  $d_0/\sigma_{d_0} < 3$ . The  
1687 longitudinal impact parameter  $z_0$  must satisfy  $|z_0 \sin \theta| < 1$  mm.

1688 As discussed previously, the muons must also be isolated. There are two types of lepton isolations  
1689 that are calculated: track-based and calorimeter-based. For muons, the track-based isolation is defined  
1690 using the scalar sum  $\sum p_T$  for tracks with  $p_T > 1$  GeV (excluding the muon's track) within a cone of  
1691  $\Delta R = 0.3$  ( $0.4$ ) for muon with  $p_T > 15$  GeV ( $10 < p_T < 15$  GeV). The final isolation requirement  
1692 is made my requiring that this scalar sum be no more than a certain fraction of the muon's  $p_T$ . This re-  
1693 quirement varies with muon  $p_T$  and the exact cuts are defined in table 5.5.

1694      The calorimeter-based muon isolation is defined using as a  $\sum E_T$  calculated from calorimeter cells  
 1695      using the same cone size as the track-based isolation but excluding cells with  $\Delta R < 0.05$  around the  
 1696      muon. This requirement is also defined as a cut on the ratio of the sum to the muon  $p_T$  and varies with  
 1697      muon  $p_T$ . The cut values are also given in table 5.5.

1698      The isolation requirements loosen as a function of  $p_T$  to allow for larger signal acceptance. At low  $p_T$ ,  
 1699      the isolation is tightened to reduce the  $W + \text{jets}$  background which arises from a misidentified lepton.

$p_T$ range (GeV)	Calorimeter isolation	Track isolation
10 – 15	0.06	0.06
15 – 20	0.12	0.08
20 – 25	0.18	0.12
> 25	0.30	0.12

Table 5.5:  $p_T$  dependent isolation requirements for muons. Muons are required to have the amount of calorimeter or track based cone sums be less than this fraction of their  $p_T$ .

### 1700 5.3.2 ELECTRONS

1701    Electrons are identified by matching reconstructed clusters in the electromagnetic calorimeter with tracks  
 1702    in the inner detector. The electrons are identified using a likelihood based method [49, 50] which takes  
 1703    into account the shower shapes in the calorimeter, the matching of tracks to clusters, and the amount of  
 1704    transition radiation in the TRT. The electrons are required to have  $|\eta| < 2.47$ , and candidates in the  
 1705    transition region between the barrel and endcap ( $1.37 < |\eta| < 1.52$ ) are excluded. As the muons, the  
 1706    electrons are required to have transverse impact parameter significance  $< 3$ , while in the longitudinal  
 1707    direction they must have  $|z_0 \sin \theta| < 0.4$  mm. Some electron requirements also vary with electron  $E_T$ ,  
 1708    and these requirements are summarized in table 5.6.

1709    The isolation for electrons are defined similarly to the muons but with unique cuts on the objects in-  
 1710    cluded. The track-based isolation is defined using tracks with  $p_T > 400$  MeV with cone sizes as defined  
 1711    previously. The calorimeter-based isolation also uses the same cone size as the muon, but here the cells  
 1712    within a  $0.125 \times 0.175$  area in  $\eta \times \phi$  around the electron cluster's barycenter are excluded. The other  
 1713    difference with respect to muons is that the denominator of the isolation ratio is the electron's  $E_T$  rather  
 1714    than  $p_T$ . The isolation cuts very with electron  $E_T$  and are defined in table 5.6.

1715 The electron is also required to not be consistent with a vertex coming from a photon conversion.

$p_T$ range (GeV)	Quality cut	Calorimeter isolation	Track isolation
10 – 15	Very tight LH	0.20	0.06
15 – 20	Very tight LH	0.24	0.08
20 – 25	Very tight LH	0.28	0.10
> 25	Medium	0.28	0.10

Table 5.6:  $p_T$  dependent requirements for electrons. Electrons are required to have the amount of calorimeter or track based cone sums be less than this fraction of their  $E_T$ .

### 1716 5.3.3 JETS

1717 Jets are clustered with the anti- $k_T$  reconstruction algorithm using a radius parameter of  $R = 0.4$ . They  
1718 are required to have a jet vertex fraction (JVF) of at least 50%, meaning that half of the tracks associated  
1719 with the jet originated from the primary vertex. Jets with no tracks associated (i.e. those outside the ac-  
1720 ceptance of the ID) do not have this requirement applied. Jets are required to have  $p_T > 25$  GeV if  
1721 they are within the tracking acceptance ( $|\eta| < 2.4$ ). Jets with  $2.4 < |\eta| < 4.5$  are required to have  
1722  $p_T > 30$  GeV. This tighter requirement reduces jets from pileup in the region where JVF requirements  
1723 cannot be applied. The two highest  $p_T$  jets in the event are referred to as the “VBF” jets and used to com-  
1724 pute various analysis selections later.

1725 Identification of  $b$ -jets is done using the MV1 algorithm and is limited to the acceptance of the ID  
1726 ( $|\eta| < 2.5$ ). The operating point of MV1 that is used is the one that is 85% efficient for identifying true  
1727  $b$ -jets. This operating point has a 10.3% of mis-tagging a light quark jet as a  $b$ -jet. In order to improve  
1728 the rejection of  $b$ -jets, a lower threshold than the nominal  $p_T$  threshold described above is used. For the  
1729 purposes of counting the number of  $b$ -jets, jets with  $p_T$  down to 20 GeV are used.

### 1730 5.3.4 OVERLAP REMOVAL

1731 There are some cases where certain reconstructed objects will overlap and one will have to be chosen  
1732 (for example, an electron and a jet in the calorimeter). First, the case of lepton overlap is dealt with. If  
1733 an electron candidate extends into the muon spectrometer, it is removed. If a muon or electron have a  
1734  $\Delta R < 0.1$ , the electron is removed and the muon is kept. If two electron candidates overlap within

1735 the same radius, then the higher  $E_T$  electron is kept. Next, the overlap between leptons and jets is con-  
1736 sidered. If an electron and jet are within  $\Delta R < 0.3$  of one another, the electron is kept and the jet is  
1737 removed. However, if a muon and jet overlap within  $\Delta R < 0.3$ , the jet is kept (as it is likely that the  
1738 muon is the result of a semileptonic decay inside the jet).

1739 Once the overlap removal is complete, the final set of objects used in the analysis is defined.

#### 1740 5.4 ANALYSIS SELECTION

1741 The VBF analysis uses two distinct selections. The first is a more standard selection, referred to as “cut-  
1742 based”, that applies requirements on the VBF variables and uses  $m_T$  as the final discriminating variable.  
1743 The second is a looser selection that uses a Boosted Decision Tree (BDT) score as the final discriminator  
1744 in order to take advantage of the detailed correlations between the VBF variables. While the BDT analy-  
1745 sis is ultimately more sensitive, the cut-based serves as an important component of the analysis. First, the  
1746 cut-based allows for confirming the modeling and validity of many variables used as input to the BDT.  
1747 Second, because this is the first use of such an MVA technique in the  $H \rightarrow WW^*$  analysis, the cut-based  
1748 selection allows confirmation of the final BDT result with a more traditional analysis. The cut-based  
1749 techniques are the focus of this chapter, but connections to the BDT result will be illustrated when ap-  
1750 propriate.

1751 One important note is that because this analysis is dedicated to the measurement of the VBF pro-  
1752 duction mode of the Higgs, events coming from gluon fusion production with the Higgs decaying via  
1753  $H \rightarrow WW^* \rightarrow \ell\nu\ell\nu$  are treated as background events. This will be seen throughout the various  
1754 predictions shown.

##### 1755 5.4.1 COMMON PRE-SELECTION

1756 Both the cut-based and BDT analyses have a common pre-selection that is applied before the main signal  
1757 region requirements. The requirements on leptons are common to all  $n_j$  bins. The analysis requires two  
1758 oppositely charged leptons, with the leading lepton required to have  $p_T > 22$  GeV while the subleading  
1759 lepton must have  $p_T > 10$  GeV. Next, to remove low mass  $Z/\gamma^*$  events, a cut on the dilepton mass

1760     $m_{\ell\ell} > 10$  (12) GeV is applied in the different (same) flavor channel. In the same flavor channels, there is  
1761    an additional veto placed on the region around the Z peak, requiring that  $|m_{\ell\ell} - m_Z| > 15$  GeV.

1762    There are also requirements on the amount of missing transverse momentum in the event. These  
1763    are only applied in the same flavor channels, as in the different flavor channels  $t\bar{t}$  is the dominant back-  
1764    ground in  $n_j \geq 2$ . The BDT analysis requires  $p_T^{\text{miss}} > 40$  GeV and  $E_T^{\text{miss}} > 45$  GeV. The cut-  
1765    based analysis must select more tightly on these variables to have maximal sensitivity and thus requires  
1766     $p_T^{\text{miss}} > 50$  GeV and  $E_T^{\text{miss}} > 55$  GeV.

1767    Finally, because this analysis is focused on VBF, a requirement on the jet multiplicity is placed, with  
1768     $n_j \geq 2$ . Additionally, the analysis requires that there are no jets identified as b-quarks in the event, or  
1769     $n_b = 0$ .

#### 1770 5.4.2 CUT-BASED SELECTION

1771    The cut-based selection places sequential requirements on variables reconstructed from the VBF jets in  
1772    order to increase the signal to background ratio.

#### 1773 GENERAL BACKGROUND REDUCTION

1774    Top pair production is the primary background in the  $n_j \geq 2$  bin. Even though  $n_b = 0$  is required,  
1775    an additional variable is constructed to further suppress the top background. There is often additional  
1776    QCD radiation that accompanies the  $t\bar{t}$  system when it is produced. Therefore, a variable which tests for  
1777    the presence of this additional radiation,  $p_T^{\text{sum}}$ , is constructed. It is defined in equation 5.1.

$$p_T^{\text{sum}} = p_T^{\ell\ell} + p_T^{\text{miss}} + \sum p_T^j \quad (5.1)$$

1778    The first cut after pre-selection in the cut-based analysis requires  $p_T^{\text{sum}} < 15$  GeV to further suppress  $t\bar{t}$   
1779    production.

1780    In the different flavor channels, a cut is made to reduce the contamination from  $Z \rightarrow \tau\tau$  decays.  
1781    The di- $\tau$  invariant mass,  $m_{\tau\tau}$ , is constructed by assuming that the neutrinos from the  $\tau$  decays were  
1782    collinear with the leptons [80]. The analysis requires that this mass not be consistent with a  $Z$  by requir-

1783 ing  $m_{\tau\tau} < m_Z - 25$  GeV.

1784 VBF TOPOLOGICAL CUTS

1785 The characteristic feature of VBF production of the Higgs is the presence of two additional forward jets  
1786 coming from the incoming partons which radiate the vector bosons that make the Higgs. These jets are  
1787 forward because the outgoing partons still carry the longitudinal momentum of the incoming partons.  
1788 Figure 5.2 shows the distribution of the  $\eta$  for the leading jet in a VBF event compared to a background  
1789 top pair production event. As can be seen, the VBF jets tend to be more forward in  $\eta$ , while the  $t\bar{t}$  jets are  
1790 more central.

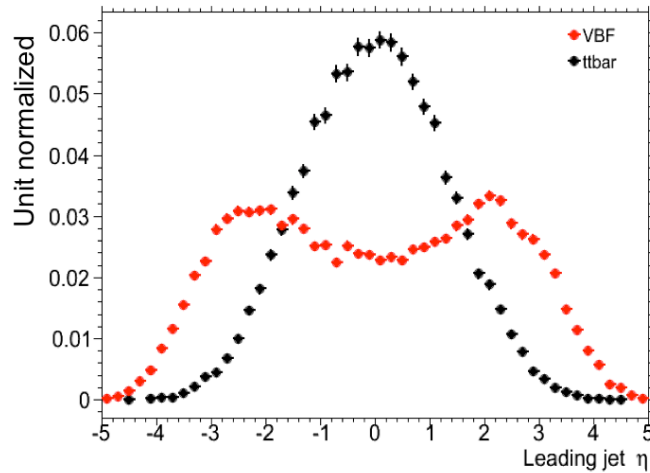


Figure 5.2: Leading jet  $\eta$  in VBF  $H \rightarrow WW^*$  (red) and  $t\bar{t}$  (black)

1791 Because the cross section for VBF production is an order of magnitude smaller than gluon fusion pro-  
1792 duction, these forward jets must be used in order to better reduce background and achieve a good signal  
1793 to background ratio. The dedicated VBF search selection requirements are constructed to maximally  
1794 exploit the features of the unique VBF topology.

1795 Requirements on the VBF jets are collectively referred to as the “VBF topological cuts”. First, a re-  
1796 quirement on the dijet invariant mass of the VBF jets,  $m_{jj}$ , is placed, requiring  $m_{jj} > 600$  GeV. Next,  
1797 the event is required to have a large gap in rapidity between the two VBF jets, or  $\Delta y_{jj} > 3.6$ . Both

1798 of these cuts put tight requirements on the presence of two forward, high  $p_T$  jets moving in opposite  
1799 directions in the longitudinal plane.

1800 Beyond requiring the presence of the two forward VBF jets, the analysis also vetoes on the presence  
1801 of any additional jets that fall between the two VBF jets. This cut is referred to as the central jet veto, or  
1802 CJV. Any events with a third jet with  $p_T > 20$  GeV whose rapidity is between the region defined by the  
1803 two VBF jets are vetoed. This can be expressed in terms of a variable called the jet centrality, defined in  
1804 equation 5.2.

$$C_{j3} = \left| \eta_{j3} - \frac{\eta_{j1} + \eta_{j2}}{2} \right| / \frac{|\eta_{j1} - \eta_{j2}|}{2}, \quad (5.2)$$

1805 Here,  $\eta_{j1}$  and  $\eta_{j2}$  are the pseudorapidities of the leading and subleading jets, respectively, while  $\eta_{j3}$  is  
1806 the pseudorapidity of the extra jet in the event (if one exists). Intuitively,  $C_{j3}$  is zero when  $\eta_{j3}$  is directly  
1807 centered between the two jets and unity when  $\eta_{j3}$  is aligned with either of the VBF jets. Thus, the CJV  
1808 can be expressed as a requirement that  $C_{j3} > 1$ .

1809 The decay products of the Higgs tend to be central as well. Thus, the analysis also requires that both  
1810 leptons in the analysis fall within the rapidity gap defined by the jets. This cut is referred to as the outside  
1811 lepton veto, or OLV. A quantitative way to define the cut is to require that the centrality of each lepton  
1812 (defined analogously to that of the third jet in equation 5.2) correspond to the lepton being within the jet  
1813 rapidity gap, or  $C_\ell < 1$  for both leptons.

1814 Figure 5.3a-c shows the  $m_{jj}$ ,  $\Delta y_{jj}$ , and  $C_{\ell 1}$  variables at the stage where all previous cuts in the se-  
1815 quence have been made. The agreement between data and Monte Carlo is good, and the bottom panels  
1816 show their power in discriminating the VBF signal from the background processes.

1817 The final signal region is also split into two bins of  $m_{jj}$ , with the first bin corresponding to  $600 \text{ GeV} <$   
1818  $m_{jj} < 1 \text{ TeV}$  and the second bin corresponding to  $m_{jj} > 1 \text{ TeV}$ . The first bin has more statistics but  
1819 also a larger contribution from background, while the second bin has lower statistics but a 1:1 signal to  
1820 background ratio.

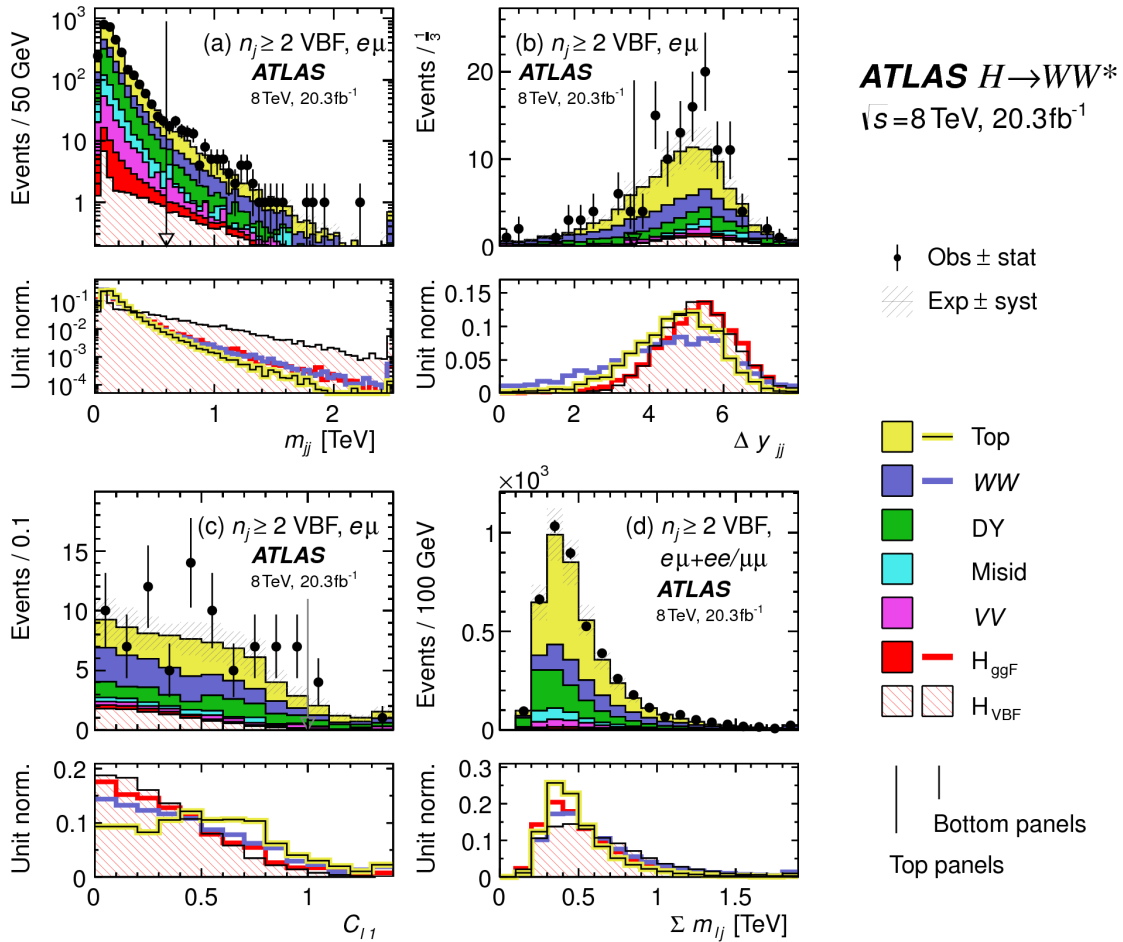


Figure 5.3: Distributions of (a)  $m_{jj}$ , (b)  $\Delta y_{jj}$ , (c)  $C_{\ell 1}$ , and (d)  $\Sigma m_{\ell j}$ , for the VBF analysis. The top panels compare simulation and data, while the bottom panels show normalized distributions for all background processes and signal [61].

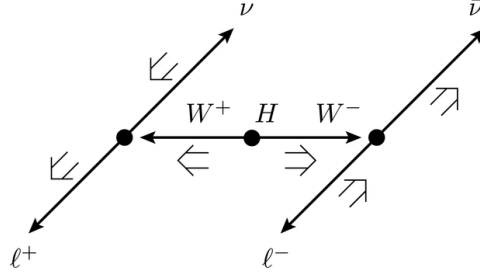


Figure 5.4: A cartoon of the WW final state. Momenta are represented with thin arrows, spins with thick arrows.  
[61]

1821 HIGGS TOPOLOGICAL CUTS

1822 The final state leptons will exhibit unique correlations due to the fact that they are arising from the decay  
 1823 of a spin zero resonance. In particular, the spins of the final state leptons and neutrinos must all cancel,  
 1824 as shown in figure 5.4. Because the neutrino has a left handed chirality and the anti-neutrino has a right  
 1825 handed chirality (in the massless neutrino approximation), the spin and momentum of the particles  
 1826 will be anti-aligned and aligned, respectively. In the transverse plane, the momenta of all four final state  
 1827 objects must cancel as well. With the constraint of having both the momenta and the spin alignments  
 1828 cancel, the final state kinematics strongly prefer having a small angle between the leptons in the trans-  
 1829 verse plane (low  $\Delta\phi_{\ell\ell}$ ). This angular correlation will also lead to low values of the di-lepton invariant  
 1830 mass  $m_{\ell\ell}$ . These unique signal final state kinematic correlations will be exploited to define the ultimate  
 1831 signal region.

1832 The analysis places additional requirements on the final state leptons. Two requirements on dilepton  
 1833 kinematics are made that are common with lower multiplicity jet bins as well. The angle between leptons  
 1834 in the transverse plane,  $\Delta\phi_{\ell\ell}$ , is required to be less than 1.8 radians. Additionally, the dilepton mass  $m_{\ell\ell}$   
 1835 is required to be less than 50 GeV.

1836 The cut-based analysis uses  $m_T$  as the final discriminating variable as in the ggF focused analysis. The  
 1837 optimal number of bins in  $m_T$  was found to be three bins, with the bin boundaries at 80 and 130 GeV.

1838 Table 5.7 shows the data and estimated signal and background yields from simulation as each cut de-  
 1839 scribed above is made. The table shows how each cut reduces specific backgrounds and how the overall

1840 signal to background ratio grows through the various selection requirements.

1841 Figure 5.5 shows an ATLAS event display of a candidate event in the final signal region.

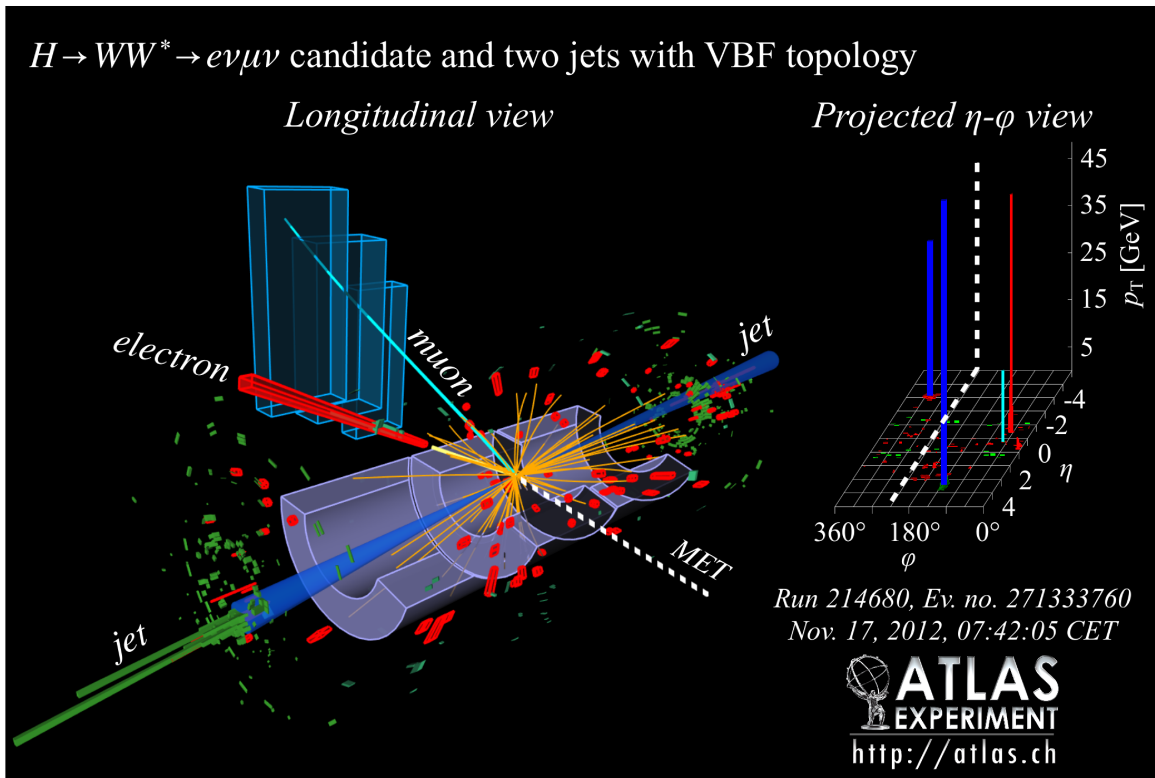


Figure 5.5: Event display of a VBF candidate event [61].

#### 1842 5.4.3 BDT-BASED SELECTION

1843 The boosted decision tree based analysis takes a different philosophy compared to the cut-based. Rather  
1844 than cutting sequentially on many variables, the BDT analysis uses many of these variables as inputs  
1845 to the BDT and the output BDT score ( $O_{\text{BDT}}$ ) as the final discriminant. The BDT is trained with the  
1846 VBF  $H \rightarrow WW^*$  simulation as the signal samples and all other processes as background, including ggF  
1847  $H \rightarrow WW^*$  production. While the BDT based analysis is treated as a separate result, it has significant  
1848 overlap with the cut-based selection.

Table 5.7: Event selection for the  $n_j \geq 2$  VBF analysis in the 8 TeV cut-based analysis [61].

Selection	Summary										Composition of $N_{\text{bkg}}$									
	$N_{\text{obs}}/N_{\text{bkg}}$	$N_{\text{obs}}$	$N_{\text{bkg}}$	$N_{\text{ggF}}$	$N_{\text{VBF}}$	$N_{\text{signal}}$	$N_{WW}$	$N_{WW}^{\text{EW}}$	$N_{t\bar{t}}$	$N_t$	$N_{\text{top}}$	$N_{WW}^{\text{QCD}}$	$N_{WW}^{\text{EW}}$	$N_{Wj}$	$N_{jj}$	$N_{\text{misid}}$	$N_{VV}$	$N_{e\mu/\mu\mu}$	$N_{\text{Drell-Yan}}$	$N_{\tau\tau}^{\text{QCD}}$
$e\mu$ sample	1.00 ± 0.00	61434	61180	85	32	26	1350	68	51810	2970	847	308	380	51	3260	46				
$n_b = 0$	1.02 ± 0.01	7818	7700	63	26	16	993	43	3000	367	313	193	273	35	2400	29				
$p_T^{\text{sum}} < 15$	1.03 ± 0.01	5787	5630	46	23	13	781	38	1910	270	216	107	201	27	2010	23				
$m_{\tau\tau} < m_Z - 25$	1.05 ± 0.02	3129	2970	40	20	9.9	484	22	1270	177	141	66	132	7.6	627	5.8				
$m_{jj} > 600$	1.31 ± 0.12	131	100	2.3	8.2	—	18	8.9	40	5.3	1.8	2.4	5.1	0.1	15	1.0				
$\Delta y_{jj} > 3.6$	1.33 ± 0.13	107	80	2.1	7.9	—	11.7	6.9	35	5.0	1.6	2.3	3.3	—	11.6	0.8				
$C_{j3} > 1$	1.36 ± 0.18	58	43	1.3	6.6	—	6.9	5.6	14	3.0	1.3	1.3	2.0	—	6.8	0.6				
$C_{\ell 1} < 1, C_{\ell 2} < 1$	1.42 ± 0.20	51	36	1.2	6.4	—	5.9	5.2	10.8	2.5	1.3	1.3	1.6	—	5.7	0.6				
$m_{\ell\ell}, \Delta\phi_{\ell\ell}, m_{\tau\tau}$	2.53 ± 0.71	14	5.5	0.8	4.7	—	1.0	0.5	1.1	0.3	0.3	0.3	0.6	—	0.5	0.2				
$ee/\mu\mu$ sample	0.99 ± 0.01	26949	27190	31	14	10.1	594	37	23440	1320	230	8.6	137	690	679	16				
$n_b, p_T^{\text{sum}}, m_{\tau\tau}$	1.03 ± 0.03	1344	1310	13	8.0	4.0	229	12.0	633	86	26	0.9	45	187	76	1.5				
$m_{jj}, \Delta y_{jj}, C_{j3}, C_\ell$	1.39 ± 0.28	26	19	0.4	2.9	0.0	3.1	5.5	1.0	0.2	0.0	0.7	3.8	0.7	0.1					
$m_{\ell\ell}, \Delta\phi_{\ell\ell}, m_{\tau\tau}$	1.63 ± 0.69	6	3.7	0.3	2.2	0.0	0.4	0.2	0.6	0.2	0.2	0.0	0.1	1.5	0.3	0.1				

1849 PRE-TRAINING SELECTION AND BDT INPUTS

1850 Before training, the common pre-selection cuts described in section 5.4.1 are applied. Additionally, the  
1851 central jet veto and outside lepton veto described in section 5.4.2 are applied. The BDT has eight input  
1852 variables, six of which are also variables that are used in the cut-based analysis. The six shared variables  
1853 are  $p_T^{\text{sum}}$ ,  $m_{jj}$ ,  $\Delta y_{jj}$ ,  $m_{\ell\ell}$ ,  $\Delta\phi_{\ell\ell}$ , and  $m_T$ . The seventh variable input in the BDT is a combination of  
1854 the variables used to do the OLV in the cut-based analysis. The BDT uses as input the sum of lepton  
1855 centralities, or  $\sum C_\ell = C_{\ell 1} + C_{\ell 2}$ . The final BDT input variable,  $\Sigma m_{\ell j}$ , is constructed to account for  
1856 the correlations between the jets and leptons in the event. It is the sum of the invariant masses of all four  
1857 possible lepton-jet combinations.

1858 Figure 5.3d shows the agreement between data and simulation for the  $\Sigma m_{\ell j}$  variable, as well as show-  
1859 ing its discriminating power. Figure 5.6 shows the distributions of the Higgs topological variables that  
1860 are shared between the cut-based and BDT analyses. Figure 5.7 shows the distributions of the VBF topo-  
1861 logical variables shared between the cut-based and BDT analyses. In both cases, the VBF yield has been  
1862 scaled by a factor of 50 to better show the shape difference compared to the backgrounds.

1863 Table ?? summarizes the cuts applied for the cut-based and analyses, as well as which variables are used  
1864 as input to the BDT.

1865 5.5 BACKGROUND ESTIMATION

1866 This section describes the procedures used to estimate backgrounds for the VBF analysis in both the  
1867 cut-based and BDT analyses.

1868 5.5.1 GENERAL STRATEGY

1869 Most of the backgrounds in the VBF analysis have shapes estimated from Monte Carlo simulation but  
1870 normalizations derived from control regions in data. In essence, a normalization factor (denoted with  
1871  $\beta$  or abbreviated as NF) is derived by scaling the MC yield in the control region to the corresponding  
1872 yield in data. Once this factor is derived, it can be used to scale the MC estimate of the background in the

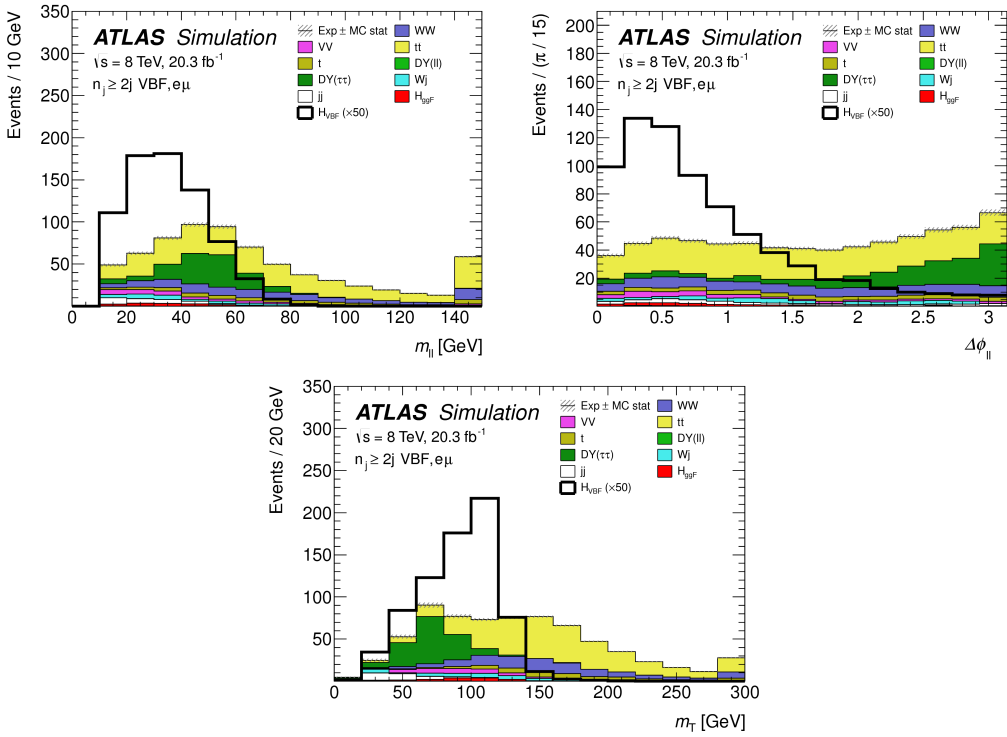


Figure 5.6: Distributions of  $m_{\ell\ell}$  (top left),  $\Delta\phi_{\ell\ell}$  (top right), and  $m_T$  (bottom), Higgs topology variables used in the selection requirements of the cut-based signal region and as inputs to the BDT result. These are plotted after all of the BDT pre-training selection cuts [61].

1873 signal region. This is illustrated in equation 5.3.

$$B_{\text{SR}}^{\text{est}} = B_{\text{SR}} \times \frac{N_{\text{CR}}}{B_{\text{CR}}} \equiv B_{\text{SR}} \times \beta \quad (5.3)$$

1874 Here,  $B$  denotes the MC yield prediction in the denoted region, while  $N$  denotes the observed number  
 1875 of events in data in the denoted region.

1876 Another way of writing the same equation, in terms of an extrapolation factor  $\alpha$  rather than a nor-  
 1877 malization factor  $\beta$ . The overall calculation is exactly the same. However, when phrased in this way, it  
 1878 shows how the uncertainty on the background estimation can be reduced. This is shown in equation 5.4.

1879

$$B_{\text{SR}}^{\text{est}} = N_{\text{CR}} \times \frac{B_{\text{SR}}}{B_{\text{CR}}} \equiv N_{\text{CR}} \times \alpha \quad (5.4)$$

1880 Phrased this way, the equation shows that with enough statistics in the control region, a large theoretical

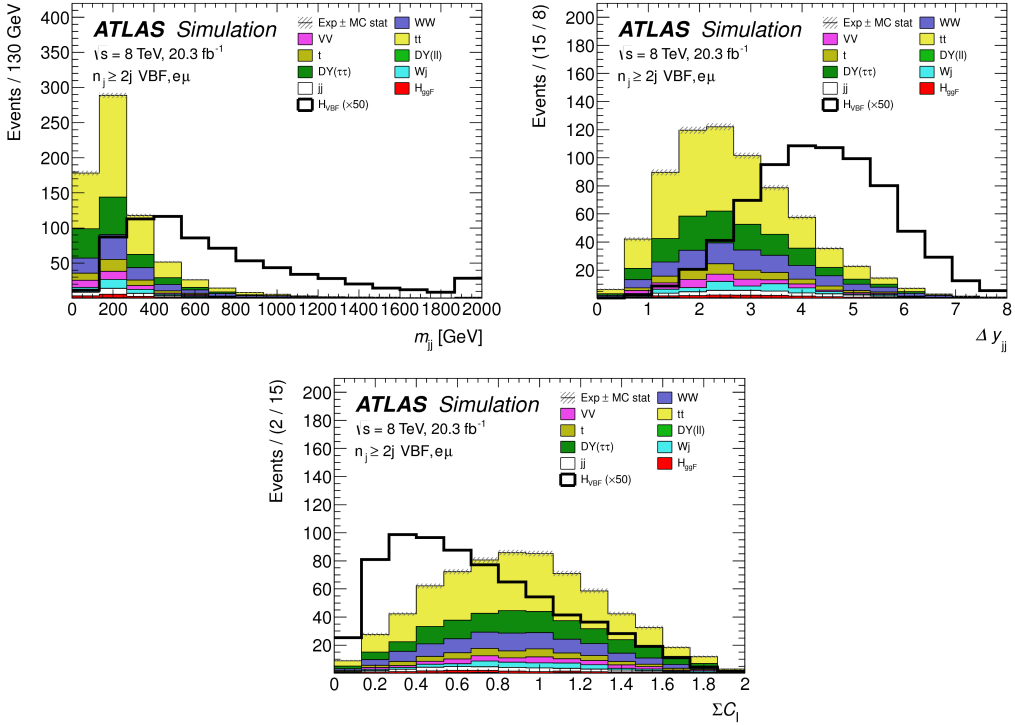


Figure 5.7: Distributions of  $m_{jj}$  (top left),  $\Delta y_{jj}$  (top right),  $\sum C_\ell$  (bottom), VBF topology variables used in the selection requirements of the cut-based signal region and as inputs to the BDT result. These are plotted after all of the BDT pre-training selection cuts [61].

uncertainty on the overall background yield in the signal region can be replaced by a small statistical uncertainty coming from the number of data events in the CR and a smaller theoretical uncertainty on the extrapolation from the control region to the signal region.

### 5.5.2 TOP BACKGROUND

The normalization factor  $\beta_t$  for the top background in the VBF analysis is derived in a region required to have one b-tagged jet, or  $n_b = 1$ . In the cut-based analysis, normalization factors are computed at every stage of the cutflow by applying the appropriate cuts in the CR. These NF are then applied to the  $t\bar{t}$  and single top event yields in the SR. In the BDT analysis, a single normalization factor is computed for each bin of  $O_{\text{BDT}}$  after applying the BDT pre-training cuts described previously. The computed normalization factors are derived with all flavor combinations combined in order to decrease statistical uncertainty. Additionally, in the BDT analysis, BDT bins 2 and 3 are merged for the same reason.

1892 Table 5.8 shows the evolution of the  $\beta_t$  through the cut-based selection. Table 5.9 shows the value  
 1893 of the  $\beta_t$  in each bin of  $O_{\text{BDT}}$ . In all cases, the computed factors are relatively consistent with unity,  
 1894 with the largest discrepancy coming in bin 1 of  $O_{\text{BDT}}$ . The normalization factors in the bins of  $O_{\text{BDT}}$   
 1895 are also consistent with those derived in the cut-based signal region, increasing confidence in the BDT  
 1896 estimation.

Cut	$\beta_t$
$p_T^{\text{sum}} < 15 \text{ GeV}$	$1.03 \pm 0.01$
$m_{\tau\tau} < m_Z - 25$	$1.05 \pm 0.01$
$m_{jj} > 600 \text{ GeV}$	$0.96 \pm 0.06$
$\Delta y_{jj} > 3.6$	$1.02 \pm 0.08$
CJV	$1.13 \pm 0.16$
OLV	$1.01 \pm 0.19$
$m_{jj} < 1 \text{ TeV}$	$0.94 \pm 0.19$
$m_{jj} > 1 \text{ TeV}$	$1.48 \pm 0.66$

Table 5.8: Top normalization factors computed at each stage of the cut-based selection. Uncertainties are statistical only.

$O_{\text{BDT}}$	$\beta_t$
Bin0	$1.09 \pm 0.02$
Bin1	$1.58 \pm 0.15$
Bin2	$0.95 \pm 0.31$
Bin3	$0.95 \pm 0.31$

Table 5.9: Top normalization factors computed for each bin of  $O_{\text{BDT}}$ . Uncertainties are statistical only.

1897 Figure 5.8 shows the  $m_{jj}$  and  $O_{\text{BDT}}$  distributions in the top control region. Overall the modeling  
 1898 looks consistent with the data.

1899 While these normalization factors can be computed and applied to the expected background yields  
 1900 listed in tables like table 5.7, in the end the normalization of the top background is profiled (meaning  
 1901 there is a dedicated Poisson constraint) and allowed to float in the final statistical fit.

### 1902 5.5.3 $Z/\gamma^* \rightarrow \tau\tau$ BACKGROUND

1903 In the different flavor channels, the  $Z/\gamma^* \rightarrow \tau\tau$  background is an important one. Di-tau production  
 1904 can produce an  $e\mu$  final state if each  $\tau$  lepton decays to a different flavor lepton.

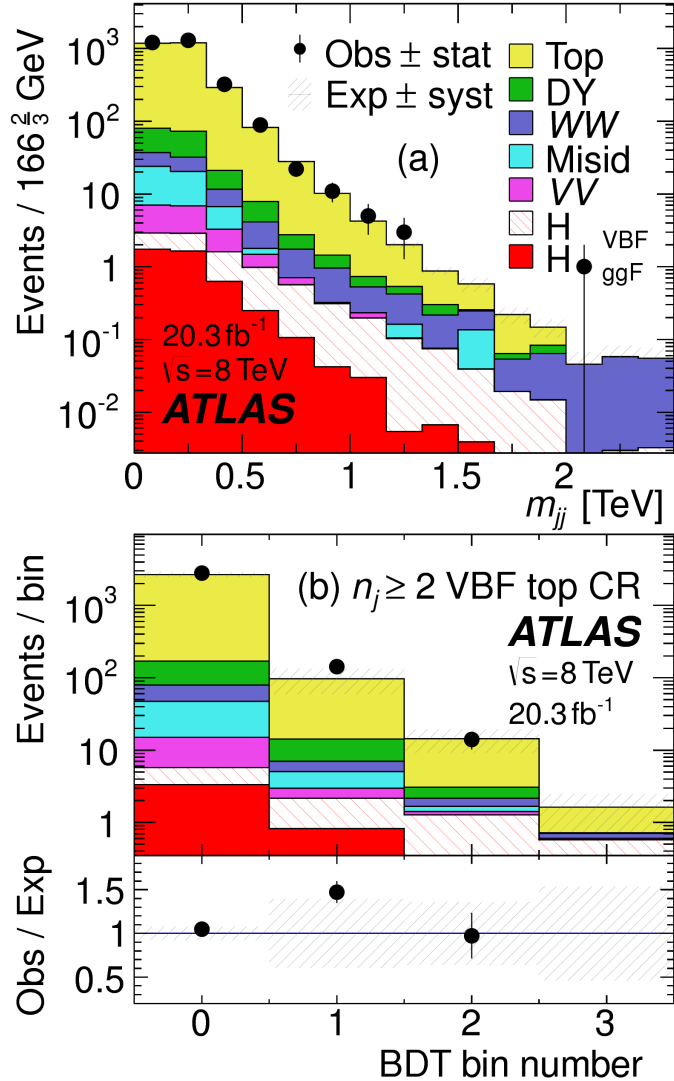


Figure 5.8: Distributions of  $m_{jj}$  (a) and  $O_{\text{BDT}}$  (b) in the VBF  $n_b = 1$  top CR [61].

In the BDT analysis, a single normalization factor for the background is derived. A control region is defined using the pre-training selection cuts, except requiring that  $|m_{\tau\tau} - m_Z| < 25 \text{ GeV}$  so that the region is enriched in  $Z/\gamma^* \rightarrow \tau\tau$  background. Additional requirements of  $m_{\ell\ell} < 80(75) \text{ GeV}$  in the different (same) flavor channel, as well as  $O_{\text{BDT}} > -0.48$  are applied to increase the purity of the region. The final  $\beta_{Z/\gamma^* \rightarrow \tau\tau}$  is calculated to be  $0.9 \pm 0.3$  (statistical uncertainty only). Because of the small contribution of this background in the BDT analysis and the large statistical uncertainty, no additional systematics are calculated. The final SR estimate is scaled by this  $\beta$  and not allowed to float in

1912 the fit.

1913 The cut-based corrections are a bit more involved because they need to be applied selection by selec-  
1914 tion, as well as in the final signal region for the fit. The region is defined including all SR cuts up to the  
1915  $Z/\gamma^* \rightarrow \tau\tau$  veto, which is instead made into a  $Z$  mass peak requirement as for the BDT region. The  
1916  $m_{\ell\ell}$  cut from the BDT region is included as well. The cut-based approach aims to correct the normal-  
1917 ization of the  $Z/\gamma^* \rightarrow \tau\tau$  background in two ways. First, an overall normalization factor is computed  
1918 from the control region. However, the VBF topological cuts are not included in this region, and apply-  
1919 ing them as is done in the top CR is not feasible due to limited statistics. So, instead, correction factors  
1920 (CF) to the cut efficiencies of the VBF cuts are derived in a same flavor  $Z \rightarrow \ell\ell$  control region, which has  
1921 significantly more statistics. The CF is simply the ratio of the cut efficiencies in data and MC derived in  
1922 this region. In the end, the overall background estimate is given by equation 5.5.

$$N_{Z/\gamma^* \rightarrow \tau\tau}^{\text{est}} = B_{Z/\gamma^* \rightarrow \tau\tau}^{\text{SR}} \times \beta_{\tau\tau} \times \frac{\epsilon_{\text{VBF cuts}}^{\text{data}}}{\epsilon_{\text{VBF cuts}}^{\text{MC}}} \quad (5.5)$$

1923 The hypothesis is that while the normalization correction must be derived in a dedicated region, the  
1924 efficiency of the VBF cuts should not be sensitive to the type of  $Z/\gamma^*$  process and thus the larger control  
1925 region can be exploited to derive the CF. Figure 5.9 shows a shape comparison for the  $m_{jj}$  variable in  
1926  $Z \rightarrow \tau\tau$  events in the signal region and  $Z \rightarrow \ell\ell$  events in the control region. The figure shows that the  
1927 shapes are indeed comparable and thus any CF derived in the same flavor control region can reliably be  
1928 applied in the signal region.

1929 Table 5.10 shows the overall normalization factor  $\beta_{\tau\tau}$  and the efficiency correction factors for the var-  
1930 ious VBF topological cuts. In general, the statistical uncertainties on the cut efficiency corrections are  
1931 quite good, and the MC tends to underestimate the efficiency of the VBF cuts for the  $Z/\gamma^* \rightarrow \tau\tau$  back-  
1932 ground. The overall normalization factor is also consistent with that calculated for the BDT analysis.

#### 1933 5.5.4 $Z/\gamma^* \rightarrow \ell\ell$ BACKGROUND

1934 In the same flavor channels, the  $Z/\gamma^* \rightarrow \ell\ell$  background is dominant and thus must be estimated  
1935 correctly. In both the BDT and cut-based analyses, the background is estimated using the so-called

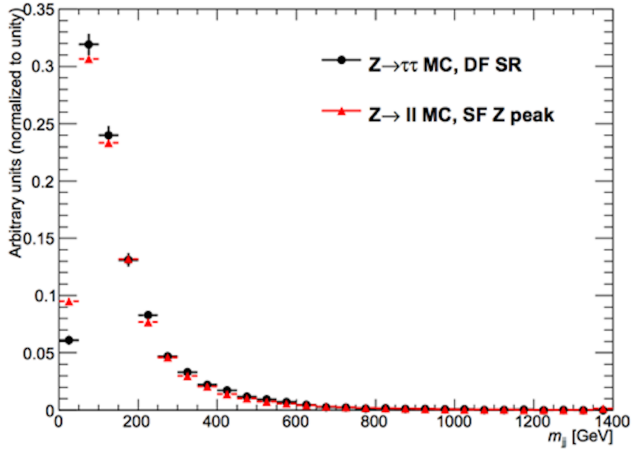


Figure 5.9: Comparison of  $m_{jj}$  shape in a same flavor  $Z \rightarrow \ell\ell$  control region and the VBF cut-based signal region.

$\beta_{\tau\tau}$	$0.97 \pm 0.04$
Cut	Correction factors
$m_{jj} > 600$ GeV	$1.09 \pm 0.01$
$\Delta y_{jj} > 3.6$	$1.14 \pm 0.02$
CJV	$1.20 \pm 0.02$
OLV	$1.17 \pm 0.03$
$m_{jj} < 1$ TeV	$1.17 \pm 0.06$
$m_{jj} > 1$ TeV	$1.18 \pm 0.13$

Table 5.10:  $Z/\gamma^* \rightarrow \tau\tau$  correction factors for the VBF cut-based analysis. Uncertainties are statistical only.

<sup>1936</sup> “ABCD” method. The ABCD method creates four different regions by defining cuts on two variables.  
<sup>1937</sup> One of the regions (A) is the signal region, while the other regions are defined by inverting one of both  
<sup>1938</sup> of the cuts. in this case, the two variables used are  $m_{\ell\ell}$  and  $E_T^{\text{miss}}$ , because inverting either of the SR cuts  
<sup>1939</sup> on these variables will give regions rich in the  $Z/\gamma^* \rightarrow \ell\ell$  background. Figure 5.10 illustrates the general  
<sup>1940</sup> strategy for each region.

<sup>1941</sup> In both of the cut-based and BDT analyses, the Z peak region is defined with  $|m_{\ell\ell} - m_Z| < 15$  GeV.  
<sup>1942</sup> In the cut-based analysis, low  $m_{\ell\ell}$  corresponds to  $m_{\ell\ell} < 50$  GeV (this defines the cut-based SR) while  
<sup>1943</sup> in the BDT it is  $m_{\ell\ell} < 75$  GeV. In the cut-based, high and low  $E_T^{\text{miss}}$  are defined as opposite ends of  
<sup>1944</sup> the 55 GeV cut applied for the signal region definition. The BDT low  $E_T^{\text{miss}}$  region is between 25 and  
<sup>1945</sup> 45 GeV, while the high  $E_T^{\text{miss}}$  region is  $E_T^{\text{miss}} > 45$  GeV.

<sup>1946</sup> Once the regions are defined, the final signal region background estimate is done by taking the esti-

<b>Region A (SR)</b>	<b>Region C</b>
High $E_T^{\text{miss}}$	High $E_T^{\text{miss}}$
Low $m_{\ell\ell}$	Z peak
<b>Region B</b>	<b>Region D</b>
Low $E_T^{\text{miss}}$	Low $E_T^{\text{miss}}$
Low $m_{\ell\ell}$	Z peak

Figure 5.10: General illustration of the ABCD region definitions for  $Z/\gamma^* \rightarrow \ell\ell$  background estimation.

1947 mate in region B and extrapolating it to the signal region (A) by multiplying it by the ratio of regions  
1948 C and D. Effectively, the  $Z$  peak region is used to estimate the efficiency of the  $E_T^{\text{miss}}$  cut in data, and  
1949 then this efficiency is applied in the low  $m_{\ell\ell}$  region. An additional correction is also applied for the non-  
1950 closure of the method in MC. This is summarized in equations 5.6 and 5.7.

$$N_{Z/\gamma^*\rightarrow\ell\ell}^{\text{SR}} = N_{Z/\gamma^*\rightarrow\ell\ell}^{\text{B}} \times \frac{N_{Z/\gamma^*\rightarrow\ell\ell}^{\text{C}}}{N_{Z/\gamma^*\rightarrow\ell\ell}^{\text{D}}} \times f_{\text{corr}} \quad (5.6)$$

$$f_{\text{corr}} = \frac{B_{\text{MC}}^{\text{A}}/B_{\text{MC}}^{\text{B}}}{B_{\text{MC}}^{\text{C}}/B_{\text{MC}}^{\text{D}}} \quad (5.7)$$

1951 Here, the  $N$  refer to data yields in each region with the non  $Z/\gamma^*$  backgrounds subtracted, while  $B$   
1952 refer to the  $Z/\gamma^*$  yields in MC in each region.

1953 A normalization factor  $\beta_{\ell\ell}$  is computed for each analysis as the ratio of the predicted data yield to  
1954 the MC yield in the SR. The shape of the BDT distribution is taken from data region B, while the shape  
1955 of the  $m_T$  distribution in the cut-based analysis is taken from  $Z/\gamma^*$  MC in the SR. The values of the  
1956  $\beta_{\ell\ell}$  in the cut-based and BDT analyses from this method are summarized in table 5.11. They are quite  
1957 consistent with one another within the statistical uncertainties. In the cut-based analysis, the same cut  
1958 efficiency correction factors shown in table 5.10 are also applied (in product with the  $\beta_{\ell\ell}$ ) in the same  
1959 flavor channels to this background, as they were derived in the  $Z$  peak region.

	$\beta_t$
BDT Bin 1	$1.01 \pm 0.15$
BDT Bin 2	$0.89 \pm 0.28$
Cut-based	$0.81 \pm 0.21$

Table 5.II:  $Z/\gamma^* \rightarrow \ell\ell$  normalization factors for cut-based and BDT analyses. Uncertainties are statistical only.

### 1960 5.5.5 $WW$ AND OTHER DIBOSON BACKGROUNDS

1961 The  $WW$  and other diboson backgrounds have both their shape and normalization taken from MC  
 1962 simulation. They are validated in dedicated control regions and found to agree with data well.

1963 As  $WW$  is the largest of these backgrounds and is irreducible, validating the estimate is of particular  
 1964 importance. The validation region is constructed by requiring the pre-selection cuts on leptons and  $m_{\ell\ell}$ ,  
 1965  $n_b = 0$ , and  $m_T > 100$  GeV. The  $m_{T2}$  variable [81] is an additional discriminant that will isolate  
 1966 the  $WW$  background, and a requirement of  $m_{T2} > 160$  GeV is placed to define the  $WW$  validation  
 1967 region. This cut gives a 60% purity for the validation region. The derived normalization factor in the  
 1968 region is  $1.15 \pm 0.19$  and is thus consistent with unity. Figure 5.II shows the  $m_{T2}$  distribution and how  
 1969 it distinguishes the  $WW$  background.

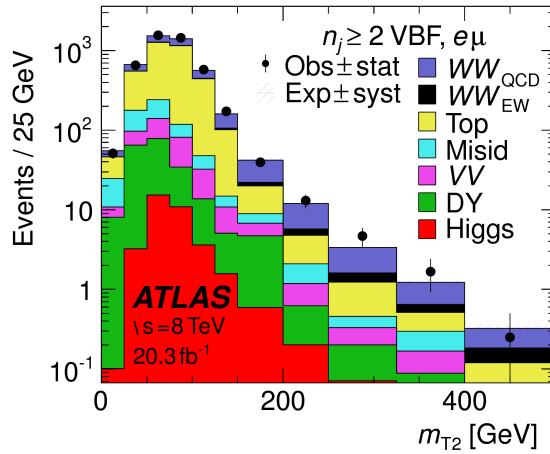


Figure 5.II: Distribution of  $m_{T2}$  in the  $WW$  validation region of the VBF analysis [61].

1970    5.5.6 HIGGS PRODUCTION VIA GLUON-GLUON FUSION

1971    Because this analysis is dedicated to measuring the VBF contribution to Higgs production, the com-  
1972    ponent of Higgs production from gluon-gluon fusion is treated as a background. The shape is taken  
1973    directly from simulation, using the generators described in table 5.4. In the final combined fit of all dif-  
1974    ferent signal regions, the normalization is controlled by either a combined signal strength parameter  $\mu$ ,  
1975    which controls the normalization of both ggF and VBF production, or a separate parameter  $\mu_{\text{ggF}}$  de-  
1976    pending on the interpretation being presented in the final results.

1977    5.5.7 BACKGROUNDS WITH MISIDENTIFIED LEPTONS

1978    As discussed previously, the  $W + \text{jets}$  and QCD multijet backgrounds are derived with fully data-driven  
1979    methods. These backgrounds do not make a large contribution to the final VBF signal region but their  
1980    estimation methods are discussed briefly here.

1981     $W + \text{jETS}$  BACKGROUND

1982    The  $W + \text{jets}$  background enters the signal region by having one of the jets mis-reconstructed as a lep-  
1983    ton. The background is estimated by constructing a control sample with two leptons, where one lepton  
1984    passes the usual lepton quality cuts but the second lepton fails one of those cuts (also known as the “anti-  
1985    identified” lepton). This control region is rich in the  $W + \text{jets}$  contribution because if a second lepton is  
1986    reconstructed in a  $W + \text{jets}$  event it is likely to be poor quality. The purity of this  $W + \text{jets}$  control sample  
1987    is 85% to 90% depending on the exact configuration of leptons in the final state.

1988    The signal region estimate of  $W + \text{jets}$  is estimated by extrapolation from the control sample to the sig-  
1989    nal region using extrapolation factors derived in a  $Z + \text{jets}$  control sample in data. The extrapolation fac-  
1990    tor is the ratio of the number of lepton candidates satisfying all quality criteria to the number of lepton  
1991    candidates anti-identified. This ratio is measured in bins of  $p_T$  and  $\eta$ . Thus, the final signal region esti-  
1992    mate (binned as the extrapolation factor is binned) is simply the number of events in the anti-identified  
1993    lepton control sample multiplied by the extrapolation factor derived from the  $Z + \text{jets}$  control sample.

1994    Figure 5.12 shows the extrapolation factors derived for electrons and muons.

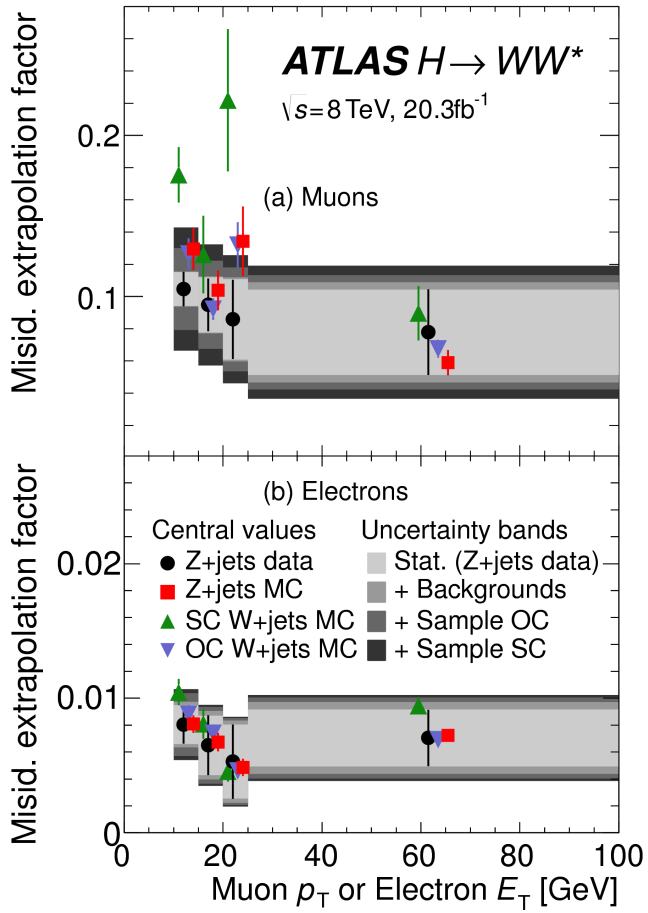


Figure 5.12: Extrapolation factors for the  $W + \text{jets}$  estimate derived for muons (a) and electrons (b) as a function of lepton  $p_T$  [61].

1995    QCD MULTIJET BACKGROUND

1996    The method for estimating the multijet background is very similar to the  $W + \text{jets}$  estimation method.  
1997    The control sample in this case has two anti-identified leptons but otherwise satisfies all signal region  
1998    requirements. The extrapolation factor is estimated from a multijet sample and applied twice to the  
1999    control sample.

2000    5.5.8 BACKGROUND COMPOSITION IN FINAL SIGNAL REGION

2001    After all of these estimation procedures, the final signal region composition can be calculated. The esti-  
2002    mated yields are all shown in table 5.7. Figure 5.13 shows the relative percentages of the different back-

ground for the different flavor and same flavor final states. In  $e\mu$ , the leading backgrounds are top backgrounds, ggF Higgs, and SM  $WW$  production. In  $ee/\mu\mu$ , the leading background is Drell-Yan, followed by top and ggF Higgs.

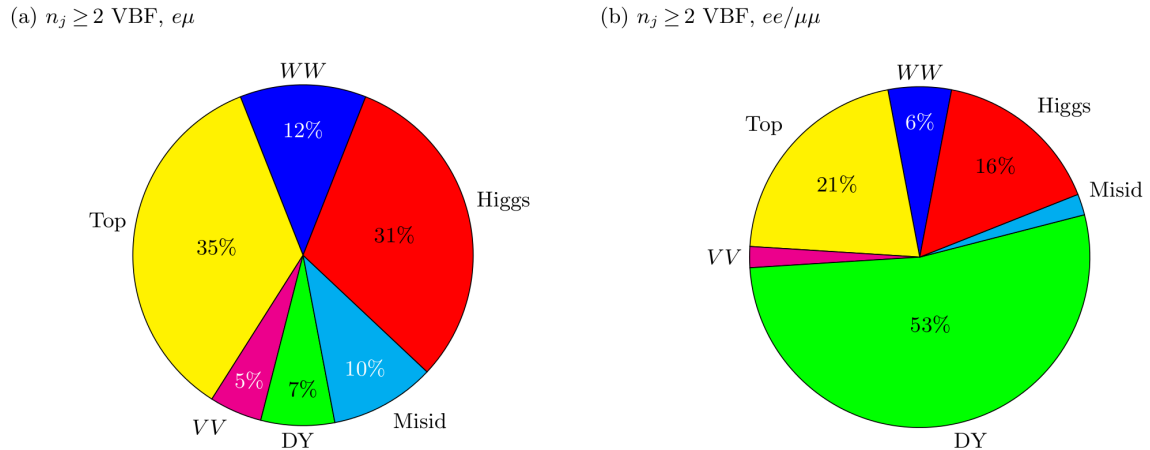


Figure 5.13: Background composition in final VBF signal region [61].

## 5.6 SYSTEMATIC UNCERTAINTIES

There are two main types of systematic uncertainties that are assessed for the analysis. First, theoretical uncertainties associated with the various signal and background yield estimates are discussed. Then, experimental uncertainties due to detector effects are shown. Normalization uncertainties refer to uncertainties that affect the cross section of the process in question in the signal region being probed. Shape uncertainties refer to systematic uncertainties that affect the shape of the final discriminating variable (either  $m_T$  or  $O_{BDT}$ ).

### 5.6.1 THEORETICAL UNCERTAINTIES

There are four main components to theoretical uncertainties assigned to signal and background processes taken from Monte Carlo. Each one is a different source of variation in the overall acceptance for that process. The first involves variation of the QCD renormalization and factorization scales used in the calculation. In this case, the two scales are varied independently and simultaneously by factors of two high or low and quantifying the resulting variation in normalization and shape for the process. This

approximates the correction to the cross section that would come from including the next order of the QCD calculation (referred to as scale uncertainty). Next, there is an uncertainty associated with the PDF set used in generating the events. The uncertainty eigenvectors for the given PDF set are studied, and the envelope of maximal variation is taken as an uncertainty. Finally, there are two uncertainties associated with the choice of MC software (referred to as PDF uncertainty). An uncertainty associated with the generator chosen for the hard scattering process is evaluated by keeping the parton showering software constant but varying the matrix element generator and taking the maximal variation as an uncertainty (referred to as the generator uncertainty). The converse variation can also be done, where the matrix element generator remains constant and the generator used for the underlying event/parton shower modeling is varied (referred to as the UE/PS uncertainty). In cases where the background is normalized in a control region, the systematic uncertainty arises from variations of the extrapolation factor  $\alpha$  between the CR and the SR, which can affect the normalization of the background in the SR.

There are two additional uncertainties that are applied to the Higgs processes as well. First, there are uncertainties assigned to the Higgs total production cross section. Then, there are uncertainties assigned based on the fact that the analysis is done in exclusive jet bins and it is possible for signal events to migrate from one bin to the next depending on the presence or absence of jets. These are assigned using the Jet Veto Efficiency (JVE) procedure [18, 82] for ggF events and the Stewart-Tackmann (ST) method [83] for VBF production.

Table 5.12 shows the total theory uncertainties on the backgrounds in the cut-based analysis. These are the sum in quadrature of the uncertainties from each of the variations described above.

Process	Theory syst. (%)
ggF $H$	48
Top	26
QCD $WW$	37
$Z/\gamma^* \rightarrow \tau\tau$	6.1

Table 5.12: Systematic uncertainties for various processes in the cut-based VBF analysis, given in units of % change in yield. Values are given for the low  $m_{jj}$  signal region.

Figures 5.14 and 5.15 show the variations in the extrapolation factor from the PDF and QCD uncertainties on the top background estimate, binned in  $m_T$ , for the cut-based analysis. In both cases, there

2041 was no significant shape uncertainty but normalization uncertainties were assigned according to the  
 2042 maximal variation. These uncertainties enter into the 26% total uncertainty on top quoted in table 5.12  
 2043 While the estimate for the same-flavor  $Z/\gamma^* \rightarrow \ell\ell$  background is data-driven, there is still a sys-  
 2044 tematic uncertainty taken for the non-closure of the method in Monte Carlo. This is taken as the max-  
 2045 imum of the deviation of the non-closure factor  $f_{\text{corr}}$  from unity and its uncertainty, or  $\max(|1 -$   
 2046  $f_{\text{corr}}|, \delta f_{\text{corr}})$ . For the cut-based analysis this non-closure uncertainty 23%, while for the BDT analy-  
 2047 sis it is 17%.

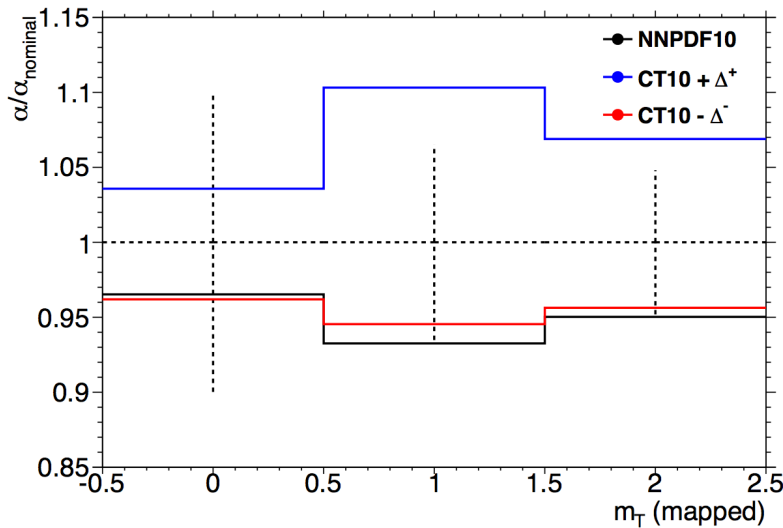


Figure 5.14: Variations in the top background extrapolation factor in the cut-based analysis due to PDF uncertainties, binned in  $m_T$ .

### 2048 5.6.2 EXPERIMENTAL UNCERTAINTIES

2049 In this analysis, the theoretical uncertainties end up being the most dominant, but there are some ex-  
 2050 perimental uncertainties that make a contribution as well. The first is the uncertainty on the measured  
 2051 integrated luminosity, which affects backgrounds whose normalization is taken from MC and is mea-  
 2052 sured to be 2.8% in the 8 TeV dataset [84]. The dominant sources of uncertainty overall are uncertainties  
 2053 on the jet energy scale and resolution and the  $b$ -tagging efficiency. Additional sources include lepton  
 2054 uncertainties on identification, resolution, and trigger efficiency, as well as uncertainties on the missing  
 2055 transverse momentum .

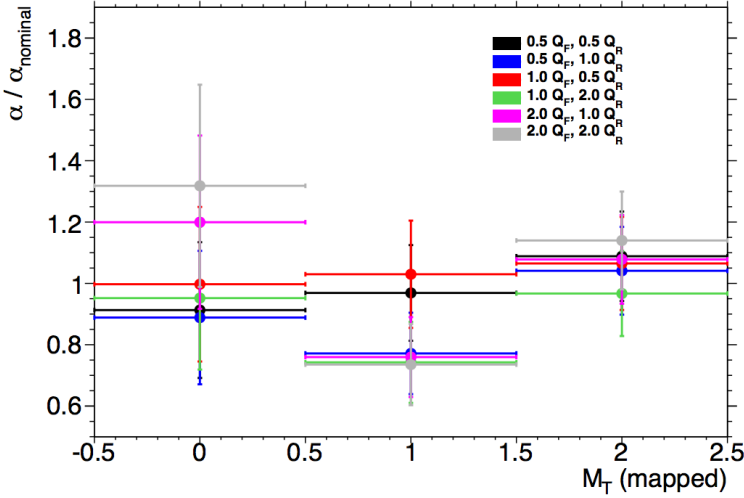


Figure 5.15: Variations in the top background extrapolation factor in the cut-based analysis due to QCD scale uncertainties, binned in  $m_T$ .

The jet energy scale uncertainty is split into several independent components, including jet-flavor dependent calorimeter response uncertainties, uncertainties on modeling of pile-up interactions, uncertainties on extrapolation from the central to forward detector regions, and MC non-closure [85]. The uncertainty on energy scale for jets used in this analysis ranges from 1% to 7% depending on the jet  $p_T$  and  $\eta$ . The jet energy resolution varies from 5% to 20%, with uncertainties ranging from 2% to 40% (the largest uncertainties occurring at the selection threshold).

The b-tagging efficiency is independently measured in data samples enriched in dileptonic decays of  $t\bar{t}$  events or in events where a muon is reconstructed in the vicinity of a jet [86, 87]. The efficiencies and their uncertainties are binned in  $p_T$  and decomposed into uncorrelated components using an eigenvector method [88]. Uncertainties on the efficiency range from 1% to 7.8%. The uncertainty on the rate of misidentification of  $c$ -jets as  $b$ -jets ranges from 6-14%, while the uncertainty on the rate of light jet mis-tagging ranges from 9-19% depending on  $p_T$  and  $\eta$ .

The total experimental uncertainties on different signal and background components are summarized in table 5.13. They are compared to the level of other statistical and systematic uncertainties as well. Overall, the experimental uncertainties are sub-dominant compared to the statistical and theoretical uncertainties.

Sample	Total error	Stat. error	Expt. syst. err.	Theo. syst. err.
$n_j \geq 2$ VBF-enriched				
$N_{\text{sig}}$	13	-	6.8	12
$N_{\text{bkg}}$	9.2	4.7	6.4	4.5
$N_{WW}$	32	-	14	28
$N_{\text{top}}$	15	9.6	7.6	8.5
$N_{\text{misid}}$	22	-	12	19
$N_{VV}$	20	-	12	15
$N_{\tau\tau}$ (DY)	40	25	31	2.9
$N_{ee/\mu\mu}$ (DY)	19	11	15	-

Table 5.13: Composition of the post-fit uncertainties (in %) on the total signal ( $N_{\text{sig}}$ ), total background ( $N_{\text{bkg}}$ ), and individual background yields in the VBF analysis [61].

## 2072 5.7 RESULTS

2073 While the combined results of all the  $H \rightarrow WW^*$  sub-analyses will be discussed in the next chapter, this  
 2074 section presents the results of the VBF specific analysis and interpretations. As table 5.7 shows, the final  
 2075 cut-based signal region contains 20 events in data with  $m_T < 150$  GeV, 14 coming from the  $e\mu$  channel  
 2076 and 6 coming from the  $ee + \mu\mu$  channel. The BDT analysis has many more candidates due to its looser  
 2077 selection, and the yields in each bin of  $O_{\text{BDT}}$  are shown in table 5.14.

2078 Figure 5.16(a) shows the final distribution of data candidates compared to the expected  $m_T$  distri-  
 2079 bution for signal and background. The data are very consistent with a VBF Higgs hypothesis. Fig-  
 2080 ure 5.16(b) shows where the data candidates fall in the two-dimensional binning of  $m_T$  and  $m_{jj}$  used  
 2081 in the fit for the cut-based analysis.

2082 Figure 5.17 shows the distributions of  $O_{\text{BDT}}$  and  $m_T$  in the VBF BDT analysis. Again the data are  
 2083 quite consistent with a VBF Higgs hypothesis.

2084 Because the cut-based result is used as a validation for the BDT analysis and the two signal regions are  
 2085 not fully orthogonal, it is interesting to explore which events overlap between the two analyses. Of the  
 2086 twenty events in the cut-based signal region, only seven were not selected by the BDT analysis, while the  
 2087 other thirteen also enter the BDT signal region. Figure 5.18 shows where the different analysis candidates  
 2088 lie in the  $m_{jj}$ - $m_T$  plane. This shows clearly that the advantage of the BDT analysis is that it can extract

(a) Before the BDT classification

Selection	Summary						Composition of $N_{\text{bkg}}$													
	$N_{\text{obs}}/N_{\text{bkg}}$	$N_{\text{bkg}}$	$N_{\text{obs}}$	$N_{\text{bkg}}$	$N_{\text{signal}}$	$N_{\text{eggF}}$	$N_{\text{VBF}}$	$N_{\text{VH}}$	$N_{WW}^{\text{SD}}$	$N_{WW}^{\text{EW}}$	$N_{t\bar{t}}$	$N_t$	$N_{Wj}$	$N_{jj}$	$N_{VV}$	$N_{\text{missid}}$	$N_{\text{Drell-Yan}}$	$N_{e/\mu}^{\text{SD}}$	$N_{e/\mu}^{\text{EW}}$	$N_{\tau\tau}^{\text{SD}}$
$e\mu$ sample	$1.04 \pm 0.04$	718	689	13	15	2.0	90	II	327	42	29	23	31	2.2	130	2				
$ee/\mu\mu$ sample	$1.18 \pm 0.08$	469	397	6.0	7.7	0.9	37	3	132	17	5.2	1.2	10.1	168	23	1				
(b) Bins in $O_{\text{BDT}}$																				
$e\mu$ sample																				
Bin 0 (not used)	$1.02 \pm 0.04$	661	650	8.8	3.0	1.9	83	9	313	40	26	21	28	2.2	126	1				
Bin 1	$0.99 \pm 0.16$	37	37	3.0	4.2	0.1	5.0	1.0	17	3.1	3.3	1.8	2.6	—	4.0	0.2				
Bin 2	$2.26 \pm 0.63$	14	6.2	1.2	4.2	—	1.5	0.5	1.8	0.3	0.4	0.3	0.8	—	0.3	0.3				
Bin 3	$5.41 \pm 2.32$	6	1.1	0.4	3.1	—	0.3	0.2	0.3	0.1	—	—	0.1	—	0.1	0.1				
$ee/\mu\mu$ sample																				
Bin 0 (not used)	$1.91 \pm 0.08$	396	345	3.8	1.3	0.8	33	2	123	16	4.1	1.1	8.8	137	20.5	0.5				
Bin 1	$0.82 \pm 0.14$	53	45	1.5	2.2	0.1	3.0	0.5	10.4	1.8	0.8	0.2	0.9	26	1.7	0.1				
Bin 2	$1.77 \pm 0.49$	14	7.9	0.6	2.5	—	0.8	0.3	1.1	0.2	0.2	—	0.3	4.4	0.3	0.1				
Bin 3	$6.32 \pm 2.87$	6	0.9	0.2	1.7	—	0.1	0.2	0.2	—	—	—	0.7	—	—	—				

Table 5.14: Event selection for the VBF BDT analysis. The event yields in (a) are shown after the pre-selection and the additional requirements applied before the BDT classification (see text). The event yields in (b) are given in bins in  $O_{\text{BDT}}$  after the classification [61].

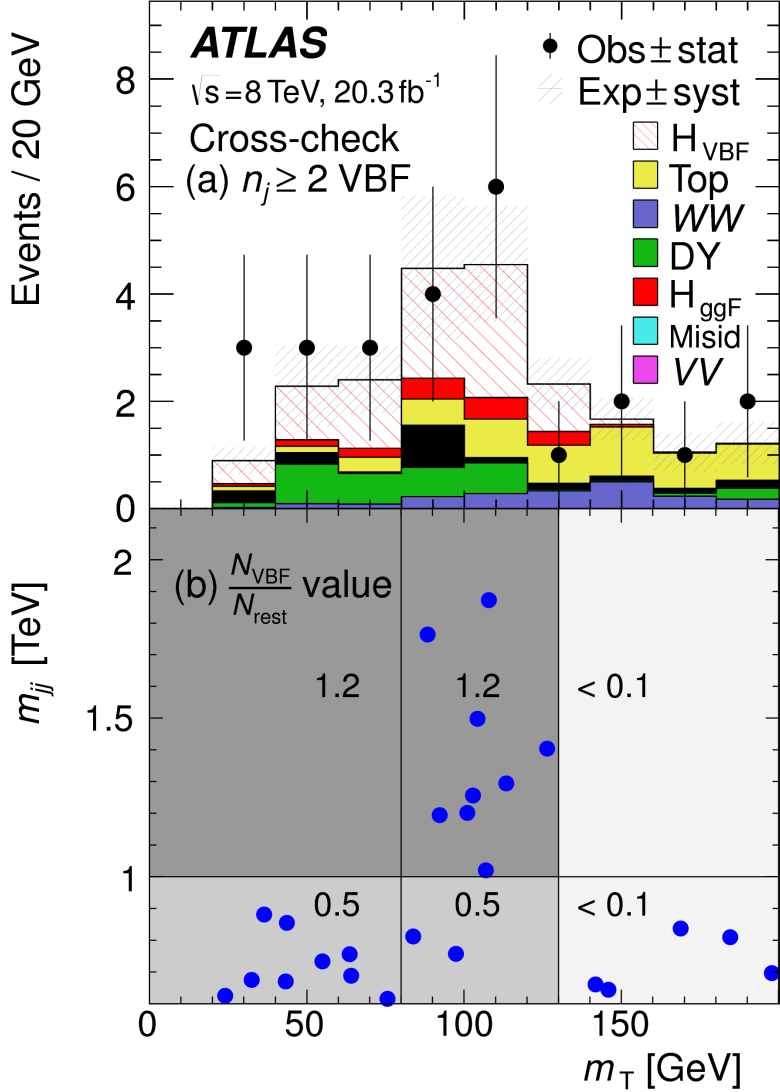


Figure 5.16: Post-fit distributions in the cut-based VBF analysis. Panel (a) shows the one-dimensional  $m_T$  distribution, while (b) shows the data candidates split into the bins of  $m_T$  and  $m_{jj}$  used in the final fit [61].

signal candidates lower  $m_{jj}$  region due to its ability to recognize correlations with other variables.  
 While the context of these results in the broader  $H \rightarrow WW^*$  statistical analysis will be presented in the next chapter, the significance of the VBF observation can be shown here. In the BDT analysis, the expected signal significance was  $2.7\sigma$ , while the observed significance was  $3.1\sigma$ . In the cut-based analysis, the expected significance was  $2.1\sigma$  and the observed significance was  $3.0\sigma$ . The compatibility between these two results can be evaluated by computing the probability of observing a larger difference

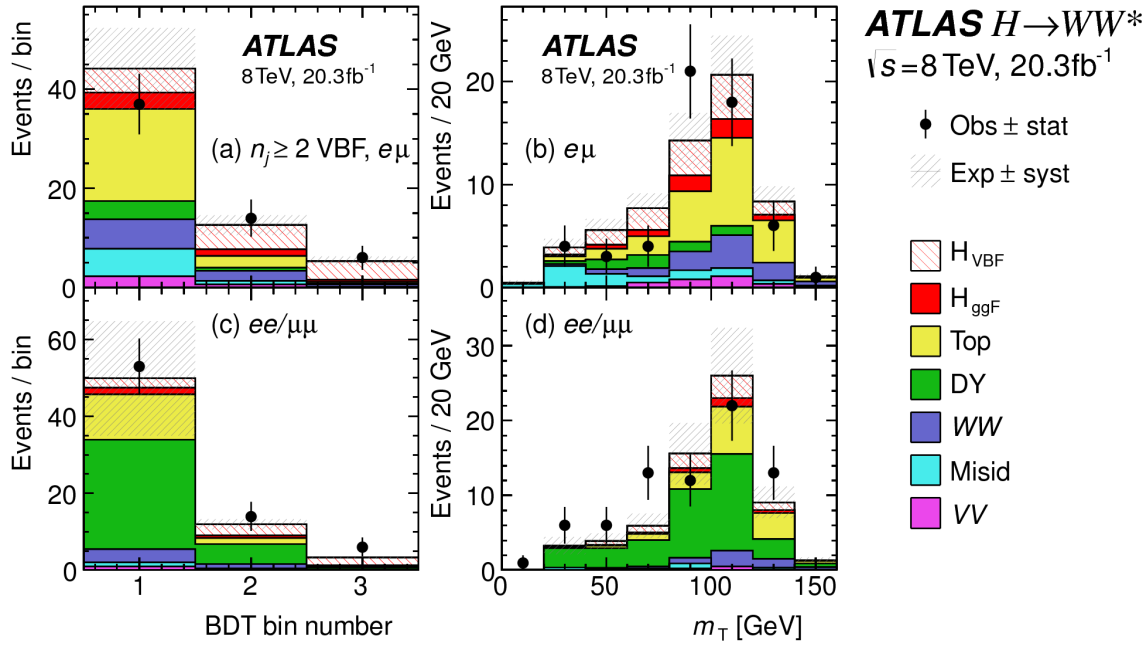


Figure 5.17: Postfit distributions in the BDT VBF analysis [61].

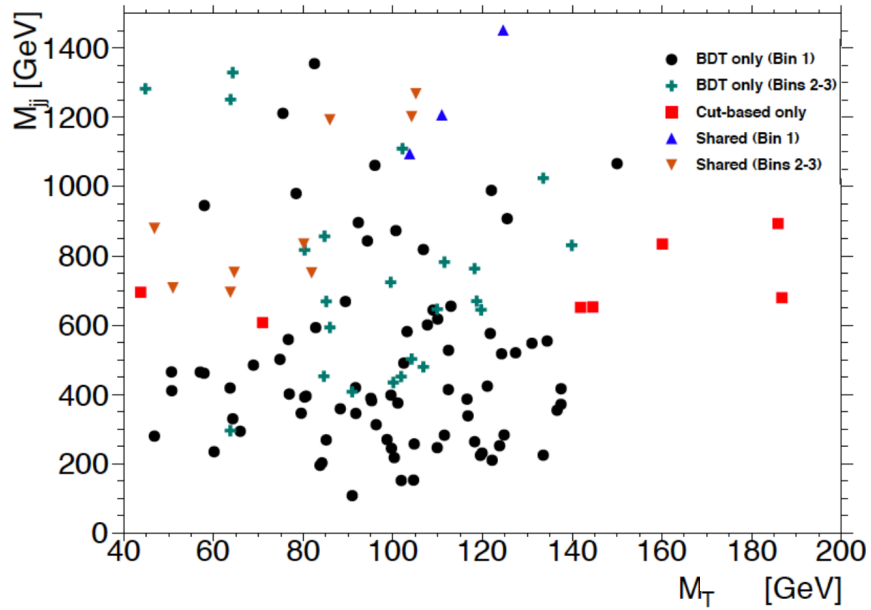


Figure 5.18: Overlap between cut-based and BDT VBF signal region candidates in the  $m_{jj}$ - $m_T$  plane.

2095 in  $Z_0$  values than the one measured. Using toy Monte Carlo with the ggF signal strength fixed to unity  
2096 and considering only statistical uncertainties, this probability is computed to be 79%, indicating good  
2097 agreement between the analyses. This result represents the first observation of the vector boson fusion  
2098 production of a Higgs boson.

*The feeling is less like an ending than just another  
starting point.*

Chuck Palahniuk

# 6

2099

2100

## Combined Run I $H \rightarrow WW^* \rightarrow \ell\nu\ell\nu$

2101

## results

2102

### 6.1 INTRODUCTION

2103

In the final statistical analysis of  $H \rightarrow WW^* \rightarrow \ell\nu\ell\nu$ , the dedicated gluon-gluon fusion and vector boson fusion sensitive signal regions are all combined into a single fit to determine the main parameters of interest, the Higgs signal strength  $\mu$  and mass  $m_H$ . Therefore, while the specific requirements applied for the VBF sensitive analysis are discussed in chapter 5, the final measurement of these parameters can only be discussed in combination with the results of the ggF dedicated analysis. For example, because ggF Higgs production is considered a background in the VBF analysis, the ggF dedicated signal regions can actually constrain the normalization of this background in the VBF dedicated region.

2104

This chapter presents the combined interpretation of results in the  $H \rightarrow WW^* \rightarrow \ell\nu\ell\nu$  analysis

SR category $i$				Fit var.	
$n_j$ , flavor	$\otimes m_{\ell\ell}$	$\otimes p_T^{\ell 2}$	$\otimes \ell_2$		
$n_j = 0$	$e\mu$	$\otimes [10, 30, 55]$	$\otimes [10, 15, 20, \infty]$	$\otimes [e, \mu]$	$m_T$
	$ee/\mu\mu$	$\otimes [12, 55]$	$\otimes [10, \infty]$		$m_T$
$n_j = 1$	$e\mu$	$\otimes [10, 30, 55]$	$\otimes [10, 15, 20, \infty]$	$\otimes [e, \mu]$	$m_T$
	$ee/\mu\mu$	$\otimes [12, 55]$	$\otimes [10, \infty]$		$m_T$
$n_j \geq 2$ ggF	$e\mu$	$\otimes [10, 55]$	$\otimes [10, \infty]$		$m_T$
$n_j \geq 2$ VBF	$e\mu$	$\otimes [10, 50]$	$\otimes [10, \infty]$		$O_{\text{BDT}}$
	$ee/\mu\mu$	$\otimes [12, 50]$	$\otimes [10, \infty]$		$O_{\text{BDT}}$

Table 6.1: All signal regions definitions input into final statistical fit [61].

for gluon fusion and vector boson fusion Higgs production. First, the results of the dedicated gluon fusion search are presented. Then, a comparison of the individual production mode signal strengths ( $\mu_{\text{ggF}}$  and  $\mu_{\text{VBF}}$  and a measurement of the combined signal strength ( $\mu$ ) are shown. Subsequently, the measured values of the Higgs couplings to fermions and vector bosons is presented. Finally, the cross section measurement for ggF and VBF production are shown.

## 6.2 RESULTS OF DEDICATION GLUON FUSION $H \rightarrow WW^* \rightarrow \ell\nu\ell\nu$ SEARCH

The details of the dedicated gluon fusion  $H \rightarrow WW^* \rightarrow \ell\nu\ell\nu$  search are not discussed in this thesis and instead left to more comprehensive sources [61]. However, a brief summary of the results are essential for describing the results of the full analysis and interpreting the results of the dedicated VBF search in this broader context.

Table 6.1 shows the individual signal regions that were input into the final statistical fit. The ggF dedicated bins use  $m_T$  as their discriminating variable and are separated into bins of  $p_T$  of the subleading lepton as well. The VBF dedicated bin uses the  $O_{\text{BDT}}$  distribution as its final discriminant.

Table 6.2 shows the yields in the various signal regions in both data and expected signal and back-

2125 grounds. The yields for signal and background are all scaled according to the final normalizations calcu-  
2126 lated in the fit.

	$N_{\text{obs}}$	$N_{\text{bkg}}$	$N_{\text{ggF}}$	$N_{\text{VBF}}$
$n_j = 0$	3750	$3430 \pm 90$	$300 \pm 50$	$8 \pm 4$
$n_j = 1$	1596	$1470 \pm 40$	$102 \pm 26$	$17 \pm 5$
$n_j \geq 2, \text{ggF } e\mu$	1017	$960 \pm 40$	$37 \pm 11$	$13 \pm 1.4$
$n_j \geq 2, \text{VBF}$	130	$99 \pm 9$	$7.7 \pm 2.6$	$21 \pm 3$

Table 6.2: Post-fit yields in the different ggF and VBF dedicated signal regions [61].

2127 Figure 6.1 shows the final post-fit  $m_T$  distribution in the  $n_j \leq 1$  regions. The data are very consistent  
with the hypothesis of ggF Higgs production. These yields are used as input, along with the VBF results

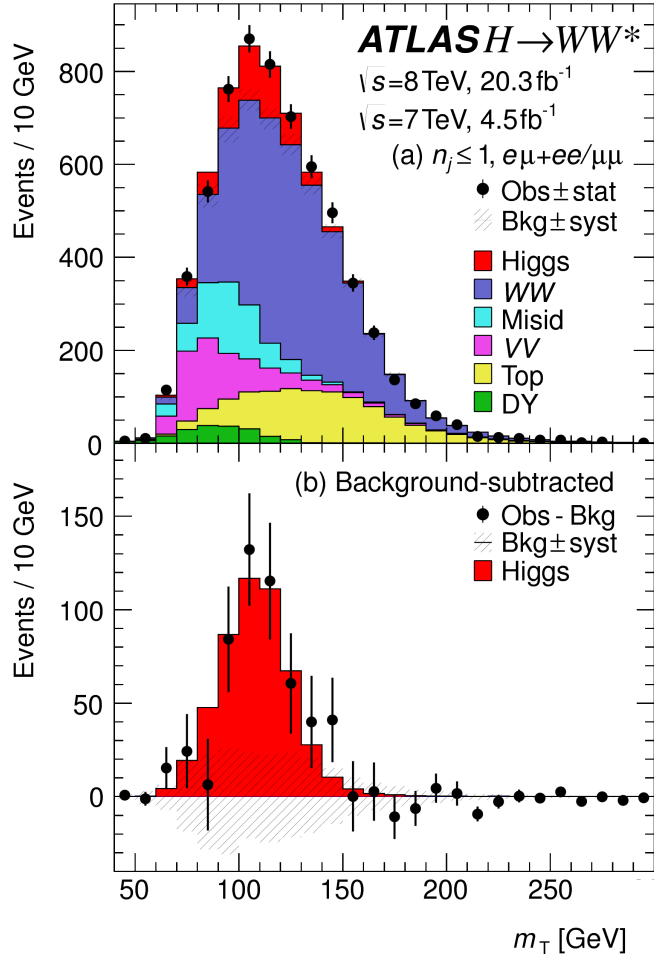


Figure 6.1: Post-fit  $m_T$  distribution in the  $n_j \leq 1$  regions [61].

2128

2129 in chapter 5, for the physical interpretation of results presented in subsequent sections.

2130 **6.3 SIGNAL STRENGTH MEASUREMENTS IN ggF AND VBF PRODUCTION**

2131 When all of the signal regions are combined in the fit, there can be a combined measurement of the sig-  
 2132 nal strength as well as the individual ggF and VBF signal strengths. The combined signal strength is the  
 2133 ratio of the sum of the gluon fusion and VBF cross sections to the theory prediction, or a signal strength  
 2134 for the total Higgs production cross section that this analysis is sensitive to. The final measured com-  
 2135 bined signal strength  $\mu$  is measured shown in equation 6.1.

$$\begin{aligned} \mu &= 1.09 \quad {}^{+0.16}_{-0.15} \text{ (stat.)} \quad {}^{+0.08}_{-0.07} \left( \text{expt syst} \right) \quad {}^{+0.15}_{-0.12} \left( \text{theo syst} \right) \quad \pm 0.03 \left( \text{lumi syst} \right) \\ &= 1.09 \quad {}^{+0.16}_{-0.15} \text{ (stat)} \quad {}^{+0.17}_{-0.14} \text{ (syst)} \\ &= 1.09 \quad {}^{+0.23}_{-0.21}. \end{aligned} \tag{6.1}$$

2136 Figure 6.2 gives the best fit signal strength  $\hat{\mu}$  as a function of the hypothesized Higgs mass. The value  
 2137 at 125.36 GeV corresponds to the  $\mu$  quoted in equation 6.1. This value of the Higgs mass is used because  
 2138 it is the most precise mass measurement from ATLAS, a result of the combined  $\gamma\gamma$  and  $ZZ$  mass mea-  
 2139 surements [89].

2140 As explained in chapter 3, a probability  $p_0$  can be computed using the test statistic  $q_0$  to quantify the  
 2141 probability that the background could fluctuate to produce an excess at least as large as the one observed  
 2142 in the data. The local  $p_0$  value is shown in figure 6.3 as a function of  $m_H$ . The minimum  $p_0$  value is  
 2143 at  $m_H = 130$  GeV and corresponds to a significance of  $6.1\sigma$ . The curve is relatively flat and the sig-  
 2144 nificance is the same at 125.36 GeV within the quoted precision. The expected significance for a signal  
 2145 with strength  $\mu = 1.0$  is  $5.8\sigma$ . This represents the first discovery level significance measurement in the  
 2146  $H \rightarrow WW^* \rightarrow \ell\nu\ell\nu$  analysis.

2147 All the results presented so far in this section have been for the combined gluon fusion and VBF pro-  
 2148 duction modes. However, each signal strength can be calculated separately in the likelihood as well.  
 2149 There are two ways to do this. First, the likelihood can be parameterized in terms of a single parameter,

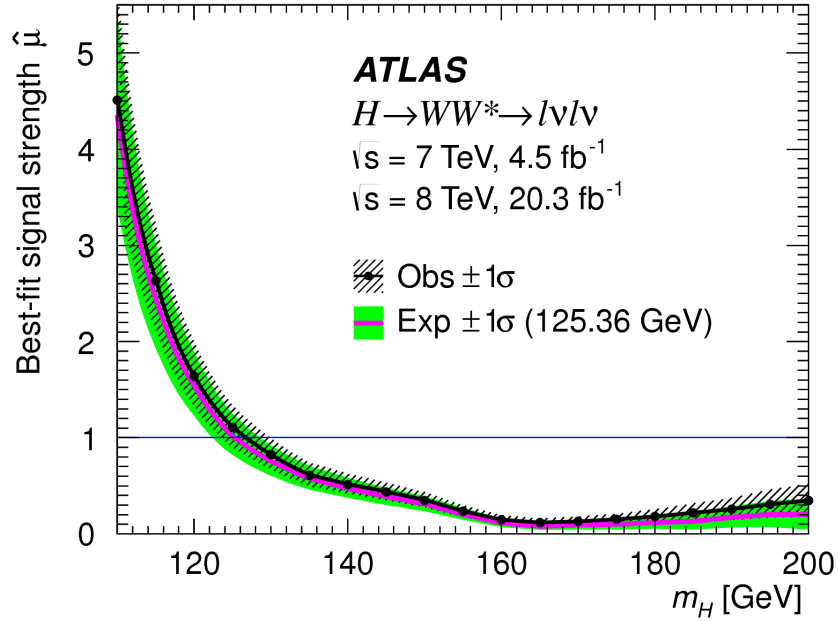


Figure 6.2: Best fit signal strength  $\hat{\mu}$  as a function of hypothesized  $m_H$  [61].

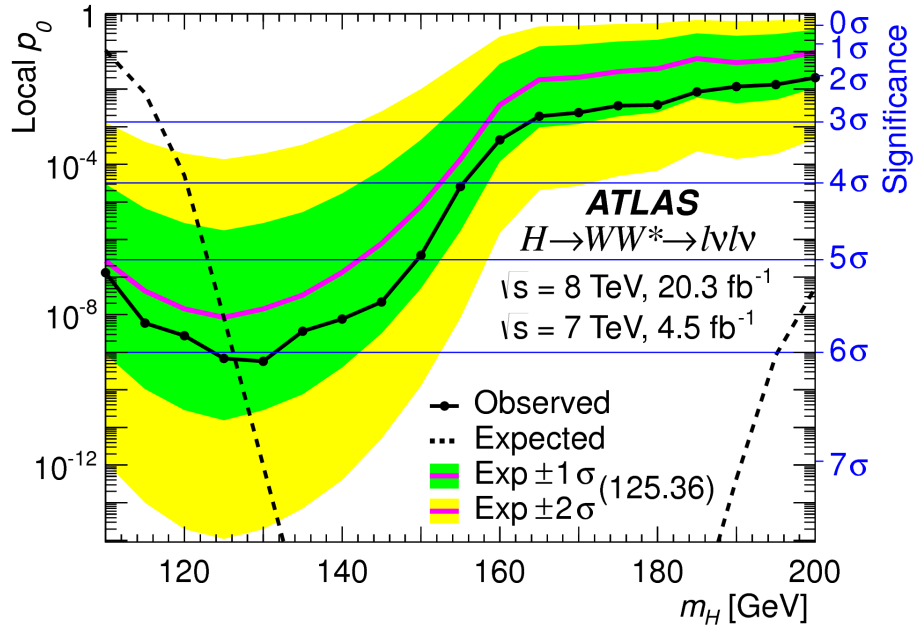


Figure 6.3: Local  $p_0$  as a function of  $m_H$  [61].

the ratio of the VBF and gluon fusion signal strengths. With this method, the significance of the VBF observation can be evaluated. Figure 6.4 shows the likelihood as a function of the ratio  $\mu_{\text{VBF}}/\mu_{\text{ggF}}$ .

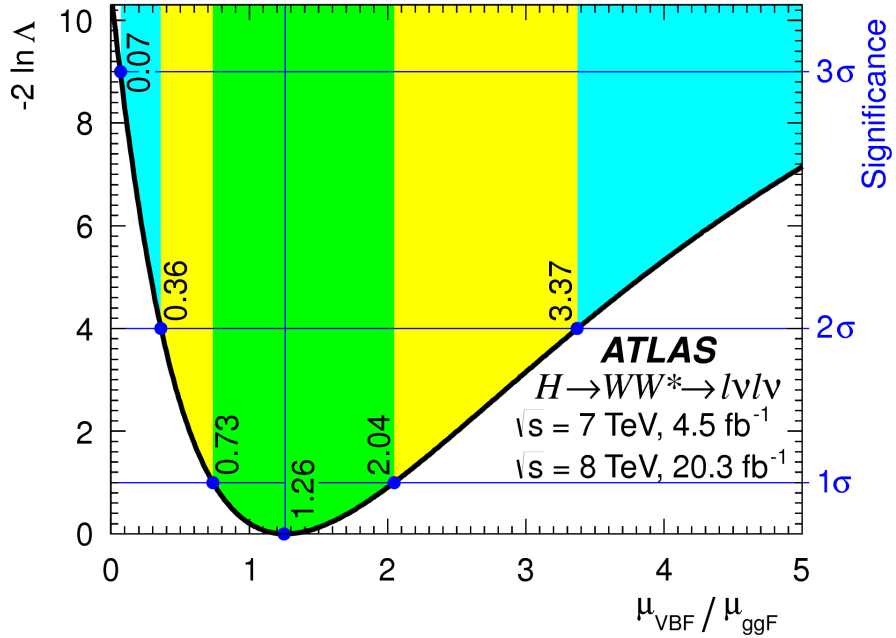


Figure 6.4: Likelihood as a function of  $\mu_{\text{VBF}} / \mu_{\text{ggF}}$  [61].

2152     The best fit value of the ratio of signal strengths is shown in equation 6.2. Within the quoted uncer-  
 2153     tainties, it is consistent with a ratio of unity.

$$\frac{\mu_{\text{VBF}}}{\mu_{\text{ggF}}} = 1.26^{+0.61}_{-0.45} (\text{stat.})^{+0.50}_{-0.26} (\text{syst.}) = 1.26^{+0.79}_{-0.53} \quad (6.2)$$

2154     The null hypothesis for VBF production corresponds to a ratio of  $\mu_{\text{VBF}} / \mu_{\text{ggF}} = 0$ . The likelihood in  
 2155     figure 6.4 gives a significance of  $3.2\sigma$  at  $\mu_{\text{VBF}} / \mu_{\text{ggF}} = 0$ , as quoted in chapter 5.

2156     In addition to the ratio of signal strengths, each signal strength can be varied independently in the  
 2157     likelihood as well. Figure 6.5 shows the two dimensional likelihood scan in the  $\mu_{\text{ggF}}-\mu_{\text{VBF}}$  plane. The  
 2158     best fit values of the two signal strengths are shown in equation 6.3. Both are consistent with unity  
 2159     within their uncertainties.

$$\begin{aligned} \mu_{\text{ggF}} &= 1.02 \pm 0.19^{+0.22}_{-0.18} = 1.02^{+0.29}_{-0.26} \\ \mu_{\text{VBF}} &= 1.27 \pm 0.40^{+0.44}_{-0.21} = 1.27^{+0.53}_{-0.45}. \end{aligned} \quad (6.3)$$

(stat.) (syst.)

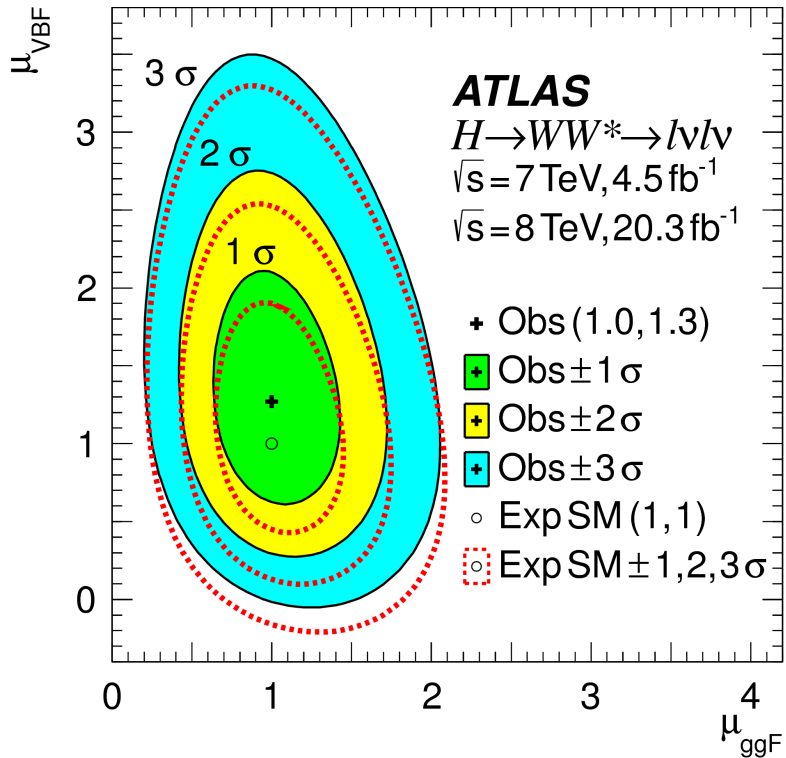


Figure 6.5: Likelihood scan as a function of  $\mu_{\text{VBF}}$  and  $\mu_{\text{ggF}}$  [61].

## 2160 6.4 MEASUREMENT OF HIGGS COUPLINGS TO VECTOR BOSONS AND FERMIONS

2161 Similar to the parameterization of signal strength, the couplings of the Higgs to fermions and bosons can  
 2162 also be parameterized. The parameter of interest in this case is  $\kappa$ , or the ratio of the measured coupling  
 2163 to the standard model expectation. Both the fermion and boson couplings have these so-called scale fac-  
 2164 tors,  $\kappa_F$  for fermions and  $\kappa_V$  for bosons. Gluon fusion production is sensitive to the fermion couplings  
 2165 through the top quark loops in its production, while VBF production is sensitive to the vector boson  
 2166 couplings in its production. Both modes are sensitive to the vector boson couplings in their decays. The  
 2167 signal strengths will have dependence on the coupling scale factors as described in equation 6.4 [18].

$$\begin{aligned}\mu_{\text{ggF}} &\propto \frac{\kappa_F^2 \cdot \kappa_V^2}{(\mathcal{B}_{H \rightarrow f\bar{f}} + \mathcal{B}_{H \rightarrow gg}) \kappa_F^2 + (\mathcal{B}_{H \rightarrow VV}) \kappa_V^2} \\ \mu_{\text{VBF}} &\propto \frac{\kappa_V^4}{(\mathcal{B}_{H \rightarrow f\bar{f}} + \mathcal{B}_{H \rightarrow gg}) \kappa_F^2 + (\mathcal{B}_{H \rightarrow VV}) \kappa_V^2}.\end{aligned}\quad (6.4)$$

<sup>2168</sup> Figure 6.6 shows the two-dimensional likelihood scan of  $\kappa_F$  and  $\kappa_V$ . The best-fit values are given in  
<sup>2169</sup> equation 6.5. The best-fit values are consistent with unity within their uncertainties.

$$\begin{aligned} \kappa_F &= 0.93 & +0.24 & +0.21 & = 0.93 & +0.32 \\ \kappa_V &= 1.04 & +0.07 & +0.07 & = 1.04 & \pm 0.11. \end{aligned} \quad (6.5)$$

(stat.) (syst.)

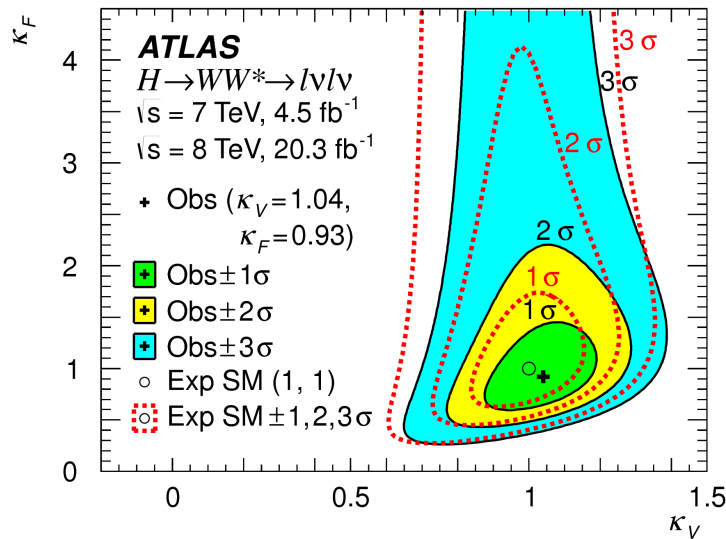


Figure 6.6: Likelihood scan as a function of  $\kappa_F$  and  $\kappa_V$  [61].

<sup>2170</sup>

## <sup>2171</sup> 6.5 HIGGS PRODUCTION CROSS SECTION MEASUREMENT

<sup>2172</sup> Another measurement that comes naturally from the signal strength numbers quoted earlier is the pro-  
<sup>2173</sup> duction cross section and 7 and 8 TeV for both gluon fusion and VBF production. The general equa-  
<sup>2174</sup> tion for calculating the cross section is given in equation 6.6.

$$\begin{aligned} (\sigma \cdot \mathcal{B}_{H \rightarrow WW^*})_{\text{obs}} &= \frac{(N_{\text{sig}})_{\text{obs}}}{\mathcal{A} \cdot \mathcal{C} \cdot \mathcal{B}_{WW \rightarrow \ell\nu\ell\nu}} \cdot \frac{1}{\int L dt} \\ &= \hat{\mu} \cdot (\sigma \cdot \mathcal{B}_{H \rightarrow WW^*})_{\text{exp}} \end{aligned} \quad (6.6)$$

2175  $(N_{\text{sig}})_{\text{obs}}$  is the number of events observed in data.  $\mathcal{A}$  is the geometric and kinematic acceptance of the  
 2176 detector, while  $\mathcal{C}$  is the efficiency of the signal region selection for events that are reconstructed in the  
 2177 detector. The branching ratio of a  $WW$  system to leptons must also be divided out. The production  
 2178 cross section depends on the center of mass energy and the production mode desired (gluon fusion or  
 2179 VBF), and so three separate cross section measurements are quoted in equation 6.7.

$$\begin{aligned}
 \sigma_{\text{ggf}}^{\text{7TeV}} \cdot \mathcal{B}_{H \rightarrow WW^*} &= 2.0 \pm 1.7 \quad {}^{+1.2}_{-1.1} = 2.0 \quad {}^{+2.1}_{-2.0} \text{ pb} \\
 \sigma_{\text{ggf}}^{\text{8TeV}} \cdot \mathcal{B}_{H \rightarrow WW^*} &= 4.6 \pm 0.9 \quad {}^{+0.8}_{-0.7} = 4.6 \quad {}^{+1.2}_{-1.1} \text{ pb} \\
 \sigma_{\text{vbf}}^{\text{8TeV}} \cdot \mathcal{B}_{H \rightarrow WW^*} &= 0.51 \quad {}^{+0.17}_{-0.15} \quad {}^{+0.13}_{-0.08} = 0.51 \quad {}^{+0.22}_{-0.17} \text{ pb.}
 \end{aligned} \tag{6.7}$$

(stat.) (syst.)

2180 The predicted cross section values for gluon fusion are  $3.3 \pm 0.4$  pb at 7 TeV and  $4.2 \pm 0.5$  pb at 8 TeV,  
 2181 consistent with the measured values within their uncertainties. For vector boson fusion, the predicted  
 2182 cross section is  $0.35 \pm 0.02$  pb, again consistent with the measured value.

## 2183 6.6 CONCLUSION

2184 The combined analysis of the gluon fusion and vector boson fusion processes in  $H \rightarrow WW^* \rightarrow \ell\nu\ell\nu$   
 2185 in the 7 and 8 TeV datasets has yielded the first discovery level significance for Higgs production in this  
 2186 decay channel. Additionally, precise measurements of the couplings to vector bosons and fermions are  
 2187 given. Finally, signal strengths and cross sections for each production mode are measured. Figure 6.7  
 2188 shows the  $H \rightarrow WW^* \rightarrow \ell\nu\ell\nu$  measurements in comparison with other Higgs decay channels in  
 2189 ATLAS. The measurement of signal strength from this channel remains the most sensitive in both the  
 2190 gluon fusion and VBF production modes for the Run 1 dataset.

**ATLAS**

### Individual analysis

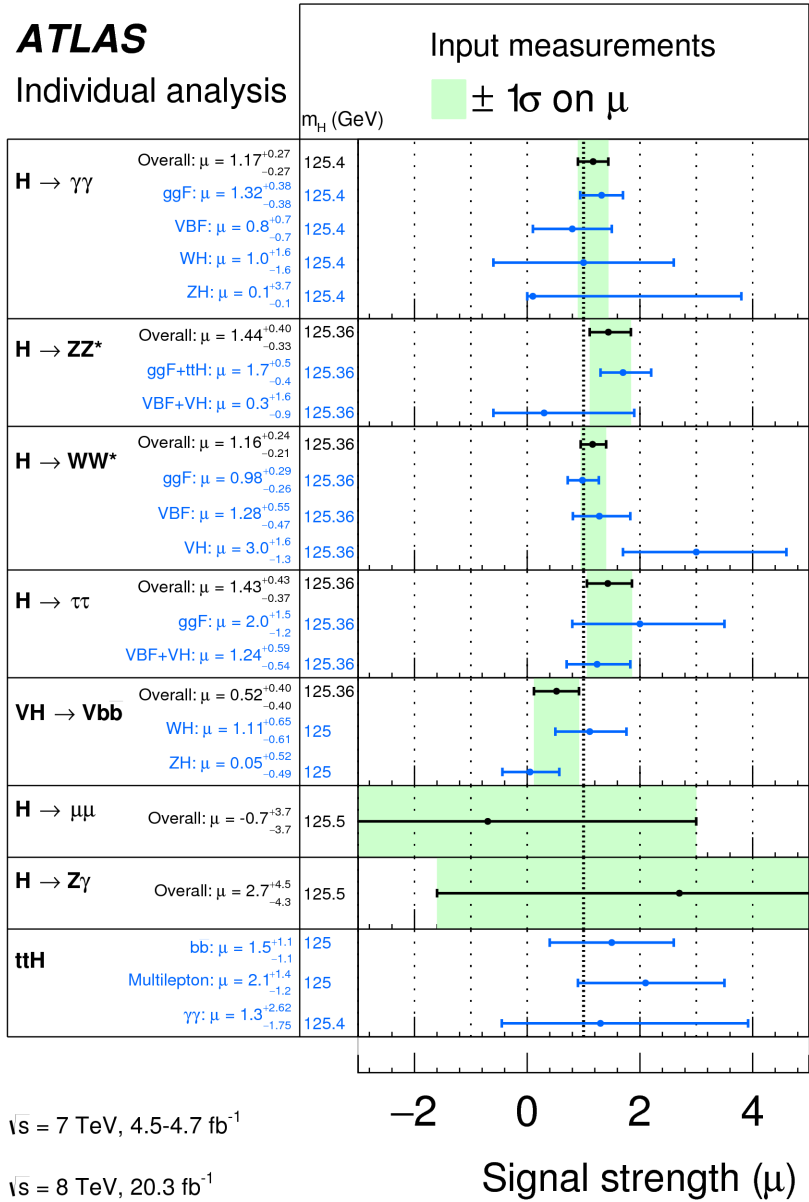


Figure 6.7: Comparison of signal strength measurements in different Higgs decay channels on ATLAS [90].

2191

## Part III

2192

Search for Higgs pair production in the

2193

$HH \rightarrow b\bar{b}b\bar{b}$  channel in LHC Run 2 at  $\sqrt{s} =$

2194

13 TeV

*Passion is in all great searches and is necessary to all creative endeavors.*

W. Eugene Smith

# 7

2195

## 2196 Search for Higgs pair production in boosted 2197 $b\bar{b}b\bar{b}$ final states

### 2198 7.1 INTRODUCTION

2199 After the discovery of the Higgs boson in the ATLAS Run 1 dataset and the subsequent measurements  
2200 of its properties, the Higgs transformed into a potential tool in searches for physics beyond the Stan-  
2201 dard Model. The pair production cross section of the Higgs can be enhanced through BSM physics.  
2202 Studying di-Higgs production also probes the Higgs self-coupling, shedding light on the structure  
2203 of the Higgs potential. This chapter presents a search for resonant production of a Higgs pair in the  
2204  $X \rightarrow HH \rightarrow b\bar{b}b\bar{b}$  final state in  $3.2 \text{ fb}^{-1}$  of data collected at  $\sqrt{s} = 13 \text{ TeV}$ . In particular, this  
2205 chapter focuses on a search for this final state in the regime where  $m_X$  is large ( $\gtrsim 1 \text{ TeV}$ ) and the Higgs  
2206 bosons in the decay are significantly boosted. A tailored selection for this boosted selection, using novel

2207 techniques in jet substructure and  $b$ -tagging, is discussed. Then, the data-driven background estimate is  
 2208 presented. Finally, the results of the search are shown. The signal models used as benchmarks are a spin-  
 2209 2 Randall Sundrum graviton (RSG) and a narrow width spin-0 resonance. These models are described  
 2210 in more detail in Chapter 1. Limits on signal models are reserved for the next chapter where the results of  
 2211 this chapter are combined with the results of a separate selection dedicated to the lower  $m_X$  regime.

## 2212 7.2 MOTIVATION

2213 With the center of mass energy increase from  $\sqrt{s} = 8$  TeV to  $\sqrt{s} = 13$  TeV, the LHC and ATLAS  
 2214 are able to probe new resonances at higher mass scales than previously accessible in Run 1. This is a  
 2215 powerful motivator for searching for a new resonance in the early 13 TeV data. Figure 7.1 shows the  
 2216 ratios of parton luminosities between 8 and 13 TeV for different resonance masses. For a resonance of  
 2217  $M_X = 2$  TeV, the cross section at  $\sqrt{s} = 13$  TeV is roughly a factor of 10 larger than at  $\sqrt{s} = 8$  TeV.

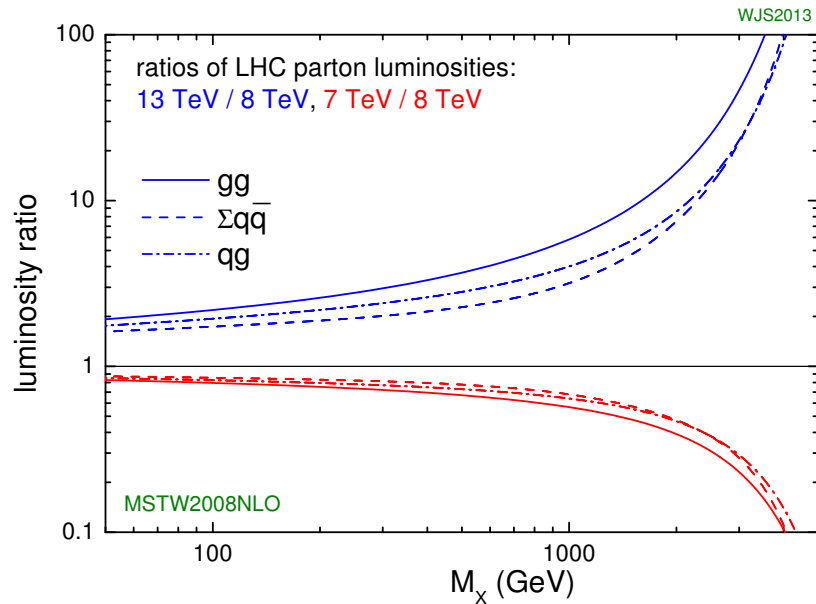


Figure 7.1: Parton luminosity ratios as a function of resonance mass  $M_X$  for 13/8 TeV and 7/8 TeV [91].

2218 Higgs pair production offers a vast array of unprobed regions of phase space where searches for BSM  
 2219 physics can be made. Chapter 1 discusses some possibilities for both resonant and non-resonant enhance-

ment of the di-Higgs production cross section. Given the increased mass reach of the LHC in Run 2, it is particularly important to focus on resonant searches at high  $m_X$ . One consideration when conducting a search in the  $HH$  final state is which decay modes of the Higgs to consider. Figure 7.2 shows the branching ratio of the  $HH$  final state for different combinations of decays of each individual Higgs. As the largest branching ratio for the 125 GeV Higgs is  $H \rightarrow b\bar{b}$ , the  $HH \rightarrow b\bar{b}b\bar{b}$  branching ratio is also the largest at 33%.

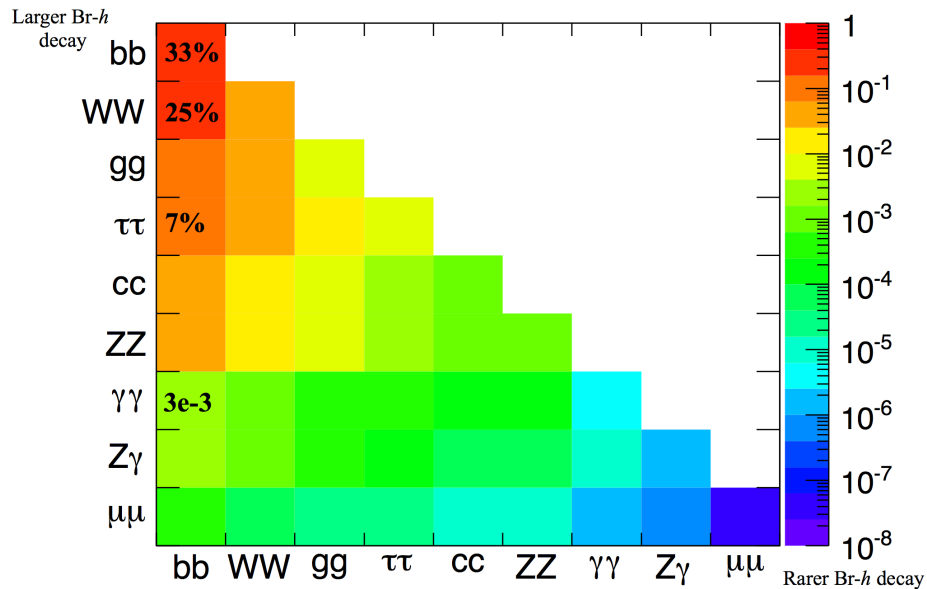


Figure 7.2: Summary of  $HH$  branching ratios [92].

At high  $m_X$ , the Higgs bosons resulting from the decay of a heavy resonance will have large  $p_T^*$ . The  $\Delta R$  between the decay products of the Higgs is inversely proportional to the Higgs  $p_T$ , as shown in equation 7.1.

$$\Delta R \approx \frac{2m}{p_T} \quad (7.1)$$

Figure 7.3 shows the minimum  $\Delta R$  between truth level  $B$  decay vertices in simulation samples for Randall-Sundrum gravitons of different masses. The figure shows that as the mass of the graviton increases, the  $\Delta R$  distribution between the  $b$  quarks in the Higgs decay tends to shift to lower values. Because of this effect, it is necessary to tailor a selection to target these merged  $b$ -jets.

\*In the limit that  $m_H \ell \ell m_X$ , the Higgs  $p_T$  is roughly  $m_X/2$ .

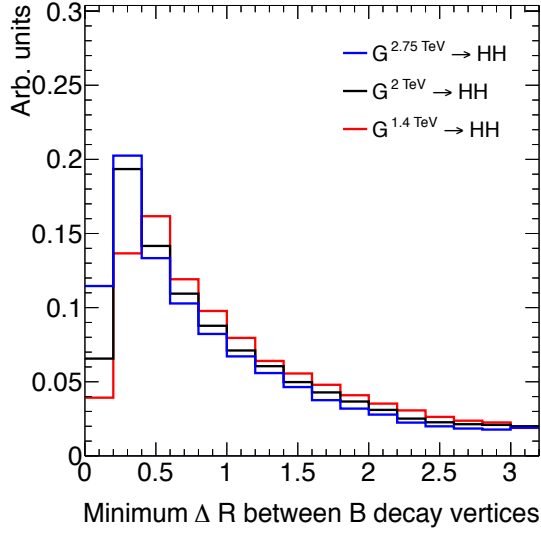


Figure 7.3: Minimum  $\Delta R$  between  $B$  decay vertices for different RSG masses in a  $G_{KK}^* \rightarrow HH \rightarrow 4b$  sample with  $c = 1$

2233 7.3 DATA AND SIMULATION SAMPLES

2234 7.3.1 SIGNAL MODELS

2235 While the resonance search is by its nature generic (as it is a simple search for a peak in the  $4b$  invariant  
 2236 mass spectrum), there are two signal models that the selection requirements have been optimized for.  
 2237 The first is Randall-Sundrum (RSG) model, where a tower of massive spin-2 Kaluza-Klein gravitons  
 2238 is predicted. The second is a heavy narrow spin-0 resonance, the so-called “heavy Higgs”. This type of  
 2239 resonance arises, for example, in the two Higgs doublet model (2HDM). More details about the physics  
 2240 of these models and their motivation is given in chapter 1.

2241 Signal graviton ( $G_{KK}^*$ ) events are generated at leading order (LO) with **MADGRAPH5 v2.2.2** [93].  
 2242 The PDF set used is the **NNPDF2.3 LO** set [94]. For modeling parton shower and hadronization in jets,  
 2243 **PYTHIA 8.186** is used with the A14 tune [73, 95]. The free parameters in the RSG model are the graviton mass and the coupling constant  $c \equiv k/\bar{M}_{\text{Pl}}$ <sup>†</sup>. Both the production cross section and width of the graviton are proportional to  $c^2$ . Samples are generated at both  $c = 1$  and  $c = 2$  for a variety of mass

---

<sup>†</sup> $k$  is the curvature constant for the warped extra dimension and  $\bar{M}_{\text{Pl}}$  is the Planck mass divided by  $8\pi$

2246 points between 300 GeV and 3 TeV.

2247 The second signal sample is a heavy spin-0 resonance  $H$  with a fixed width of  $\Gamma_H = 1$  GeV. This  
2248 is generated with **MADGRAPH5** and uses the **CT10** PDF set [76]. The parton shower and hadronization  
2249 are handled by **HERWIG ++** with the **CTEQ6L1** PDF set and the **UEEE5** event tune [77, 96, 97]. Because  
2250 the width and branching ratios depend on 2HDM parameters, each mass point generated with this fixed  
2251 width corresponds to a different point in the 2HDM parameter phase space. Mass points are generated  
2252 between 300 GeV and 1 TeV as with the RSG signal samples.

### 2253 7.3.2 BACKGROUND SAMPLES

2254 While the dominant **QCD** multijet background is estimated with a fully data-driven method, the sub-  
2255 dominant backgrounds  $t\bar{t}$  and  $Z$ +jets are modeled with some input from simulation.

2256  $t\bar{t}$  events are simulated at next-to-leading order (NLO) with the **POWHEG-BOX** version 1 generator us-  
2257 ing the **CT10** PDF set [98]. The parton shower, hadronization, and underlying event are simulated with  
2258 **PYTHIA 6.428** with the **CTEQ6L1** PDF set [72]. The Perugia 2012 tune is used [99]. NNLO QCD cor-  
2259 rections to the cross sections are computed in **Top++ 2.0** [100]. The top quark mass is set to 172.5 GeV.  
2260 The shapes of distributions in  $t\bar{t}$  are taken from MC while the normalization is taken from data.

2261 Finally, the  $Z$ +jets background is simulated with **PYTHIA 8.186** and the **NNPDF2.3** LO PDF set. This  
2262 background is negligible compared to the others and is taken fully from MC.

### 2263 7.3.3 DATA SAMPLE AND TRIGGER

2264 This analysis is done on  $3.2 \text{ fb}^{-1}$  of data taken in 2015 at  $\sqrt{s} = 13$  TeV. The details of the machine  
2265 conditions during this time can be found in Chapter 2. Only data which was taken during stable beam  
2266 conditions with all detectors functioning is used. Events must pass a trigger which requires a single  
2267 360 GeV large radius ( $R = 1.0$ ) jet to be reconstructed in the HLT. Figure 7.4 shows the trigger effi-  
2268 ciency for various trigger options as a function of graviton mass. Above  $m_G > 1$  TeV, the single large  
2269 radius jet trigger is 99% efficient for events passing the signal selection.

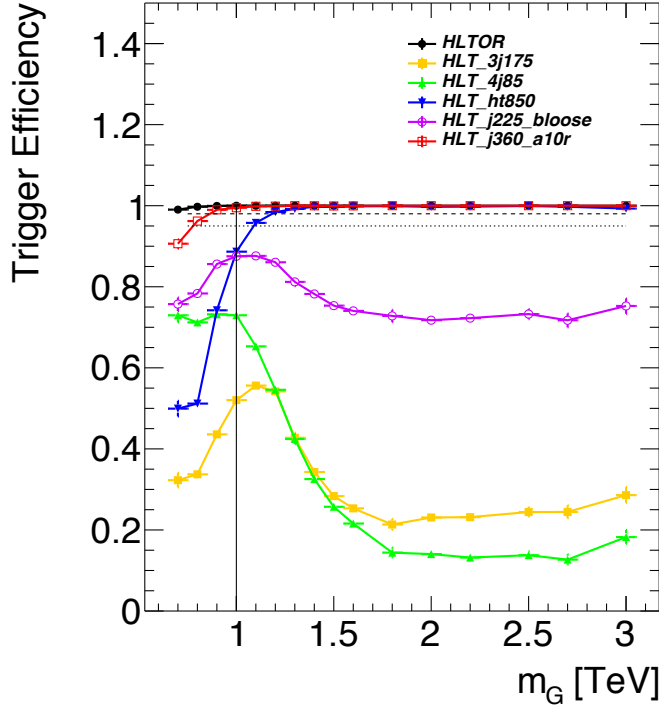


Figure 7.4: Trigger efficiency for events passing all signal region selections as a function of mass in  $G_{KK}^* \rightarrow HH \rightarrow 4b$  samples with  $c = 1$  [101]. In the trigger names, “ $j$ ” refers to a jet or jets. “ht” refers to  $H_T$ , the scalar sum of transverse momenta in the event. “bloose” refers to a loose  $b$ -tagging requirement applied to the jet. “a10r” refers to anti- $k_T$  jets with  $R = 1.0$ . The numbers at the end are the thresholds on the given quantity in GeV.

## 2270 7.4 EVENT RECONSTRUCTION AND OBJECT SELECTION

2271 The boosted selection first begins by defining a unique set of objects that can be exploited to increase  
 2272 signal efficiency in the kinematic regime where the final state  $b$ -jets are very merged.

### 2273 7.4.1 LARGE RADIUS ( $R = 1.0$ ) JETS

2274 The first step towards reconstructing the final state is to define objects that can be used to measure the  
 2275 kinematics of the Higgs bosons. In the boosted selection anti- $k_T$  jets with a radius parameter of 1.0  
 2276 are used. These jets are much larger in angular size than the typical  $R = 0.4$  jets and are intended to  
 2277 encompass both jets resulting from the Higgs decay<sup>‡</sup>. The jets are built from clusters in the calorimeter

<sup>‡</sup>This is in contrast to the resolved selection, which uses two  $R = 0.4$  anti- $k_T$  jets for each Higgs

2278 calibrated with local calibration weighting [56].

2279 Because of the large extent of these jets, great care must be taken to remove potential contributions of  
2280 calorimeter clusters from pile-up. This is done using a technique called jet trimming [102]. With trim-  
2281 ming, the constituents of the large radius jet are re-clustered with a smaller radius with the  $k_T$  algorithm.  
2282 Then, these so-called subjets are removed from the larger jet if  $p_T^{\text{subjet}}/p_T^{\text{jet}} < f_{\text{cut}}$ . In this analysis, the  
2283 subjet radius is  $R = 0.2$  and  $f_{\text{cut}} = 0.05$ . Trimming has been shown to improve the mass resolution  
2284 of large radius jets. Figure 7.5 shows the effect of trimming on the large radius jet mass ( $M_J$ ). Because  
2285 the large radius jet fully contains the higgs decay products, its invariant mass should correspond to the  
2286 125 GeV mass of the Higgs. The trimming algorithm brings the jet mass much closer to the expected  
2287 Higgs mass and improves the mass resolution.

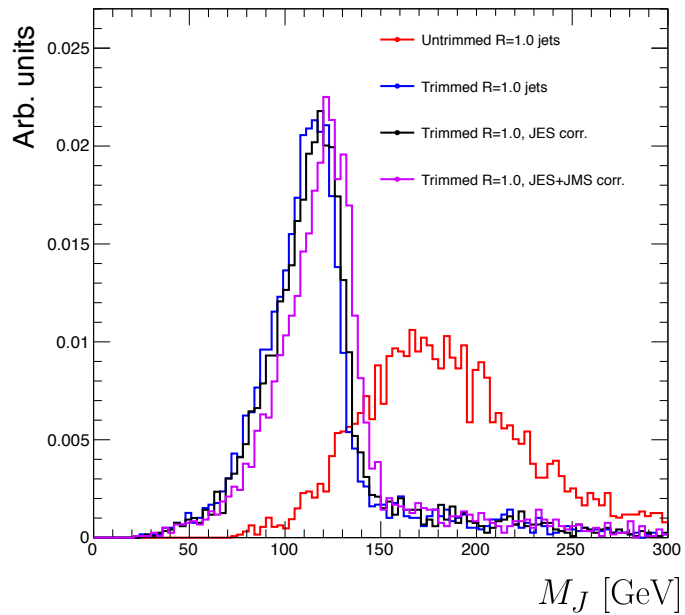


Figure 7.5: Comparison of untrimmed and trimmed jet masses for large radius jets in a RSG sample with  $m_{G_{KK}^*} = 1 \text{ TeV}$ . JES (JMS) refers to the standard jet energy (mass) scale calibration for ATLAS [56].

2288 The large radius jets are required to satisfy  $250 < p_T < 1500 \text{ GeV}$ . They must also be within  
2289  $|\eta| < 2.0$  in order to ensure that the full jet is within the inner detector tracking volume. Finally, they  
2290 are required to have  $M_J > 50 \text{ GeV}$ . The upper  $p_T$  cut and lower threshold on mass are applied to  
2291 correspond to the kinematic range where uncertainties are available in ATLAS calibrations [103, 104].

2292 7.4.2 TRACK JETS AND  $b$ -TAGGING

2293 Because the  $b$ -jets from boosted Higgs decays are so close together (as illustrated in figure 7.3), narrow  
2294 radius jets are required to fully resolve both  $b$ -jets. The minimum radius feasible for jets based on calorime-  
2295 ter deposits is determined by the calorimeter granularity. However, because  $b$ -tagging relies on informa-  
2296 tion from the inner detector, it is possible to define another type of jet that can have a smaller radius and  
2297 better  $b$ -tagging resolution. These jets are called “track jets” [104, 105].

2298 Track jets are formed by applying the usual anti- $k_T$  clustering algorithm to tracks that are required  
2299 to be consistent with the primary vertex. After the jet axis has been determined using these tracks, a sec-  
2300 ond step of track association is also performed to add tracks that can be useful for  $b$ -tagging [105]. In this  
2301 analysis, the tracks are clustered with a radius parameter of  $R = 0.2$ . This radius has been shown to  
2302 give good performance in boosted Higgs tagging [104, 105]. Figure 7.6 shows a comparison among dif-  
2303 ferent track jet radii of the efficiency for reconstructing two  $b$ -jets from each Higgs in a RSG sample as a  
function of mass. Track jets with radius of 0.2 give the best performance, especially at high mass. In this

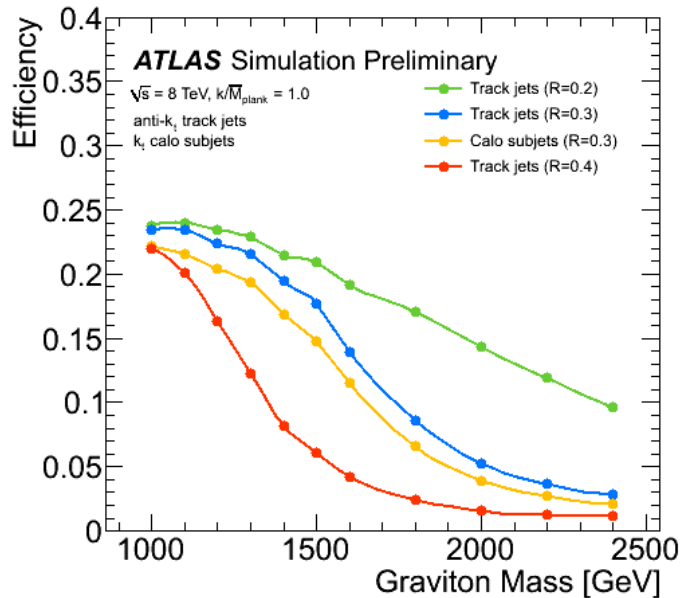


Figure 7.6: Efficiency of finding two  $b$ -jets from each Higgs in an RSG event using calorimeter jets with  $R = 0.3$  or different track jet radii [105]

2305 analysis, track jets are required to have  $p_T > 10$  GeV and  $|\eta| < 2.5$ . They must also have at least two  
2306 tracks.

### 2307 7.4.3 MUONS

2308 Muons are used in this study to correct the four-momenta of calorimeter jets by accounting for semi-  
2309 leptonic  $b$  decays. The muons used are combined ID and MS muons which must satisfy tight identifica-  
2310 tion requirements [52]. The muons must have  $p_T > 4$  GeV and  $|\eta| < 2.5$ . Table 7.1 summarizes the  
2311 object requirements described in this section.

	$R$	$p_T$	$ \eta $	$M$
Calorimeter jets	1.0	$250 < p_T < 1500$ GeV	$< 2.0$	$> 50$ GeV
Track jets	0.2	$> 10$ GeV	$< 2.5$	-
Muons	-	4 GeV	$< 2.5$	-

Table 7.1: Summary of requirements on objects used in the  $X \rightarrow HH \rightarrow b\bar{b}b\bar{b}$  search

### 2312 7.5 EVENT SELECTION

2313 The first requirement in the boosted selection is for  $\geq 2$  large radius jets satisfying the selections outlined  
2314 above. The two highest momentum large-R jets in the event are referred to as “Higgs candidates”. The  
2315 leading jet is required to have  $p_T > 350$  GeV.

2316 Track jets satisfying the object selections are matched to Higgs candidate jets via ghost association [106].  
2317 Each Higgs candidate must have at least 2 track jets associated with it. These basic requirements are illus-  
2318 trated in figure 7.7

2319 The QCD multijet background produces less central jets than high mass resonances, so there is an ad-  
2320 ditional requirement that the two Higgs candidates be close together in  $\eta$ . The large-R jets are required  
2321 to satisfy  $|\Delta\eta(JJ)| < 1.7$ .

2322 The final set of requirements ensures that the Higgs candidates are consistent with expected proper-  
2323 ties of the 125.0 GeV Higgs. First, a variable ( $X_{hh}$ ) is defined to measure the consistency of both of the

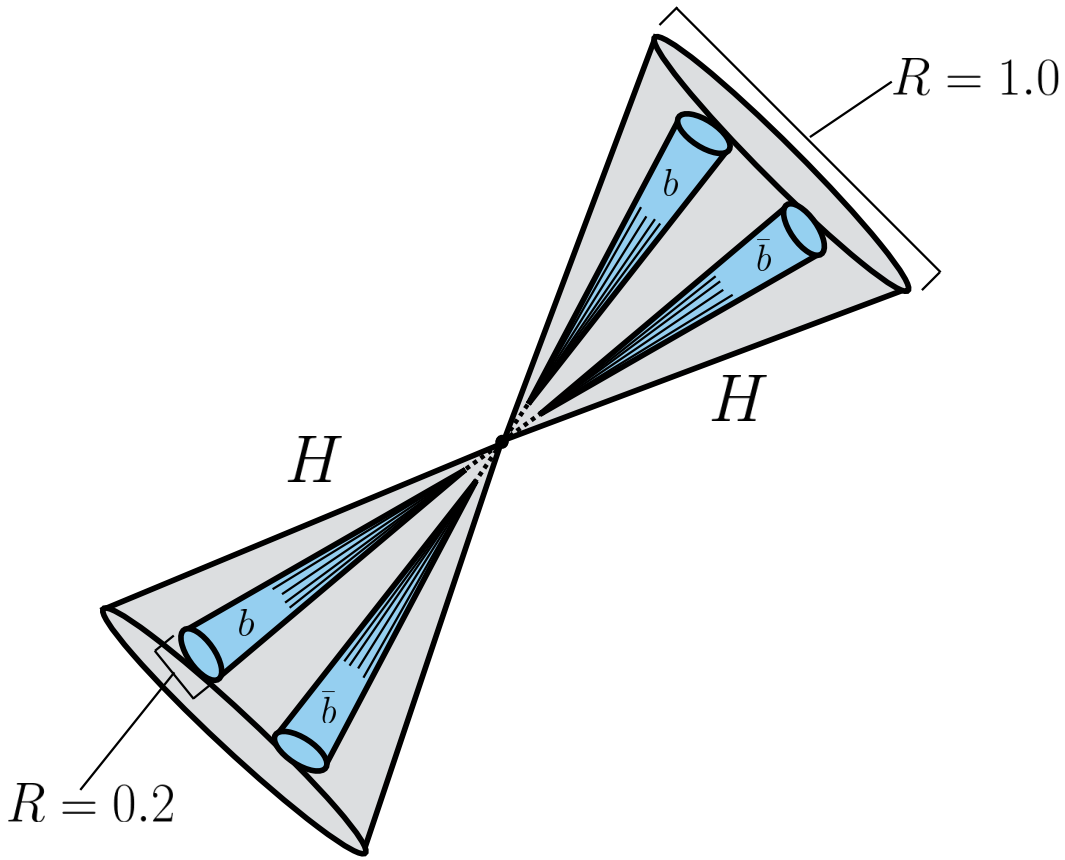


Figure 7.7: Illustration of the boosted selection requirements on Higgs candidates. Each large-radius calorimeter jet (Higgs candidate) must contain two track jets

<sup>2324</sup> Higgs candidate jets with the SM Higgs mass. This is shown in equation 7.2.

$$X_{hh} = \sqrt{\left(\frac{M_J^{\text{lead}} - 124 \text{ GeV}}{0.1 M_J^{\text{lead}}}\right)^2 + \left(\frac{M_J^{\text{sublead}} - 115 \text{ GeV}}{0.1 M_J^{\text{sublead}}}\right)^2} \quad (7.2)$$

<sup>2325</sup> The mass values in the  $X_{hh}$  formula are optimized to maximize signal efficiency. The sub-leading jet  
<sup>2326</sup> typically has a lower mass due to semi-leptonic  $b$  decays and final state radiation.  $X_{hh}$  effectively acts as  
<sup>2327</sup> a  $\chi^2$  measurement of the consistency of the two Higgs candidate masses with the signal hypothesis. The  
<sup>2328</sup> denominators of each term ( $0.1 M$ ) give the uncertainty on the mass measurement for the large radius  
<sup>2329</sup> jets. Events are required to satisfy  $X_{hh} < 1.6$ .

<sup>2330</sup> The last requirement applied is on the number of  $b$ -tagged track jets. There are two signal regions de-

fined. The first requires exactly four  $b$ -tagged track jets, two in each Higgs candidate (known as the  $4b$  signal region). At high resonance masses, this requirement is inefficient, so an additional signal region requiring only three  $b$ -tagged track jets is also defined (known as the  $3b$  signal region). While this has a larger background it is also more efficient for high resonance masses. For both signal regions, threshold on MV<sub>2</sub> score is chosen such that the algorithm is 77% efficiency in finding true  $b$ -jets<sup>§</sup>. Different working points were tested and this was found to be optimal. Appendix A has more details on this optimization.

Before making the requirement on  $X_{hh}$ , the masses of the Higgs candidates are corrected for semi-leptonic  $b$  decays using muons with the criteria outlined in the previous section. Any muons within a  $\Delta R < 0.2$  of a  $b$ -tagged track jet have their four-momenta added to the four-momentum of the Higgs candidate. This correction does not affect the pre-selection requirements but does affect the  $X_{hh}$  requirement and the final invariant mass distribution used.

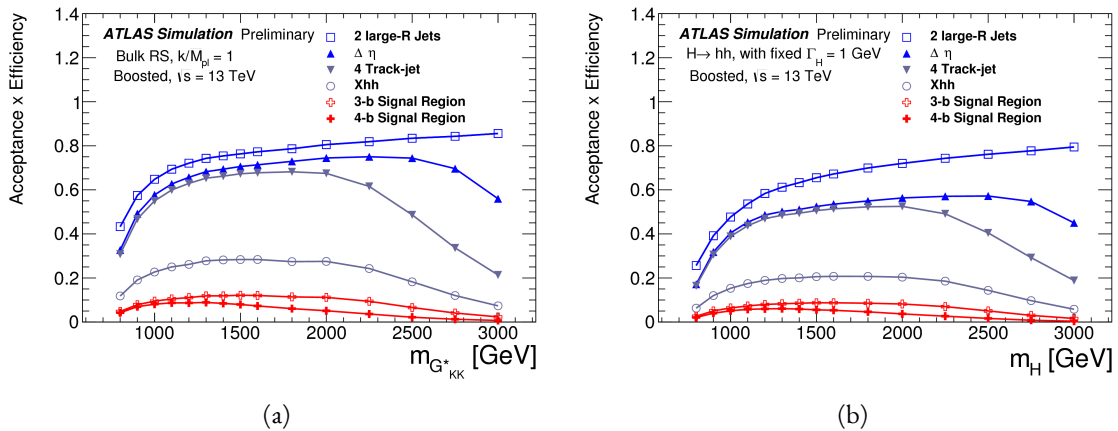


Figure 7.8: Acceptance  $\times$  efficiency as a function of mass for (a) RSG and (b) narrow heavy scalar signal models [107].

Figure 7.8 shows the product of acceptance and efficiency as a function of mass for both the RSG and narrow heavy scalar resonance signal models. After  $m_X > 1$  TeV, the efficiency of the  $4b$  requirement begins to decline. After  $m_X > 2$  TeV, the efficiency of requiring two track jets in each Higgs candidate begins to decline as well. Both of these behaviors illustrate the difficulty of resolving the merged decay

<sup>§</sup>The specific MV<sub>2</sub> algorithm chosen is MV<sub>2c20</sub>, where the fraction of charm events used in the training is 20%

2347 products at high mass. More details on the degradation of the  $b$ -tagging efficiency at high masses are  
2348 shown in appendix B.

2349 Figure 7.9 shows a more detailed comparison of the signal efficiency in the  $3b$  vs  $4b$  signal regions for  
2350 the RSG model. The efficiencies shown here are relative to all prior selection requirements.

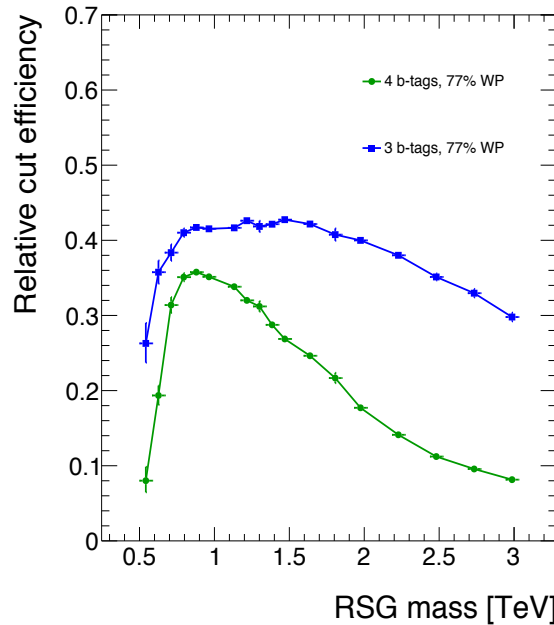


Figure 7.9: Efficiency of requiring 3 or 4  $b$ -tagged track jets vs. RSG mass. The efficiency quoted is relative to the previous selection requirements (rather than an absolute efficiency).

2351 The final discriminating variable used in the boosted analysis is  $M_{2J}$ , the invariant mass of the two  
2352 Higgs candidates. In order to improve the mass resolution, the four-momenta of each Higgs candidate  
2353 are scaled by  $m_h/M_J$ . The effect of this correction is small in the boosted analysis but is done for consistency  
2354 with the resolved selection.

2355 Table 7.2 shows the effect of the selection requirements on signal and background simulations as well  
2356 as data.

## 2357 7.6 DATA-DRIVEN BACKGROUND ESTIMATION

2358 The largest background to this final state is QCD multijet production, constituting 80-90% of the total  
2359 background. Because of the difficulties in modeling higher order QCD processes, this background is

Selection	Data	$m_{G_{KK}^*} = 1\text{TeV}$	$m_{G_{KK}^*} = 2\text{TeV}$	$t\bar{t}$	$Z + \text{jets}$
$N(\text{fiducial large-R jets}) \geq 2$	2202396	23.3	0.48	32345.2	4255.7
leading large-R jet $p_T > 350\text{ GeV}$	1873741	22.9	0.48	26511.7	3649.9
Both large-R jet $m > 50\text{ GeV}$	1854625	21.2	0.47	24369.8	3575.8
Both large-R jet $p_T < 1500\text{ GeV}$	1853601	21.2	0.46	24346.5	3572.9
$ \Delta\eta(JJ)  < 1.7$	1435273	20.8	0.44	20751.0	3265.8
$\geq 2$ track-jets per large-R jet	1224727	19.8	0.40	18234.5	2692.6
$3 b\text{-tags}, X_{hh} < 1.6$	316	3.4	0.067	46.7	2.0
$4 b\text{-tags}, X_{hh} < 1.6$	20	2.9	0.030	1.4	0.0

Table 7.2: Effect of boosted selection on data, RSG signal models,  $t\bar{t}$ , and  $Z + \text{jets}$ . The numbers from simulation are normalized with the MC generator cross section and do not take into account the data driven estimates described in section 7.6 [108].

estimated with a fully data-driven method. The only other non-negligible background is  $t\bar{t}$ , constituting the other 10-20%. Due to the presence of  $t\bar{t}$  in the sideband region where the QCD background will be estimated, the normalization of the QCD and  $t\bar{t}$  backgrounds are simultaneously estimated.

### 7.6.1 MASS REGION DEFINITIONS

The first step in the data-driven background estimate is to define a sideband mass region where the background normalization can be derived. Additionally, a control region is defined where the background estimate can be validated. The control (CR) and sideband (SB) regions are defined using a radial distance in the two-dimensional large-R jet mass plane,  $R_{hh}$ , which is defined in equation 7.3.

$$R_{hh} = \sqrt{(M_J^{\text{lead}} - 124\text{ GeV})^2 + (M_J^{\text{sublead}} - 115\text{ GeV})^2} \quad (7.3)$$

Events in the sideband region are required to fail the signal region  $X_{hh} < 1.6$  requirement and have  $R_{hh} > 35.8\text{ GeV}$ . The control region consists of those events which are not in the signal or sideband regions. Figure 7.10 shows the definition of the signal, control, and sideband mass regions. Table 7.3 summarizes the mass region selections for the three different regions used in the analysis.

<sup>¶</sup>The  $Z + \text{jets}$  background is a sub-percent level contribution

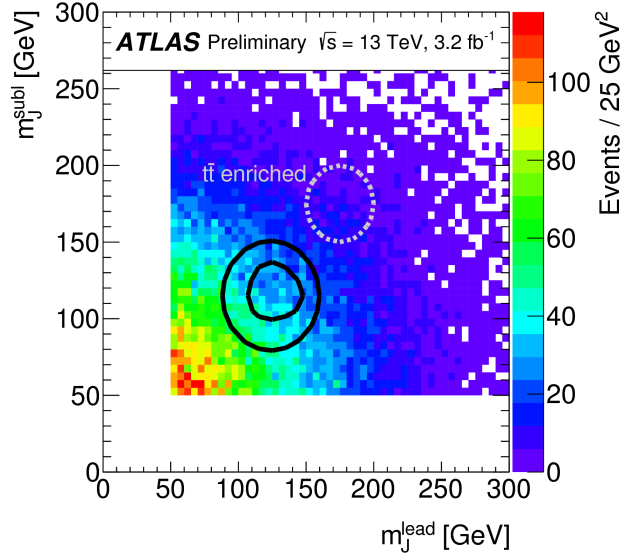


Figure 7.10:  $M_j^{\text{sublead}}$  vs.  $M_j^{\text{lead}}$  in a 2  $b$ -tag data sample. The signal region is defined by the inner black contour ( $X_{hh} < 1.6$ ) and the sideband region is defined by the outer contour ( $R_{hh} > 35.8 \text{ GeV}$ ). The region between the black contours is the control region. The mass region which is enriched in  $t\bar{t}$  background is also shown for illustration. [107]

Region	Requirement	Notes
Signal Region (SR)	$X_{hh} < 1.6$	-
Control Region (CR)	$R_{hh} < 35.8 \text{ GeV}$ and $X_{hh} > 1.6$	Used for validation of background estimates
Sideband Region (SB)	$R_{hh} > 35.8 \text{ GeV}$	Used to derive background normalization

Table 7.3: Mass region definitions used for background estimation

### 2372 7.6.2 BACKGROUND ESTIMATION

2373 The method for estimating the background in this analysis is similar to the ABCD method presented in  
 2374 Chapter 5. In this case, the two handles used to define different regions for the estimate are the number  
 2375 of  $b$ -tagged track jets and the mass regions. A region requiring exactly two  $b$ -tagged track jets in one large-  
 2376 R jet (referred to as the 2-tag or  $2b$  region) is defined for use in the background estimate. The number of  
 2377 expected background events in the  $3b$  and  $4b$  signal regions is then given by equation 7.4.

$$N_{\text{bkg}}^{3(4)-\text{tag},\text{SR}} = \mu_{\text{Multijet}} N_{\text{Multijet}}^{2-\text{tag},\text{SR}} + \beta_{t\bar{t}} N_{t\bar{t}}^{3(4)-\text{tag},\text{SR}} + N_{Z+\text{jets}}^{3(4)-\text{tag},\text{SR}} \quad (7.4)$$

2378 In this equation,  $N_{\text{bkg}}^{3(4)-\text{tag}}$  is the expected number of background events in the  $3b$  or  $4b$  signal regions.  
 2379  $N_{\text{Multijet}}^{2-\text{tag}}$  is the number of multijet events in the 2-tag region.  $N_{t\bar{t}}^{3(4)-\text{tag}}$  is the number of  $t\bar{t}$  events  
 2380 predicted in the MC for the  $3b$  or  $4b$  signal region, and the variable is similarly defined for the  $Z+\text{jets}$   
 2381 background. The  $\beta_{t\bar{t}}$  parameter is a scale factor used to correct the normalization of the  $t\bar{t}$  estimate in  
 2382 the signal region.  $\mu_{\text{Multijet}}$  is an extrapolation factor that is derived in the sideband region and used to  
 2383 estimate the ratio of 2-tag events to 3(4)-tag events in the signal region. It is defined in equation 7.5.

$$\mu_{\text{Multijet}} = \frac{N_{\text{Multijet}}^{3(4)-\text{tag},\text{SB}}}{N_{\text{Multijet}}^{2-\text{tag},\text{SB}}} = \frac{N_{\text{data}}^{3(4)-\text{tag},\text{SB}} - \beta_{t\bar{t}} N_{t\bar{t}}^{3(4)-\text{tag},\text{SB}} - N_{Z+\text{jets}}^{3(4)-\text{tag},\text{SB}}}{N_{\text{data}}^{2-\text{tag},\text{SB}} - \beta_{t\bar{t}} N_{t\bar{t}}^{2-\text{tag},\text{SB}} - N_{Z+\text{jets}}^{2-\text{tag},\text{SB}}} \quad (7.5)$$

2384 The  $t\bar{t}$  scale factor ( $\beta_{t\bar{t}}$ ) and the QCD multijet extrapolation factor ( $\mu_{\text{Multijet}}$ ) are estimated together in  
 2385 a simultaneous fit in the sideband region. Then, the number of events in the 2-tag signal region is used,  
 2386 along with the  $t\bar{t}$  estimate in the  $3b$  and  $4b$  signal regions and  $\mu_{\text{Multijet}}$ , to estimate the total number of  
 2387 background events in the two final signal regions. The shape of the final discriminant  $M_{2J}$  is also taken  
 2388 from the 2-tag signal region where there are more statistics. This method is illustrated graphically in  
 2389 figure 7.II.

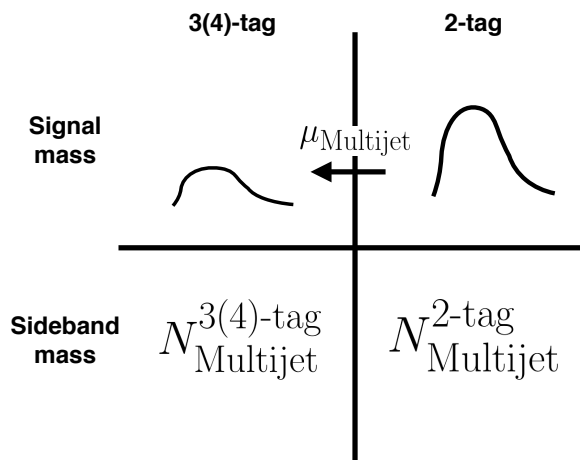


Figure 7.II: An illustration of the data-driven background estimation technique for the boosted analysis

2390 In the  $3b$  region, the fit yields values of  $\mu_{\text{Multijet}} = 0.160 \pm 0.03$  and  $\beta_{t\bar{t}} = 1.02 \pm 0.09$ . In the  $4b$   
 2391 region, the fit gives  $\mu_{\text{Multijet}} = 0.0091 \pm 0.0007$  and  $\beta_{t\bar{t}} = 0.82 \pm 0.39$ . The uncertainties quoted

are statistical only. The larger uncertainties in the  $4b$  values indicate the lower statistics available in that region.

Figure 7.12 shows the distributions of data and background estimates in the  $3b$  and  $4b$  sideband regions after the background fit has been done. The normalizations are constrained from the fit to match that of the data, but good modeling of the shape of the mass of the leading large-R jet is seen as well. The shapes of the kinematic distributions in the  $4b$  region are taken from the  $3b$  region due to the better MC statistics in that region.

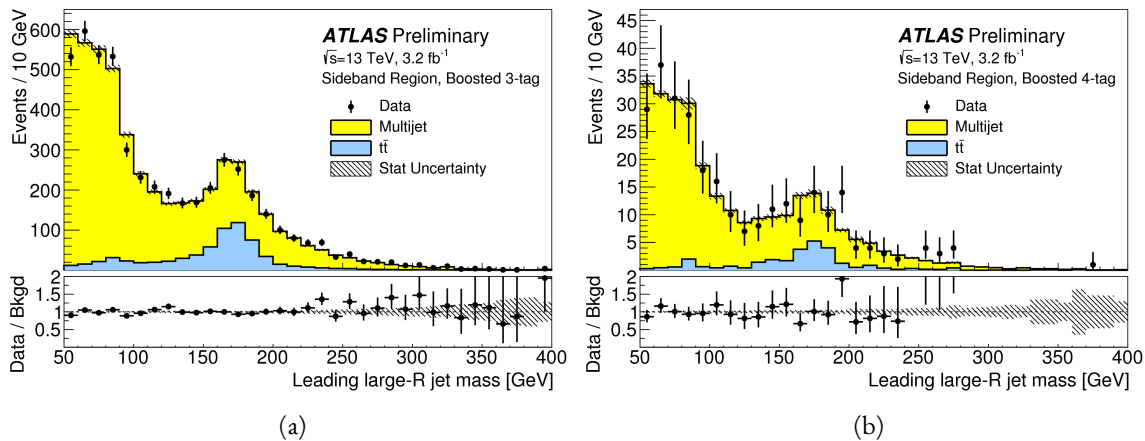


Figure 7.12: Leading large- $R$  jet mass in the  $3b$  (a) and  $4b$  (b) sideband regions. The multijet and  $t\bar{t}$  backgrounds are estimated using the data-driven methods described above. Because their normalizations are derived in the sideband region, the total background normalization is constrained by default to match the normalization of the data [107].

2399 7.6.3 BACKGROUND SHAPE FIT

As mentioned in the previous section, the background shape in the 3-tag and 4-tag signal regions is taken from the 2-tag signal mass region. Due to the limited statistics available, the background shapes are additionally smoothed after being extrapolated to the 3-tag and 4-tag signal regions. Only the data in the range  $900 < M_{2J} < 2000$  GeV is included in the fit due to the limited statistics available above 2 TeV. Both the  $t\bar{t}$  and QCD multijet background are independently fit with an exponential shape,  $y = e^{ax+b}$ . Other shapes are considered and used for the systematic uncertainties. Table 7.4 shows the fit values for the parameters. Because both the 3b and 4b QCD shapes come from the 2-tag region, the slopes derived

2407 are very similar.

	$a$	$b$
QCD (4b)	$0.00545 \pm 0.00021$	$5.44 \pm 0.24$
$t\bar{t}$ (4b)	$0.00746 \pm 0.00021$	$4.88 \pm 0.36$
QCD (3b)	$0.00545 \pm 0.00021$	$8.30 \pm 0.24$
$t\bar{t}$ (3b)	$0.00746 \pm 0.00021$	$8.58 \pm 0.36$

Table 7.4: Parameters derived for exponential fit to background  $M_{2J}$  shape in the 3b and 4b signal regions [108]

#### 2408 7.6.4 VALIDATION OF BACKGROUND ESTIMATE

2409 The background estimate can be validated by using the method to estimate the number of events in the  
 2410 control mass region rather than the signal mass region. Figure 7.13 shows the  $M_{2J}$  distribution in the 3b  
 2411 and 4b control regions, comparing data and background estimates. In both cases, both the background  
 2412 shape and normalization are consistent with the data, indicating good agreement. The ratio of data to  
 2413 the background estimates is also fit to a line in the figure to test for any shape difference. The slope of the  
 2414 line is within  $1\sigma$  (from the fit uncertainties) of flat, further indicating that the data is consistent with the  
 2415 background estimate in the control region.

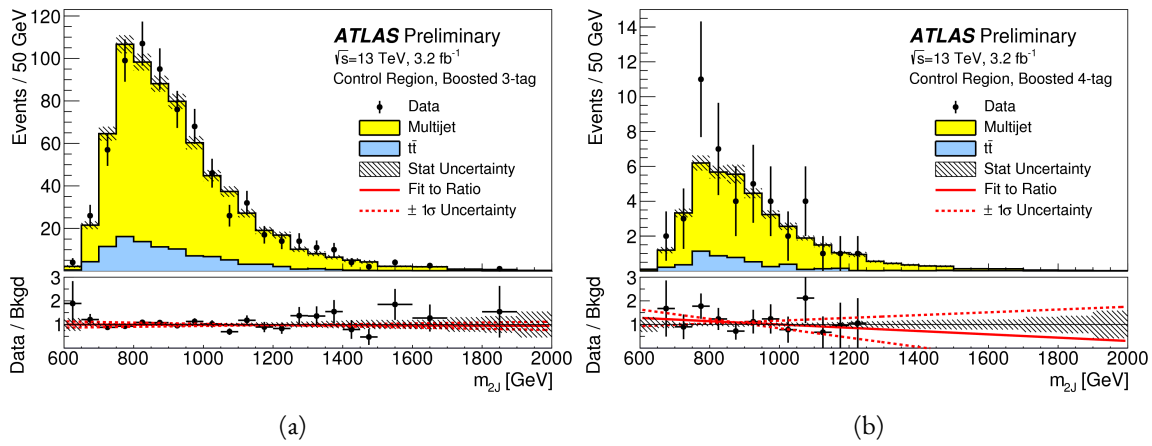


Figure 7.13: Di-jet invariant mass ( $M_{2J}$ ) in the 3b (a) and 4b (b) control regions. The multijet and  $t\bar{t}$  backgrounds  
 are estimated using the data-driven methods described above [107].

2416 Table 7.5 shows the yields in data and background estimates in the 3-tag and 4-tag sideband and con-  
 2417 trol regions. Again, here, it can be seen that the total number of predicted background events from the

<sup>2418</sup> data driven method is consistent with the number of data events in the region.

Sample (3-tag)	Sideband Region	Control Region
Multijet	$4328 \pm 27$	$607 \pm 10$
$t\bar{t}$	$683.5 \pm 8.1$	$99.6 \pm 3.1$
$Z+jets$	$31.8 \pm 3.7$	$7.7 \pm 1.8$
Total	$5043 \pm 28$	$715 \pm 11$
Data	5043	724
Sample (4-tag)	Sideband Region	Control Region
Multijet	$247.4 \pm 1.5$	$34.7 \pm 0.6$
$t\bar{t}$	$28.4 \pm 1.5$	$5.1 \pm 0.7$
$Z+jets$	$3.4 \pm 1.2$	$0.6 \pm 0.5$
Total	$279.2 \pm 2.5$	$40.3 \pm 1.0$
Data	279	45

Table 7.5: The number of events in data and predicted background events in the boosted 3-tag and 4-tag sideband and control regions. The uncertainties shown are statistical only. [107]

<sup>2419</sup> **7.7 SYSTEMATIC UNCERTAINTIES**

<sup>2420</sup> The systematic uncertainties in this analysis can be divided into two broad categories. The first type is  
<sup>2421</sup> uncertainties associated with the modeling of the signal processes. The second type of uncertainty is  
<sup>2422</sup> associated with both the shape and normalization of the background prediction.

<sup>2423</sup> **7.7.1 SIGNAL MODELING UNCERTAINTIES**

<sup>2424</sup> The signal modeling uncertainty has three main components: theoretical uncertainty on the acceptance,  
<sup>2425</sup> experimental uncertainties on the large-R jets, and experimental uncertainties on the track jets related to  
<sup>2426</sup>  $b$ -tagging. In this analysis the experimental uncertainties are the most significant.

<sup>2427</sup> The first uncertainty on signal modeling is the theoretical uncertainty on the acceptance. As explained  
<sup>2428</sup> in section 5.6.1, there are four components to this uncertainty. The first is related to missing higher order  
<sup>2429</sup> terms from the matrix element calculations which is estimated by varying the QCD renormalization and

2430 factorization scales. The second is uncertainty due to the PDF set used. The third is a generator uncer-  
2431 tainty which is estimated by modifying the generator used to model the underlying event and hadroniza-  
2432 tion. Finally, there is an uncertainty associated with the modeling of the initial state and final state radia-  
2433 tion (ISR/FSR). The total theoretical uncertainty on the signal yield is 3%, and this is dominated by the  
2434 ISR/FSR modeling.

2435 There are uncertainties on the large-R jets in both the jet energy scale (JES) and jet energy resolution  
2436 (JER) as well as the jet mass scale (JMS) and jet mass resolution (JMR). These are evaluated using  $\sqrt{s} =$   
2437 8 TeV data from Run 1 of ATLAS and extrapolated to the Run 2 beam and detector conditions using  
2438 MC<sup>¶</sup>. The details of these uncertainties can be found in reference [109].

2439 Uncertainties on the track jets are related to the  $b$ -tagging efficiency. The total uncertainty on the sig-  
2440 nal yield due to  $b$ -tagging is evaluated by propagating variations of the  $b$ -tagging efficiency through the  
2441 boosted selection requirements. The uncertainties are calculated jet-by-jet and parameterized as a func-  
2442 tion of  $b$ -jet  $p_T$  and  $\eta$  [88]. For high  $p_T$   $b$ -jets (with  $p_T > 300$  GeV), the uncertainties are extrapolated  
2443 using MC simulation from the lower  $p_T$   $b$ -jets [110].

2444 Table 7.6 shows the systematic uncertainties on the signal normalization for models with  $m_{G_{KK}^*} =$   
2445 1.5 TeV and both  $c = 1$  and  $c = 2$  as well as a narrow width heavy scalar. The dominant uncertainty  
2446 comes from  $b$ -tagging and this uncertainty is larger in the 4-tag region than the 3-tag region.

### 2447 7.7.2 BACKGROUND UNCERTAINTIES

2448 Uncertainties on the QCD multijet background normalization and shape are estimated using the control  
2449 mass region. As shown previously, the background predictions in the control region match with the  
2450 data yields within the statistical uncertainty in both the 3-tag and 4-tag control regions. As an additional  
2451 protection, the statistical uncertainty on the background prediction in the control region is assigned as a  
2452 systematic uncertainty on the normalization of the QCD background.

2453 Additional robustness tests are done by varying the definition of the control mass region and the  $b$ -  
2454 tagging requirements used to define the 2-tag sample. In all cases, the effect of the variations is found to

---

¶The uncertainties are correspondingly larger due to the uncertainty of this extrapolation.

Source	Background	$G_{\text{KK}}^*$		$H$
		$c = 1$	$c = 2$	
Luminosity	-	5.0	5.0	5.0
3-tag				
JER	< 1	< 1	< 1	< 1
JES	2	< 1	< 1	< 1
JMR	1	12	12	11
JMS	5	14	13	17
$b$ -tagging	1	23	22	23
Theoretical	-	3	3	3
Multijet Normalization	3	-	-	-
Statistical	2	1	1	1
Total	7	31	30	33
4-tag				
JER	< 1	< 1	< 1	< 1
JES	< 1	< 1	< 1	< 1
JMR	4	12	13	13
JMS	5	13	13	14
$b$ -tagging	2	36	36	36
Theoretical	-	3	3	3
Multijet Normalization	14	-	-	-
Statistical	3	1	1	1
Total	15	42	42	43

Table 7.6: Summary of systematic uncertainties in the total background and signal event yields (expressed in %) in the boosted 3-tag and 4-tag signal regions. Systematic uncertainties on the signal normalization are shown for models with  $m_{G_{\text{KK}}^*} = 1.5$  TeV and both  $c = 1$  and  $c = 2$  as well as a narrow width heavy scalar.

2455 be within the statistical uncertainties on the background normalization in the control region.

2456 Shape uncertainties on the background are evaluated using two techniques. First, as shown in figure 7.13, the ratio between the data and background prediction is fit with a linear function. The uncertainties on the slope of this fit are assigned as shape uncertainties. An additional uncertainty is assigned by using alternate power law fit functions for the smoothing of the background shape. Table 7.7 shows the alternate shapes used. The largest difference between the nominal fit function and the alternates, taking into account the  $1\sigma$  uncertainty band on each fit as well, is taken as a shape uncertainty.

Functional Form
$f_1(x) = p_0(1-x)^{p_1}x^{p_2}$
$f_2(x) = p_0(1-x)^{p_1}e^{p_2 x^2}$
$f_3(x) = p_0(1-x)^{p_1}x^{p_2}x$
$f_4(x) = p_0(1-x)^{p_1}x^{p_2}\ln x$
$f_5(x) = p_0(1-x)^{p_1}(1+x)^{p_2}x$
$f_6(x) = p_0(1-x)^{p_1}(1+x)^{p_2}\ln x$
$f_7(x) = \frac{p_0}{x}(1-x)^{p_1-p_2}\ln x$
$f_8(x) = \frac{p_0}{x^2}(1-x)^{p_1-p_2}\ln x$

Table 7.7: Alternate fit functions used to model the  $M_{JJ}$  distribution in the QCD multijet background. In the equations,  $x = M_{JJ}/\sqrt{s}$ .

2462     The uncertainties on the  $t\bar{t}$  background are obtained by propagating the various experimental varia-  
 2463     tions (JES, JER, JMS, JMR,  $b$ -tagging) through the analysis selection requirements. Table 7.6 summarizes  
 2464     the background uncertainties in the 3-tag and 4-tag regions.

2465     7.8 RESULTS

2466     Table 7.8 shows the observed yields in the 3-tag and 4-tag signal regions for the boosted analysis com-  
 2467     pared to the predicted number of background events. In the 3-tag region, 316 events are observed with  
 2468     a predicted background of  $285 \pm 19$ . In the 4-tag region, 20 events are observed with a predicted back-  
 2469     ground of  $14.6 \pm 2.4$ . Figure 7.14 shows the  $M_{JJ}$  distribution in the 3-tag and 4-tag regions. There are  
 2470     some small excesses in the data, in particular in the 3-tag region around  $M_{JJ} \approx 900$  GeV and in the  
 2471     region of  $1.6 < M_{JJ} < 2.0$  TeV. The significance of these excesses will be evaluated in the next chapter  
 2472     in the statistical combination with the resolved results.

Sample	Signal Region (3-tag)	Signal Region (4-tag)
Multijet	$235 \pm 14$	$13.5 \pm 2.4$
$t\bar{t}$	$48 \pm 22$	$1.2 \pm 1.0$
$Z+jets$	$2.0 \pm 2.2$	-
Total	$285 \pm 19$	$14.6 \pm 2.4$
Data	316	20
$G_{KK}^*$ (1000 GeV), $c = 1$	$3.4 \pm 0.9$	$2.9 \pm 1.1$

Table 7.8: Observed yields in the 3-tag and 4-tag signal regions for the boosted analysis compared to the predicted number of background events Errors correspond to the total uncertainties in the predicted event yields. The yields for a graviton with  $m_{G_{KK}^*} = 1$  TeV and  $c = 1$  are also shown. [107]

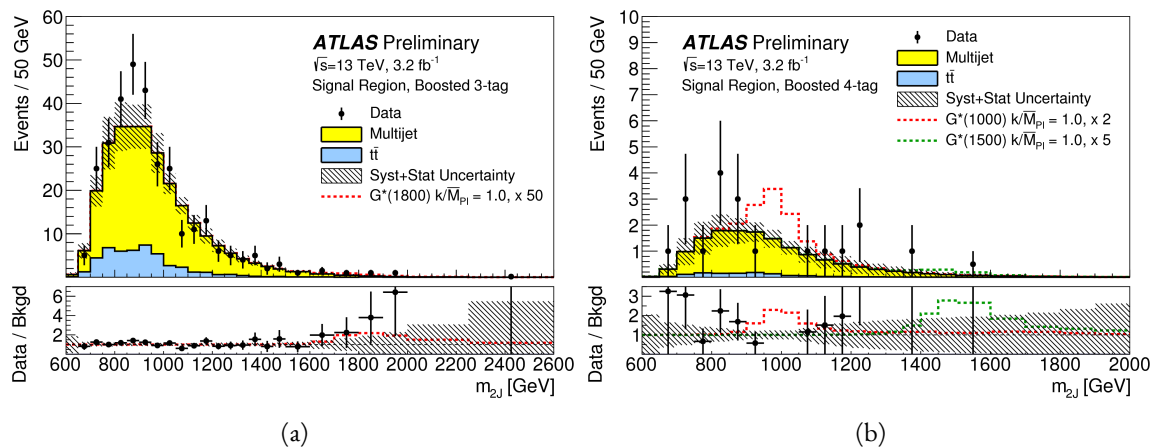


Figure 7.14: Di-jet invariant mass ( $M_{2J}$ ) in the 3b (a) and 4b (b) signal regions. The multijet and  $t\bar{t}$  backgrounds are estimated using the data-driven methods described above. In the 3b region, a graviton signal with  $m_{G_{KK}^*} = 1.8$  TeV and  $c = 1$  is overlaid, with the cross section multiplied by a factor of 50 so that the signal is visible. In the 4b region, signals with  $m_{G_{KK}^*} = 1.0$  TeV and  $m_{G_{KK}^*} = 1.5$  TeV are overlaid, both with  $c = 1$  and the yields multiplied by factors of 2 and 5 respectively [107].

*There is no real ending. It's just the place where you stop  
the story.*

Frank Herbert

# 8

2473

2474

## Combined limits from boosted and resolved searches

2475

2476

### 8.1 INTRODUCTION

2477 In order to cover the full mass range of possible resonances decaying to di-Higgs final states, two distinct  
2478 tailored selections were produced. The resolved selection is more sensitive in the mass range of  $400 < m_X < 1100$  GeV while the boosted selection is more sensitive to masses in the range  $1100 < m_X <$   
2479  $3000$  GeV. Chapter 7 presents the details of the boosted selection and results. In setting limits on spin-2  
2480 Randall-Sundrum graviton (RSG) and narrow width heavy scalar ( $H$ ) models, the results of the boosted  
2481 selection are combined with the results of the resolved selection to cover the full mass range.  
2482

2483 This chapter presents limits on signal models resulting from the  $X \rightarrow HH \rightarrow b\bar{b}b\bar{b}$  search in both  
2484 the resolved and boosted selections. It first presents a brief overview of the resolved results that go into

2485 the limit setting. Then, an overview of the statistical methods used for the search and limit setting is  
2486 given. Finally, limits on the RSG and heavy scalar models are presented.

2487 **8.2 RESOLVED RESULTS**

2488 The details of the resolved selection will not be presented here and can be found in reference [107]. In  
2489 basic terms, the selection searches for four  $R = 0.4$  b-tagged calorimeter jets (where each pair of jets is  
2490 one Higgs candidate). This is distinct from the boosted methodology which searches for merged decay  
2491 products. The backgrounds to the resolved selection are the same as those presented in Chapter 7 for the  
2492 boosted analysis.

2493 Table 8.1 shows the results for data yields and expected background in the resolved signal region. Fig-  
2494 ure 8.1 shows the  $M_{2J}$  distribution in the resolved signal region. The total number of events is consis-  
2495 tent with the prediction and no significant excess is seen. One event in the boosted 4-tag signal is shared  
2496 with the resolved signal region and has a mass of 852 GeV.

Sample	Signal Region Yield
Multijet	$43.3 \pm 2.3$
$t\bar{t}$	$4.3 \pm 3.0$
$Z + \text{jets}$	-
Total	$47.6 \pm 3.8$
Data	46
SM $hh$	$0.25 \pm 0.07$
$G_{KK}^*(800 \text{ GeV}), c = 1$	$5.7 \pm 1.5$

Table 8.1: Observed yields in the resolve selection 4-tag signal region compared to the predicted number of back-  
ground events Errors correspond to the total uncertainties in the predicted event yields. The yields for a graviton  
with  $m_{G_{KK}^*} = 800$  GeV and  $c = 1$  are also shown. [107]

2497 **8.3 SEARCH TECHNIQUE AND RESULTS**

2498 The statistical technique used for the search in this analysis is the same as that used in the  $H \rightarrow WW^*$   
2499 analysis presented in section 3.6.2. The test statistic  $q_0$  is used to define the  $p$ -values which measure the

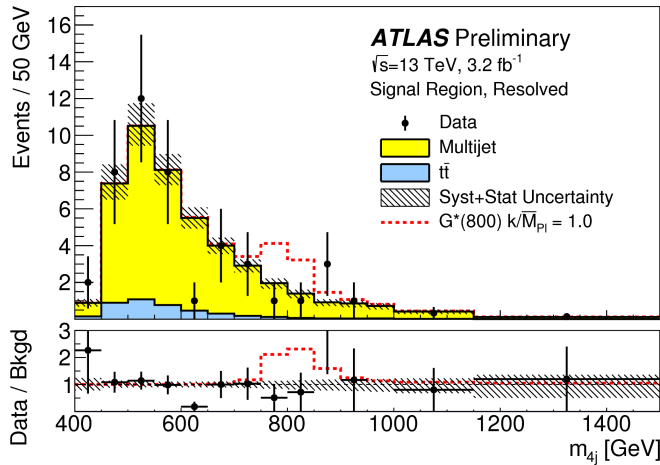


Figure 8.1: Di-jet invariant mass ( $M_{2J}$ ) in the resolved signal region. A graviton signal with  $m_{G_{KK}^*} = 800$  GeV and  $c = 1$  is overlaid. [107].

2500 compatibility of the data with the background-only hypothesis corresponding to a signal strength  $\mu =$   
 2501 0.

2502 Local  $p_0$  values are computed to quantify the probability that the background could produce a fluc-  
 2503 tuation greater than or equal to the one observed in the data. In the resolved analysis, no significant ex-  
 2504 cesses are observed. The largest discrepancy with respect to the background only hypothesis occurs near  
 2505 a resonance mass of 900 GeV and is found to be less than  $2\sigma$  in significance.

2506 In the boosted selection, the largest local excess is a broad excess in the  $3b$  signal region that begins  
 2507 near  $M_{2J} \approx 1.7$  GeV. Assuming a  $G_{KK}^*$  with this mass and  $c = 1.0$ , the local significance of this excess  
 2508 is  $2.0\sigma$ .

#### 2509 8.4 LIMIT SETTING

2510 In the absence of any significant excess observed in the data, limits on different signal models can be set.  
 2511 This section describes the limit setting procedure and presents combined results of the resolved and  
 2512 boosted analyses.

2513 8.4.1 LIMIT SETTING PROCEDURE

2514 The procedure used for setting exclusion limits in this analysis is the  $\text{CL}_s$  method [11]. The first step in  
 2515 setting the limits is to define a test statistic which will be used. For limit setting, the test statistic is shown  
 2516 in equation 8.1.

$$\widetilde{q}_\mu = \begin{cases} -2 \ln \frac{L(\mu, \hat{\theta}(\mu))}{L(0, \hat{\theta}(0))} & \hat{\mu} < 0 \\ -2 \ln \frac{L(\mu, \hat{\theta}(\mu))}{L(\hat{\mu}, \hat{\theta})} & 0 \leq \hat{\mu} < \mu \\ 0 & \hat{\mu} > \mu \end{cases} \quad (8.1)$$

2517 In the above equation,  $\mu$  is the value of the signal strength under test,  $\hat{\mu}$  is the best fit  $\mu$ ,  $\hat{\theta}$  is the  
 2518 best fit value of the nuisance parameters,  $\hat{\theta}$  is the best fit value of the nuisance parameters under the fixed  
 2519  $\mu$  value, and  $L$  is the Poisson likelihood of the data (as described in section 3.6.2).

2520 The test statistic  $\widetilde{q}_\mu$  is constructed to protect against two interesting corner cases when setting the  
 2521 upper limit on the cross section. First, it protects against negative signal strengths  $\mu$  which are unphys-  
 2522 ical. Second, it does not count excesses in the data larger than those expected by a signal strength  $\mu$  as  
 2523 evidence against the  $\mu$  hypothesis.

2524 The  $\text{CL}_s$  statistic is constructed by taking a ratio of two probabilities.  $\text{CL}_{s+b}$  is the probability that  
 2525 the signal+background hypothesis would produce a value of the test statistic that is less than or equal  
 2526 to the observed value\*.  $\text{CL}_b$  is the probability that the background only hypothesis will pro-  
 2527 duce a value of the test statistics less than or equal to the observed. The  $\text{CL}_s$  statistic is then the ratio  
 2528  $\text{CL}_{s+b}/\text{CL}_b$ . A 95% upper limit on the cross section is set at the value of  $\mu$  that makes the  $\text{CL}_s$  statistic  
 2529 less than 5%.

2530 In practice, the limits are computed numerically within an asymptotic approximation for the distri-  
 2531 bution of the test statistic  $\widetilde{q}_\mu$ . The details of this approximation can be found in reference [63].

2532 The resolved and boosted analyses are combined using a very simple procedure rather than a full sta-  
 2533 tistical combination. For each mass point tested, the limit which gives the most stringent constraint is  
 2534 used. This means that for mass points below 1.1 TeV the resolved signal region is used, while at and

---

\*Lower values of  $\widetilde{q}_\mu$  mean better compatibility

2535 above this point the combination of the orthogonal  $3b$  and  $4b$  boosted signal regions is used.

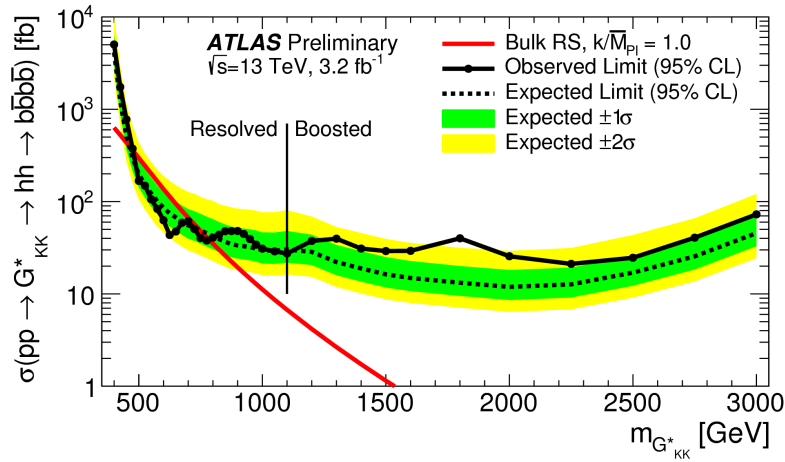
2536 **8.4.2 LIMIT SETTING RESULTS**

2537 Figure 8.2 shows the combined 95% upper bounds as a function of mass for three different models:

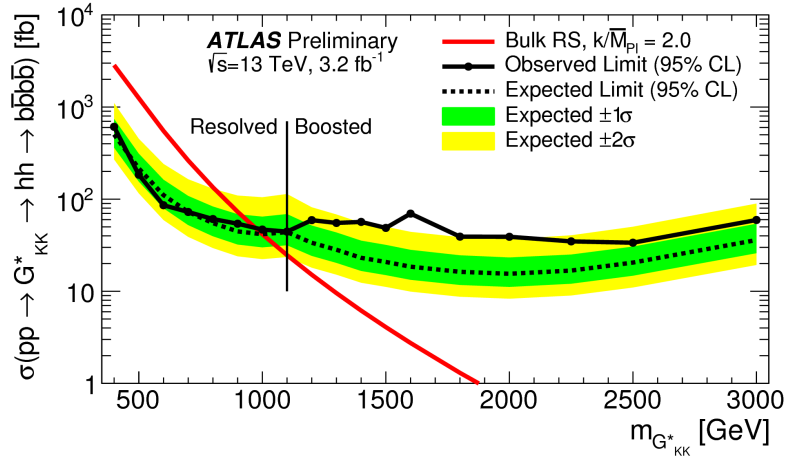
2538  $G_{\text{KK}}^*$  with  $c = 1$ ,  $G_{\text{KK}}^*$  with  $c = 2$ , and a narrow heavy scalar  $H$ .

2539 The cross section of  $\sigma(pp \rightarrow G_{\text{KK}}^* \rightarrow hh \rightarrow b\bar{b}b\bar{b})$  with  $c = 1$  is constrained to be less than 70 fb  
2540 for masses in the range  $600 < m_{G_{\text{KK}}^*} < 3000$  GeV. For the RSG model with  $c = 2$ , cross sections  
2541 limits between 40 fb and 200 fb are set for the mass range of  $500 < m_{G_{\text{KK}}^*} < 3000$  GeV. Masses in  
2542 the range of  $475 < m_{G_{\text{KK}}^*} < 785$  GeV are excluded with  $c = 1$  (with an exclusion of the range 465  
2543 to 745 GeV expected). Masses less than 980 GeV are excluded with  $c = 2$  (with an exclusion for masses  
2544 less than 1 TeV expected).

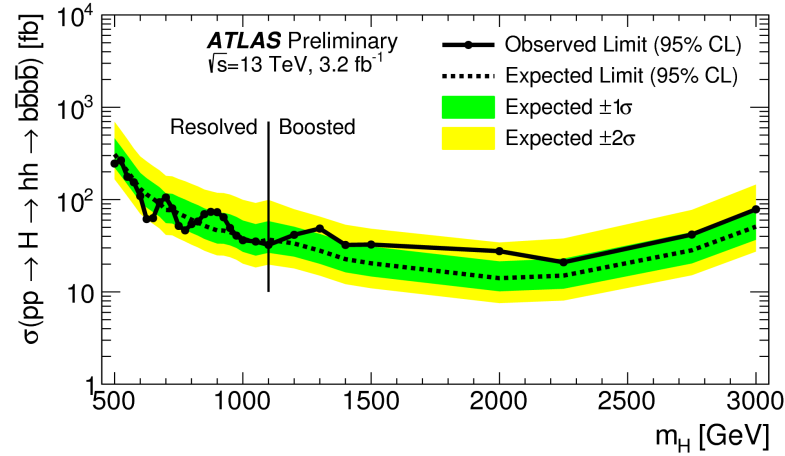
2545 In the heavy Higgs model, the cross section upper limits for  $\sigma(pp \rightarrow H \rightarrow hh \rightarrow b\bar{b}b\bar{b})$  ranges from  
2546 30 to 300 fb in the mass range of  $500 < m_H < 3000$  GeV. The resolved analysis can also set an upper  
2547 limit on the Standard Model di-Higgs production cross section discussed in chapter 3. The upper limit  
2548 on  $\sigma(pp \rightarrow hh \rightarrow b\bar{b}b\bar{b})$  in the Standard Model is constrained to be less than 1.22 pb.



(a) Bulk RS,  $c = 1$



(b) Bulk RS,  $c = 2$



(c) Spin-0 narrow-width  $H$  boson

Figure 8.2: Expected and observed upper limit as a function of mass for  $G^*_{KK}$  in the RSG model with (a)  $c = 1$  and (b)  $c = 2$ , as well as (c)  $H$  with fixed  $\Gamma_H = 1$  GeV, at the 95% confidence level in the  $CL_s$  method. [107]

2549

## Part IV

2550

## Looking ahead

# 9

2551

2552

## Conclusion

2553 This dissertation presented two distinct studies: the observation and measurement of the Higgs boson  
2554 in the  $H \rightarrow WW^* \rightarrow \ell\nu\ell\nu$  channel at  $\sqrt{s} = 7$  TeV and  $\sqrt{s} = 8$  TeV and a search for Higgs pair  
2555 production in the  $HH \rightarrow b\bar{b}b\bar{b}$  channel at  $\sqrt{s} = 13$  TeV with the ATLAS detector in  $pp$  collisions at  
2556 the Large Hadron Collider.

2557 In the  $H \rightarrow WW^* \rightarrow \ell\nu\ell\nu$ , results from both the discovery of the Higgs boson and the full  
2558 ATLAS Run 1 dataset were presented. With the full  $20.3 \text{ fb}^{-1}$  at  $\sqrt{s} = 8$  TeV and  $4.2 \text{ fb}^{-1}$  at  $\sqrt{s} =$   
2559 7 TeV, ATLAS achieved discovery level significance in the  $H \rightarrow WW^*$  channel alone and obtained  
2560 the first observation of vector boson fusion production in that channel. The combined signal strength  
2561 is measured to be  $\mu = 1.09^{+0.23}_{-0.21}$ . The total observed significance of the  $H \rightarrow WW^*$  process is ob-  
2562 served to be  $6.1\sigma$  (with  $5.8\sigma$  expected). Advanced methods for background reduction and estimation,  
2563 particularly in same-flavor lepton final states, are shown. The VBF signal strength is measured to be  
2564  $\mu_{\text{VBF}} = 1.27^{+0.53}_{-0.45}$  with an observed significance of  $3.2\sigma$  (with  $2.7\sigma$  expected).

2565 These results required many novel innovations. The increase of pileup interactions in the higher in-  
2566 stantaneous luminosity LHC conditions of 2012 led to a degradation of missing transverse momentum  
2567 resolution. As a result, the prominent  $Z/\gamma^*$ +jets background of the same flavor  $H \rightarrow WW^* \rightarrow \ell\nu\ell\nu$   
2568 final states increased greatly. New variables, including a track-based missing transverse momentum and  
2569 a measurement of the balance between the dilepton system and recoiling jets, allowed for significant re-  
2570 duction of this background. In the VBF channel, selections were optimized to exploit the unique VBF  
2571 final state topology. Incorporating these variables into a boosted decision tree technique allowed the  
2572 analysis to exceed the  $3\sigma$  observation threshold.

2573 At  $\sqrt{s} = 13$  TeV, a search for Higgs pair production in the  $b\bar{b}b\bar{b}$  final state with  $3.2 \text{ fb}^{-1}$  was con-  
2574 ducted. A signal region optimized for the boosted final states arising from high mass resonances was  
2575 constructed. This signal region utilized large-radius calorimeter jets and  $b$ -tagging with small radius track  
2576 jets to maximize the signal acceptance. No significant excesses were observed, and upper limits on cross  
2577 sections are placed for spin-2 Randall Sundrum gravitons (RSG) and narrow spin-0 resonances. The  
2578 cross section of  $\sigma(pp \rightarrow G_{\text{KK}}^* \rightarrow hh \rightarrow b\bar{b}b\bar{b})$  with  $k/\bar{M}_{\text{Pl}} = 1$  is constrained to be less than  $70 \text{ fb}$  for  
2579 masses in the range  $600 < m_{G_{\text{KK}}^*} < 3000 \text{ GeV}$ . For the RSG model with  $k/\bar{M}_{\text{Pl}} = 2$ , cross sections  
2580 limits between  $40 \text{ fb}$  and  $200 \text{ fb}$  are set for the mass range of  $500 < m_{G_{\text{KK}}^*} < 3000 \text{ GeV}$ . The cross  
2581 section upper limits for  $\sigma(pp \rightarrow H \rightarrow hh \rightarrow b\bar{b}b\bar{b})$  ranges from  $30$  to  $300 \text{ fb}$  in the mass range of  
2582  $500 < m_H < 3000 \text{ GeV}$ .

# A

2583

2584

2585

## Optimization of $b$ -tagging working point in

$X \rightarrow HH \rightarrow b\bar{b}b\bar{b}$  search

2586 To the  $3b$  and  $4b$  signal regions in the boosted  $X \rightarrow HH \rightarrow b\bar{b}b\bar{b}$  search, the MV<sub>2</sub> algorithm with a  
2587 20% fraction of charm events in training is used (MV<sub>2c20</sub>). Once the algorithm is selected, an efficiency  
2588 working point must also be chosen. This working point defines the efficiency with which true  $b$ -jets  
2589 are tagged and also fixes the overall background rejection of the algorithm. Higher efficiency working  
2590 points accept more true  $b$ -jets but also allow for more background. Five different working points (70%,  
2591 77%, 80%, 85%, 90%) are tested. With each working point, the full data driven background estimation  
2592 method is run to quantify the amount of background that will be present in the final signal region. The  
2593 significance is quantified using the median discovery significance for signal and background with Poisson

2594 errors, given in equation A.1 [112].

$$Z = \sqrt{2 \left( (s + b) \ln \left( 1 + \frac{s}{b} \right) - s \right)} \quad (\text{A.1})$$

2595 Note that in the limit where  $s$  is much smaller than  $b$ , this equation reduces to the more well known  
 2596  $s/\sqrt{b}$ .

2597 Figure A.1 shows the estimated significance as a function of signal mass in RSG  $c = 1$  models for  
 2598 the  $3b$  and  $4b$  signal regions. The 77% working point gives the best performance over a wide range of  
 2599 masses in the  $4b$  signal region. As this is the region which contributes the most to the total discovery  
 2600 significance, the 77% efficiency working point is chosen for the analysis.

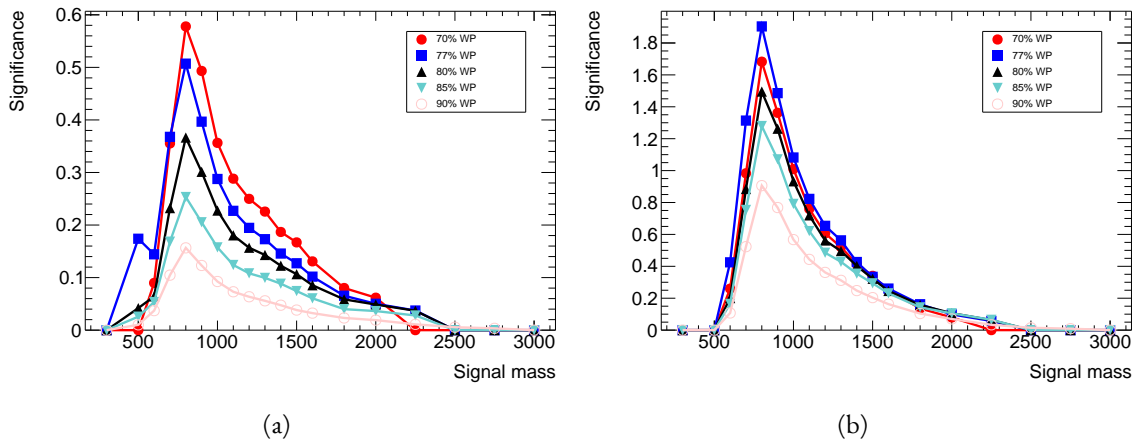


Figure A.1: Estimated significance as a function of signal mass for RSG  $c = 1$  models in the  $3b$  (a) and  $4b$  (b) regions for different  $b$ -tagging efficiency working points

# B

2601

2602

## *b*-tagging performance at high $p_T$

2603 One of the limiting factors of the signal acceptance in the *FourB full* search at high resonance masses is  
2604 the degradation of the *b*-tagging efficiency for high  $p_T$  jets. This appendix presents a study of the under-  
2605 lying causes of this degradation.

### 2606 B.I MV<sub>2</sub> ALGORITHM OVERVIEW

2607 The MV<sub>2</sub> algorithm is a boosted decision tree incorporating twenty-four input variables constructed  
2608 from three lower level input algorithms: IPxD, SVI, and JetFitter. IPxD uses the two and three dimen-  
2609 sional impact parameter information of tracks in the jet to construct templates for light, charm, and bot-  
2610 tom quarks and compute likelihood ratios. SVI is a secondary vertex reconstruction algorithm. JetFitter  
2611 attempts to fit to the full decay chain of the *B* hadron, looking for multiple decay vertices aligned along a  
2612 single axis. Figure B.1 summarizes the inputs to MV<sub>2</sub>.

IP2D and IP3D (6 inputs)	SV1 (8 inputs)	JetFitter (8 inputs)
$\log(p_b/p_u)$	Mass	Mass
$\log(p_b/p_c)$	Energy fraction	Energy fraction
$\log(p_c/p_u)$	# tracks at vertex	# vertices
	# 2 track vertices	# tracks at vertex
	Lxy	# 1 track vertices
	L3d	# 2 track vertices
	3D significance	3D significance
	$\Delta R$	$\Delta R$
Kinematics (2 inputs)		
	$p_T$	
	$\eta$	

Figure B.1: Summary of the inputs to the MV2  $b$ -tagging algorithm

2613    **B.2 CHANGES IN MV2 SCORE AT HIGH  $p_T$**

2614    The degradation of  $b$ -tagging at high  $p_T$  was studied in particular in the context of RSG models at high  
 2615    mass. Figure B.2 shows the  $p_T$  of the leading track jet inside of the leading calorimeter jet in RSG events.  
 2616    At high  $m_{G_K^*}$ , the  $p_T$  spectrum of track jets is much harder than at lower masses due to the increased  
 2617    Higgs  $p_T$ .

2618    Figure B.3 shows the MV2c2o algorithm score for the leading and subleading track jets inside of the  
 2619    leading calorimeter jet. In both cases, it can be seen that at higher RSG masses the MV2 score shifts to-  
 2620    wards more background like (negative) values. Additionally, this effect is more pronounced in the lead-  
 2621    ing track jet than the subleading.

2622    To understand what is causing this change in the MV2c2o score, the same comparisons can be made  
 2623    for the input variables of MV2c2o. The focus in these comparisons will be on the leading track jet as  
 2624    this is the one seen to have the largest difference in MV2 score. Figure B.4 shows the log likelihood ratio  
 2625     $\log(p_b/p_u)$  from the IP3D (three dimensional impact parameter) algorithm. At higher masses, the IP3D  
 2626    likelihood ratio distribution does become more background-like.

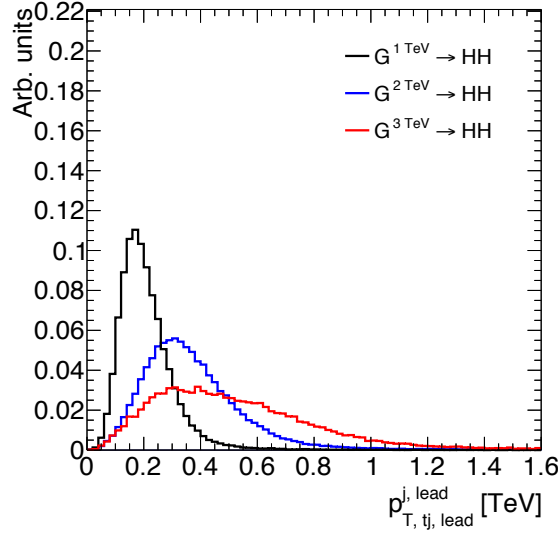


Figure B.2:  $p_T$  of the leading track jet in the leading calorimeter jet for different signal masses in RSG  $c = 1$  models

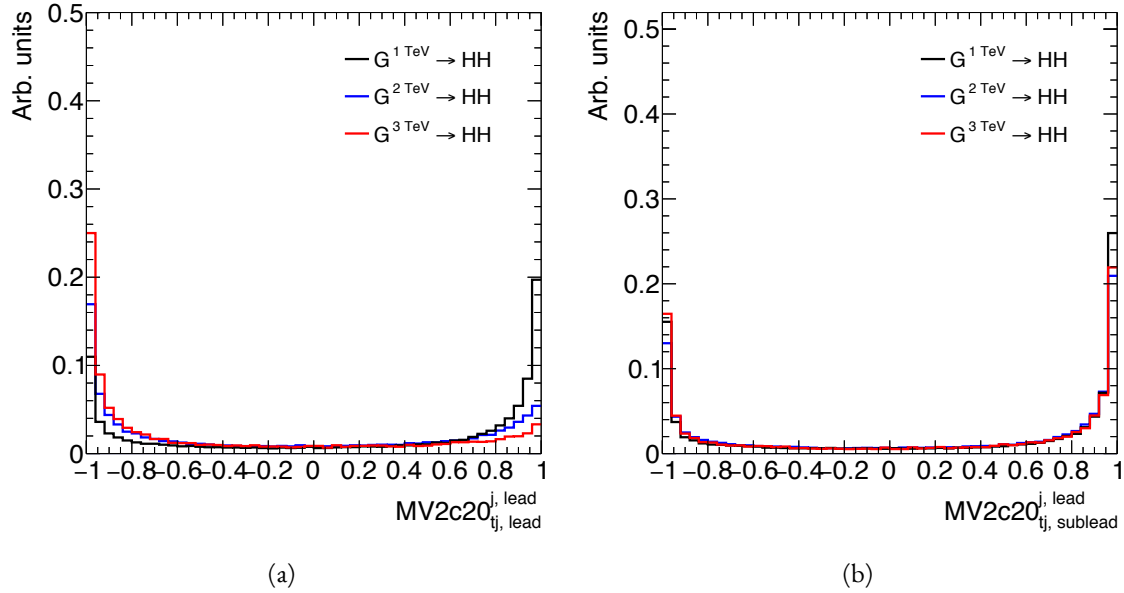


Figure B.3: MV2c20 score for the leading track jet (a) and subleading track jet (b) of the leading calorimeter jet for different signal masses in RSG  $c = 1$  models

2627     Figure B.5 shows the mass and number of tracks at the secondary vertex computed by the SV1 algo-  
 2628     rithm. When there is no secondary vertex found, the algorithm assigns a default negative value for these  
 2629     quantities. Both of these distributions show that there is a significantly larger fraction of jets where no  
 2630     secondary vertex is found in the high mass samples compared to the  $m_{G_{KK}^*} = 1$  TeV sample. The SV1

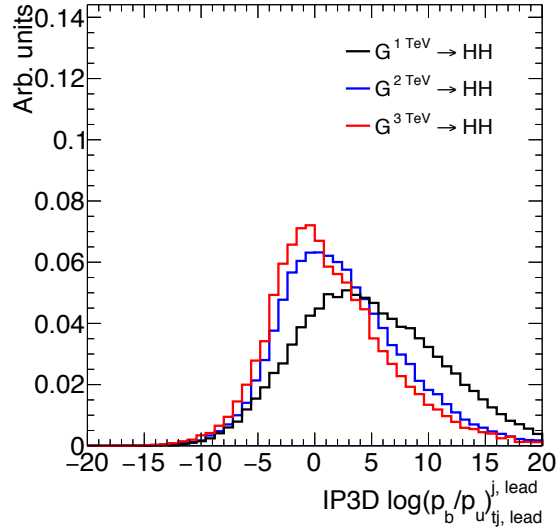


Figure B.4: IP3D log-likehood ratio ( $\log(p_b/p_u)$ ) of the leading track jet in the leading calorimeter jet for different signal masses in RSG  $c = 1$  models

algorithm's inability to find a secondary vertex could be an important factor in the overall MV<sub>2</sub> score shift, as this eliminates eight of the input variables that would normally contribute information to the algorithm.

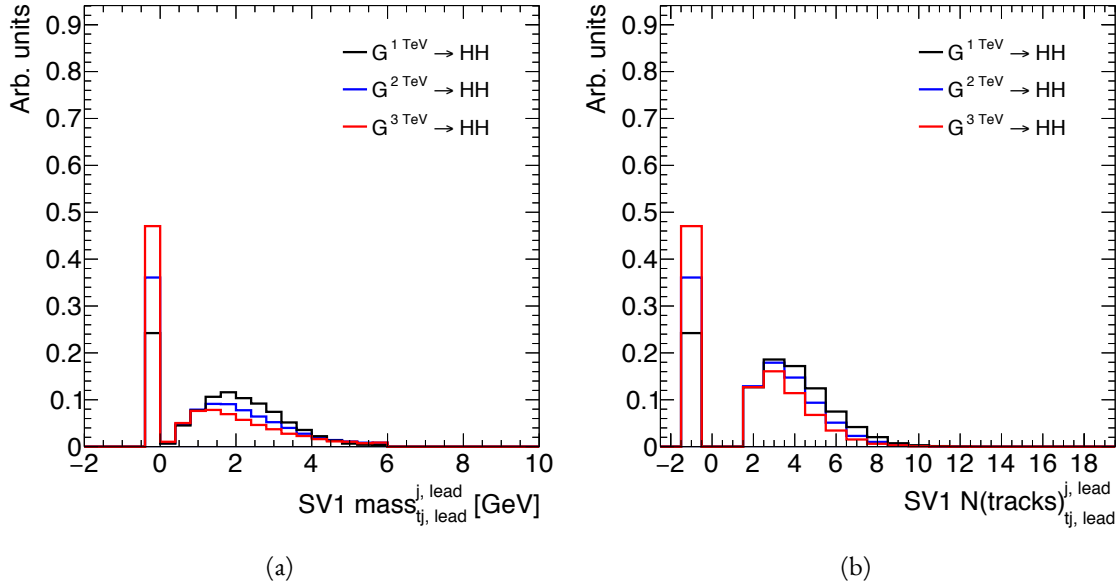


Figure B.5: Mass (a) and number of tracks (b) for the secondary vertices computed with the SV1 algorithm. When no secondary vertex is found, the quantiites are assigned to default negative values.

2634      Figure B.6 shows the same quantities for the JetFitter algorithm. In this case, there is also a change in  
 2635      the fraction of jets which have their secondary vertices successfully reconstructed, but this change is not  
 2636      as drastic as that seen in SVI. There is also an increase in the number of jets which have high values of  
 2637      mass.

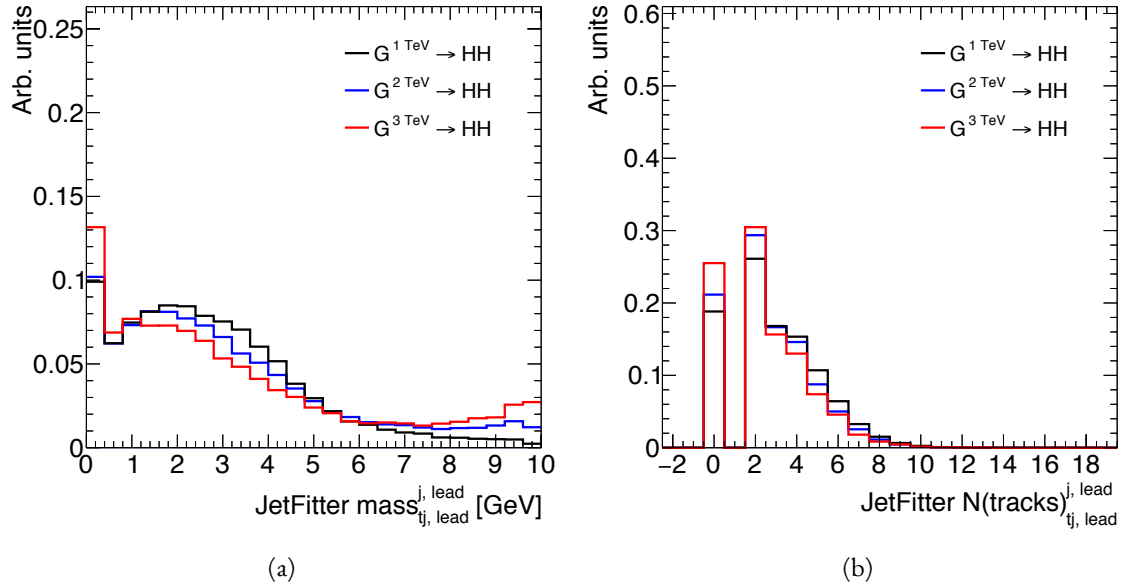


Figure B.6: Mass (a) and number of tracks (b) for vertices computed with the JetFitter algorithm. When no vertices are found, the quantities are assigned to default negative values.

### 2638      B.3    TAGGING EFFICIENCY BY INDIVIDUAL JET

2639      In the last section, the largest changes in MV<sub>2</sub> score were seen for the leading track jet inside the leading  
 2640      calorimeter jet. To confirm that the overall 4*b* tagging efficiency is indeed degrading because of degra-  
 2641      dation of the leading track jet efficiency, the tagging efficiency for each individual jet as a function of mass  
 2642      can be compared. This is shown in figure B.7. The figure shows that the leading jet tagging efficiency  
 2643      in both calorimeter jets degrades heavily, while the sub-lead jet tagging efficiency remains relatively con-  
 2644      stant.

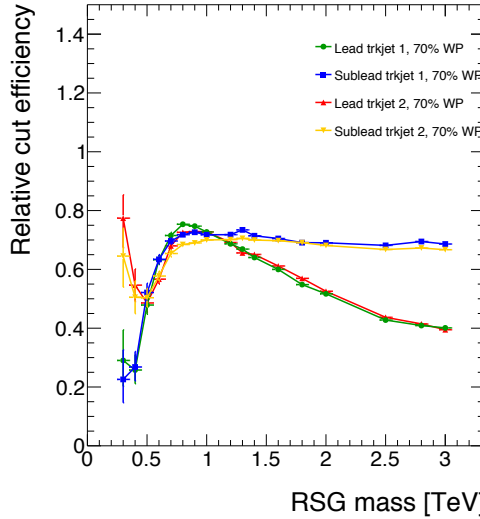


Figure B.7: MV<sub>2</sub>c<sub>20</sub>  $b$ -tagging efficiency for each of the four track jets in the boosted  $4b$  selection as a function of RSG mass for  $c = 1$  models.

2645 **B.4 EFFECT OF MULTIPLE  $b$ -QUARKS INSIDE ONE JET**

2646 One hypothesis for why the efficiency of  $b$ -tagging the leading track jet degrades is that at high masses,  
2647 the  $b$  quarks get close enough together that both of them are inside of the leading track jet. Because MV<sub>2</sub>  
2648 is not tuned for tagging multiple  $b$  quarks inside one jet, the tagging efficiency could degrade. Figure B.8  
2649 shows MV<sub>2</sub> scores and SV<sub>1</sub> mass for cases where there are two  $b$  quarks at truth level within the radius  
2650 of the leading track jet compared to cases where there is only one true  $b^*$ . This figure suggests that the  
2651 presence of two  $b$ -quarks inside the leading jet is not the cause of the degradation in efficiency. There is a  
2652 change in the shape of the MV<sub>2</sub> score distribution, but it is not nearly as pronounced as that seen in B.3  
2653 at higher masses. Additionally, the fraction of jets with no secondary vertex found is nearly identical in  
2654 the track jets with two truth  $b$ -quarks.

---

\*When two truth  $b$  quarks are required in the leading jet, the subleading jet is required to have zero. When one is required for the leading, one is also required for the subleading.

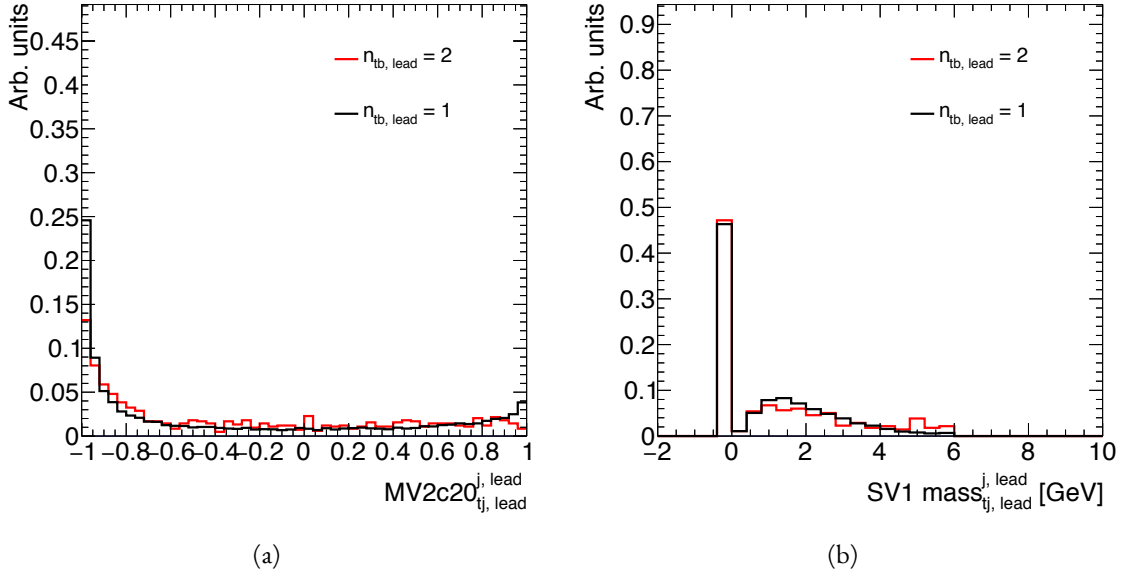


Figure B.8: MV2c20 score (a) and SV1 mass (b) for leading track jets with two truth  $b$  quarks ( $n_{tb, \text{lead}} = 2$ ) compared to those with only one truth  $b$  ( $n_{tb, \text{lead}} = 1$ ).

## 2655 B.5 CHANGES IN TRACK QUALITY AT HIGH $p_T$

2656 Another hypothesis for the degradation of the  $b$ -tagging efficiency is a decrease in track quality for high  
 2657  $p_T$   $b$  jets. One way to check the overall quality of the tracking inside the jet is to investigate quantities  
 2658 related to the leading track inside of the track jet. Figure B.9 shows the fit  $\chi^2/n_{\text{DOF}}$  and number of hits  
 2659 in the pixel detector for the leading track of the leading track jet. In both cases, the figure shows that in  
 2660 higher mass samples, the quality of the leading track inside of the track jet degrades substantially. The  
 2661 fit quality is lessened and the tracks have less hits in the pixel detector. This is likely due to the fact that  
 2662 at higher  $p_T$ , the  $B$ -hadron will sometimes live long enough to miss the IBL and first pixel layer, thus  
 2663 decreasing the number of hits on the track.

2664 To check whether this is the cause for the shift in the MV2 score and the higher difficulty in recon-  
 2665 structing secondary vertices, jets whose leading track have at least four pixel hits are compared with those  
 2666 whose tracks have less than four pixel hits. The results for the MV2 score and SV1 mass are shown in fig-  
 2667 ure B.10. Track jets where the leading track does not have at least four pixel hits are more likely to not  
 2668 have a secondary vertex reconstructed. Additionally, their MV2c20 score is shifted more significantly to

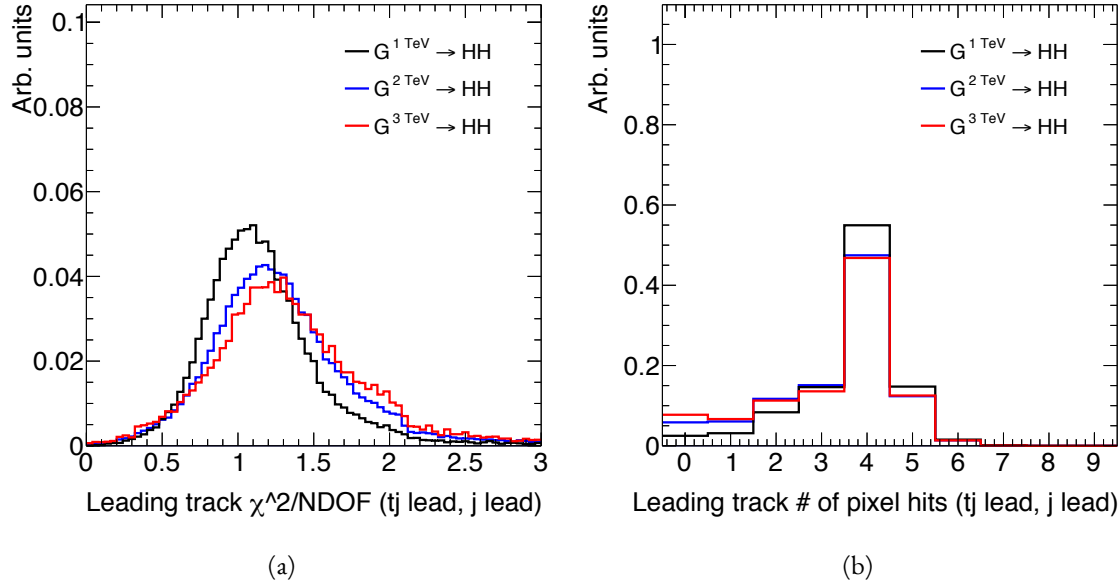


Figure B.9: Track fit  $\chi^2/n_{\text{DOF}}$  (a) and number of pixel detector hits (b) for the leading track of the leading track jet in different mass RSG  $c = 1$  samples

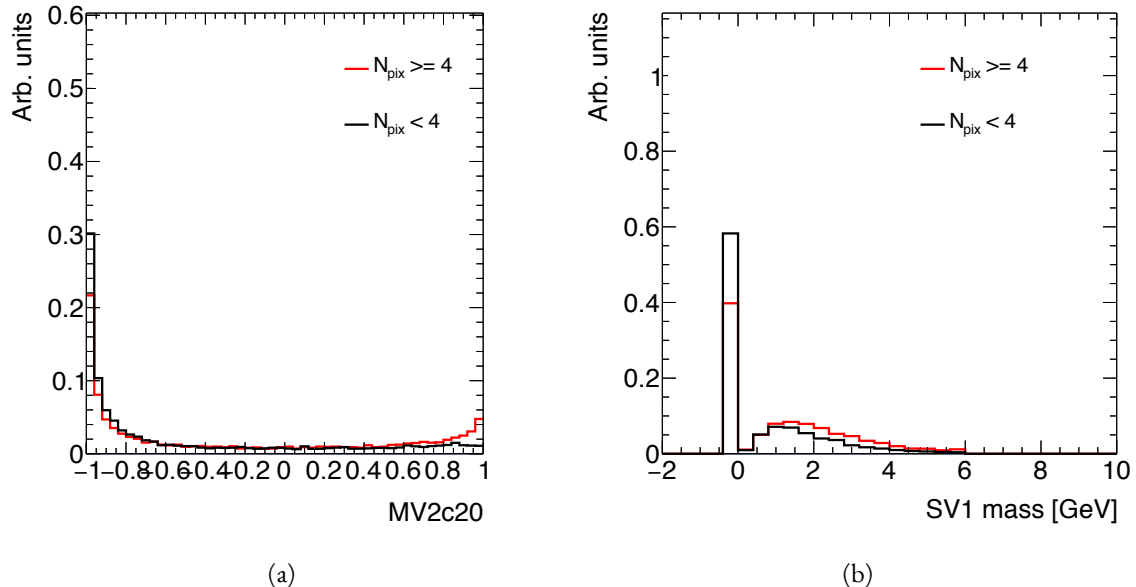


Figure B.10: MV2c20 score (a) and SV1 mass (b) for leading track jets whose leading track jet has at least four pixel hits ( $N_{\text{pix}} \geq 4$ ) compared to those which do not ( $N_{\text{pix}} < 4$ ).

<sup>2669</sup> background-like values. This seems to confirm the hypothesis that degrading track quality is responsible  
<sup>2670</sup> for the lowered  $b$ -tagging efficiency at high  $p_{\text{T}}$ .

# References

2671

- 2672 [1] Georges Aad et al. Observation of a new particle in the search for the Standard Model Higgs  
2673 boson with the ATLAS detector at the LHC. *Phys. Lett.*, B716:1–29, 2012. doi: 10.1016/j.physletb.  
2674 2012.08.020.
- 2675 [2] Serguei Chatrchyan et al. Observation of a new boson at a mass of 125 GeV with the CMS experi-  
2676 ment at the LHC. *Phys. Lett.*, B716:30–61, 2012. doi: 10.1016/j.physletb.2012.08.021.
- 2677 [3] David Griffiths. *Introduction to elementary particles*. 2008.
- 2678 [4] F. Halzen and Alan D. Martin. *QUARKS AND LEPTONS: AN INTRODUCTORY*  
2679 *COURSE IN MODERN PARTICLE PHYSICS*. 1984. ISBN 0471887412, 9780471887416.
- 2680 [5] Christopher G. Tully. *Elementary particle physics in a nutshell*. 2011.
- 2681 [6] K. A. Olive et al. Review of Particle Physics. *Chin. Phys.*, C38:090001, 2014. doi: 10.1088/  
2682 1674-1137/38/9/090001.
- 2683 [7] Matthew D. Schwartz. *Quantum Field Theory and the Standard Model*. Cambridge University  
2684 Press, 2014. ISBN 1107034736, 9781107034730. URL <http://www.cambridge.org/us/academic/subjects/physics/theoretical-physics-and-mathematical-physics/quantum-field-theory-and-standard-model>.
- 2687 [8] S. Dawson. Introduction to electroweak symmetry breaking. In *High energy physics and cos-  
2688 mology. Proceedings, Summer School, Trieste, Italy, June 29-July 17, 1998*, pages 1–83, 1998. URL  
2689 <http://alice.cern.ch/format/showfull?sysnb=0301862>.
- 2690 [9] S. L. Glashow. Partial Symmetries of Weak Interactions. *Nucl. Phys.*, 22:579–588, 1961. doi:  
2691 10.1016/0029-5582(61)90469-2.
- 2692 [10] Steven Weinberg. A Model of Leptons. *Phys. Rev. Lett.*, 19:1264–1266, 1967. doi: 10.1103/  
2693 PhysRevLett.19.1264.
- 2694 [11] A. Salam. *Elementary Particle Theory*. Almqvist and Wiksell, Stockholm, 1968.
- 2695 [12] J. Iliopoulos S.L. Glashow and L. Maiani. *D2:1285*, 1970.
- 2696 [13] R. Keith Ellis, W. James Stirling, and B. R. Webber. QCD and collider physics. *Camb. Monogr.*  
2697 *Part. Phys. Nucl. Phys. Cosmol.*, 8:1–435, 1996.

- 2698 [14] P. W. Higgs. Broken symmetries and the masses of gauge bosons. *13*:508, 1964.
- 2699 [15] P. W. Higgs. Spontaneous symmetry breakdown without massless bosons. *145*:1156, 1966.
- 2700 [16] F. Englert and R. Brout. Broken symmetry and the mass of gauge vector mesons. *13*:321, 1964.
- 2701 [17] G. S. Guralnik, C. R. Hagen, and T. W. .B. Kibble. Global conservation laws and massless parti-  
2702 cles. *Phys. Rev. Lett.*, *13*:585, 1964. doi: [10.1103/PhysRevLett.13.585](https://doi.org/10.1103/PhysRevLett.13.585).
- 2703 [18] LHC Higgs Cross Section Working Group, S. Heinemeyer, C. Mariotti, G. Passarino, and  
2704 R. Tanaka (Eds.). Handbook of LHC Higgs Cross Sections: 3, Higgs Properties. 2013.
- 2705 [19] J. Baglio, A. Djouadi, R. Gröber, M. M. Mühlleitner, J. Quevillon, and M. Spira. The mea-  
2706 surement of the Higgs self-coupling at the LHC: theoretical status. *JHEP*, *04*:151, 2013. doi:  
2707 [10.1007/JHEP04\(2013\)151](https://doi.org/10.1007/JHEP04(2013)151).
- 2708 [20] Matthew J. Dolan, Christoph Englert, and Michael Spannowsky. New Physics in LHC Higgs  
2709 boson pair production. *Phys. Rev.*, *D87*(5):055002, 2013. doi: [10.1103/PhysRevD.87.055002](https://doi.org/10.1103/PhysRevD.87.055002).
- 2710 [21] Roberto Contino, Margherita Ghezzi, Mauro Moretti, Giuliano Panico, Fulvio Piccinini, and  
2711 Andrea Wulzer. Anomalous Couplings in Double Higgs Production. *JHEP*, *08*:154, 2012. doi:  
2712 [10.1007/JHEP08\(2012\)154](https://doi.org/10.1007/JHEP08(2012)154).
- 2713 [22] R. Grober and M. Mühlleitner. Composite Higgs Boson Pair Production at the LHC. *JHEP*, *06*:  
2714 020, 2011. doi: [10.1007/JHEP06\(2011\)020](https://doi.org/10.1007/JHEP06(2011)020).
- 2715 [23] Lisa Randall and Raman Sundrum. A Large mass hierarchy from a small extra dimension. *Phys.*  
2716 *Rev. Lett.*, *83*:3370–3373, 1999. doi: [10.1103/PhysRevLett.83.3370](https://doi.org/10.1103/PhysRevLett.83.3370).
- 2717 [24] Kaustubh Agashe, Hooman Davoudiasl, Gilad Perez, and Amarjit Soni. Warped Gravitons at the  
2718 LHC and Beyond. *Phys. Rev.*, *D76*:036006, 2007. doi: [10.1103/PhysRevD.76.036006](https://doi.org/10.1103/PhysRevD.76.036006).
- 2719 [25] A. Liam Fitzpatrick, Jared Kaplan, Lisa Randall, and Lian-Tao Wang. Searching for the Kaluza-  
2720 Klein Graviton in Bulk RS Models. *JHEP*, *09*:013, 2007. doi: [10.1088/1126-6708/2007/09/013](https://doi.org/10.1088/1126-6708/2007/09/013).
- 2721 [26] Julien Baglio, Otto Eberhardt, Ulrich Nierste, and Martin Wiebusch. Benchmarks for Higgs Pair  
2722 Production and Heavy Higgs boson Searches in the Two-Higgs-Doublet Model of Type II. *Phys.*  
2723 *Rev.*, *D90*(1):015008, 2014. doi: [10.1103/PhysRevD.90.015008](https://doi.org/10.1103/PhysRevD.90.015008).
- 2724 [27] G. C. Branco, P. M. Ferreira, L. Lavoura, M. N. Rebelo, Marc Sher, and Joao P. Silva. Theory  
2725 and phenomenology of two-Higgs-doublet models. *Phys. Rept.*, *516*:1–102, 2012. doi: [10.1016/j.physrep.2012.02.002](https://doi.org/10.1016/j.physrep.2012.02.002).
- 2727 [28] Howard E. Haber and Oscar Stål. New LHC benchmarks for the  $\mathcal{CP}$ -conserving two-Higgs-  
2728 doublet model. *Eur. Phys. J.*, *C75*(10):491, 2015. doi: [10.1140/epjc/s10052-015-3697-x](https://doi.org/10.1140/epjc/s10052-015-3697-x).

- 2729 [29] Jose M. No and Michael Ramsey-Musolf. Probing the Higgs Portal at the LHC Through Reso-  
 2730       nant di-Higgs Production. *Phys. Rev.*, D89(9):095031, 2014. doi: 10.1103/PhysRevD.89.095031.
- 2731 [30] Johan Alwall, Michel Herquet, Fabio Maltoni, Olivier Mattelaer, and Tim Stelzer. MadGraph  
 2732       5:Going Beyond. *JHEP*, 1106:128, 2011. doi: 10.1007/JHEP06(2011)128.
- 2733 [31] Lyndon R Evans and Philip Bryant. LHC Machine. *J. Instrum.*, 3:S08001. 164 p, 2008. URL  
 2734       <https://cds.cern.ch/record/1129806>. This report is an abridged version of the LHC  
 2735       Design Report (CERN-2004-003).
- 2736 [32] ATLAS Collaboration. The ATLAS experiment at the CERN Large Hadron Collider. *JINST*, 3:  
 2737       S08003, 2008. doi: 10.1088/1748-0221/3/08/S08003.
- 2738 [33] CMS Collaboration. The cms experiment at the cern lhc. *Journal of Instrumentation*, 3(08):  
 2739       S08004, 2008. URL <http://stacks.iop.org/1748-0221/3/i=08/a=S08004>.
- 2740 [34] LHCb Collaoration. The LHCb Detector at the LHC. *JINST*, 3:S08005, 2008. doi: 10.1088/  
 2741       1748-0221/3/08/S08005.
- 2742 [35] ALICE Collaboration. The alice experiment at the cern lhc. *Journal of Instrumentation*, 3(08):  
 2743       S08002, 2008. URL <http://stacks.iop.org/1748-0221/3/i=08/a=S08002>.
- 2744 [36] Lyndon Evans. The Large Hadron Collider. In Holstein, BR and Haxton, WC and Jawahery,  
 2745       A, editor, *ANNUAL REVIEW OF NUCLEAR AND PARTICLE SCIENCE, VOL 61*,  
 2746       volume 61 of *Annual Review of Nuclear and Particle Science*, pages 435–466. 2011. doi: {10.1146/}  
 2747       annurev-nucl-102010-130438}.
- 2748 [37] ATLAS Collaboration. Luminosity Determination in  $pp$  Collisions at  $\sqrt{s} = 7$  TeV Using the  
 2749       ATLAS Detector at the LHC. *Eur. Phys. J.*, C 71:1630, 2011. doi: 10.1140/epjc/s10052-011-1630-5.
- 2750 [38] Mike Lamont for the LHC team. The First Years of LHC Operation for Luminosity Production.  
 2751       International Particle Accelerator Conference, 2013. URL [https://accelconf.web.cern.ch/accelconf/IPAC2013/talks/moyab101\\_talk.pdf](https://accelconf.web.cern.ch/accelconf/IPAC2013/talks/moyab101_talk.pdf).
- 2753 [39] Paul Collier for the LHC team. LHC Machine Status. CERN Resource Review Board, 2015.  
 2754       URL <https://cds.cern.ch/record/2063924/files/CERN-RRB-2015-119.PDF>.
- 2755 [40] Track Reconstruction Performance of the ATLAS Inner Detector at  $\sqrt{s} = 13$  TeV. Technical  
 2756       Report ATL-PHYS-PUB-2015-018, CERN, Geneva, Jul 2015. URL <http://cds.cern.ch/record/2037683>.

- 2758 [41] M Capeans, G Darbo, K Einsweiller, M Elsing, T Flick, M Garcia-Sciveres, C Gemme, H Perneg-  
2759 ger, O Rohne, and R Vuillermet. ATLAS Insertable B-Layer Technical Design Report. Tech-  
2760 nical Report CERN-LHCC-2010-013, ATLAS-TDR-19, CERN, Geneva, Sep 2010. URL  
2761 <https://cds.cern.ch/record/1291633>.
- 2762 [42] ATLAS Collaboration. ATLAS Trigger Operations Public Results. 2015. URL <https://twiki.cern.ch/twiki/bin/view/AtlasPublic/TriggerOperationPublicResults>.
- 2764 [43] ATLAS Collaboration. ATLAS Luminosity Public Results, Run 1. 2012. URL <https://twiki.cern.ch/twiki/bin/view/AtlasPublic/LuminosityPublicResults>.
- 2766 [44] ATLAS Collaboration. ATLAS Luminosity Public Results, Run 2. 2015. URL <https://twiki.cern.ch/twiki/bin/view/AtlasPublic/LuminosityPublicResultsRun2>.
- 2768 [45] T Kawamoto, S Vlachos, L Pontecorvo, J Dubbert, G Mikenberg, P Iengo, C Dallapiccola,  
2769 C Amelung, L Levinson, R Richter, and D Lellouch. New Small Wheel Technical Design Re-  
2770 port. Technical Report CERN-LHCC-2013-006, ATLAS-TDR-020, CERN, Geneva, Jun 2013.  
2771 URL <https://cds.cern.ch/record/1552862>. ATLAS New Small Wheel Technical Design  
2772 Report.
- 2773 [46] Y. Giomataris, Ph. Rebours, J.P. Robert, and G. Charpak. Micromegas: a high-granularity  
2774 position-sensitive gaseous detector for high particle-flux environments. *Nuclear Instruments  
2775 and Methods in Physics Research Section A: Accelerators, Spectrometers, Detectors and As-  
2776 sociated Equipment*, 376(1):29 – 35, 1996. ISSN 0168-9002. doi: [http://dx.doi.org/10.1016/0168-9002\(96\)00175-1](http://dx.doi.org/10.1016/0168-9002(96)00175-1). URL <http://www.sciencedirect.com/science/article/pii/0168900296001751>.
- 2777 [47] T. Alexopoulos, J. Burnens, R. de Oliveira, G. Glonti, O. Pizzirussi, V. Polychronakos,  
2778 G. Sekhniaidze, G. Tsipolitis, and J. Wotschack. A spark-resistant bulk-micromegas chamber for  
2779 high-rate applications. *Nuclear Instruments and Methods in Physics Research Section A: Acceler-  
2780 ators, Spectrometers, Detectors and Associated Equipment*, 640(1):110 – 118, 2011. ISSN 0168-9002.  
2781 doi: <http://dx.doi.org/10.1016/j.nima.2011.03.025>. URL <http://www.sciencedirect.com/science/article/pii/S0168900211005869>.
- 2784 [48] Joao Pequenao and Paul Schaffner. An computer generated image representing how ATLAS  
2785 detects particles. Jan 2013. URL <https://cds.cern.ch/record/1505342>.
- 2787 [49] Improved electron reconstruction in ATLAS using the Gaussian Sum Filter-based model for  
2788 bremsstrahlung. Technical Report ATLAS-CONF-2012-047, CERN, Geneva, May 2012. URL  
2789 <https://cds.cern.ch/record/1449796>.

- 2790 [50] Electron efficiency measurements with the ATLAS detector using the 2012 LHC proton-proton  
2791 collision data. Technical Report ATLAS-CONF-2014-032, CERN, Geneva, Jun 2014. URL  
2792 <https://cds.cern.ch/record/1706245>.
- 2793 [51] Georges Aad et al. Electron and photon energy calibration with the ATLAS detector using LHC  
2794 Run 1 data. *Eur. Phys. J.*, C74(10):3071, 2014. doi: 10.1140/epjc/s10052-014-3071-4.
- 2795 [52] Georges Aad et al. Measurement of the muon reconstruction performance of the ATLAS detec-  
2796 tor using 2011 and 2012 LHC proton–proton collision data. *Eur. Phys. J.*, C74(11):3130, 2014. doi:  
2797 10.1140/epjc/s10052-014-3130-x.
- 2798 [53] W Lampl, S Laplace, D Lelas, P Loch, H Ma, S Menke, S Rajagopalan, D Rousseau, S Snyder,  
2799 and G Unal. Calorimeter Clustering Algorithms: Description and Performance. Technical  
2800 Report ATL-LARG-PUB-2008-002. ATL-COM-LARG-2008-003, CERN, Geneva, Apr 2008.  
2801 URL <https://cds.cern.ch/record/1099735>.
- 2802 [54] Georges Aad et al. Topological cell clustering in the ATLAS calorimeters and its performance in  
2803 LHC Run 1. 2016.
- 2804 [55] Matteo Cacciari, Gavin P. Salam, and Gregory Soyez. The Anti-k(t) jet clustering algorithm.  
2805 *JHEP*, 04:063, 2008. doi: 10.1088/1126-6708/2008/04/063.
- 2806 [56] Monte Carlo Calibration and Combination of In-situ Measurements of Jet Energy Scale, Jet En-  
2807 ergy Resolution and Jet Mass in ATLAS. Technical Report ATLAS-CONF-2015-037, CERN,  
2808 Geneva, Aug 2015. URL <http://cds.cern.ch/record/2044941>.
- 2809 [57] Georges Aad et al. Performance of  $b$ -Jet Identification in the ATLAS Experiment. 2015.
- 2810 [58] Expected performance of the ATLAS  $b$ -tagging algorithms in Run-2. Technical Report ATL-  
2811 PHYS-PUB-2015-022, CERN, Geneva, Jul 2015. URL <http://cds.cern.ch/record/2037697>.
- 2812
- 2813 [59] Georges Aad et al. Performance of Missing Transverse Momentum Reconstruction in Proton-  
2814 Proton Collisions at 7 TeV with ATLAS. *Eur. Phys. J.*, C72:1844, 2012. doi: 10.1140/epjc/  
2815 s10052-011-1844-6.
- 2816 [60] Performance of Missing Transverse Momentum Reconstruction in ATLAS studied in Proton-  
2817 Proton Collisions recorded in 2012 at 8 TeV. Technical Report ATLAS-CONF-2013-082, CERN,  
2818 Geneva, Aug 2013. URL <http://cds.cern.ch/record/1570993>.
- 2819 [61] ATLAS Collaboration. Observation and measurement of Higgs boson decays to  $WW^*$  with the  
2820 ATLAS detector. *Phys. Rev. D*, 92(012006), 2015.

- 2821 [62] Aaron James Armbruster. Discovery of a Higgs Boson with the ATLAS detector. 2013. CERN-  
2822 THESIS-2013-047.
- 2823 [63] G. Cowan, K. Cranmer, E. Gross, and O. Vitells. Asymptotic formulae for likelihood-based tests  
2824 of new physics. *Eur. Phys. J., C* 71:1554, 2011. doi: 10.1140/epjc/s10052-011-1554-0.
- 2825 [64] ATLAS Collaboration. Limits on the production of the Standard Model Higgs Boson in  $pp$   
2826 collisions at  $\sqrt{s} = 7$  TeV with the ATLAS detector. *Eur. Phys. J., C* 71:1728, 2011. doi: 10.1140/  
2827 epjc/s10052-011-1728-9.
- 2828 [65] ATLAS Collaboration. Performance of the ATLAS muon trigger in  $pp$  collisions at  $\sqrt{s} = 8$   
2829 TeV. *Eur. Phys. J. C*, (arXiv:1408.3179. CERN-PH-EP-2014-154):75. 19 p, Aug 2014. URL <https://cds.cern.ch/record/1749694>.
- 2831 [66] ATLAS collaboration. Electron trigger performance in 2012 ATLAS data, 2015. ATLAS-COM-  
2832 DAQ-2015-091.
- 2833 [67] Paolo Nason. A new method for combining NLO QCD with shower Monte Carlo algorithms.  
2834 *JHEP*, 11:040, 2004.
- 2835 [68] B. P. Kersevan and E. Richter-Was. The Monte Carlo event generator AcerMC version 2.0 with  
2836 interfaces to PYTHIA 6.2 and HERWIG 6.5. 2004.
- 2837 [69] Nikolas Kauer and Giampiero Passarino. Inadequacy of zero-width approximation for a light  
2838 Higgs boson signal. 2012.
- 2839 [70] T. Gleisberg, Stefan Hoeche, F. Krauss, M. Schonherr, S. Schumann, et al. Event generation with  
2840 SHERPA 1.1. *JHEP*, 0902:007, 2009. doi: 10.1088/1126-6708/2009/02/007.
- 2841 [71] Michelangelo L. Mangano et al. ALPGEN, a generator for hard multiparton processes in  
2842 hadronic collisions. *JHEP*, 0307:001, 2003. doi: 10.1088/1126-6708/2003/07/001.
- 2843 [72] Torbjorn Sjostrand, Stephen Mrenna, and Peter Z. Skands. PYTHIA 6.4 Physics and Manual.  
2844 *JHEP*, 0605:026, 2006. doi: 10.1088/1126-6708/2006/05/026.
- 2845 [73] Torbjorn Sjostrand, Stephen Mrenna, and Peter Z. Skands. A Brief Introduction to PYTHIA 8.1.  
2846 *Comput.Phys.Commun.*, 178:852–867, 2008. doi: 10.1016/j.cpc.2008.01.036.
- 2847 [74] G. Corcella et al. HERWIG 6: An event generator for hadron emission reactions with interfering  
2848 gluons (including super-symmetric processes). *JHEP*, 01:010, 2001. doi: 10.1088/1126-6708/2001/  
2849 01/010.
- 2850 [75] J. M. Butterworth, Jeffrey R. Forshaw, and M. H. Seymour. Multiparton interactions in photo-  
2851 production at HERA. *Z. Phys., C* 72:637, 1996. doi: 10.1007/s002880050286.

- 2852 [76] Jun Gao, Marco Guzzi, Joey Huston, Hung-Liang Lai, Zhao Li, et al. The CT10 NNLO Global  
 2853 Analysis of QCD. *Phys. Rev.*, D89:033009, 2014. doi: 10.1103/PhysRevD.89.033009.
- 2854 [77] P. M. Nadolsky. Implications of CTEQ global analysis for collider observables. *Phys. Rev.*, D 78:  
 2855 013004, 2008. doi: 10.1103/PhysRevD.78.013004.
- 2856 [78] A. Sherstnev and R. S. Thorne. Parton distributions for the LHC. *Eur. Phys. J.*, C 55:553, 2009.  
 2857 doi: 10.1140/epjc/s10052-008-0610-x.
- 2858 [79] S. Agostinelli et al. GEANT4, a simulation toolkit. *Nucl. Instrum. Meth.*, A 506:250, 2003. doi:  
 2859 10.1016/S0168-9002(03)01368-8.
- 2860 [80] R.K. Ellis, I. Hinchliffe, M. Soldate, and J.J. Van Der Bij. Higgs decay to  $\tau+\tau$ -a possible signature  
 2861 of intermediate mass higgs bosons at high energy hadron colliders. *Nuclear Physics B*, 297(2):  
 2862 221 – 243, 1988. ISSN 0550-3213. doi: [http://dx.doi.org/10.1016/0550-3213\(88\)90019-3](http://dx.doi.org/10.1016/0550-3213(88)90019-3). URL  
 2863 <http://www.sciencedirect.com/science/article/pii/0550321388900193>.
- 2864 [81] Eilam Gross and Ofer Vitells. Transverse mass observables for charged Higgs boson searches at  
 2865 hadron colliders. *Phys. Rev.*, D81:055010, 2010. doi: 10.1103/PhysRevD.81.055010.
- 2866 [82] J. R. Andersen et al. Les Houches 2013: Physics at TeV Colliders: Standard Model Working  
 2867 Group Report. 2014.
- 2868 [83] I. Stewart and F. Tackmann. Theory uncertainties for Higgs mass and other searches using jet  
 2869 bins. *Phys. Rev.*, D 85:034011, 2012. doi: 10.1103/PhysRevD.85.034011.
- 2870 [84] ATLAS Collaboration. Luminosity Determination in  $pp$  Collisions at  $\sqrt{s} = 7$  TeV Using the  
 2871 ATLAS Detector at the LHC. *Eur. Phys. J.*, C 71:1630, 2011. doi: 10.1140/epjc/s10052-011-1630-5.
- 2872 [85] Jet energy scale and its systematic uncertainty in proton-proton collisions at  $\sqrt{s} = 7$  tev with  
 2873 atlas 2011 data. *ATLAS-CONF-2013-004*, 2013.
- 2874 [86] Calibrating the  $b$ -tag efficiency and mistag rate in  $35 \text{ pb}^{-1}$  of data with the atlas detector.  
 2875 *ATLAS-CONF-2011-089*, 2011.
- 2876 [87] ATLAS Collaboration. Measurement of the  $b$ -tag Efficiency in a Sample of Jets Containing  
 2877 Muons with  $5 \text{ fb}^{-1}$  of Data from the ATLAS Detector. *ATLAS-CONF-2012-043*, 2012. URL  
 2878 <http://cdsweb.cern.ch/record/1435197>.
- 2879 [88] ATLAS Collaboration. Calibration of  $b$ -tagging using dileptonic top pair events in a combinatorial  
 2880 likelihood approach with the ATLAS experiment. (ATLAS-CONF-2014-004), 2014. URL  
 2881 <http://cds.cern.ch/record/1664335>.

- 2882 [89] Georges Aad et al. Measurement of the Higgs boson mass from the  $H \rightarrow \gamma\gamma$  and  $H \rightarrow ZZ^* \rightarrow$   
 2883  $4\ell$  channels with the ATLAS detector using  $25\text{ fb}^{-1}$  of  $pp$  collision data. *Phys. Rev.*, D90(5):  
 2884 052004, 2014. doi: 10.1103/PhysRevD.90.052004.
- 2885 [90] Georges Aad et al. Measurements of the Higgs boson production and decay rates and coupling  
 2886 strengths using  $pp$  collision data at  $\sqrt{s} = 7$  and  $8\text{ TeV}$  in the ATLAS experiment. *Eur. Phys. J.*,  
 2887 C76(1):6, 2016. doi: 10.1140/epjc/s10052-015-3769-y.
- 2888 [91] W.J. Stirling.  $7/8$  and  $13/8\text{ TeV}$  LHC luminosity ratios. 2013. URL [http://www.hep.ph.ic.ac.uk/~wstirlin/plots/lhclumi7813\\_2013\\_v0.pdf](http://www.hep.ph.ic.ac.uk/~wstirlin/plots/lhclumi7813_2013_v0.pdf).
- 2890 [92] J Alison. Experimental Studies of hh. Oct 2014. URL <http://cds.cern.ch/record/1952581>.
- 2892 [93] J. Alwall et al. The automated computation of tree-level and next-to-leading order differential  
 2893 cross sections, and their matching to parton shower simulations. *JHEP*, 07:079, 2014.
- 2894 [94] Richard D. Ball et al. Parton distributions with LHC data. *Nucl. Phys. B*, 867:244, 2013.
- 2895 [95] ATLAS Collaboration. ATLAS Run 1 Pythia8 tunes. (ATL-PHYS-PUB-2014-021), Nov 2014.  
 2896 URL <https://cds.cern.ch/record/1966419>.
- 2897 [96] M. Bahr et al. Herwig++ Physics and Manual. *Eur. Phys. J. C*, 58:639–707, 2008. doi: 10.1140/  
 2898 epjc/s10052-008-0798-9.
- 2899 [97] Stefan Gieseke, Christian Rohr, and Andrzej Siodmok. Colour reconnections in Herwig++. *Eur.*  
 2900 *Phys. J. C*, 72:2225, 2012. doi: 10.1140/epjc/s10052-012-2225-5.
- 2901 [98] Simone Alioli, Paolo Nason, Carlo Oleari, and Emanuele Re. A general framework for imple-  
 2902 menting NLO calculations in shower Monte Carlo programs: the POWHEG BOX. *JHEP*, 06:  
 2903 043, 2010.
- 2904 [99] Peter Zeiler Skands. Tuning Monte Carlo Generators: The Perugia Tunes. *Phys. Rev. D*, 82:  
 2905 074018, 2010. doi: 10.1103/PhysRevD.82.074018.
- 2906 [100] Michal Czakon and Alexander Mitov. Top++: A Program for the Calculation of the Top-Pair  
 2907 Cross-Section at Hadron Colliders. 2011.
- 2908 [101] Baojia (Tony) Tong. Private communication.
- 2909 [102] D. Krohn, J. Thaler, and L.-T. Wang. Jet Trimming. *JHEP*, 02:084, 2010. doi: 10.1007/  
 2910 JHEP02(2010)084.
- 2911 [103] ATLAS Collaboration. Identification of Boosted, Hadronically Decaying W Bosons and Com-  
 2912 parisons with ATLAS Data Taken at  $\sqrt{s} = 8\text{ TeV}$ . 2015.

- 2913 [104] Expected Performance of Boosted Higgs ( $\rightarrow b\bar{b}$ ) Boson Identification with the ATLAS Detector  
2914 at  $\sqrt{s} = 13$  TeV. Technical Report ATL-PHYS-PUB-2015-035, CERN, Geneva, Aug 2015. URL  
2915 <https://cds.cern.ch/record/2042155>.
- 2916 [105] Flavor Tagging with Track Jets in Boosted Topologies with the ATLAS Detector. Technical  
2917 Report ATL-PHYS-PUB-2014-013, CERN, Geneva, Aug 2014. URL [https://cds.cern.ch/](https://cds.cern.ch/record/1750681)  
2918 [record/1750681](https://cds.cern.ch/record/1750681).
- 2919 [106] Matteo Cacciari and Gavin P. Salam. Pileup subtraction using jet areas. *Phys. Lett. B*, 659:119,  
2920 2008. doi: 10.1016/j.physletb.2007.09.077.
- 2921 [107] Search for pair production of Higgs bosons in the  $b\bar{b}b\bar{b}$  final state using proton-proton collisions  
2922 at  $\sqrt{s} = 13$  TeV with the ATLAS detector. Technical Report ATLAS-CONF-2016-017, CERN,  
2923 Geneva, Mar 2016. URL <https://cds.cern.ch/record/2141006>.
- 2924 [108] Qi Zeng. Private communication.
- 2925 [109] ATLAS Collaboration. Identification of boosted, hadronically-decaying  $W$  and  $Z$  bosons in  
2926  $\sqrt{s} = 13$  TeV Monte Carlo Simulations for ATLAS. (ATL-PHYS-PUB-2015-033), Aug 2015.  
2927 URL <https://cds.cern.ch/record/2041461>.
- 2928 [110] ATLAS Collaboration. Performance of  $b$ -Jet Identification in the ATLAS Experiment. 2015.
- 2929 [111] Alexander L. Read. Presentation of search results: The CL(s) technique. *J. Phys. G*, 28:2693,  
2930 2002. doi: 10.1088/0954-3899/28/10/313.
- 2931 [112] Glen Cowan, Eilam Gross. Discovery significance with statistical uncertainty in the background  
2932 estimate. 2008. URL <http://www.pp.rhul.ac.uk/~cowan/stat/notes/SigCalcNote.pdf>.



**T**HIS THESIS WAS TYPESET using L<sup>A</sup>T<sub>E</sub>X, originally developed by Leslie Lamport and based on Donald Knuth's T<sub>E</sub>X.

The body text is set in 11 point Egenolff-Berner Garamond, a revival of Claude Garamont's humanist typeface. The above illustration, *Science Experiment 02*, was created by Ben Schlitter and released under CC BY-NC-ND 3.0. A template that can be used to format a PhD dissertation with this look & feel has been released under the permissive AGPL license, and can be found online at [github.com/asm-products/Dissertate](https://github.com/asm-products/Dissertate) or from its lead author, Jordan Suchow, at [suchow@post.harvard.edu](mailto:suchow@post.harvard.edu).